AD-A068 758 AIR FORCE AVIONICS LAB WRIGHT-PATTERSON AFB OH F/G 20/14
THE EFFECT OF IONOSPHERIC SCINTILLATIONS FADING ON AIRCRAFT-TO---ETC(U)
FEB 79 A J JOHNSON

UNCLASSIFIED AFAL-TR-78-171 NL

1 OF 2

AD A068758

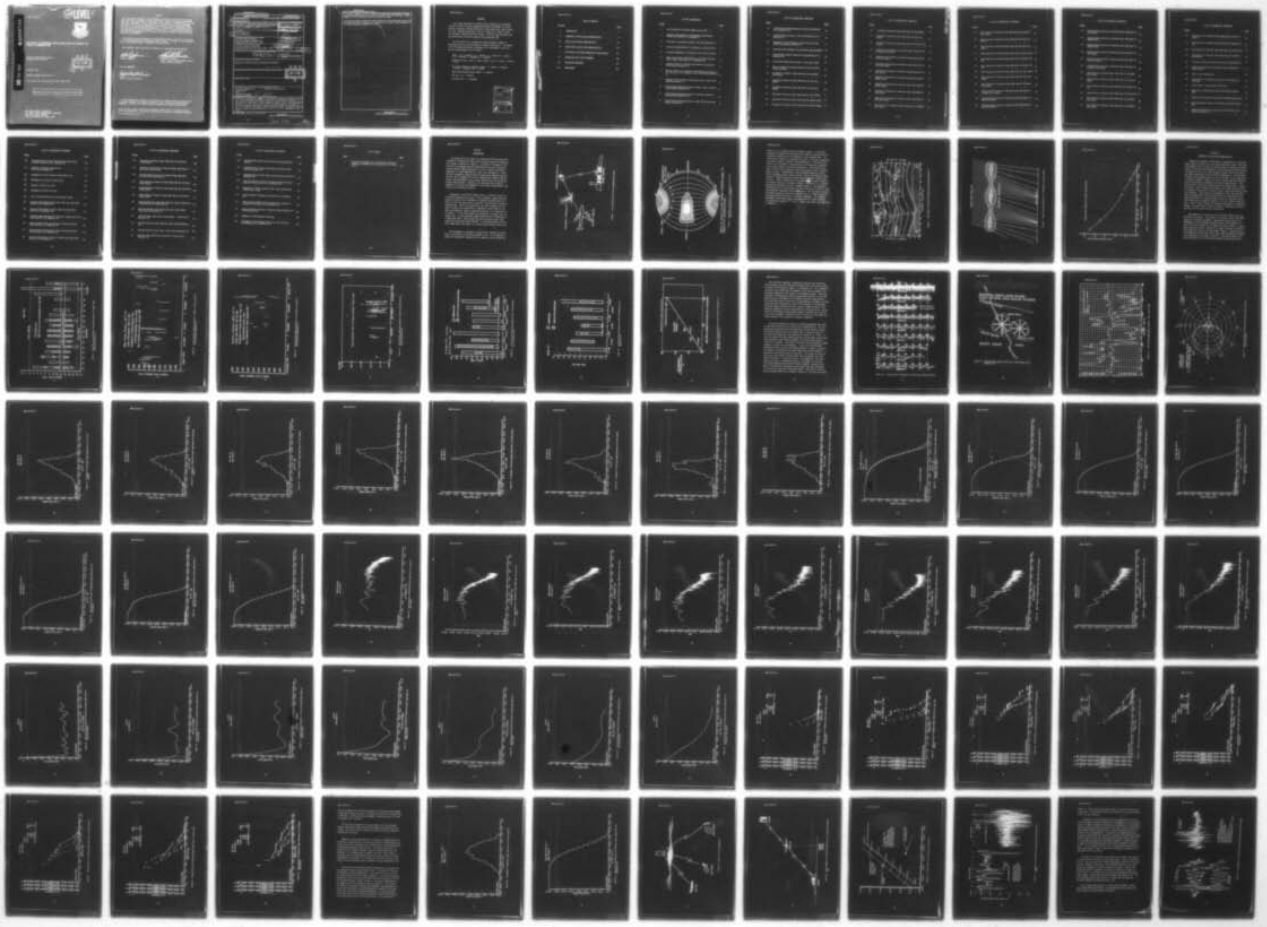

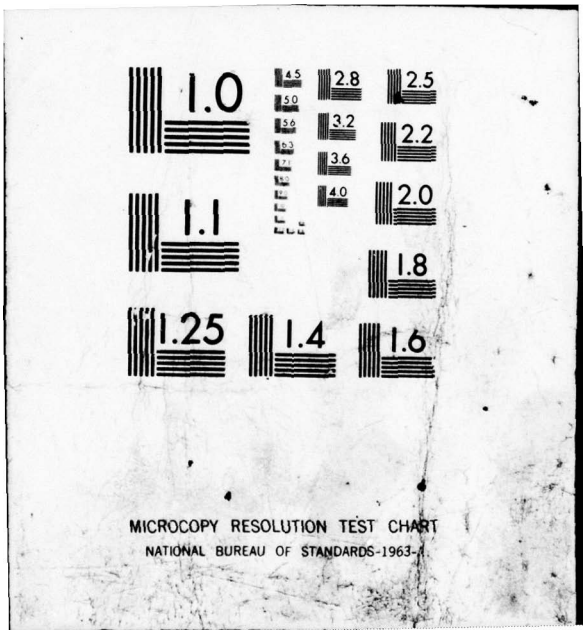
1.0
1.1
1.25
1.4
1.6
1.8
2.0
2.2
2.5
2.8
3.2
3.6
4.0
4.5
5.0
5.6
6.3
7.1
8.0
9.0
MICROCOPY RESOLUTION TEST CHART
NATIONAL BUREAU OF STANDARDS-1963-A

AD A068758

DDC FILE COPY

AFAL-TR-78-171

(2) LEVEL II

THE EFFECT OF IONOSPHERIC SCINTILLATION FADING ON AIRCRAFT-TO-SATELLITE COMMUNICATIONS

Avionics Communication Branch
System Avionics Division

DDC
RECEIVED
MAY 21 1979
B

February 1979

TECHNICAL REPORT AFAL-TR-78-171

Final Report for Period January 1976 to May 1978

Approved for public release; distribution unlimited.

AIR FORCE AVIONICS LABORATORY
AIR FORCE WRIGHT AERONAUTICAL LABORATORY
AIR FORCE SYSTEM COMMAND
WRIGHT-PATTERSON AFB, OHIO 45433

79 05 15 051

NOTICE

When Government drawings, specifications, or other data are used for any purpose other than in connection with a definitely related Government procurement operation, the United States Government thereby incurs no responsibility nor any obligation whatsoever; and the fact that the government may have formulated, furnished, or in any way supplied the said drawings, specifications, or other data, is not to be regarded by implication or otherwise as in any manner licensing the holder or any other person or corporation, or conveying any rights or permission to manufacture, use, or sell any patented invention that may in any way be related thereto.

This report has been reviewed by the Information Office (OI) and is releasable to the National Technical Information Service (NTIS). At NTIS, it will be available to the general public, including foreign nations.

This technical report has been reviewed and is approved for publication.

ALLEN L. JOHNSON,
Project Engineer

CHARLES C. GAUDER
Chief, Avionic Communications Branch
System Avionics Division

FOR THE COMMANDER

RAYMOND E. SIFERD, Lt Col, USAF
Chief
System Avionics Division

"If your address has changed, if you wish to be removed from our mailing list, or if the addressee is no longer employed by your organization please notify AFAL/AAD ,W-PAFB, OH 45433 to help us maintain a current mailing list".

Copies of this report should not be returned unless return is required by security considerations, contractual obligations, or notice on a specific document.

AIR FORCE/56780/24 April 1979 — 400

UNCLASSIFIED

SECURITY CLASSIFICATION OF THIS PAGE (When Data Entered)

REPORT DOCUMENTATION PAGE	READ INSTRUCTIONS BEFORE COMPLETING FORM
1. REPORT NUMBER: AFAL-TR-78-171	2. GOVT ACCESSION NO. / 3. RECIPIENT'S CATALOG NUMBER
4. TITLE (and Subtitle): THE EFFECT OF IONOSPHERIC SCINTILLATION FADING ON AIRCRAFT-TO-SATELLITE COMMUNICATIONS	5. TYPE OF REPORT & PERIOD COVERED: Final Technical Report. Jan 76 - May 78
7. AUTHOR(s): Allen L. Johnson	8. CONTRACT OR GRANT NUMBER(s)
9. PERFORMING ORGANIZATION NAME AND ADDRESS: Systems Avionics Division, Air Force Avionics Laboratory, Wright-Patterson AFB, Ohio 45433	10. PROGRAM ELEMENT, PROJECT, TASK AREA & WORK UNIT NUMBERS: Project 1227, Task 122703, Work Unit 12270313
11. CONTROLLING OFFICE NAME AND ADDRESS: Air Force Avionics Laboratory, Wright-Patterson Air Force Base, Ohio 45433	12. REPORT DATE: Feb 1979 / 13. NUMBER OF PAGES: 160
14. MONITORING AGENCY NAME & ADDRESS (if different from Controlling Office)	15. SECURITY CLASS. (of this report): Unclassified / 15a. DECLASSIFICATION/DOWNGRADING SCHEDULE

16. DISTRIBUTION STATEMENT (of this Report)

Approved for Public Release; Distribution Unlimited.

63431F

17. DISTRIBUTION STATEMENT (of the abstract entered in Block 20, if different from Report)

DDC RECEIVED MAY 21 1979 B

18. SUPPLEMENTARY NOTES

19. KEY WORDS (Continue on reverse side if necessary and identify by block number)

Satellite Communication
Scintillation
Fading
Polar Scintillation
Ionospheric Anomalies
Equatorial Scintillation

20. ABSTRACT (Continue on reverse side if necessary and identify by block number)

Ionospheric scintillation fading on a UHF earth-to-satellite communication link has a strong dependence on season, time-of-day, and geographic location. In the equatorial region ± 20° from the magnetic equator, 20 to 30 dB fades can be expected 1 to 2 hours after sunset during the equinox period. Airborne terminals may experience fade rates as fast as 1 fade per second to as slow as 1 fade in 90 seconds, depending on the direction of flight. The amplitude fading follows a power low distribution with a rate of F^{-2} to F^{-4} depending on fade rate.

DD FORM 1 JAN 73 1473 EDITION OF 1 NOV 65 IS OBSOLETE

UNCLASSIFIED

SECURITY CLASSIFICATION OF THIS PAGE (When Data Entered)

AD A070 670

In the polar region an airborne terminal may experience ionospheric scintillation more often than near the equator but usually with less amplitude. Polar fading of 10 dB or less may occur 10 to 30% of the time.

In the mid latitudes occasional random ionospheric scintillation may occur, but the fade depth and occurrence are so small as to pose only a minor annoyance to an airborne satellite communication system.

FOREWORD

This report describes an in-house effort conducted in the Systems Avionics Division, Avionics Communication Branch (AFAL/AAD), Air Force Avionics Laboratory, Wright-Patterson Air Force Base, Ohio, under Project No. 1227, "Terminal Technology," Task No. 122703 "Test Efforts," Work Unit 12270313 "SATCOM Flight Test Effort." The work reported herein was performed during the period January 1976 through May 1978.

The test effort was a cooperative venture between a number of Government agencies with the support of several contractors. The support of the following individuals and agencies was instrumental in the successful accomplishment of this effort:

AFAL: T. A. Grizinski, R. L. Swanson, J. J. Foshee, R. C. Beach, W. O. Fischbach, P. Heidkamp, G. J. Johnson

4950th Test Wing: Capt. R. Ewart, T/Sgt J. Cary, P. Frank, S. Wilson, R. Chin

Air Force Geophysics Laboratory (AFGL): J. Aarons, H. Whitney, J. Mullen, J. Buchau, Capt. E. Weber

Naval Ocean Systems Center (NOSC): R. Hopkins

ESL Inc: Dr. C. Prettie

Sylvania Corp.: K. Dusenbury

ACCESSION for
NTIS White Section ☑
DDC Buff Section ☐
UNANNOUNCED ☐
JUSTIFICATION
BY
DISTRIBUTION/AVAILABILITY CODES
Dist. AVAIL. and/or SPECIAL
A

TABLE OF CONTENTS

SECTION		PAGE
I	INTRODUCTION	1
II	EQUATORIAL SCINTILLATION CHARACTERISTICS	8
III	POLAR SCINTILLATION CHARACTERISTICS	87
IV	MIDLATITUDE SCINTILLATION CHARACTERISTICS	110
V	ARTIFICIALLY DISTURBED IONOSPHERIC SCINTILLATION	112
VI	CORRELATION WITH OTHER PHENOMENA	142
VII	MITIGATION TECHNIQUES	147
VIII	CONCLUSIONS	151

LIST OF ILLUSTRATIONS

FIGURE		PAGE
1	Air-To-Satellite-To-Ground Communication Path	2
2	Geographic Distribution of Ionospheric Scintillation Fading (From Aarons et al Reference 3)	3
3	World Map of Invariant Latitude (From Crane Reference 7)	5
4	Simplified Representation of Ionospheric Focusing Effect	6
5	Frequency Dependence of Ionospheric Scintillation Fading	7
6	Model of Estimated Scintillation $\geq$ 4.5 dB Over the Equatorial Region (From BASU et al Reference 10)	9
7	Seasonal Pattern of 250 MHz Fades Observed at Kwajalein (From Nichols Reference 11)	9
8	Monthly Contour Plot Showing the Percentage Occurrence of SI $\geq$ 60 ($S_4 \geq 0.3$) at Huancayo, Peru (From Aarons Reference 4)	10
9	Duration of Scintillation Fading Occurrence in Guam (From Johnson Reference 12)	11
10	Scintillation Fading Occurrence in Manus Island, Australia (From Barkham Reference 13)	12
11	Scintillation Fading Occurrence in Innisfail, Australia (From Barkham Reference 13)	13
12	Scintillation Fading Occurrence in Guam (From Paulson and Hopkins Reference 6)	14

LIST OF ILLUSTRATIONS (CONTINUED)

FIGURE		PAGE
13	Scintillation Fading Occurrence in Peru (From Whitney et al Reference 14)	15
14	Scintillation Occurrence In Peru (From Whitney et al Reference 14)	16
15	Dependence of Scintillation on Solar Activity (From Paulson and Hopkins Reference 6)	17
16	Equatorial UHF Ionospheric Scintillation Fade Variations	19
17	Scintillation Studies Flight Path (From Whitney et al Reference 14)	20
18	Scintillation Amplitude and Rate: Peru Local Flight	21
19	Ratio of Airborne-to-Ground Fade Rate versus Aircraft Flight Direction	22
20	Histogram of Received Signal Amplitude for Extremely Fast Fading	24
21	Histogram of Received Signal Amplitude for Very Fast Fading	25
22	Histogram of Received Signal Amplitude for Very Fast Fading	26
23	Histogram of Received Signal Amplitude for Fast Fading	27
24	Histogram of Received Signal Amplitude for Medium Fading	28
25	Histogram of Received Signal Amplitude for Medium Fading	29

LIST OF ILLUSTRATIONS (CONTINUED)

FIGURE		PAGE
26	Histogram of Received Signal Amplitude for Slow Fading	30
27	Histogram of Received Signal Amplitude for Very Slow Fading	31
28	Histogram of Received Signal Amplitude for Extremely Slow Fading	32
29	Cumulative Distribution of Received Signal Amplitude for Extremely Fast Fading	33
30	Cumulative Distribution of Received Signal Amplitude for Very Fast Fading	34
31	Cumulative Distribution of Received Signal Amplitude for Very Fast Fading	35
32	Cumulative Distribution of Received Signal Amplitude for Fast Fading	36
33	Cumulative Distribution of Received Signal Amplitude for Medium Fading	37
34	Cumulative Distribution of Received Signal Amplitude for Medium Fading	38
35	Cumulative Distribution of Received Signal Amplitude for Slow Fading	39
36	Cumulative Distribution of Received Signal Amplitude for Very Slow Fading	40
37	Power Spectrum of Received Signal Amplitude for Extremely Fast Fading	41

LIST OF ILLUSTRATIONS (CONTINUED)

FIGURE		PAGE
38	Power Spectrum of Received Signal Amplitude for Extremely Fast Fading	42
39	Power Spectrum of Received Signal Amplitude for Very Fast Fading	43
40	Power Spectrum of Received Signal Amplitude for Very Fast Fading	44
41	Power Spectrum of Received Signal Amplitude for Fast Fading	45
42	Power Spectrum of Received Signal Amplitude for Medium Fading	46
43	Power Spectrum of Received Signal Amplitude for Medium Fading	47
44	Power Spectrum of Received Signal Amplitude for Slow Fading	48
45	Power Spectrum of Received Signal Amplitude for Very Slow Fading	49
46	Power Spectrum of Received Signal Amplitude for Extremely Slow Fading	50
47	Autocorrelation Function of Received Signal Amplitude for Extremely Fast Fading	51
48	Autocorrelation Function of Received Signal Amplitude for Very Fast Fading	52
49	Autocorrelation Function of Received Signal Amplitude for Very Fast Fading	53

LIST OF ILLUSTRATIONS (CONTINUED)

FIGURE		PAGE
50	Autocorrelation Function of Received Signal Amplitude for Fast Fading	54
51	Autocorrelation Function of Received Signal Amplitude for Medium Fading	55
52	Autocorrelation Function of Received Signal Amplitude for Medium Fading	56
53	Autocorrelation Function of Received Signal Amplitude for Slow Fading	57
54	Autocorrelation Function of Received Signal Amplitude for Very Slow Fading	58
55	Autocorrelation Function of Received Signal Amplitude for Extremely Slow Fading	59
56	Fading Period of Received Signal Amplitude for Extremely Fast Fading	60
57	Fading Period of Received Signal Amplitude for Very Fast Fading	61
58	Fading Period of Received Signal Amplitude for Medium Fading	62
59	Fading Period of Received Signal Amplitude for Slow Fading	63
60	Fading Period of Received Signal Amplitude for Extremely Slow Fading	64
61	Fade Duration of Received Signal Amplitude for Extremely Fast Fading	65

LIST OF ILLUSTRATIONS (CONTINUED)

FIGURE		PAGE
62	Fade Duration of Received Signal Amplitude for Very Fast Fading	66
63	Fade Duration of Received Signal Amplitude for Medium Fading	67
64	Fade Duration of Received Signal Amplitude for Slow Fading	68
65	Fade Duration of Received Signal Amplitude for Extremely Slow Fading	69
66	Histogram of Received Signal Amplitude for Ground Station	71
67	Cumulative Distribution of Received Signal Amplitude for Ground Station	72
68	Pacific Test Configuration	73
69	Displacement of Aircraft Ground Track to Intercept Satellite Ray	74
70	Ground Track of Scintillation Flight Test	75
71	Comparison of Airborne and Ground Scintillation Fading Data	76
72	Comparison of Airborne and Ground Scintillation Fading Data	78
73	Cross-Correlation Function for Airborne and Ground Fading Data	79
74	Equatorial Received Signal Amplitude Scintillation (From Prettie Reference 16)	80

LIST OF ILLUSTRATIONS (CONTINUED)

FIGURE		PAGE
75	Equatorial Received Signal Phase Scintillation (From Prettie Reference 16)	81
76	Equatorial Received Signal Amplitude Scintillation (From Prettie Reference 16)	82
77	Equatorial Received Signal Phase Scintillation (From Prettie Reference 16)	83
78	Comparison of Equatorial Scintillation Fading Parameters	84
79	Simultaneous UHF and SHF Scintillation Fading	86
80	High Latitude Scintillation Fading Occurrence for December (From Aarons et al Reference 5)	88
81	High Latitude Scintillation Fading Occurrence for June (From Aarons et al Reference 5)	89
82	Representation of Five High Latitude Ionospheric Paths (From Aarons et al Reference 3)	90
83	Compilation of Ground and Airborne Scintillation Test Results (From Aarons et al Reference 3)	91
84	Cumulative Distribution of Scintillation Index (From Aarons et al Reference 3)	94
85	Polar Locations Where Scintillation Fading Was Encountered	94
86	Greenland Locations Where Scintillation Was Encountered	95
87	Received Signal Amplitude Variations During Polar Scintillation	96

LIST OF ILLUSTRATIONS (CONTINUED)

FIGURE		PAGE
88	Histogram of Received Signal Amplitude for Polar Scintillation	97
89	Histogram of Received Signal Amplitude for Polar Scintillation	98
90	Cumulative Distribution of Received Signal Amplitude for Polar Scintillation	99
91	Cumulative Distribution of Received Signal Amplitude for Polar Scintillation	100
92	Autocorrelation Function of Received Signal Amplitude for Polar Scintillation	101
93	Autocorrelation Function of Received Signal Amplitude for Polar Scintillation	102
94	Fading Period of Received Signal Amplitude for Polar Scintillation	103
95	Fading Period of Received Signal Amplitude for Polar Scintillation	104
96	Fading Duration of Received Signal Amplitude for Polar Scintillation	105
97	Fading Duration of Received Signal Amplitude for Polar Scintillation	106
98	Power Spectrum of Received Signal Amplitude for Polar Scintillation	107
99	Power Spectrum of Received Signal Amplitude for Polar Scintillation	108

LIST OF ILLUSTRATIONS (CONTINUED)

FIGURE		PAGE
100	Detrended Received Signal Recordings for Polar Scintillation (From Rino et al Reference 8)	109
101	Examples of Ringing Irregularities (From Slack Reference 21)	111
102	Propagation of Free Electrons Along Field Lines	113
103	Development of Ionized Irregularities	114
104	Movement of Barium Ion Cloud	115
105	Photograph of Barium Ion Cloud	116
106	Plot of Aircraft Ground Track During Test Flight	117
107	Received Signal Amplitude for Early Time Ion Cloud (From Prettie et al Reference 22)	120
108	Received Signal Phase for Early Time Ion Cloud (From Prettie et al Reference 22)	121
109	Received Signal Amplitude for Partially Striated Ion Cloud (From Prettie et al Reference 22)	122
110	Received Signal Phase for Partially Striated Ion Cloud (From Prettie et al Reference 22)	123
111	Received Signal Amplitude for Fully Striated Ion Cloud (From Prettie et al Reference 22)	124
112	Received Signal Phase for Fully Striated Ion Cloud (From Prettie et al Reference 22)	125

LIST OF ILLUSTRATIONS (CONTINUED)

FIGURE		PAGE
113	Histogram of Received Signal Amplitude for Artificial Scintillation	126
114	Cumulative Distribution of Received Signal Amplitude for Artificial Scintillation	127
115	Autocorrelation Function of Received Signal Amplitude for Artificial Scintillation	128
116	Power Spectrum of Received Signal Amplitude for Artificial Scintillation	129
117	Fading Duration of Received Signal Amplitude for Artificial Scintillation	130
118	Fading Period of Received Signal Amplitude for Artificial Scintillation	131
119	Predicted Received Signal Amplitude for Single Irregularity (From Prettie et al Reference 22)	132
120	Measured Received Signal Amplitude (Early Time Effect) (From Prettie Reference 16)	133
121	Received Signal Phase (Early Time Effect) - (From Prettie Reference 16)	134
122	Expanded Received Signal Amplitude (From Prettie Reference 16)	135
123	Expanded Received Signal Phase (From Prettie Reference 16)	136
124	Received Signal Amplitude Scintillation (From Prettie Reference 16)	137

LIST OF ILLUSTRATIONS (CONTINUED)

FIGURE		PAGE
125	Received Signal Phase Scintillation (From Prettie Reference 16)	138
126	Expanded Received Signal Amplitude Scintillation (From Prettie Reference 16)	139
127	Expanded Received Signal Phase Scintillation (From Prettie Reference 16)	140
128	Cross Correlation of Uplink and Downlink Received Signal Amplitude (From Prettie et al Reference 22)	141
129	Comparison of 50 MHz Jicamarca Radar Return and 250 MHz Scintillation Fading	143
130	Airborne Digital Ionograms (From Buchau et al Reference 23)	144
131	6300 Å Airglow Showing Electron Depletion in Equatorial Ionosphere (From Weber et al Reference 15)	146
132	Cross Correlation Function of Received Signal Amplitude on Two UHF Satellites	148
133	Geometry of Fade Mitigation Technique	149
134	Histogram of Scintillation Index Levels for Ancon Peru (From Whitney et al Reference 14)	152

LIST OF TABLES

TABLE		PAGE
1	Occurrence Frequencies of Scintillation Indices by Regimes for September Test (From Aarons et al Reference 3)	92

SECTION I

INTRODUCTION

The objective of this report is to describe the limitations which ionospheric irregularities impose upon aircraft-to-satellite communication systems as depicted in Figure 1. The effect of ionospheric scintillation on ground-to-satellite communications has been extensively reported [Aarons, et al (References 1,2,3,4,5), Paulson and Hopkins (Reference 6), Crane (Reference 7), Rino, et al Reference 8]. While the same ionospheric irregularities are causing the communication problem for both the ground and aircraft communication terminal, the resultant characteristics of the airborne fading differ from the ground fading characteristics. Therefore, the techniques which might be employed to alleviate the ionospheric scintillation fading effects will differ for the airborne situation.

Ionospheric scintillation fading occurs as a result of sharp ion or electron gradients which occur in the ionosphere. These sharp gradients are caused by the ionospheric irregularities which tend to refract or focus the radio waves as they pass from the earth's surface to the satellite. While the irregularities can occur anywhere over the earth's surface, the probability of occurrence is more likely in the polar and equatorial region as depicted by Aarons, et al (Reference 3) in Figure 2. In the polar regions the occurrence is greatest near the auroral oval. In the equatorial region scintillation is predominantly a night-time effect, usually occurring one to two hours after local sunset and lasting past local midnight. In the midlatitudes scintillation seldom occurs and usually is of short duration when it does occur.

The development of ionospheric irregularities leading to scintillation is controlled by the earths magnetic field. In the equatorial region the ionospheric irregularities are magnetic field alignned and

Figure 1. Air-To-Satellite-To-Ground Communication Path

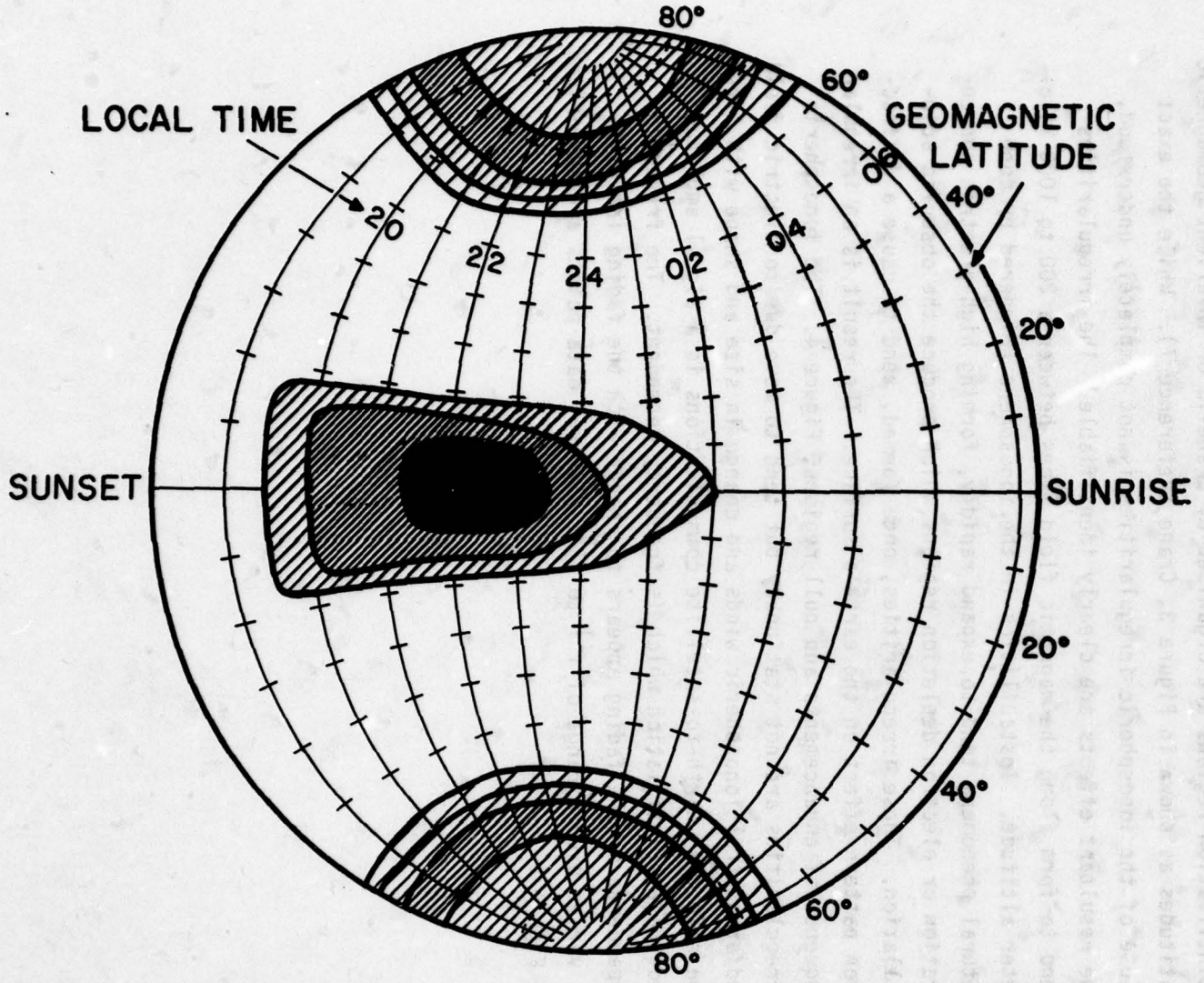

Figure 2. Geographic Distribution of Ionospheric Scintillation Fading (From Aarons et al Reference 3)

extend ± 15° in latitude around the magnetic equator. In the high latitudes the magnetic field controls the location of the partide precipitation responsible for the formation of the irregularities. The scintillation regions are organized by L-shells or invarient geomagnetic latitudes as shown in Figure 3, Crane (Reference 7). While the exact cause of the ionospheric irregularities is not completely understood, the resultant effects are clearly identifiable. The irregularities tend to form along the magnetic field lines between a 200 to 1000 kilometer altitude. Instabilities in the ionosphere triggered by some natural phenomena tend to expand rapidly, forming high electron concentration or electron depletion regions which produce the observed scintillation. These irregularities, once formed, tend to cause a diffraction pattern effect on the earth's surface. The result is an irregular sequence of enhancements and null regions, Figure 4. The ionospheric irregularities are not stationary but tend to move due to electric field and/or neutral ionospheric winds and change in size and shape with time. The effect on earth-to-satellite communications is a signal amplitude and phase scintillation which is frequency dependent. The frequency dependence of the fading appears to change with the fading intensity. It varies over a range of f^{-1} to f^{-3}. Several data points are summarized in Figure 5.

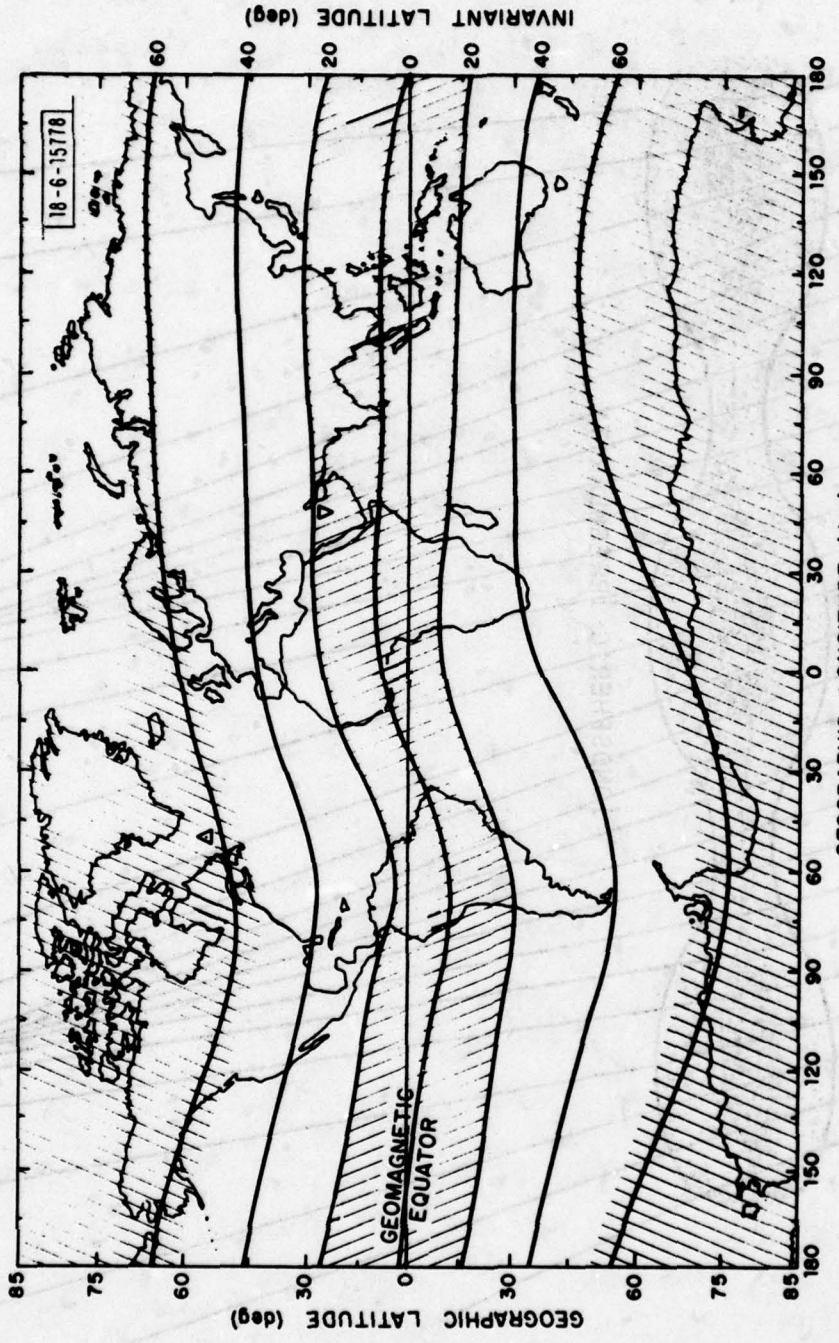

Figure 3. World Map of Invariant Latitude (From Crane Reference 7)

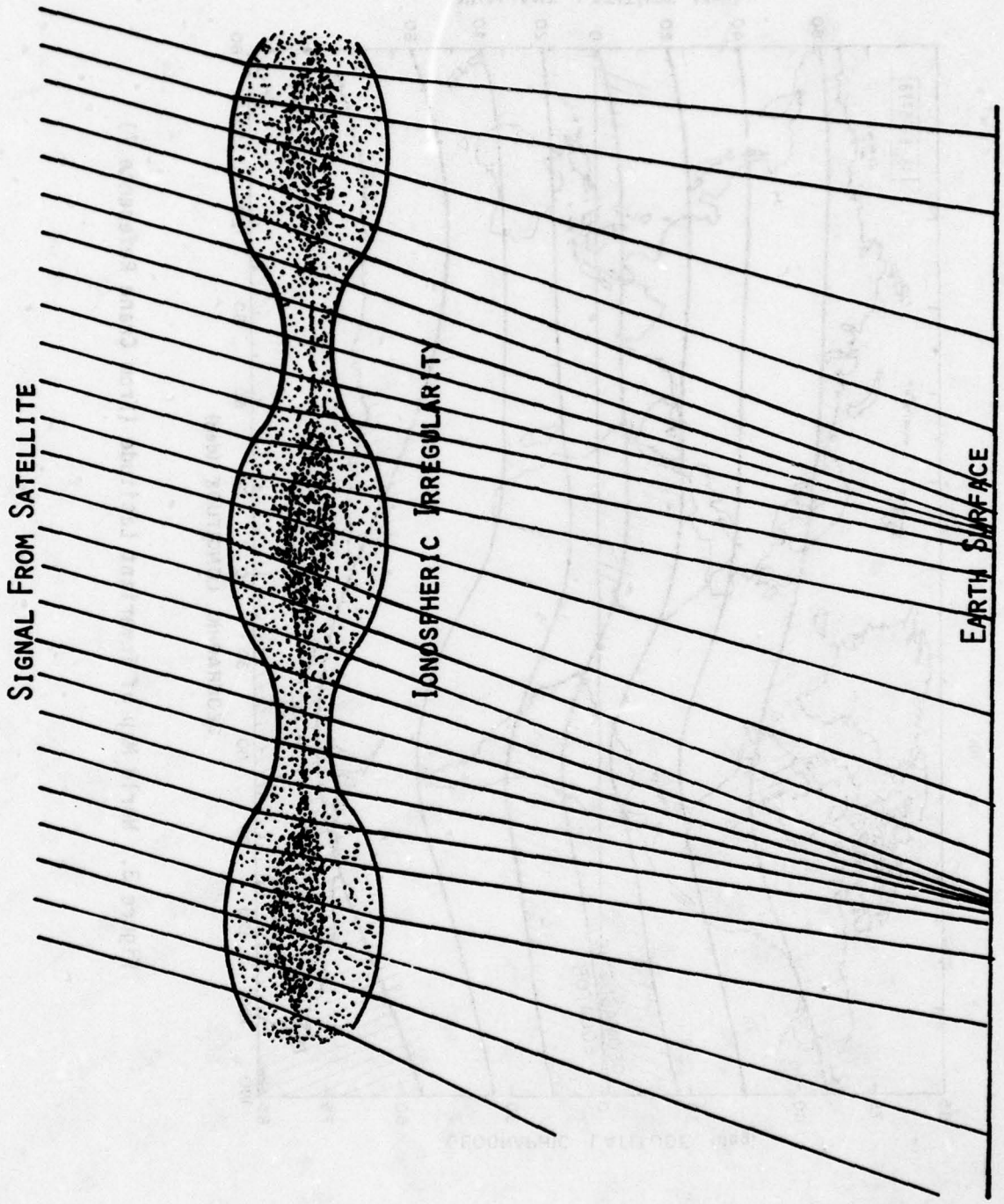

Figure 4. Simplified Representation of Ionospheric Focusing Effect

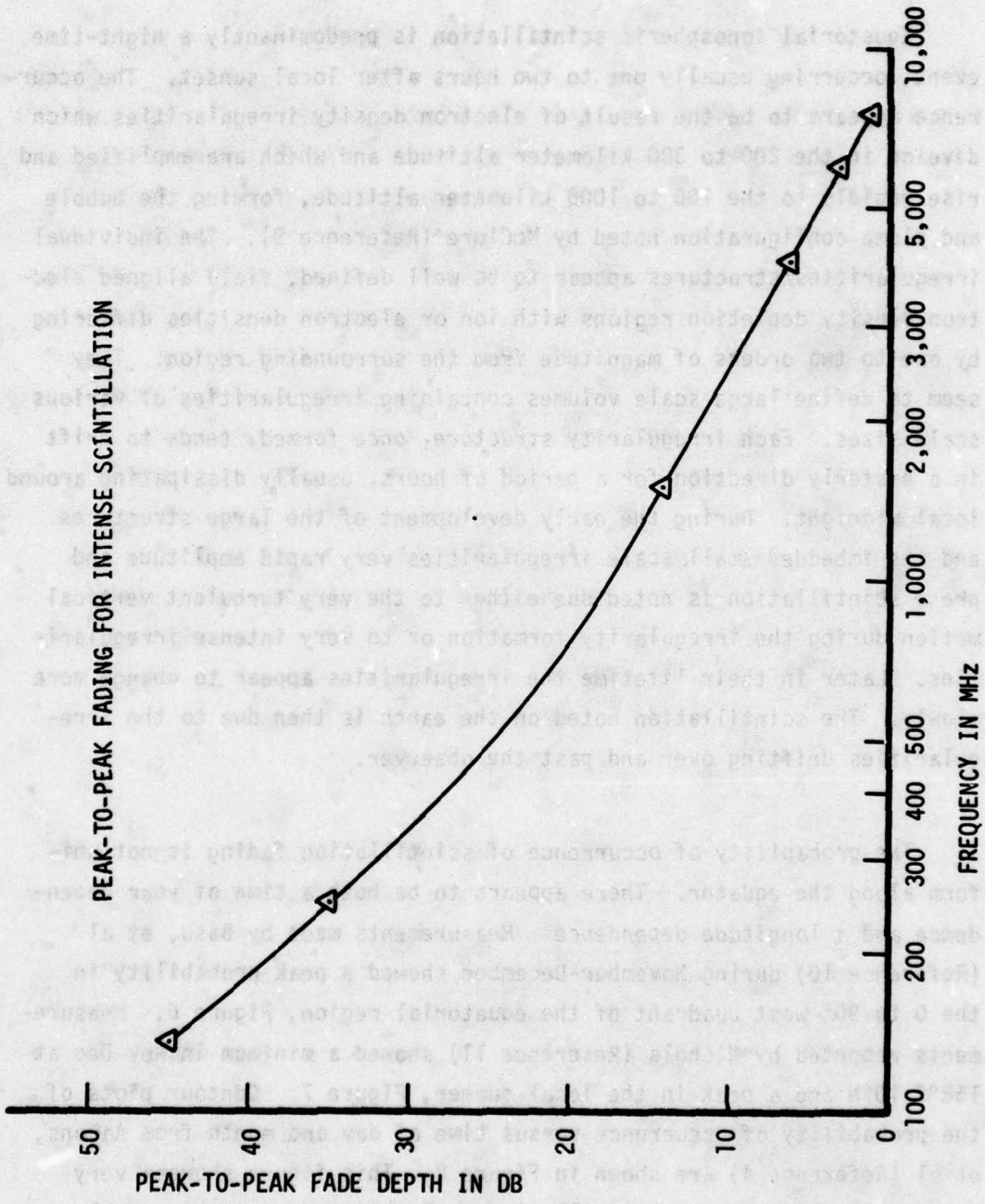

Figure 5. Frequency Dependence of Ionospheric Scintillation Fading

SECTION II

EQUATORIAL SCINTILLATION CHARACTERISTICS

Equatorial ionospheric scintillation is predominantly a night-time event, occurring usually one to two hours after local sunset. The occurrence appears to be the result of electron density irregularities which develop in the 200 to 300 kilometer altitude and which are amplified and rise rapidly to the 700 to 1000 kilometer altitude, forming the bubble and plume configuration noted by McClure (Reference 9). The individual irregularities/structures appear to be well defined, field aligned electron density depletion regions with ion or electron densities differing by one to two orders of magnitude from the surrounding region. They seem to define large scale volumes containing irregularities of various scale sizes. Each irregularity structure, once formed, tends to drift in a easterly direction for a period of hours, usually dissipating around local midnight. During the early development of the large structures and the imbedded small scale irregularities very rapid amplitude and phase scintillation is noted due either to the very turbulent vertical motion during the irregularity formation or to very intense irregularities. Later in their lifetime the irregularities appear to change more slowly. The scintillation noted on the earth is then due to the irregularities drifting over and past the observer.

The probability of occurrence of scintillation fading is not uniform along the equator. There appears to be both a time of year dependence and a longitude dependence. Measurements made by Basu, et al (Reference 10) during November-December showed a peak probability in the 0 to 90° west quadrant of the equatorial region, Figure 6. Measurements reported by Nichols (Reference 11) showed a minimum in Nov-Dec at 168°E 10°N and a peak in the local summer, Figure 7. Contour plots of the probability of occurrence versus time of day and month from Aarons, et al (Reference 4) are shown in Figure 8. This figure shows a very definite peaking of the scintillation probability during the vernal

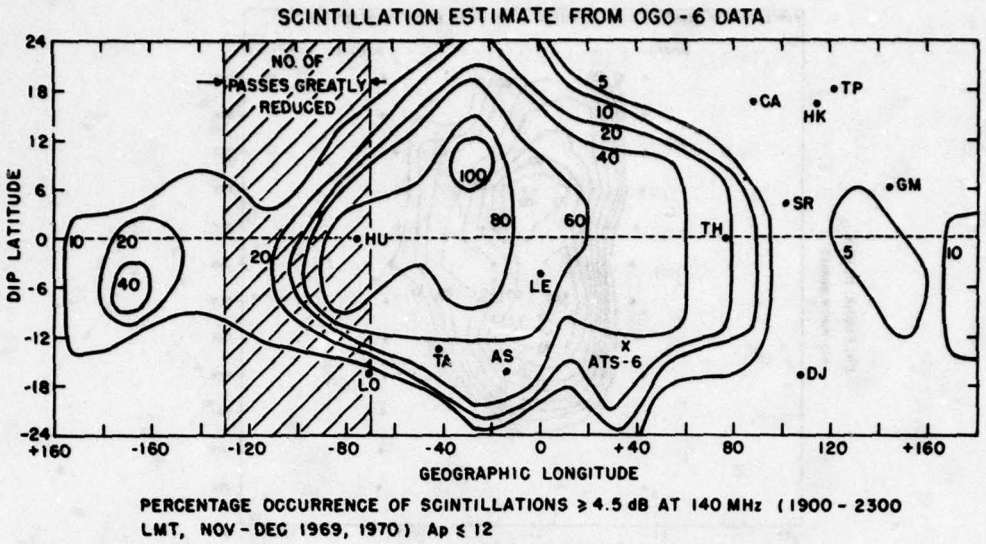

Figure 6. Model of Estimated Scintillation $\geq$ 4.5 dB Over the Equatorial Region (From BASU et al Reference 10)

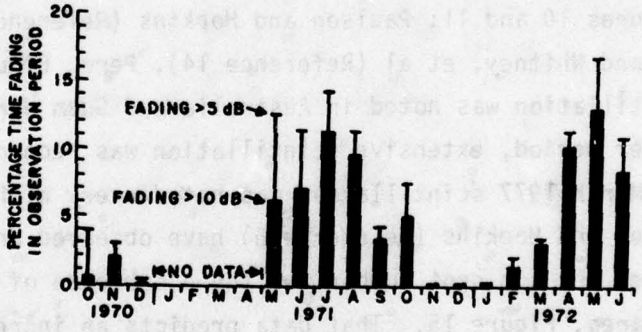

Figure 7. Seasonal Pattern of 250 MHz Fades Observed at Kwajalein (From Nichols Reference 11)

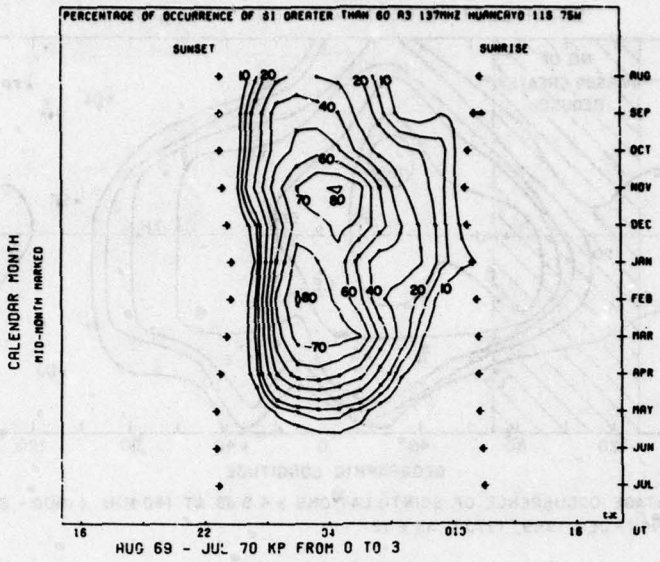

Figure 8. Monthly Contour Plot Showing the Percentage Occurrence of SI $\geq$ 60 ($S_4 \geq 0.3$) at Huancayo, Peru (From Aarons Reference 4)

and autumnal equinox periods. The nightly occurrence of scintillation at Guam was shown by Johnson (Reference 12), Figure 9. During the Fall of 1976 scintillation occurrence data was taken by Barkham (Reference 13) in Australia, Figures 10 and 11; Paulson and Hopkins (Reference 6) in Guam, Figure 12; and Whitney, et al (Reference 14), Peru, Figure 13. While little scintillation was noted in Australia and Guam during the mid to late October period, extensive scintillation was recorded in Peru. During a test in March 1977 scintillation was noted every night in Peru, Figure 14. Paulson and Hopkins (Reference 6) have observed an apparent correlation between the sun spot number and the occurrence of scintillation in the Guam area, Figure 15. That data predicts an increased activity of equatorial scintillation with the upcoming sun spot maximum in 1981.

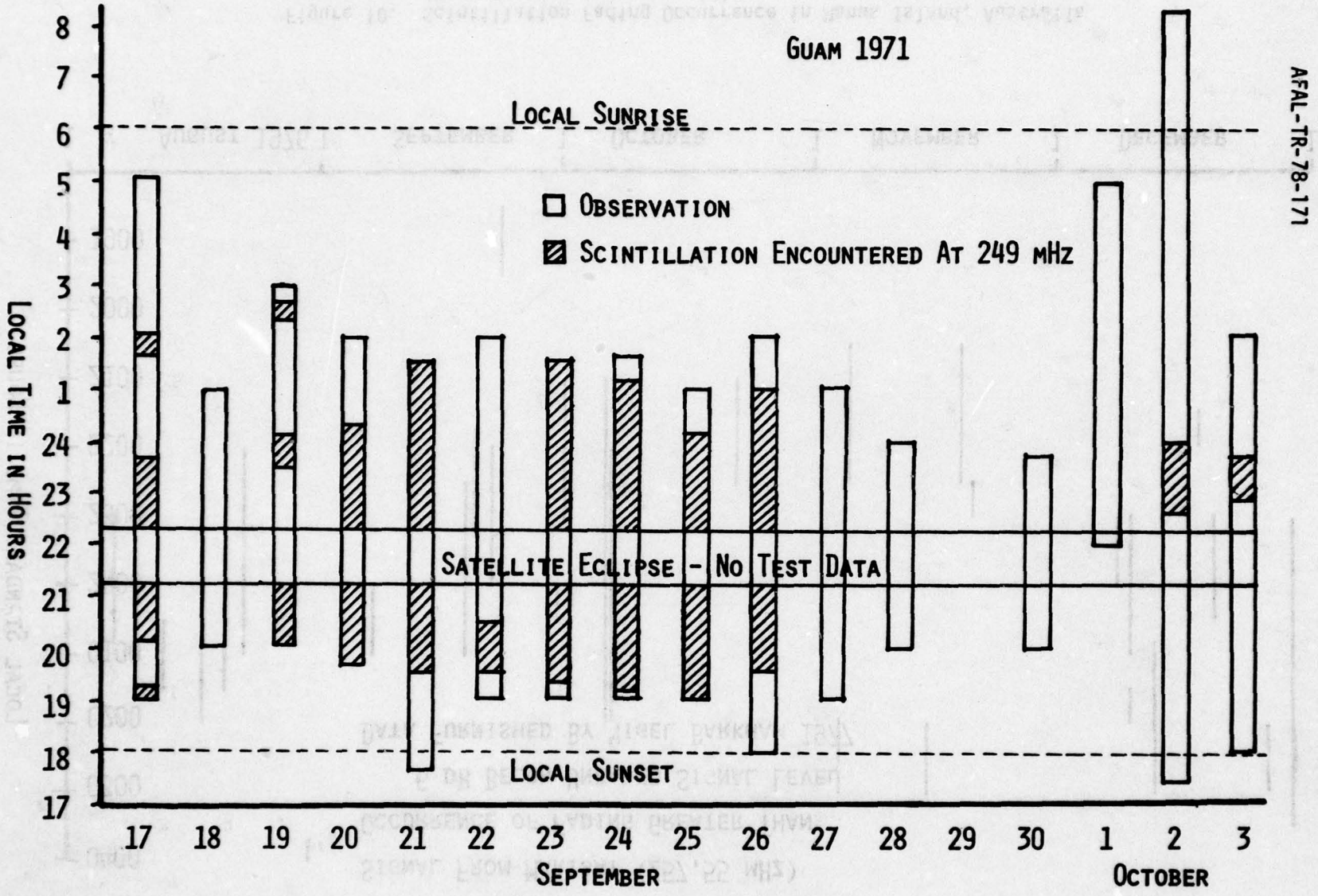

Figure 9. Duration of Scintillation Fading Occurrence in Guam (From Johnson Reference 12)

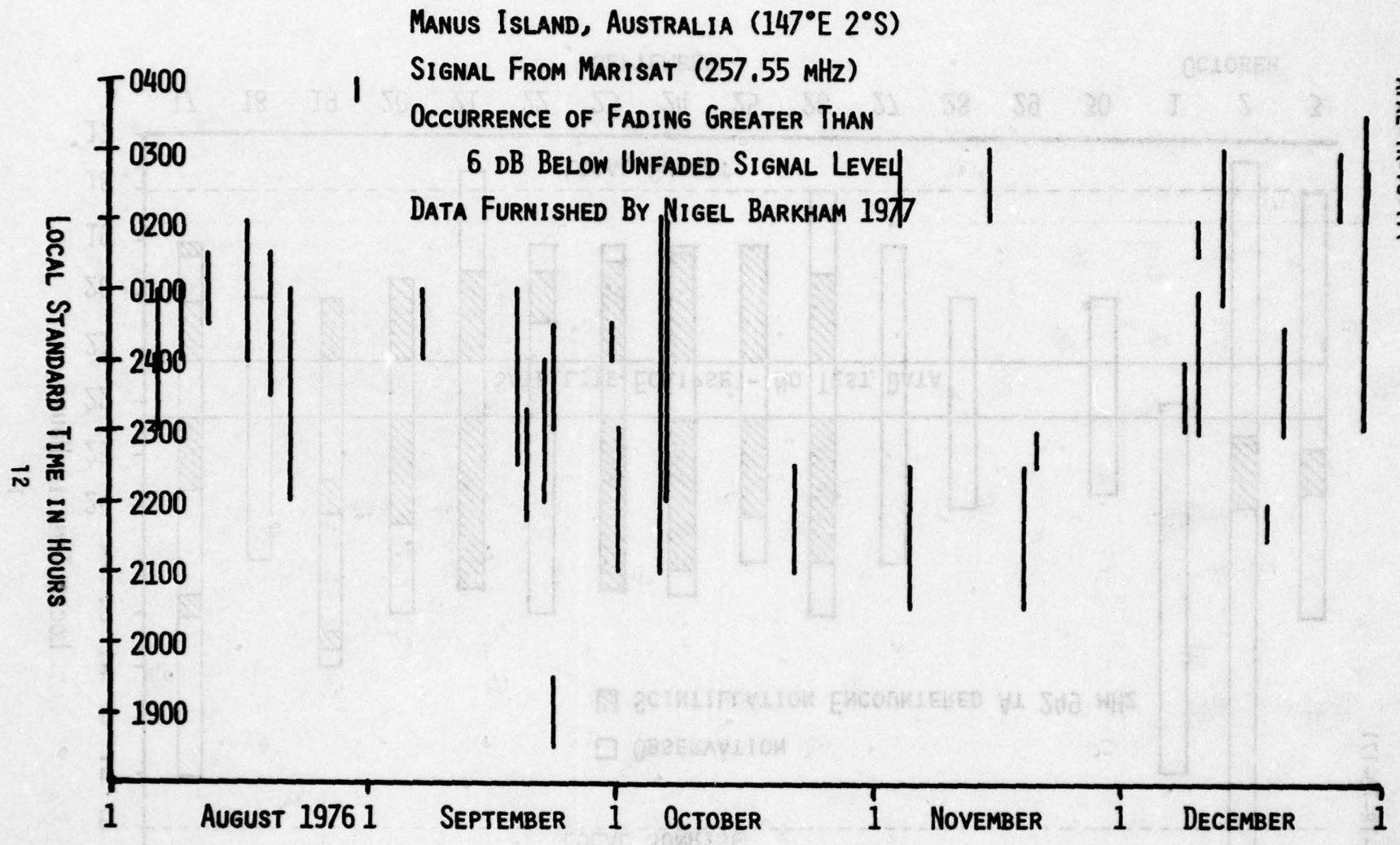

Figure 10. Scintillation Fading Occurrence in Manus Island, Australia (From Barkham Reference 13)

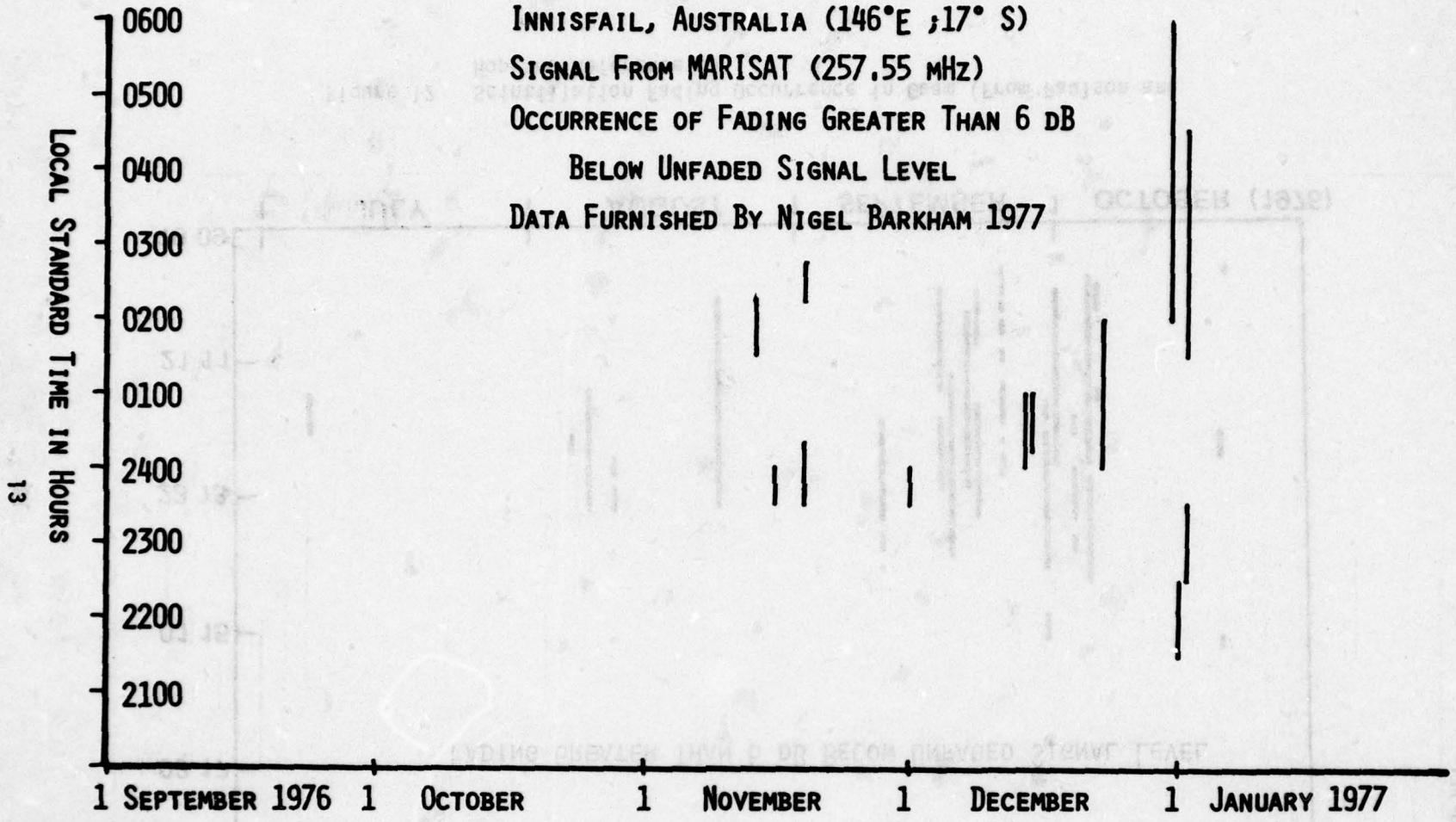

Figure 11. Scintillation Fading Occurrence in Innisfail, Australia (From Barkham Reference 13)

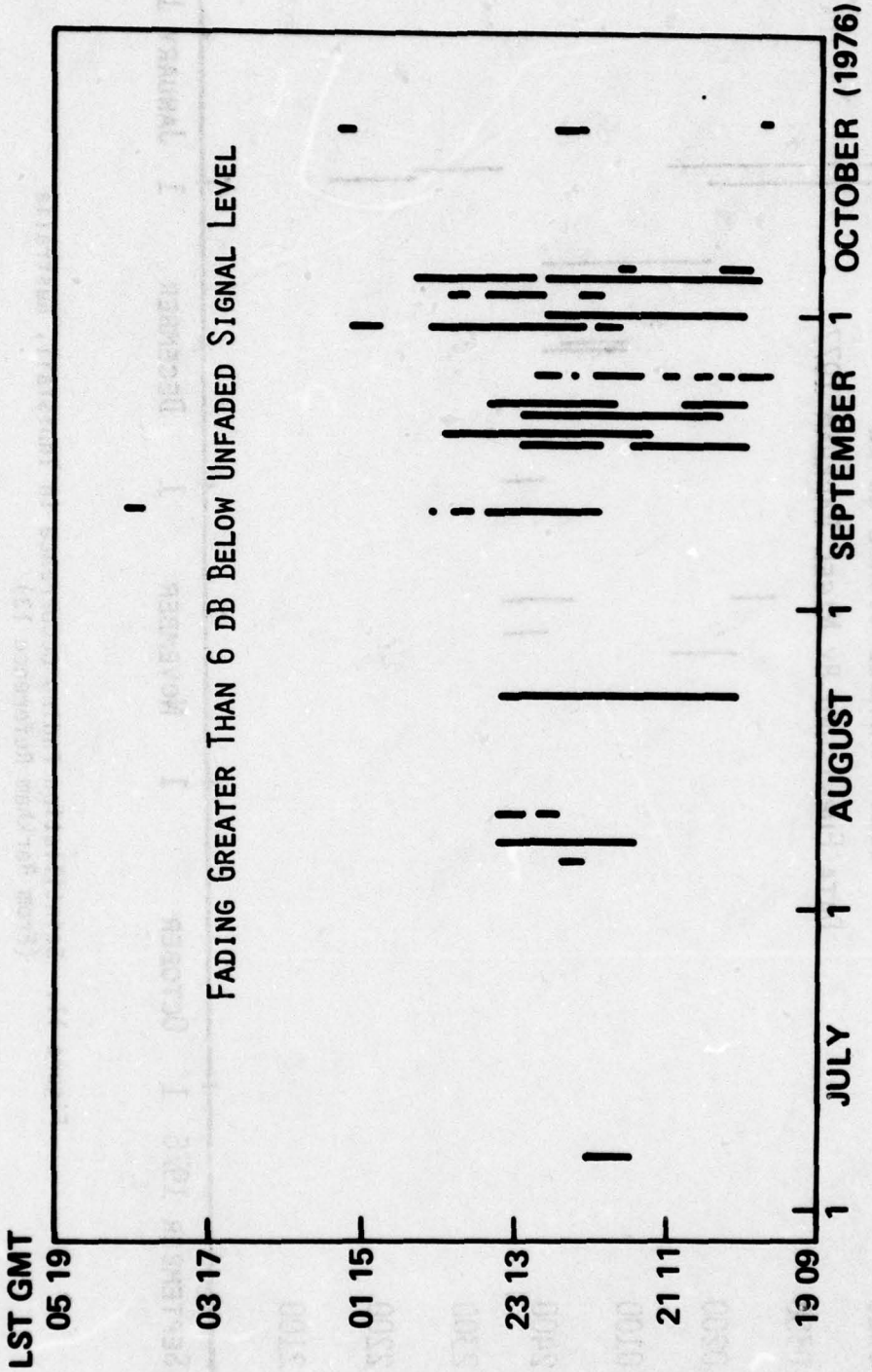

Figure 12. Scintillation Fading Occurrence in Guam (From Paulson and Hopkins Reference 6)

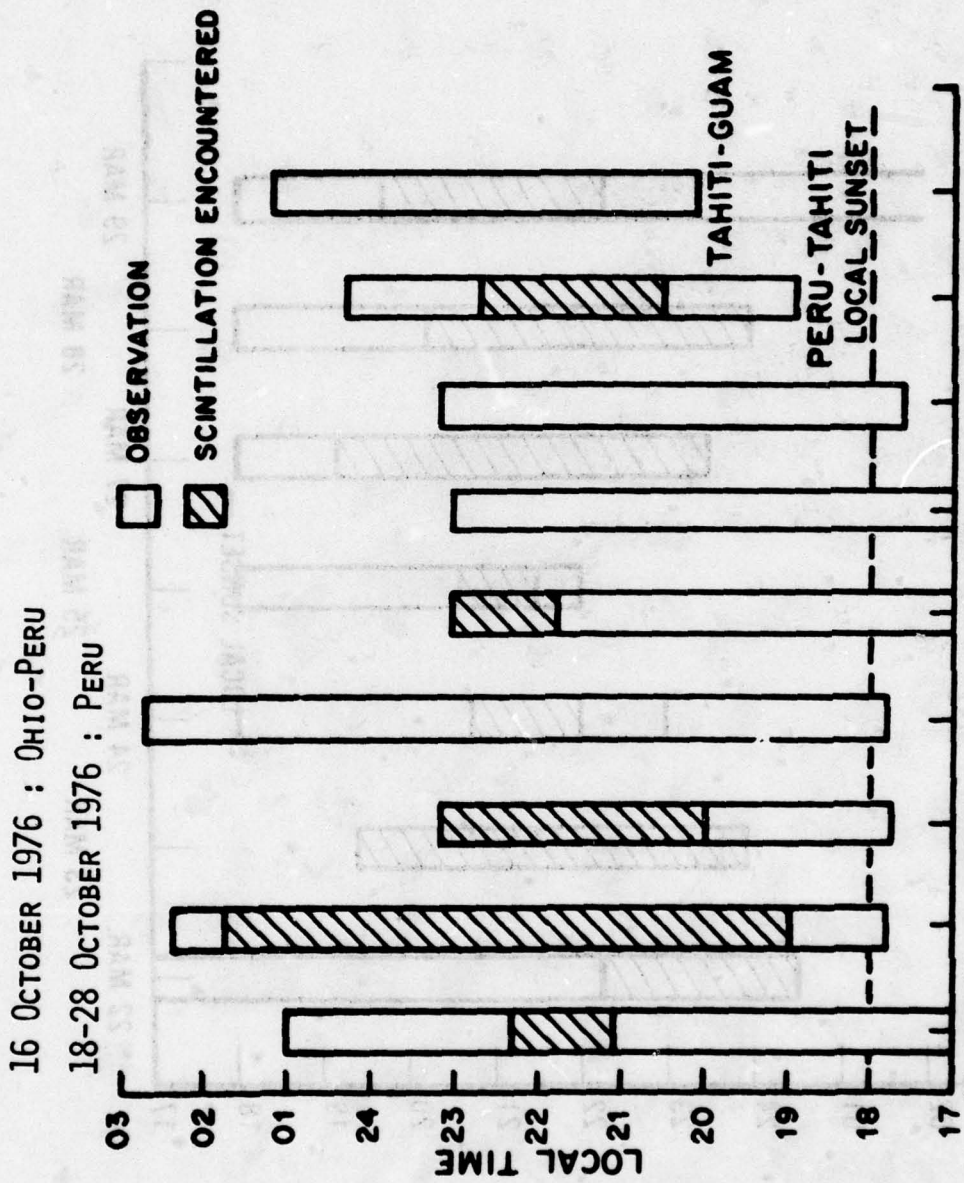

Figure 13. Scintillation Fading Occurrence in Peru (From Whitney et al Reference 14)

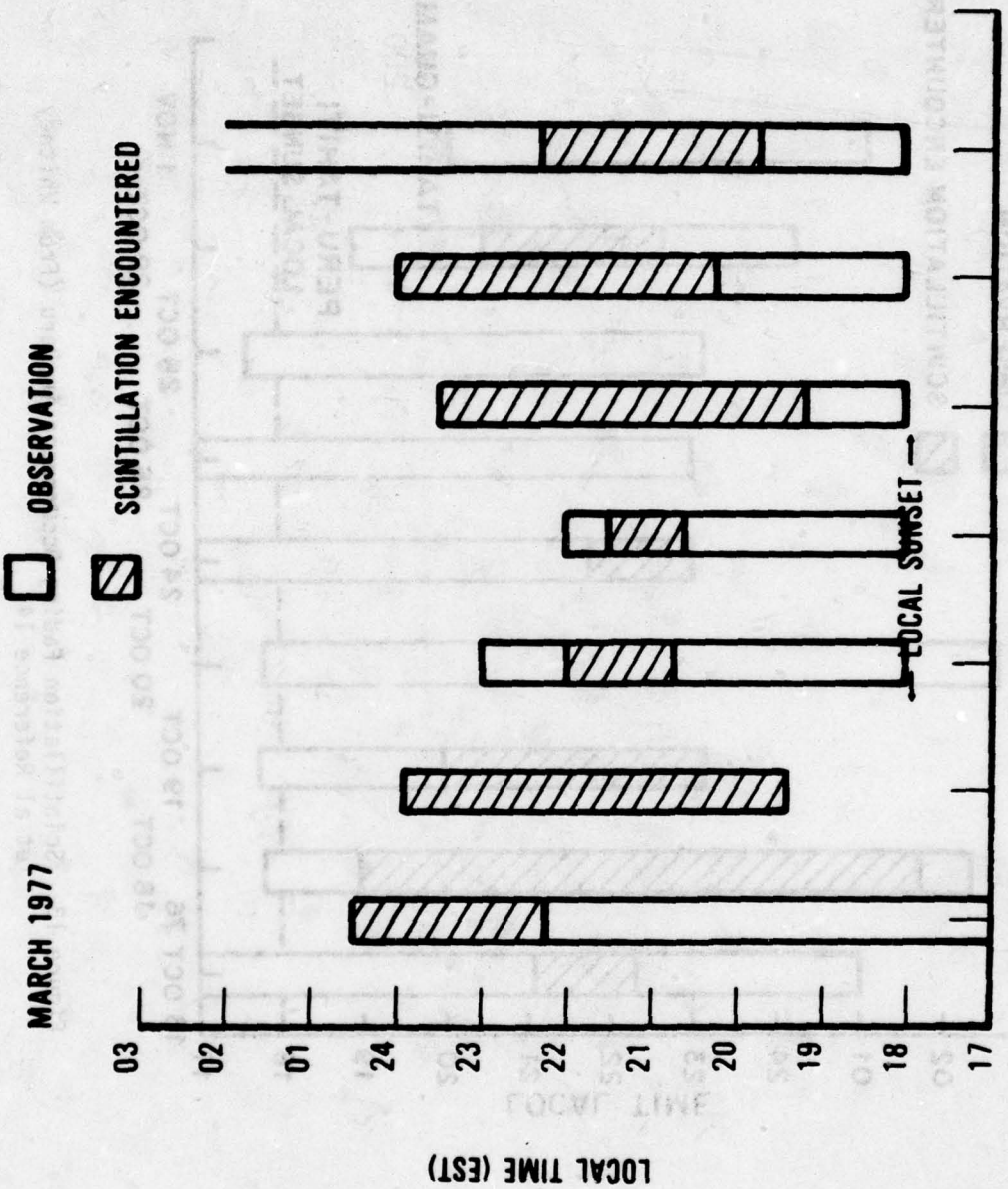

Figure 14. Scintillation Occurrence in Peru (From Whitney et al Reference 14)

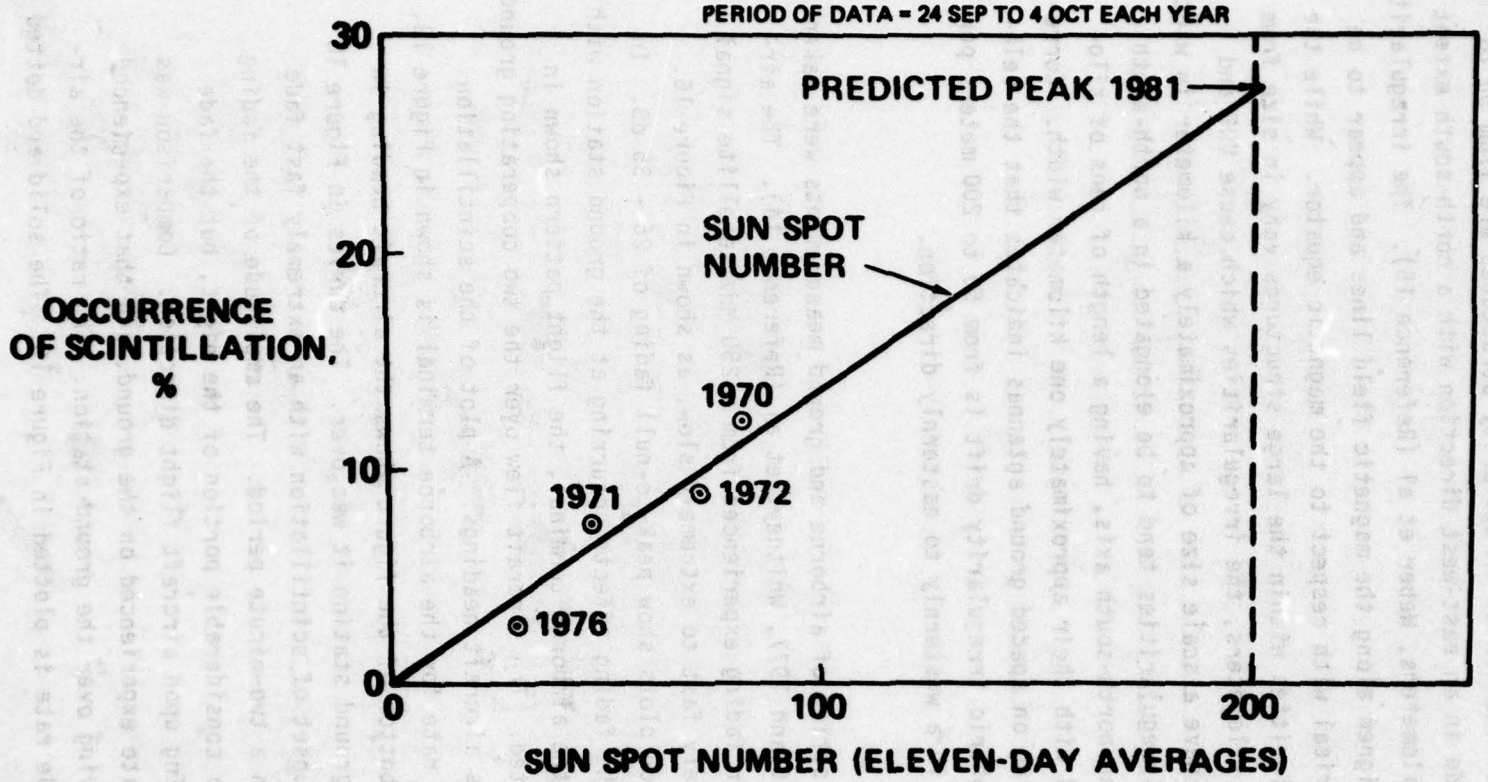

Figure 15. Dependence of Scintillation on Solar Activity (From Paulson and Hopkins Reference 6)

The individual equatorial irregularity structures are from 50 to 200 kilometers wide in an east-west direction with a north-south extent of 2000 to 3000 kilometers, Weber et al (Reference 15). The irregularity structures are aligned along the magnetic field lines and appear to be relatively symmetrical with respect to the magnetic equator. While the individual irregularities within the large structures vary in size from meters to tens of kilometers, the irregularities which cause VHF and UHF scintillation have a scale size of approximately a kilometer in width. These individual irregularities tend to be elongated in a north-south direction along the north-south axis, having a length of tens of kilometers as compared with their approximately one kilometer width. Correlation of the fading on spaced ground antennas indicates that the velocity of the ionospheric irregularity drift is from 50 to 200 meters per second, generally in a westernly to easternly direction.

An extensive series of airborne and ground measurements were taken in Peru during 1976 and 1977, Whitney, et al (Reference 14). The airborne scintillation fading experienced from a 250 MHz satellite signal varied from extremely fast to extremely slow, as shown in Figure 16. The signal amplitude plots show peak-to-null fading of 25 - 35 dB. In order to compare the fading effects occurring at the ground station with those observed by the airborne terminal, the flight pattern shown in Figure 17 was adopted. The aircraft flew over the two cooperating ground stations at various aircraft headings. A plot of the scintillation amplitude and fade rate for the airborne terminal is shown in Figure 18. The legend at the bottom of the figure shows the aircraft heading in addition to which ground station it was over. The curves in Figure 18 show a very rapid onset of scintillation with an extremely fast fade rate of 90 fades in a two-minute period. The amplitude of the fading remains high over a considerable portion of the night, but the fade rate varies depending upon aircraft flight direction. Comparison was made of the fade rate experienced on the ground, and that experienced in the aircraft flying over the ground station. The ratio of the airborne-to-ground fade rate is plotted in Figure 19. The solid and dotted

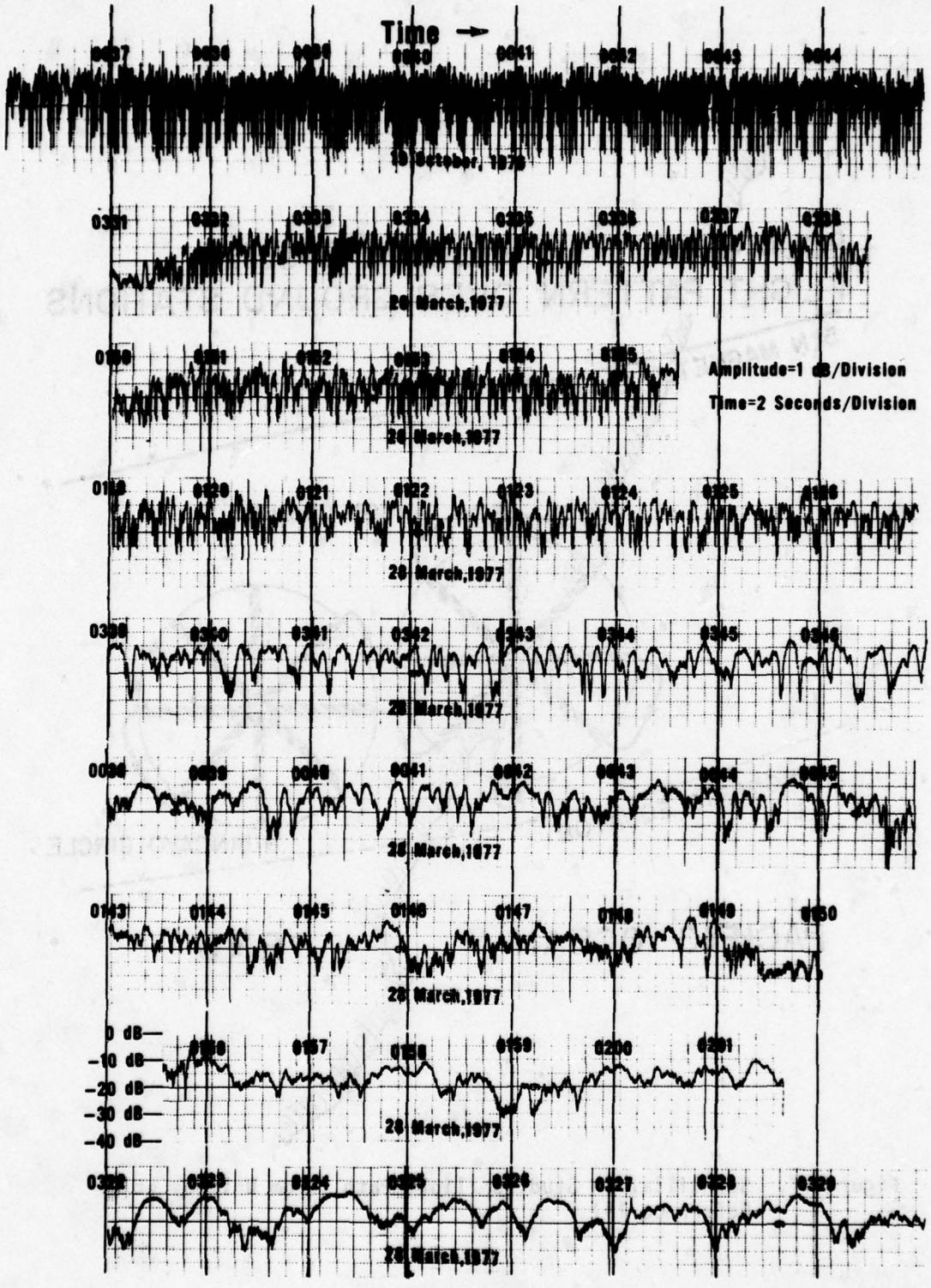

Figure 16. Equatorial UHF Ionospheric Scintillation Fade Variations

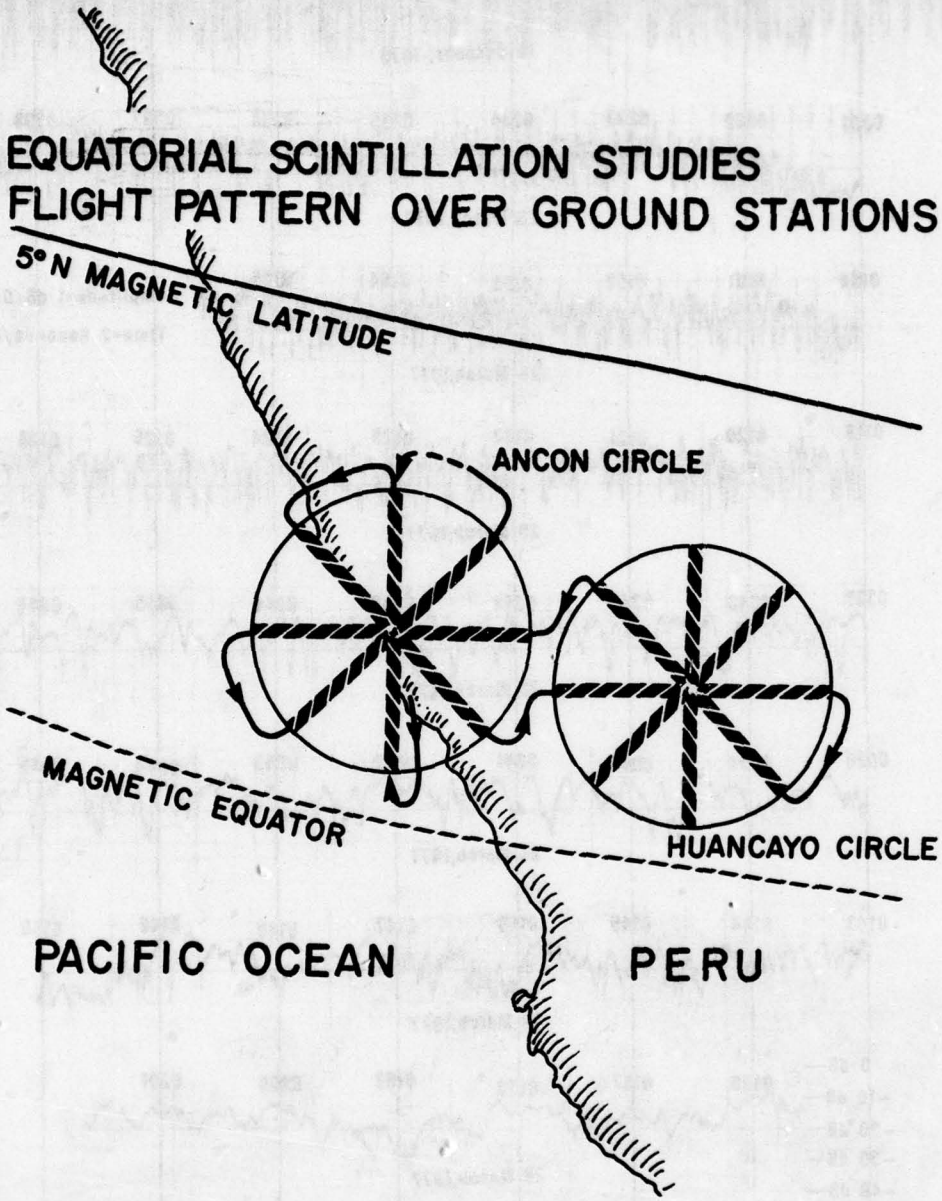

Figure 17. Scintillation Studies Flight Path (From Whitney et al Reference 14)

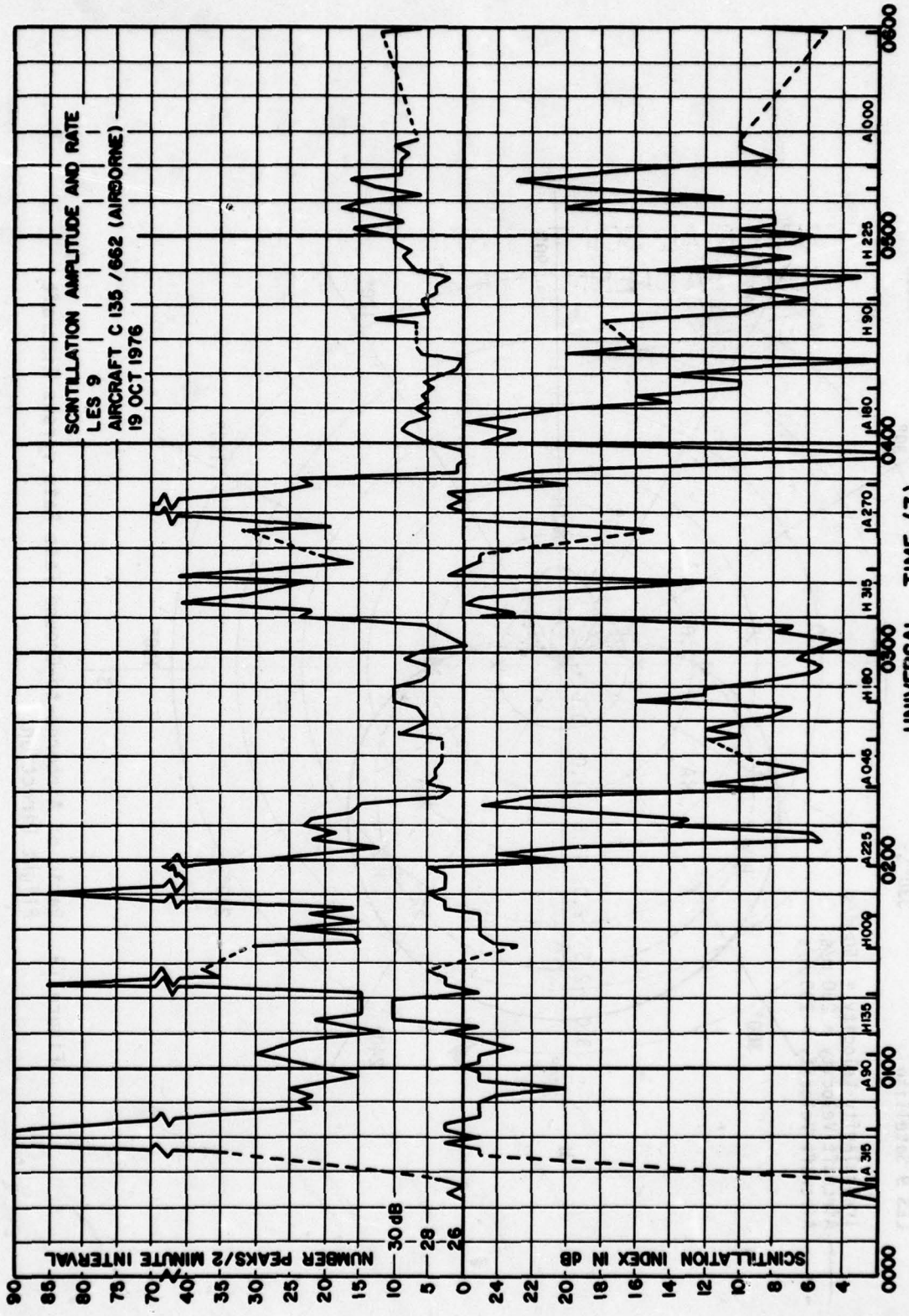

Figure 18. Scintillation Amplitude and Rate: Peru Local Flight

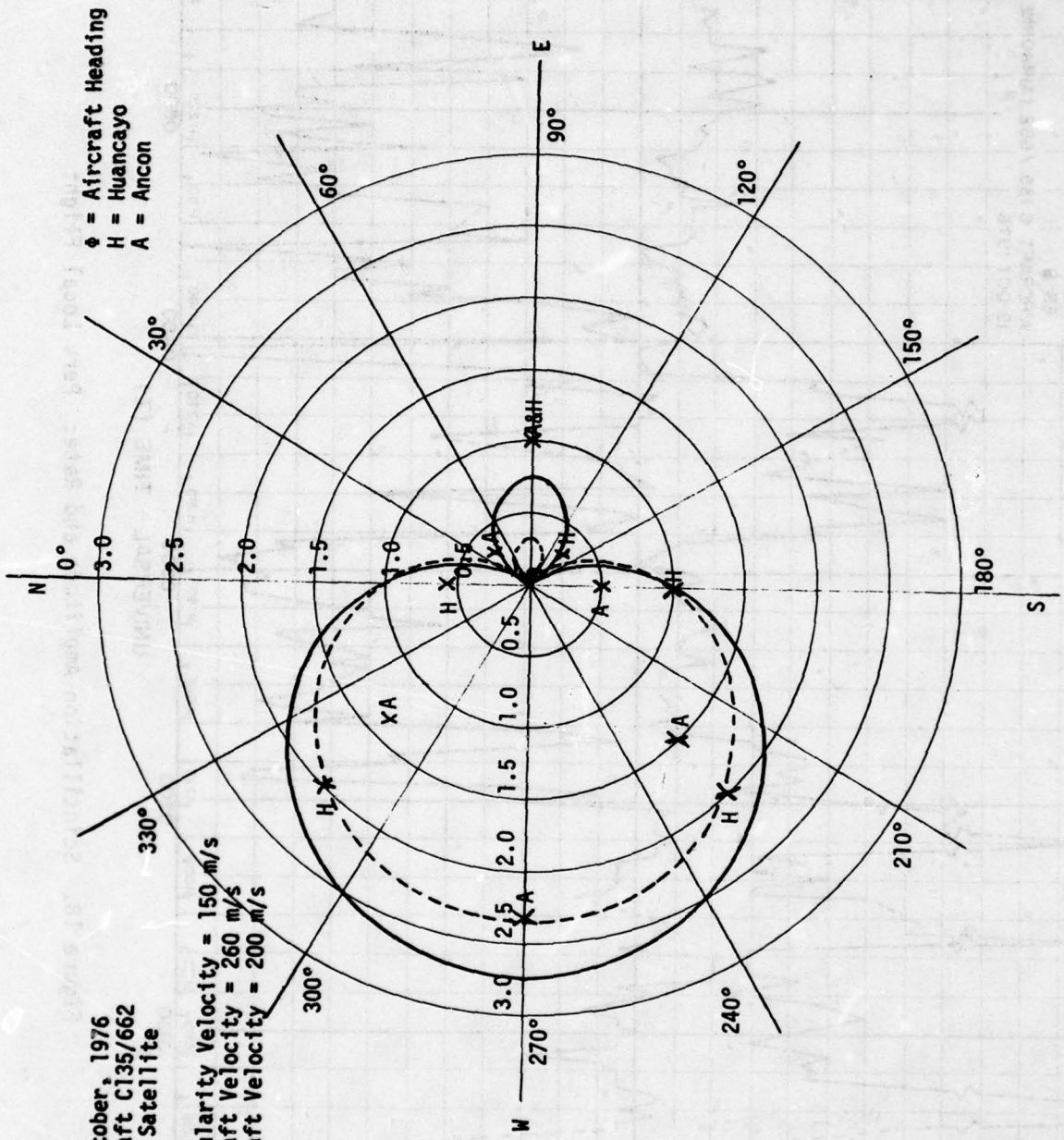

Figure 19. Ratio of Airborne-to-Ground Fade Rate versus Aircraft Flight Direction

curves are the theoretical speed-up factors which would be expected from a constant aircraft velocity as the aircraft flies in different directions. Due to the effect of local winds the actual aircraft velocity over the ground varies with heading. However, the ratio of air-to-ground fading correlates very well with the theoretically predicted fade rate ratio. The data showed that when flying in a westerly direction, fade rates of two to three times faster than the ground fade rate could be experienced on the airborne terminal. When flying in a northeasterly or southeasterly direction, extremely slow fade rates can be experienced. Histograms of the fade amplitude for the various fade rates recorded are shown in Figures 20 through 28. They show roughly the same fade distribution independent of fade rate. The cumulative distribution of a fade amplitude is shown in Figures 29 to 37 for the various rates of fading. Again, these curves indicate that for deep fading the cumulative distribution closely approximates a Rayleigh distribution and is independent of fade rate. However, a Fourier analysis of the amplitude fading data shows a marked change in the frequency components making up the fade structure. For very rapid fading the power spectra tends to decrease as the ratio of the frequencies raised to the-4 power (f^{-4}), as shown in Figures 38, 39, and 40. For medium fading the fading decreased at f^{-3}, as shown in Figures 41 through 43. For very slow fading the power spectra tends to decrease at an f^{-2} or less, shown in Figures 44 to 46. The auto correlation function decreases to half its initial amplitude in less than two-tenths of a second for the extremely fast fading, Figure 47. That time increases to 7 or 8 seconds as the fade rate decreases, Figures 48 to 55.

The period of the fading (time between successive crossings of the reference level) and the duration of fading (time which the signal remains below the reference level) are important characteristics in the design of any mitigation technique. Plots of the period and duration referenced to 4, 8, and 12 dB below the measured mean signal level are presented in Figures 56 through 65 for fast and slow fading examples.

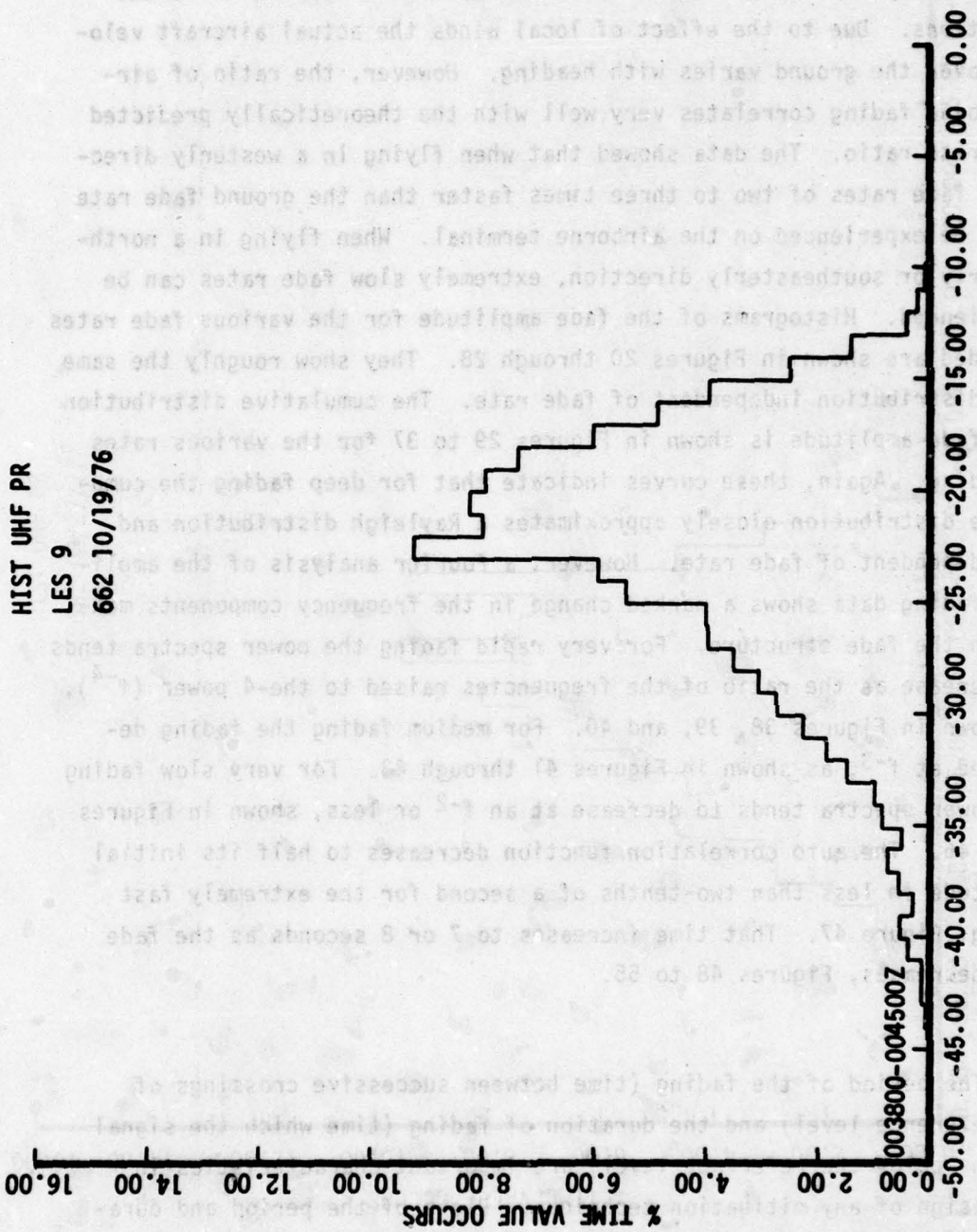

Figure 20. Histogram of Received Signal Amplitude for Extremely Fast Fading

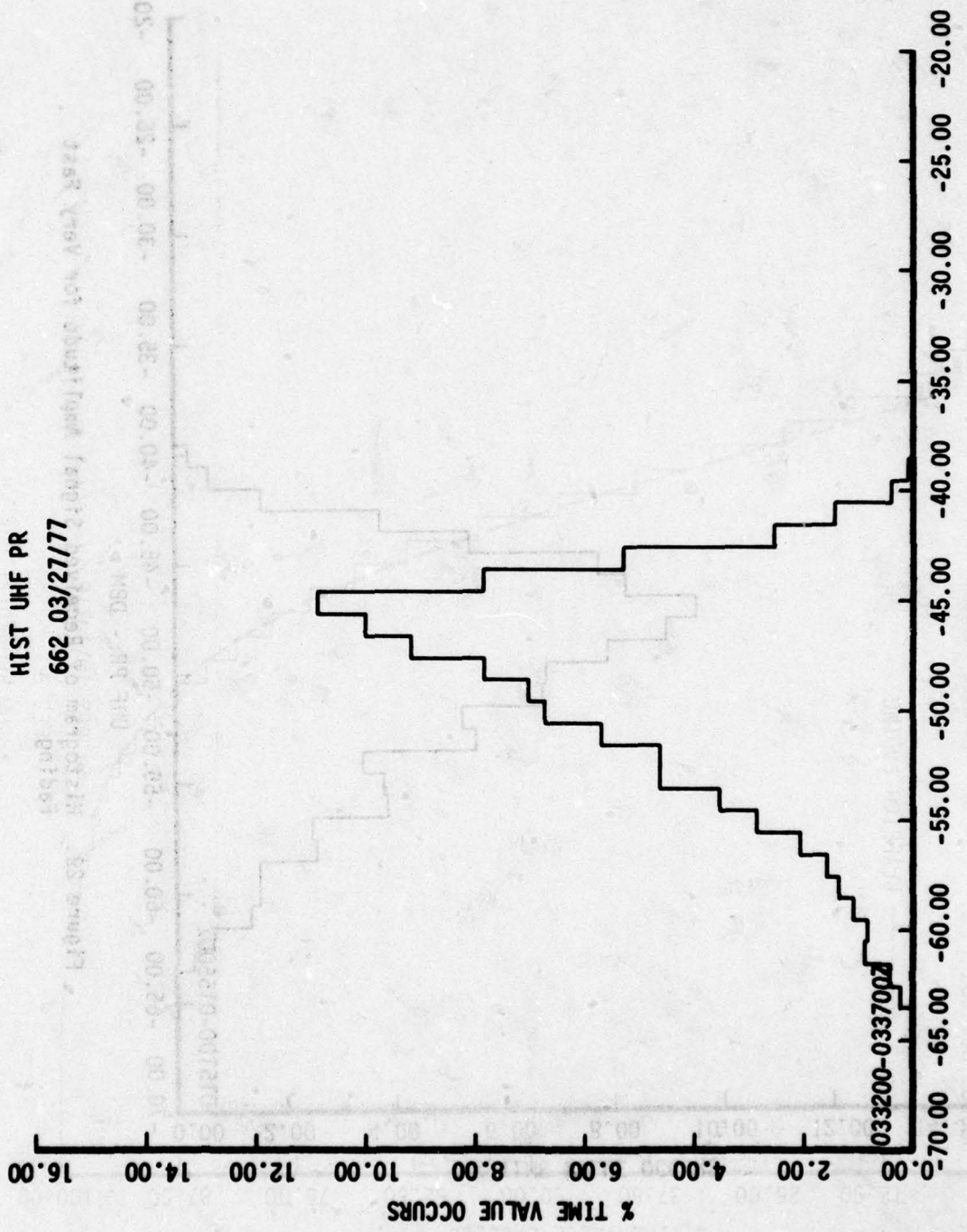

Figure 21. Histogram of Received Signal Amplitude for Very Fast Fading

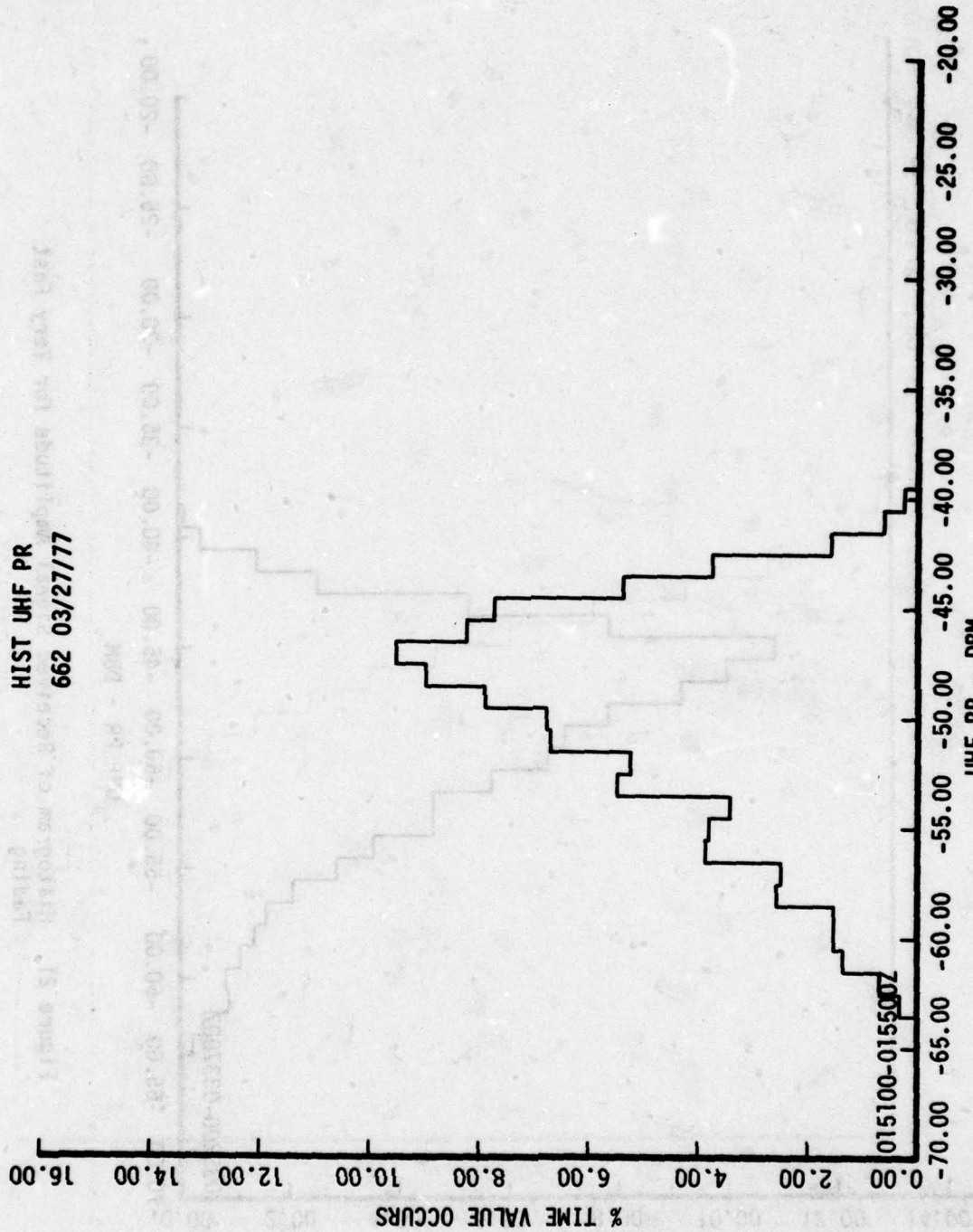

Figure 22. Histogram of Received Signal Amplitude for Very Fast Fading

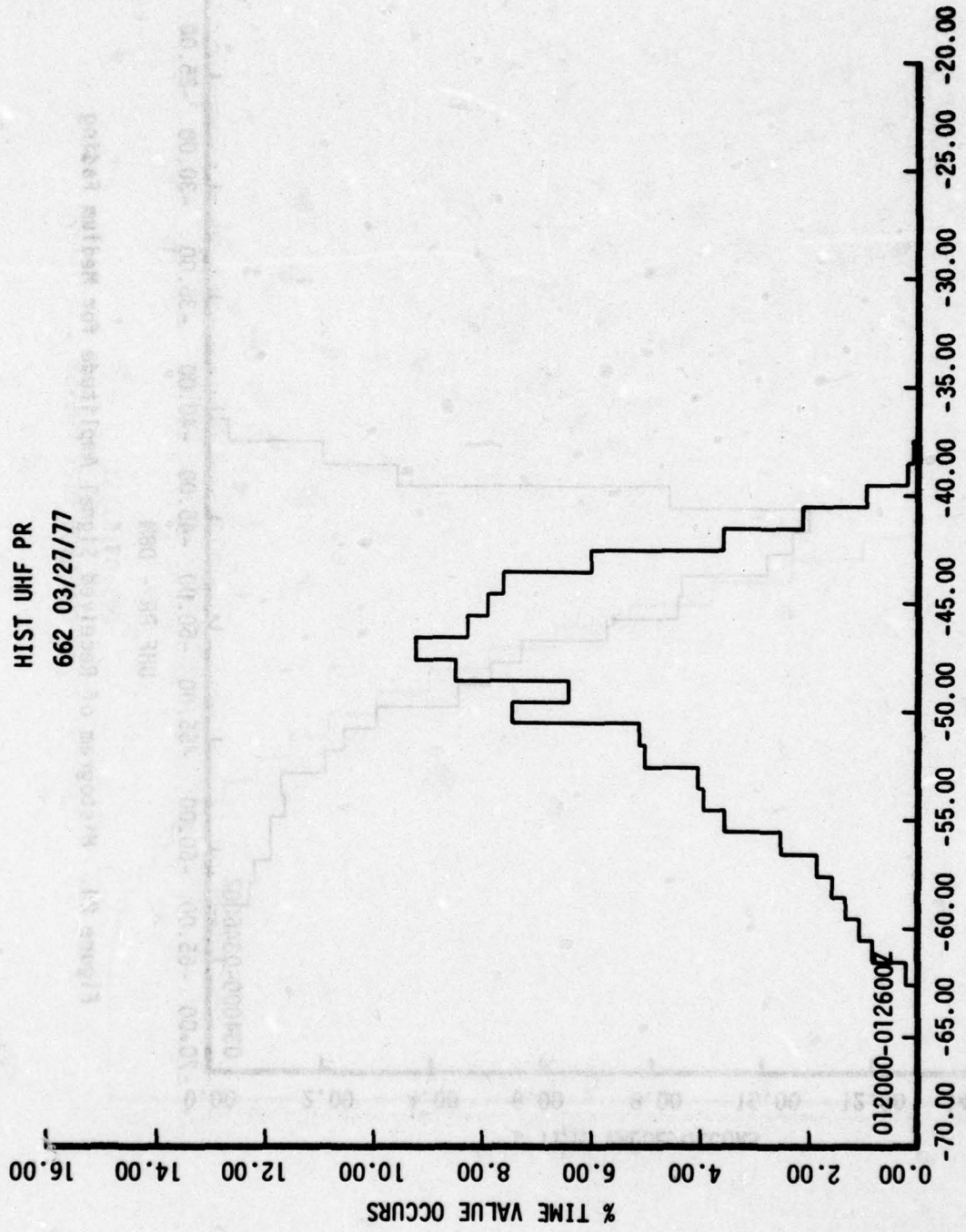

Figure 23. Histogram of Received Signal Amplitude for Fast Fading

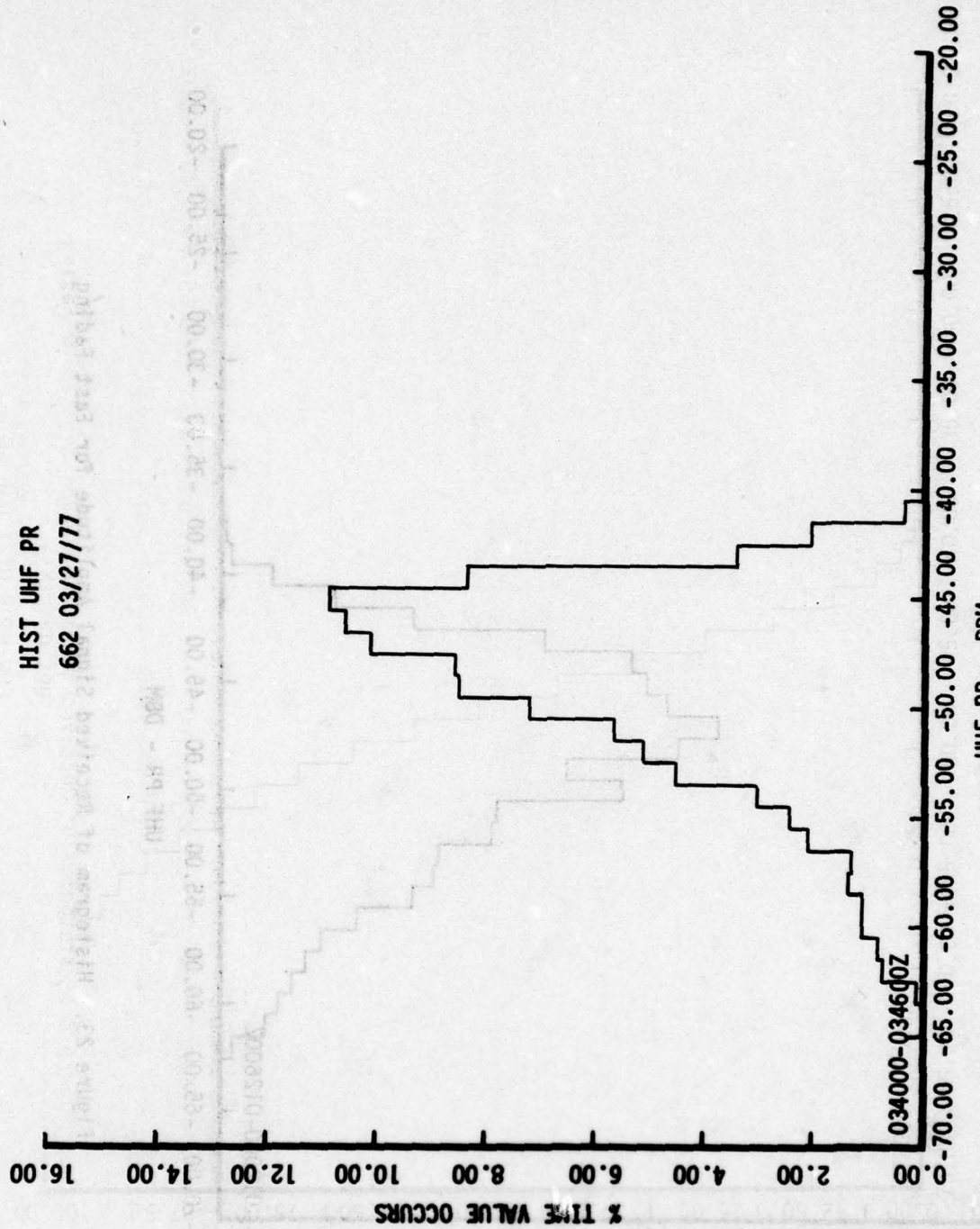

Figure 24. Histogram of Received Signal Amplitude for Medium Fading

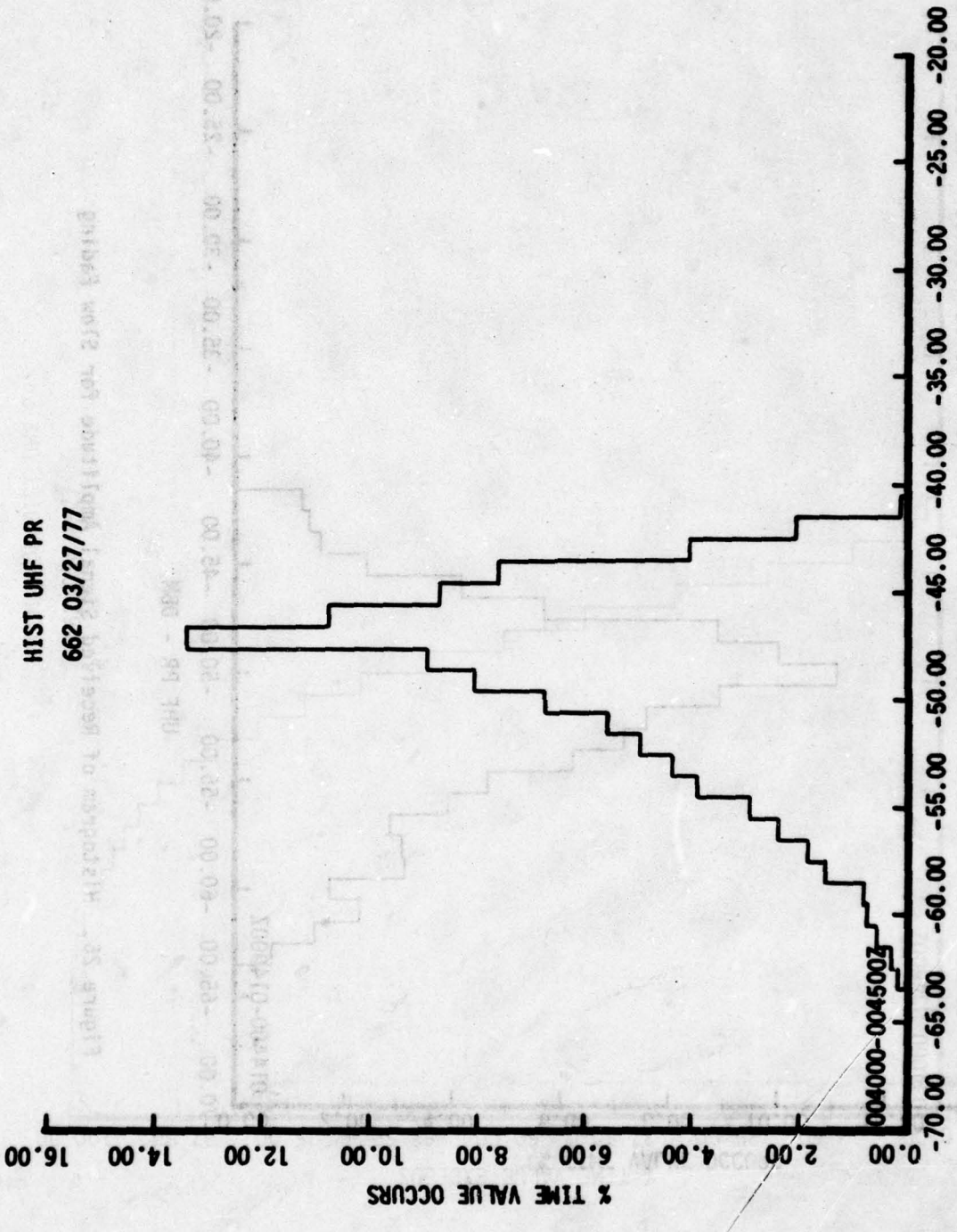

Figure 25. Histogram of Received Signal Amplitude for Medium Fading

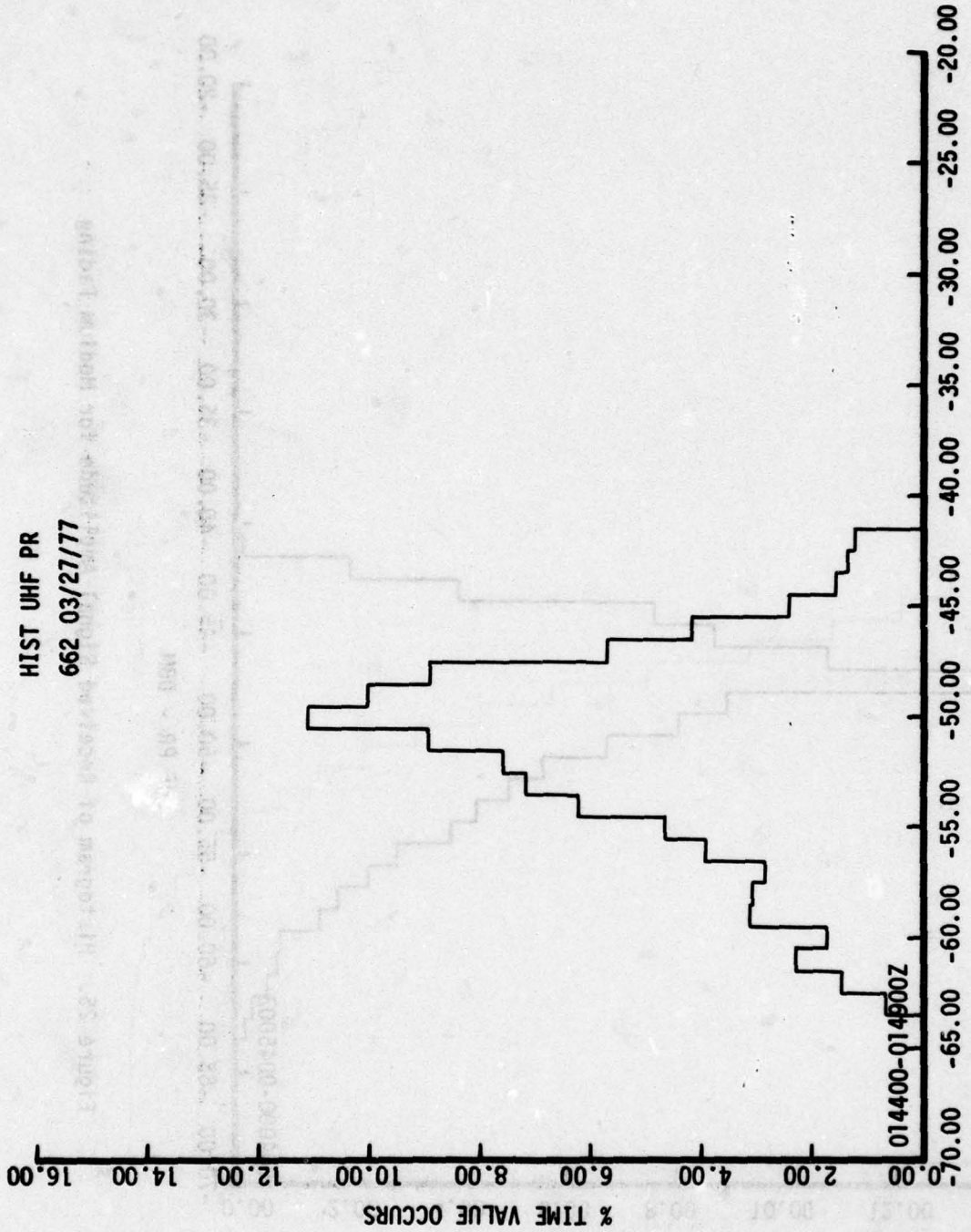

Figure 26. Histogram of Received Signal Amplitude for Slow Fading

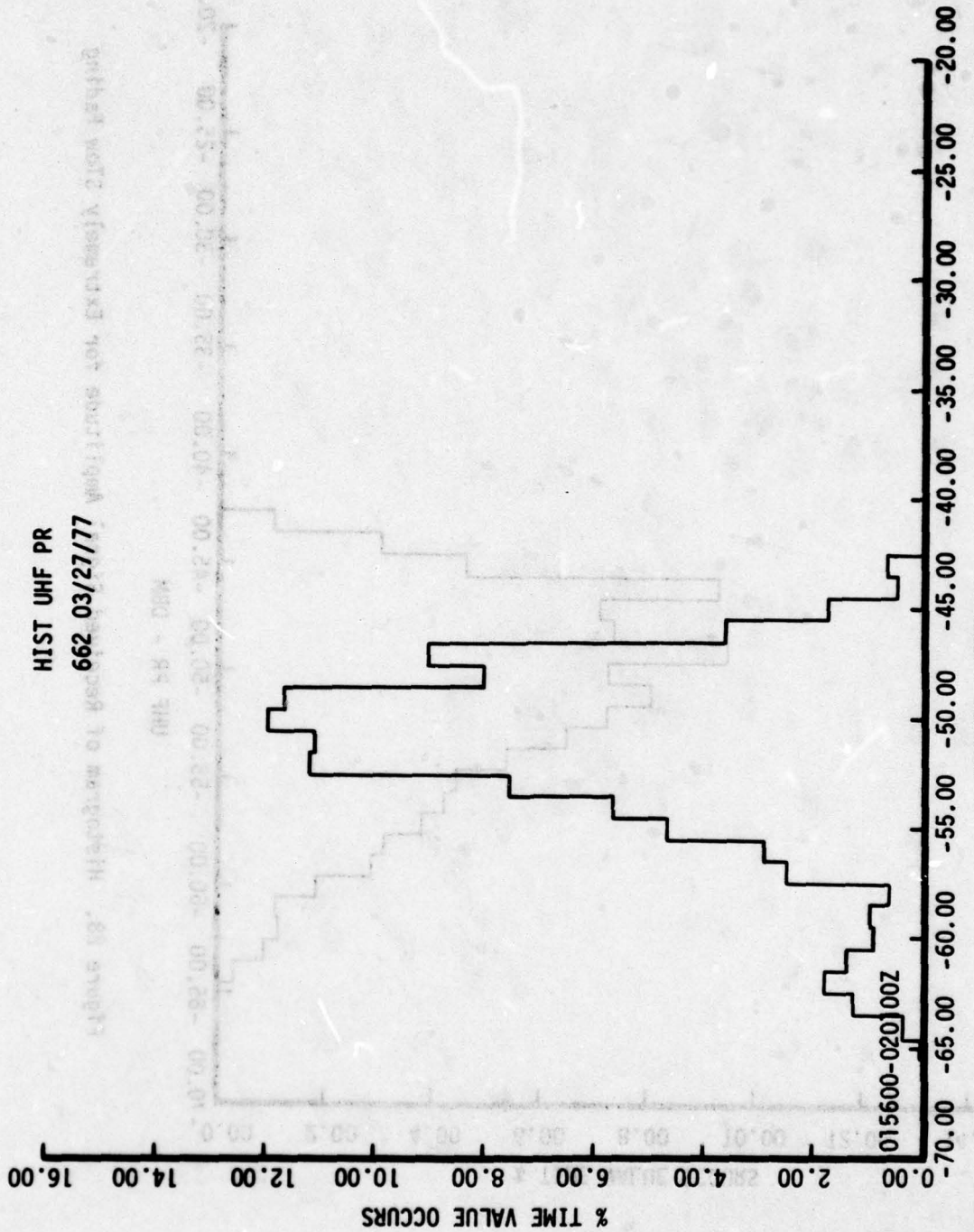

Figure 27. Histogram of Received Signal Amplitude for Very Slow Fading

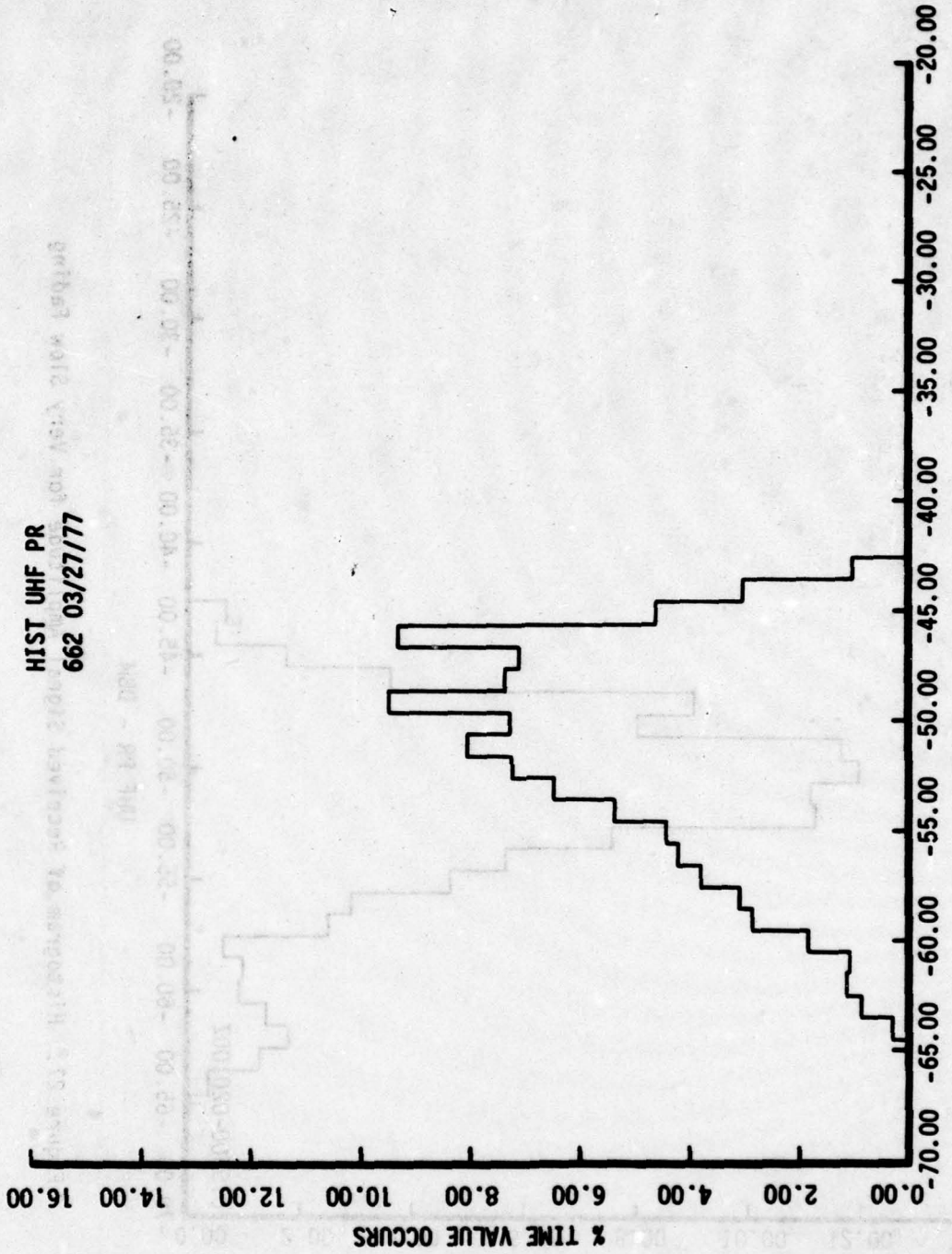

Figure 28. Histogram of Received Signal Amplitude for Extremely Slow Fading

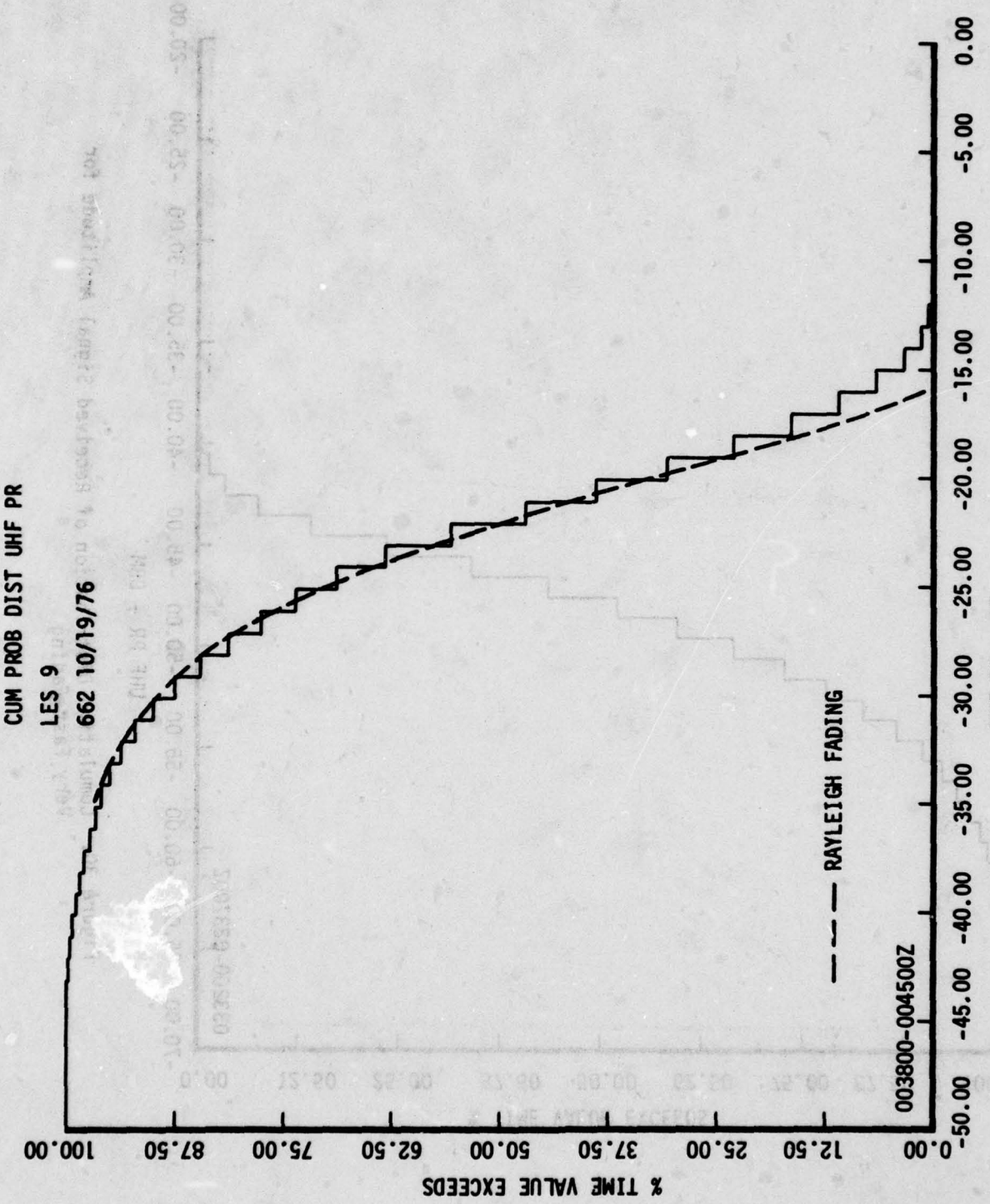

Figure 29. Cumulative Distribution of Received Signal Amplitude for Extremely Fast Fading

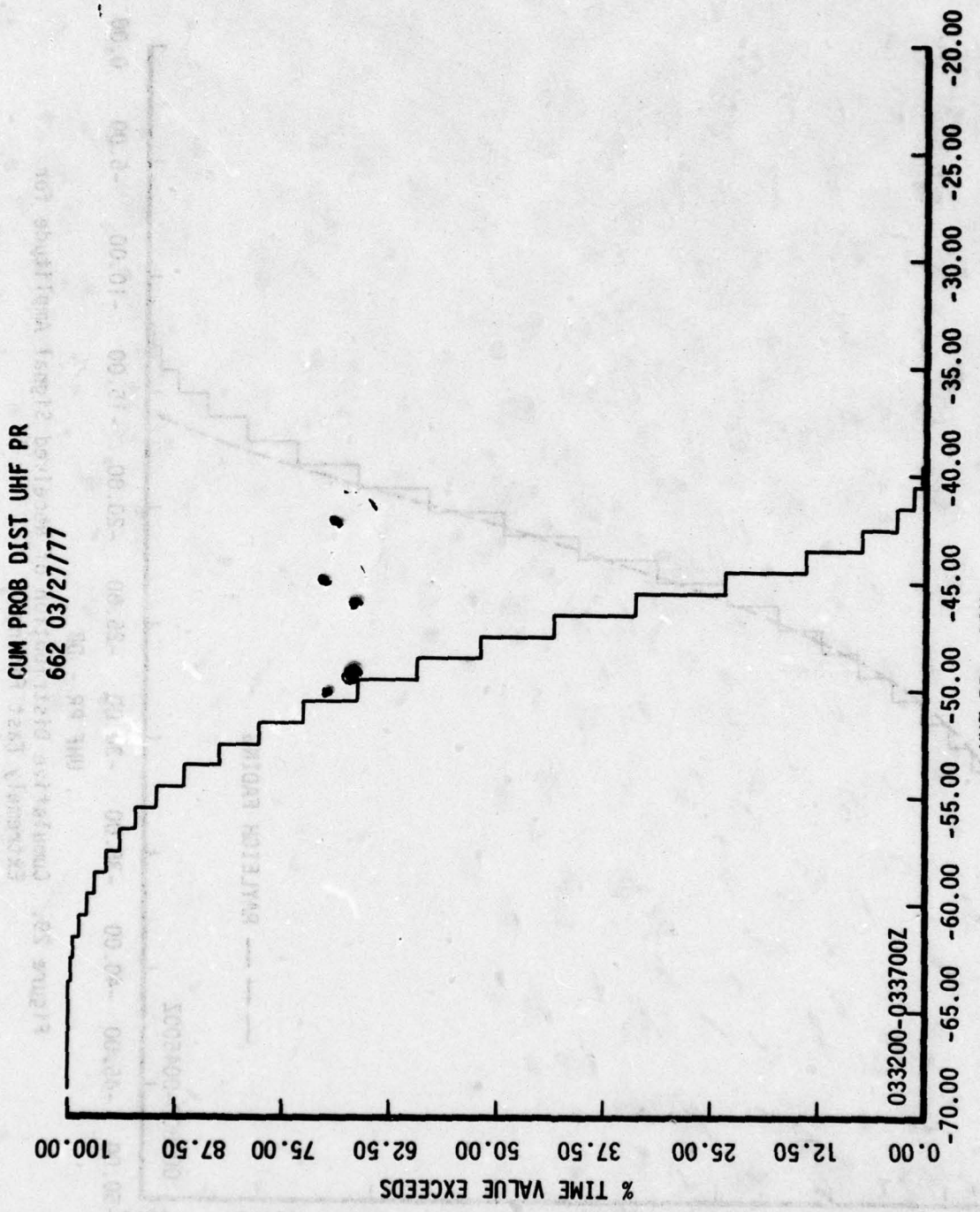

Figure 30. Cumulative Distribution of Received Signal Amplitude for Very Fast Fading

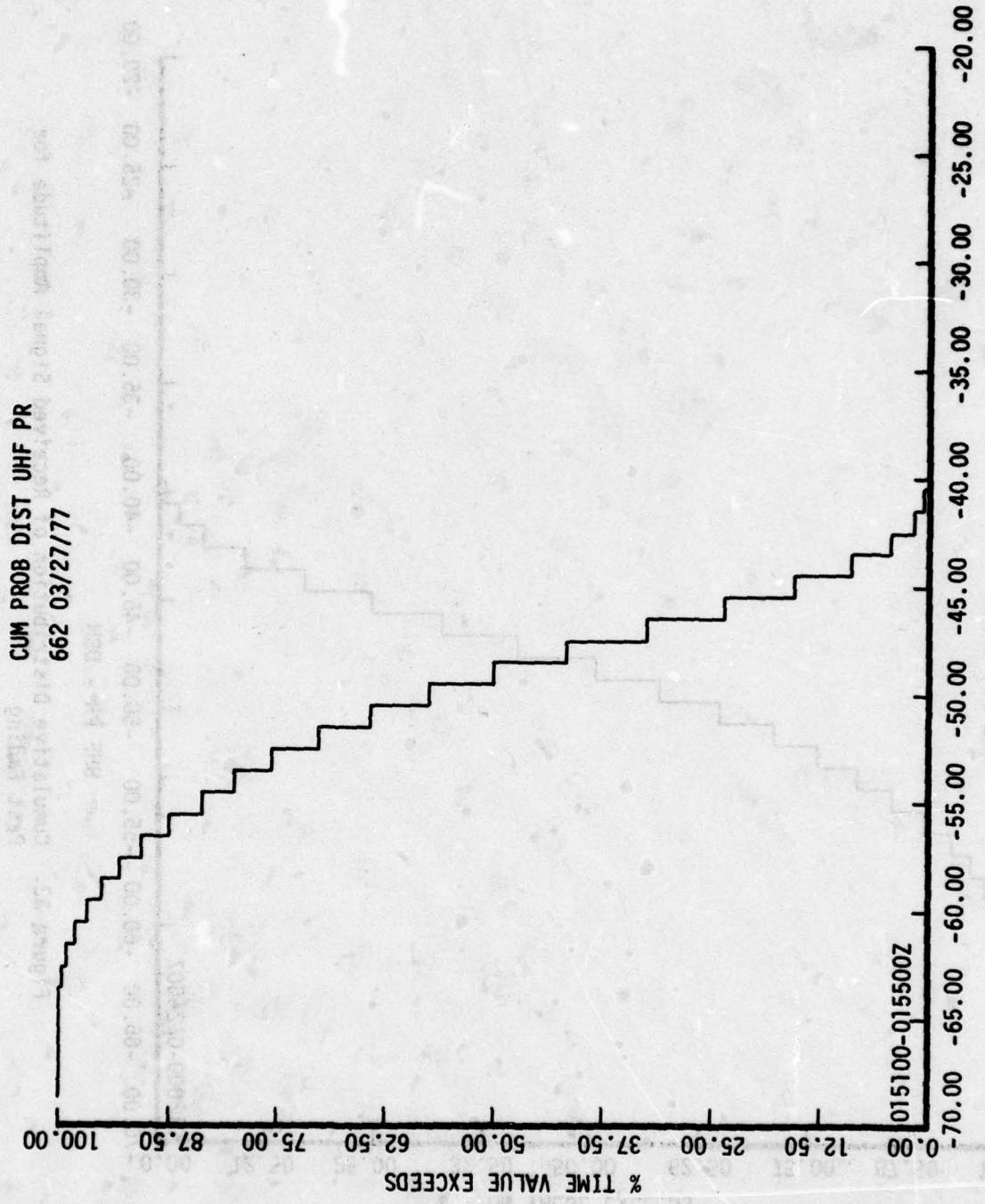

Figure 31. Cumulative Distribution of Received Signal Amplitude for Very Fast Fading

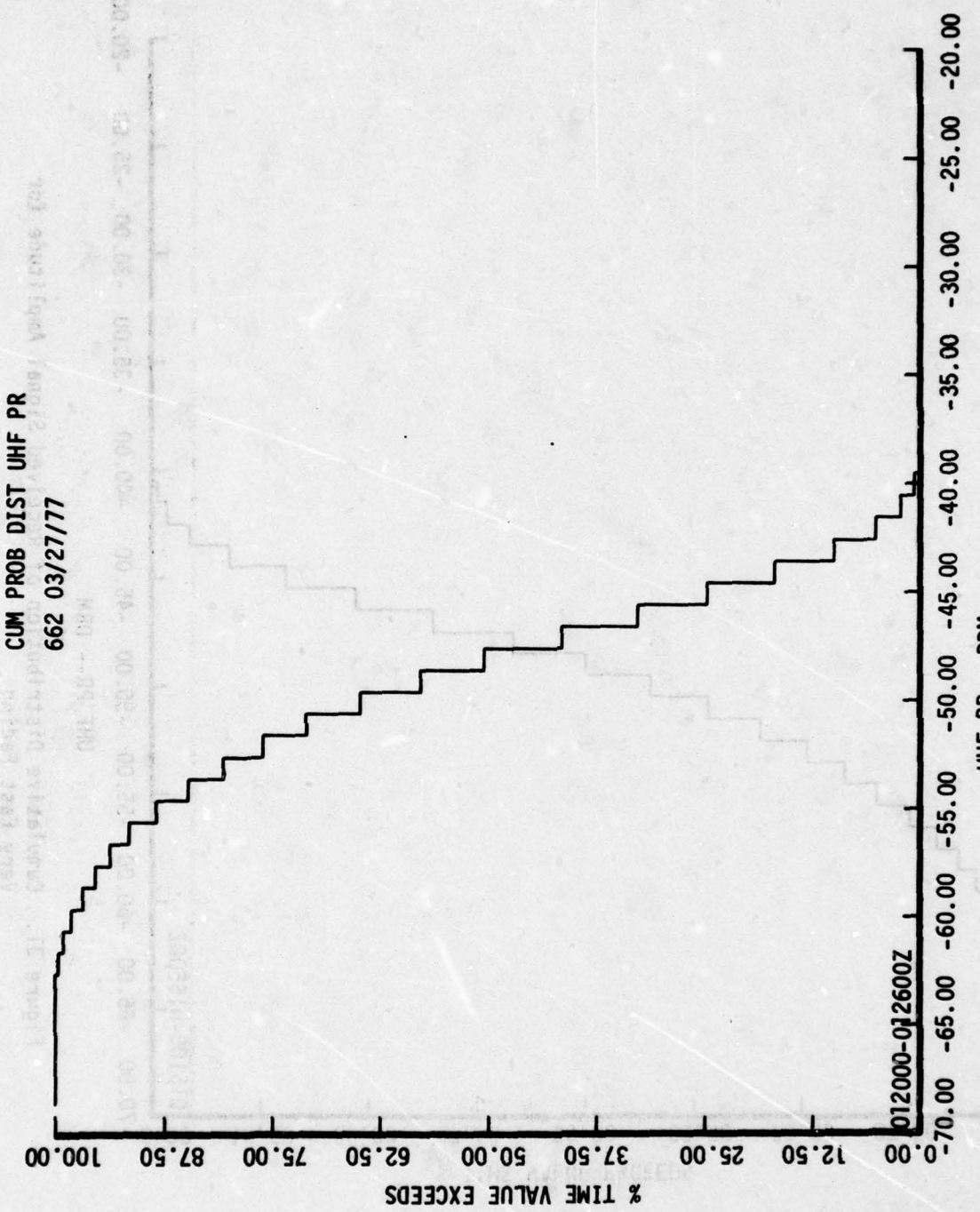

Figure 32. Cumulative Distribution of Received Signal Amplitude for Fast Fading

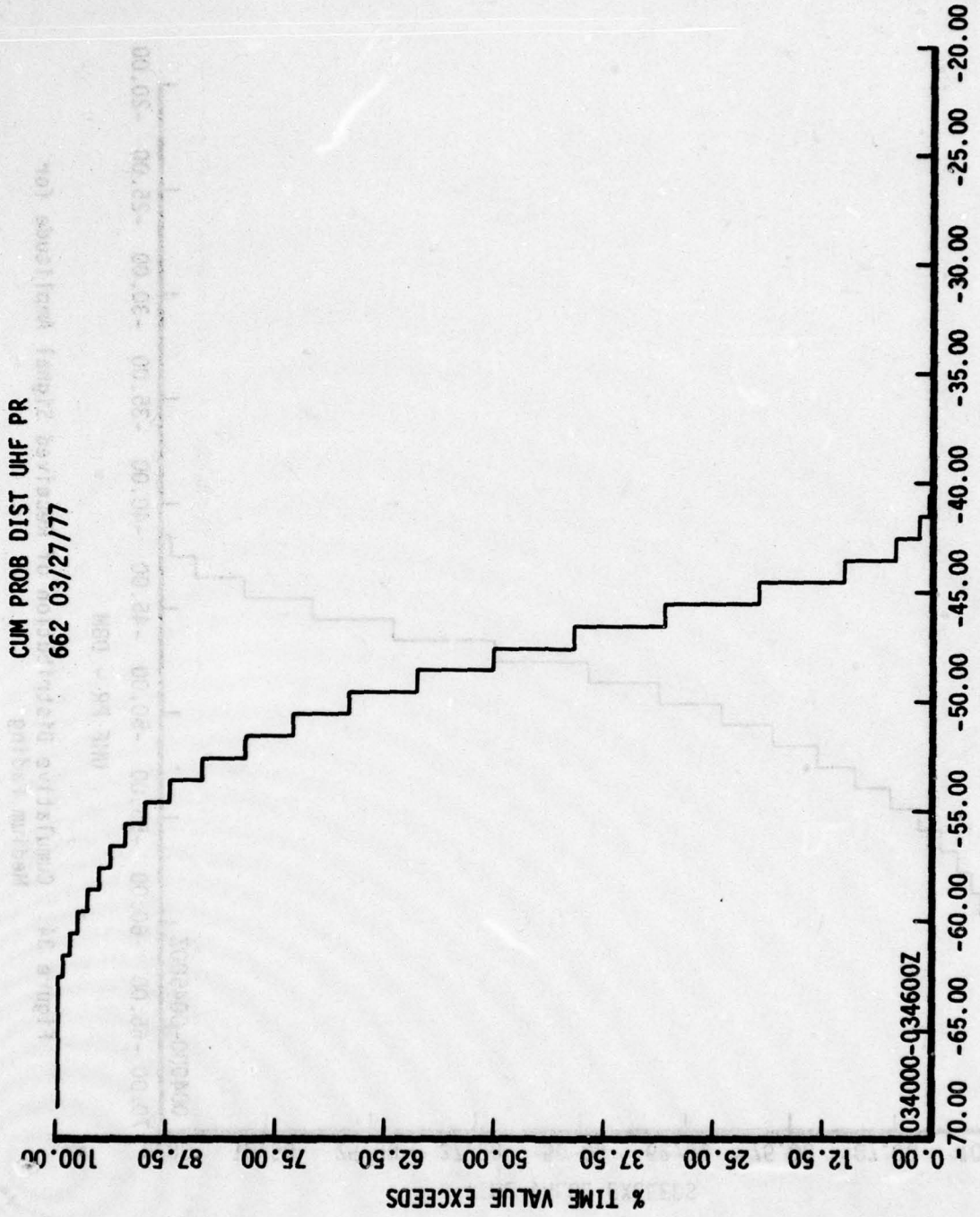

Figure 33. Cumulative Distribution of Received Signal Amplitude for Medium Fading

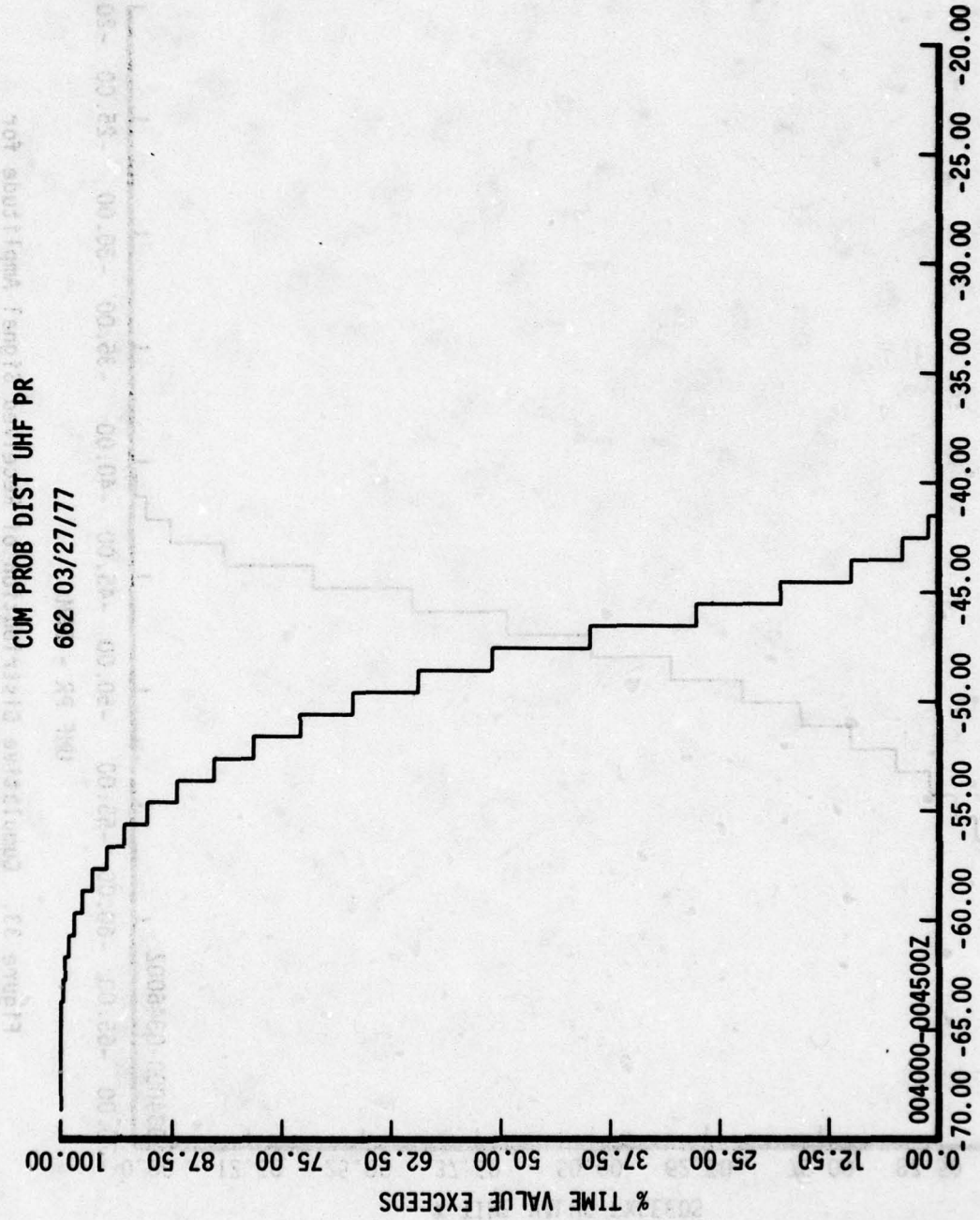

Figure 34. Cumulative Distribution of Received Signal Amplitude for Medium Fading

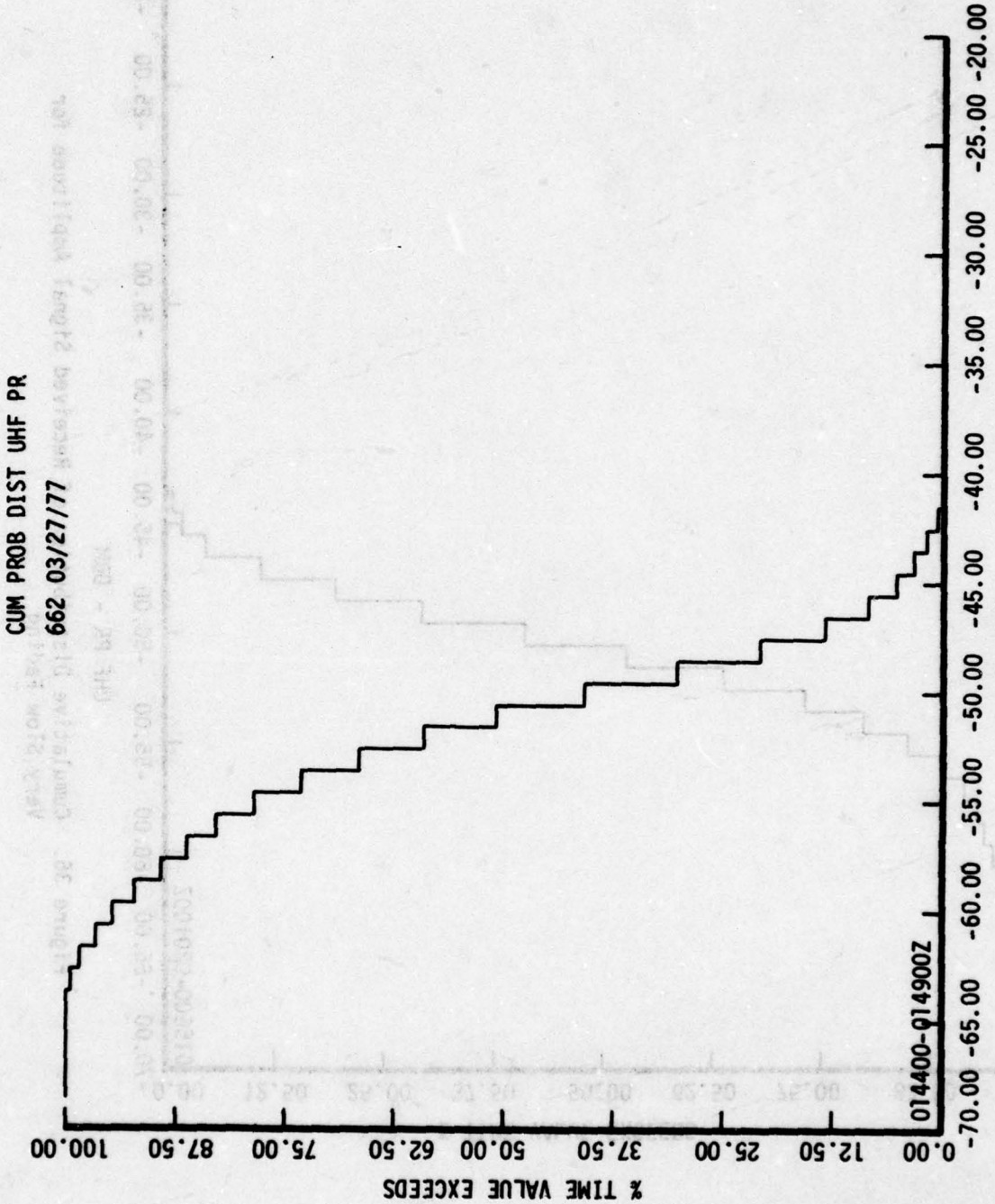

Figure 35. Cumulative Distribution of Received Signal Amplitude for Slow Fading

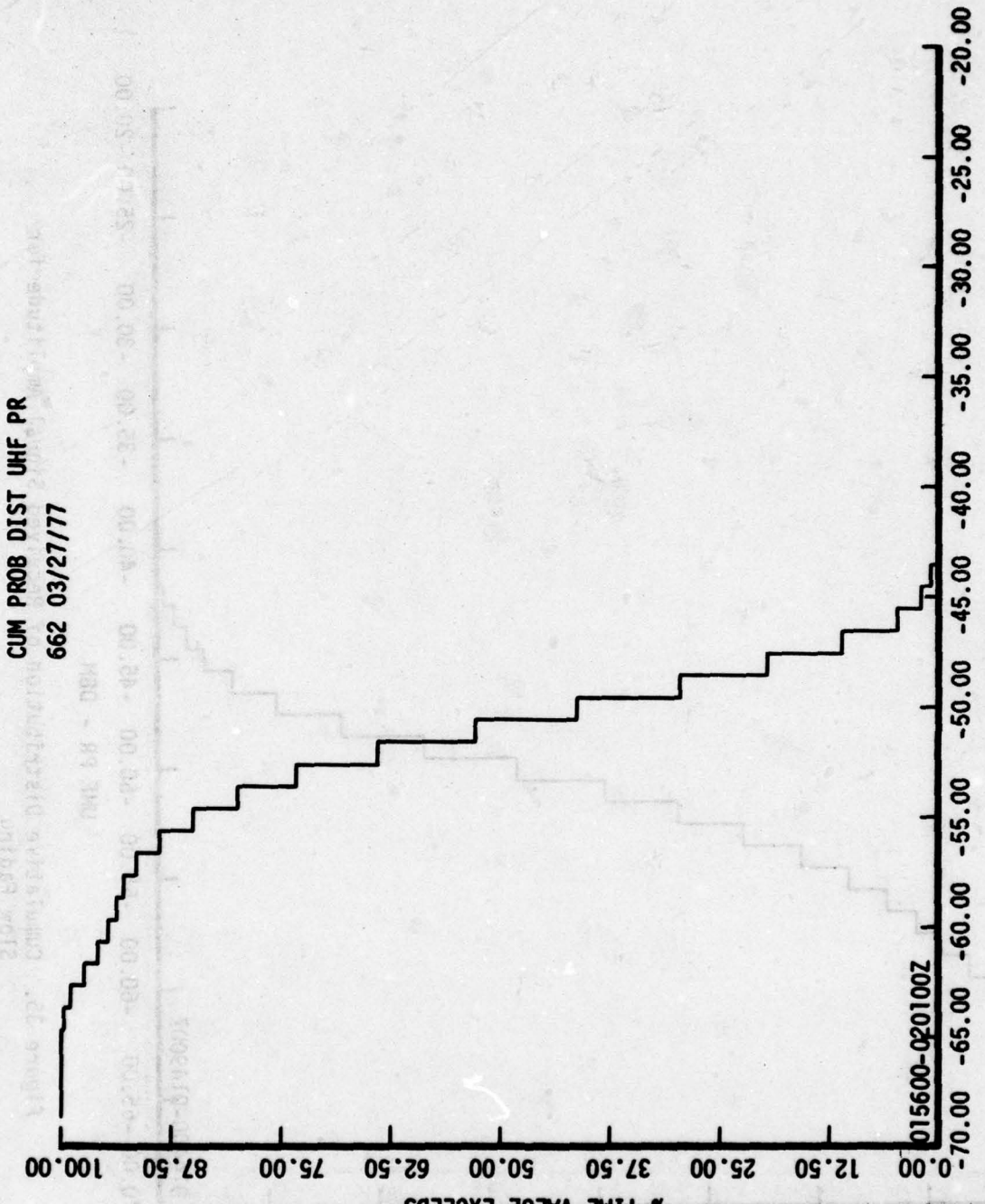

Figure 36. Cumulative Distribution of Received Signal Amplitude for Very Slow Fading

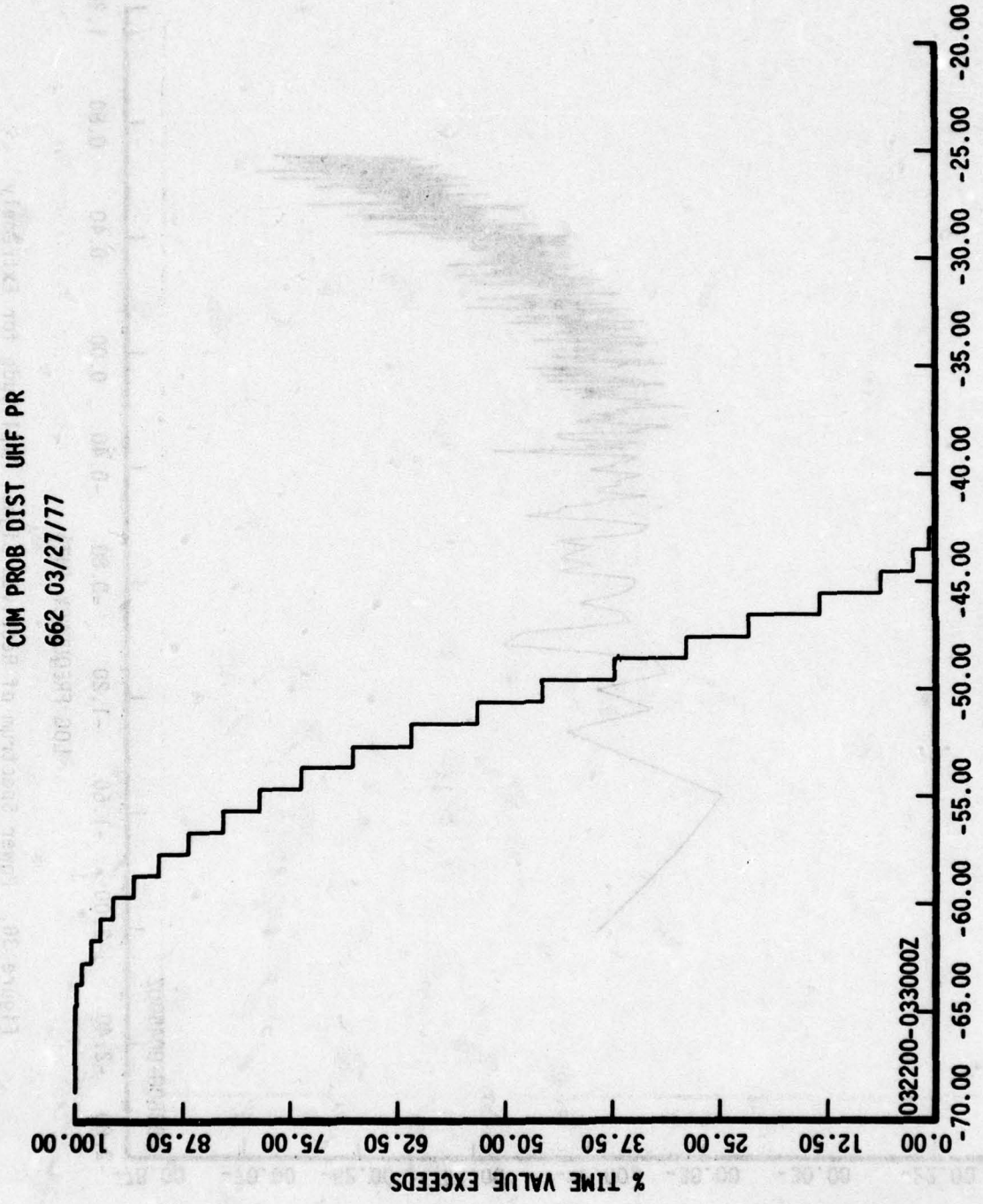

Figure 37. Power Spectrum of Received Signal Amplitude for Extremely Fast Fading

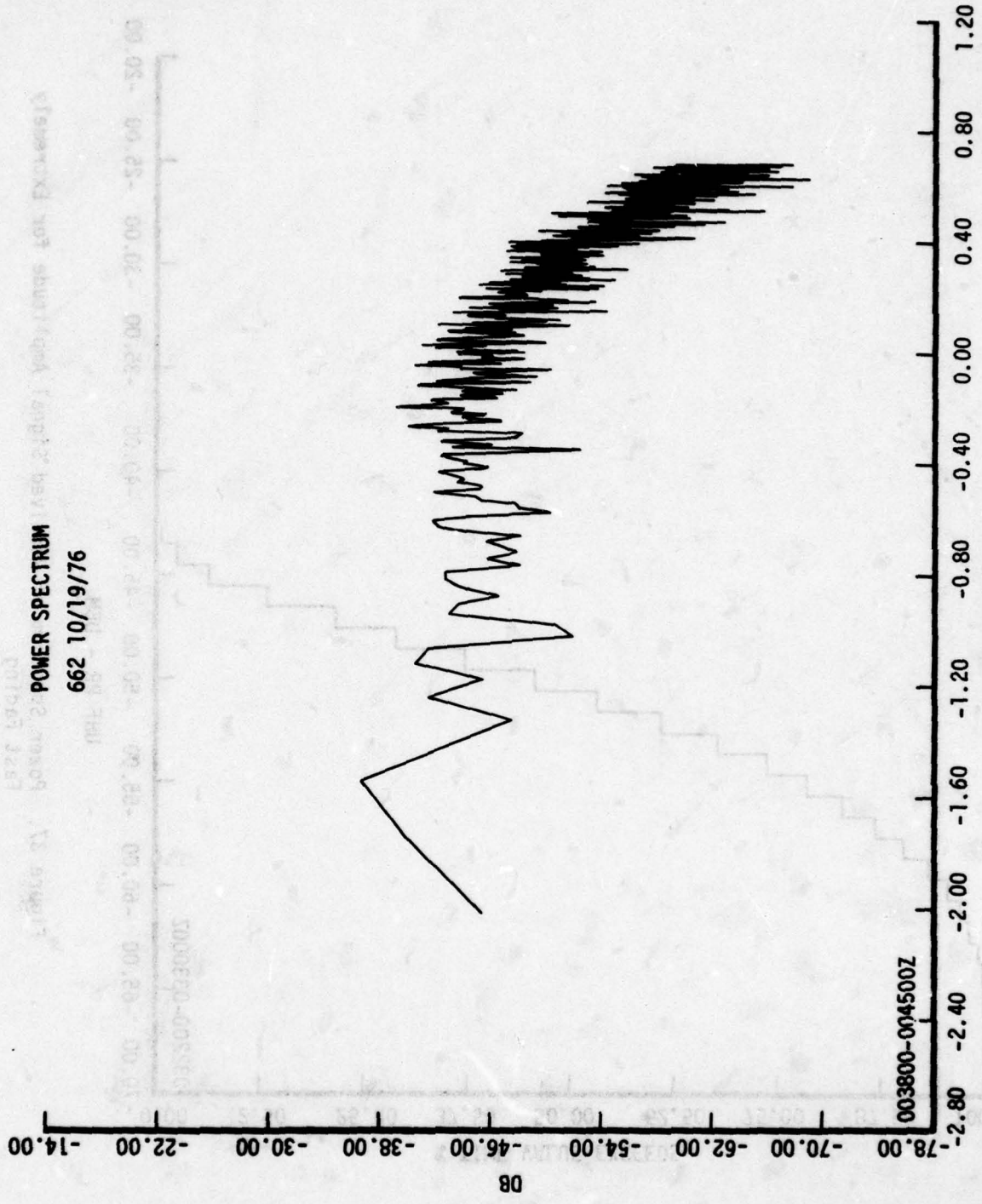

Figure 38. Power Spectrum of Received Signal Amplitude for Extremely Fast Fading

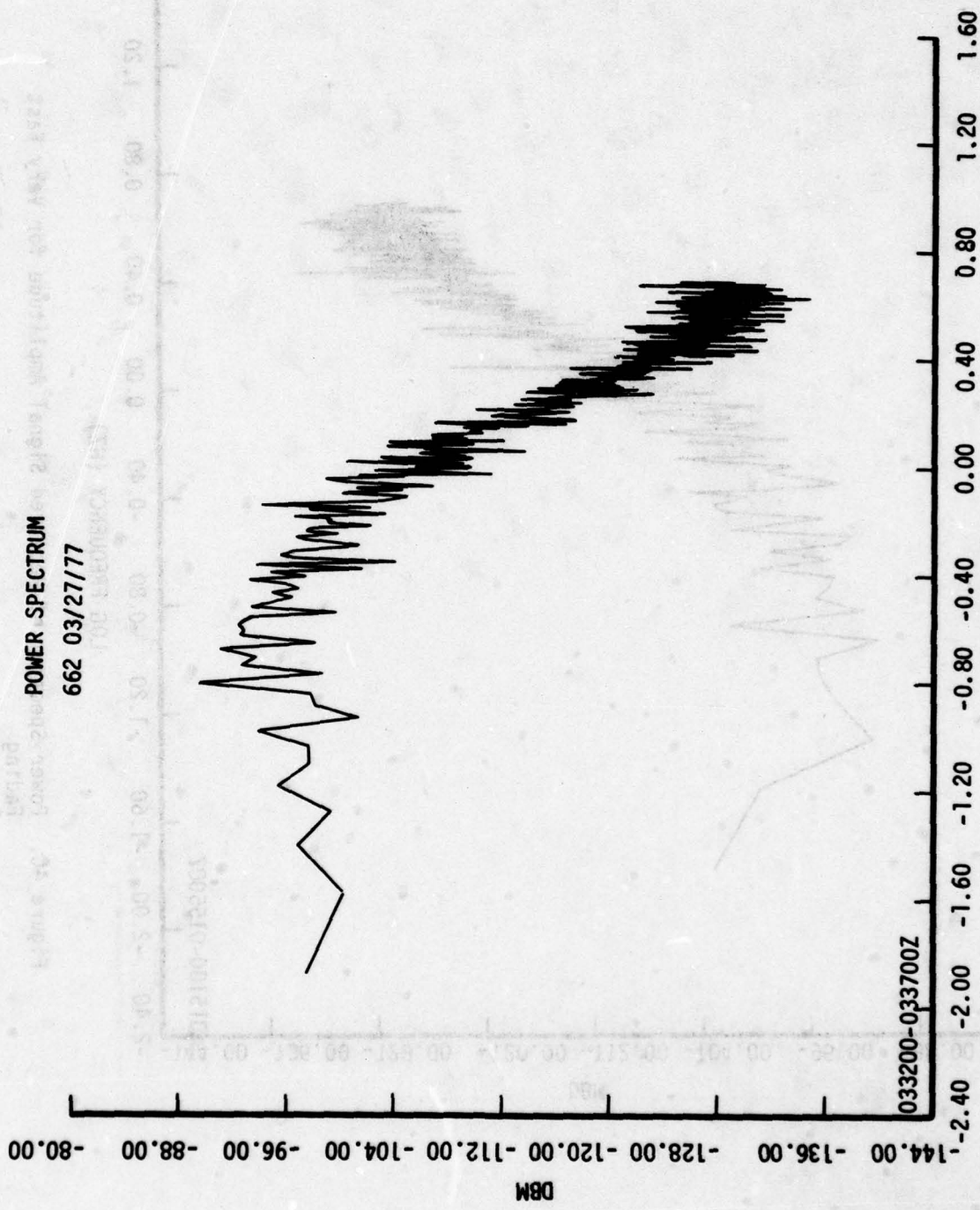

Figure 39. Power Spectrum of Received Signal Amplitude for Very Fast Fading

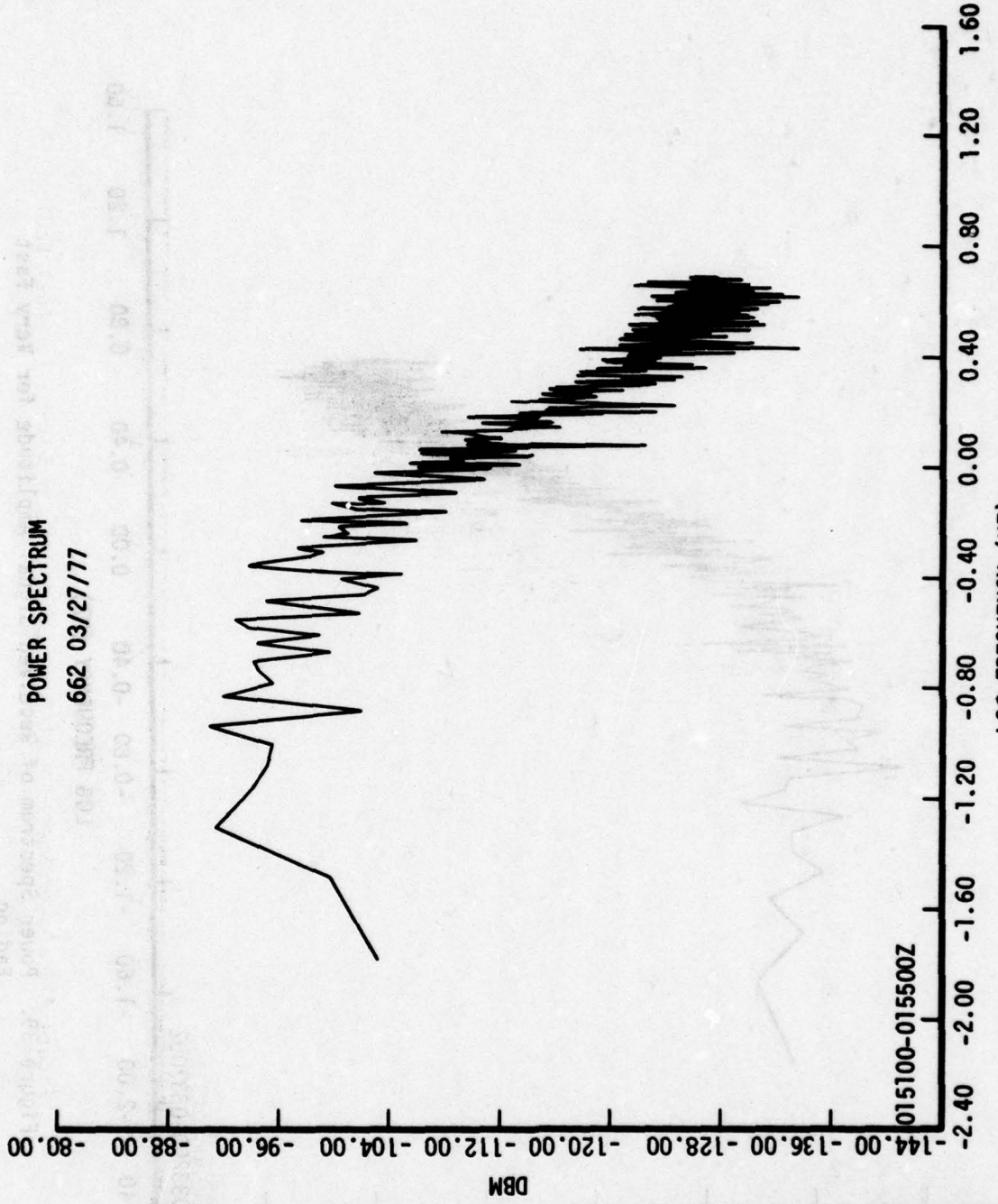

Figure 40. Power Spectrum of Received Signal Amplitude for Very Fast Fading

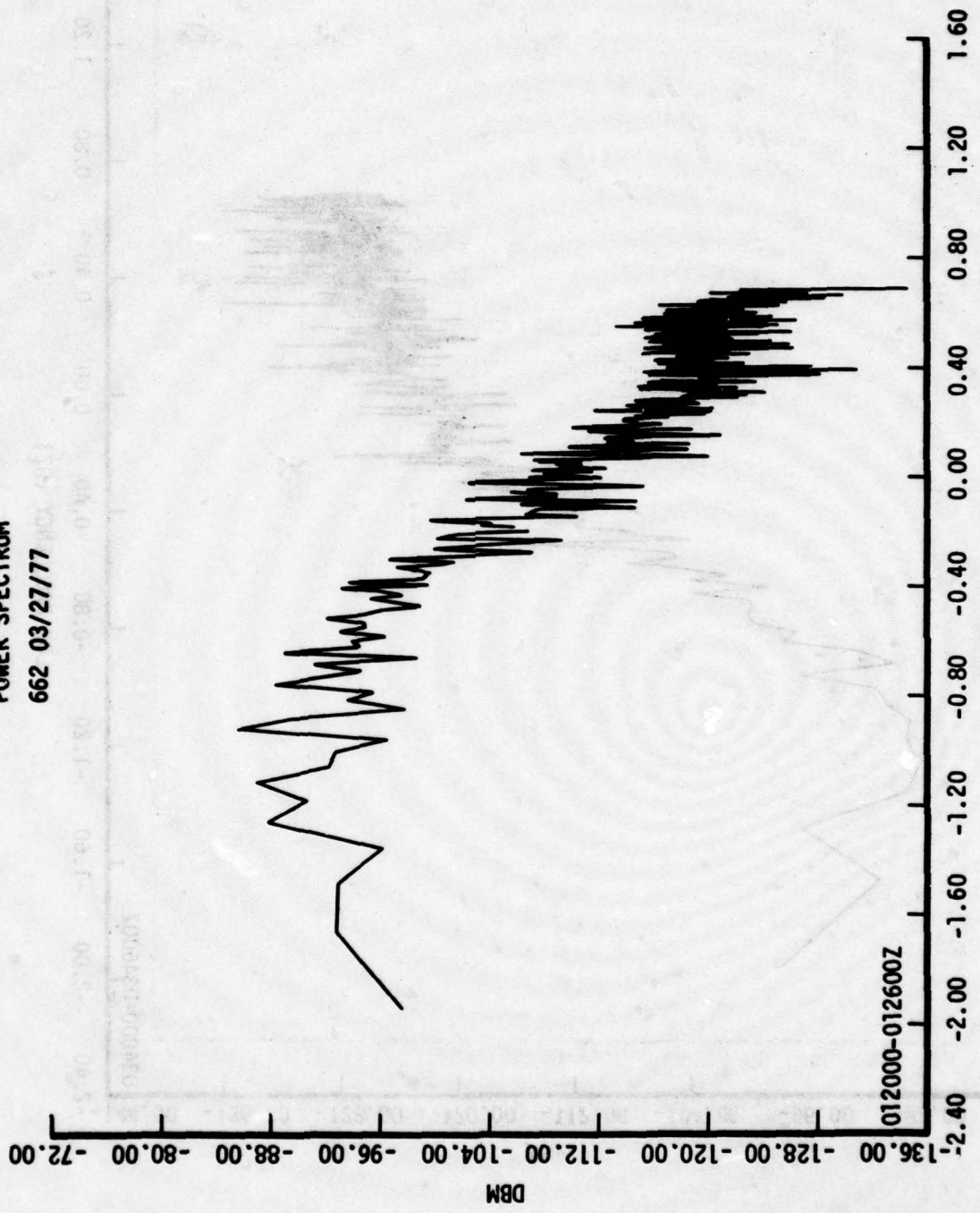

Figure 41. Power Spectrum of Received Signal Amplitude for Fast Fading

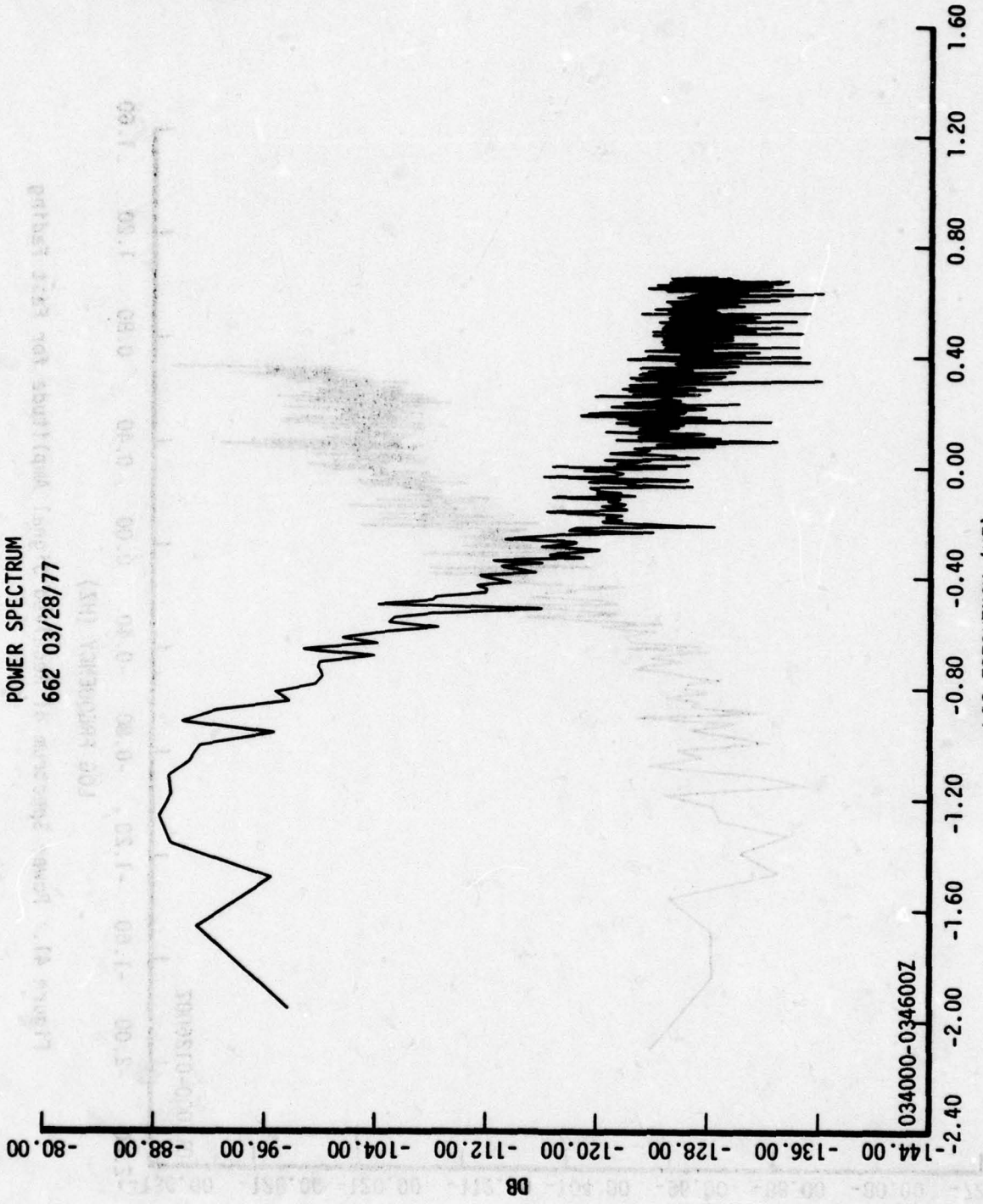

Figure 42. Power Spectrum of Received Signal Amplitude for Medium Fading

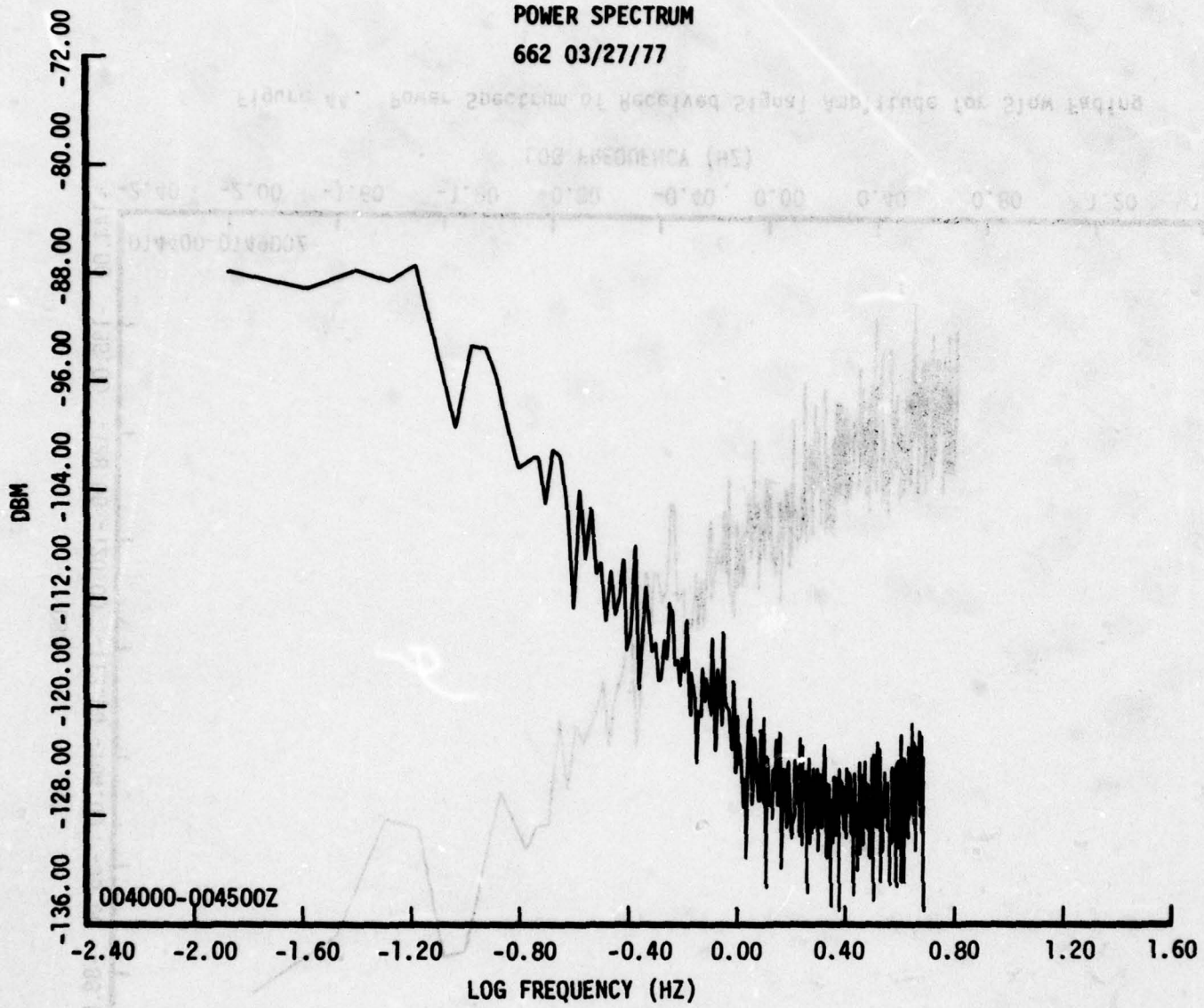

Figure 43. Power Spectrum of Received Signal Amplitude for Medium Fading

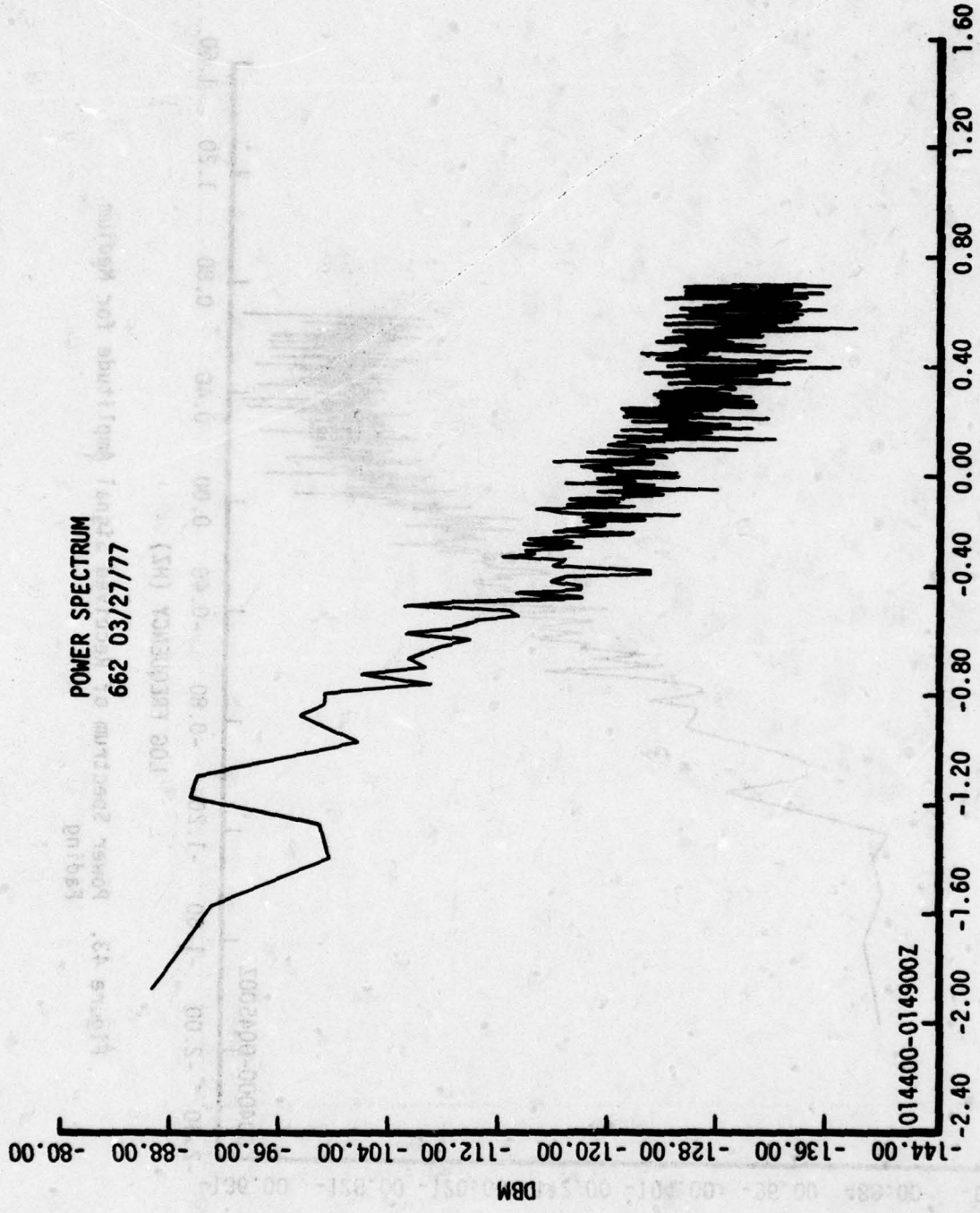

Figure 44. Power Spectrum of Received Signal Amplitude for Slow Fading

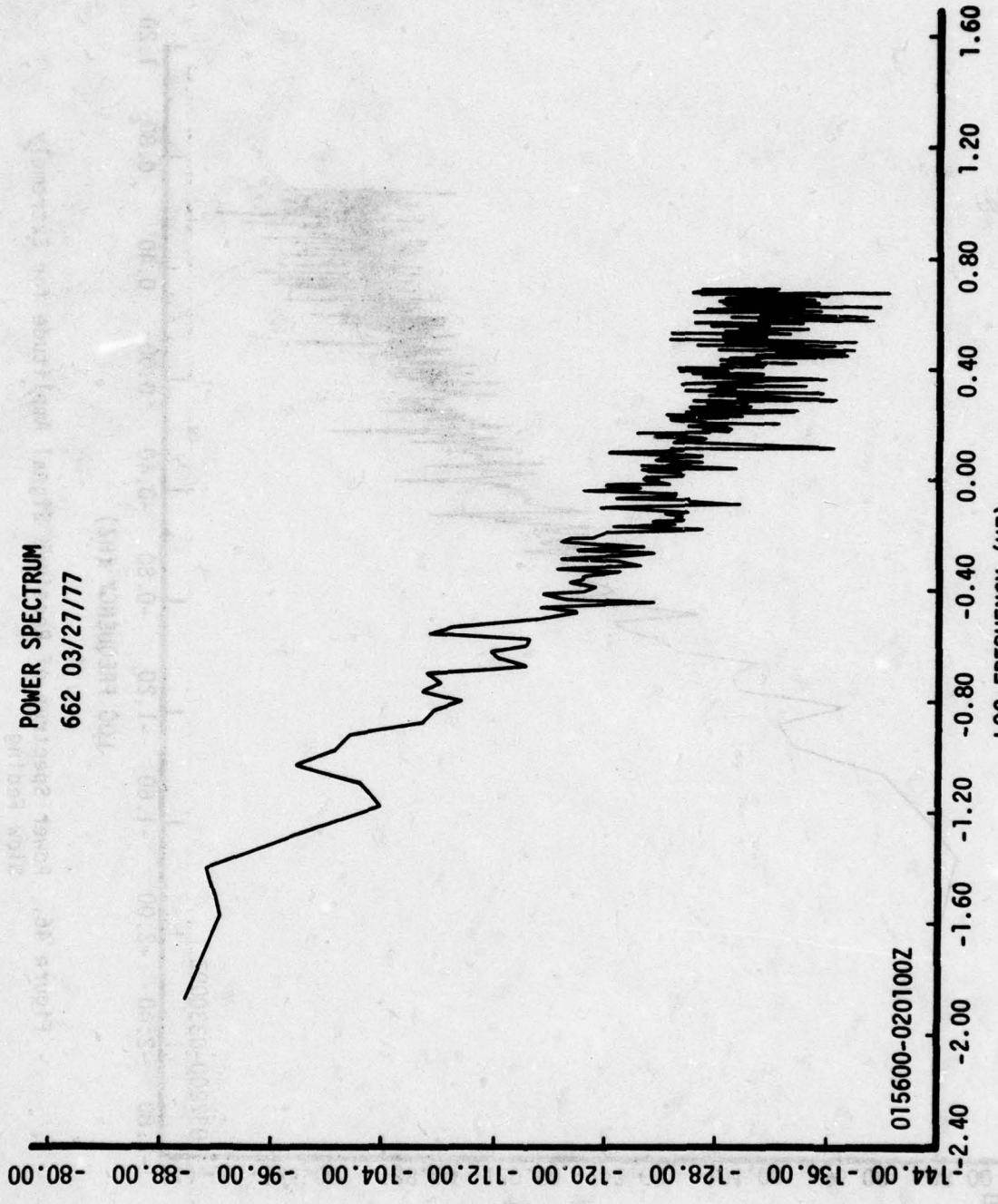

Figure 45. Power Spectrum of Received Signal Amplitude for Very Slow Fading

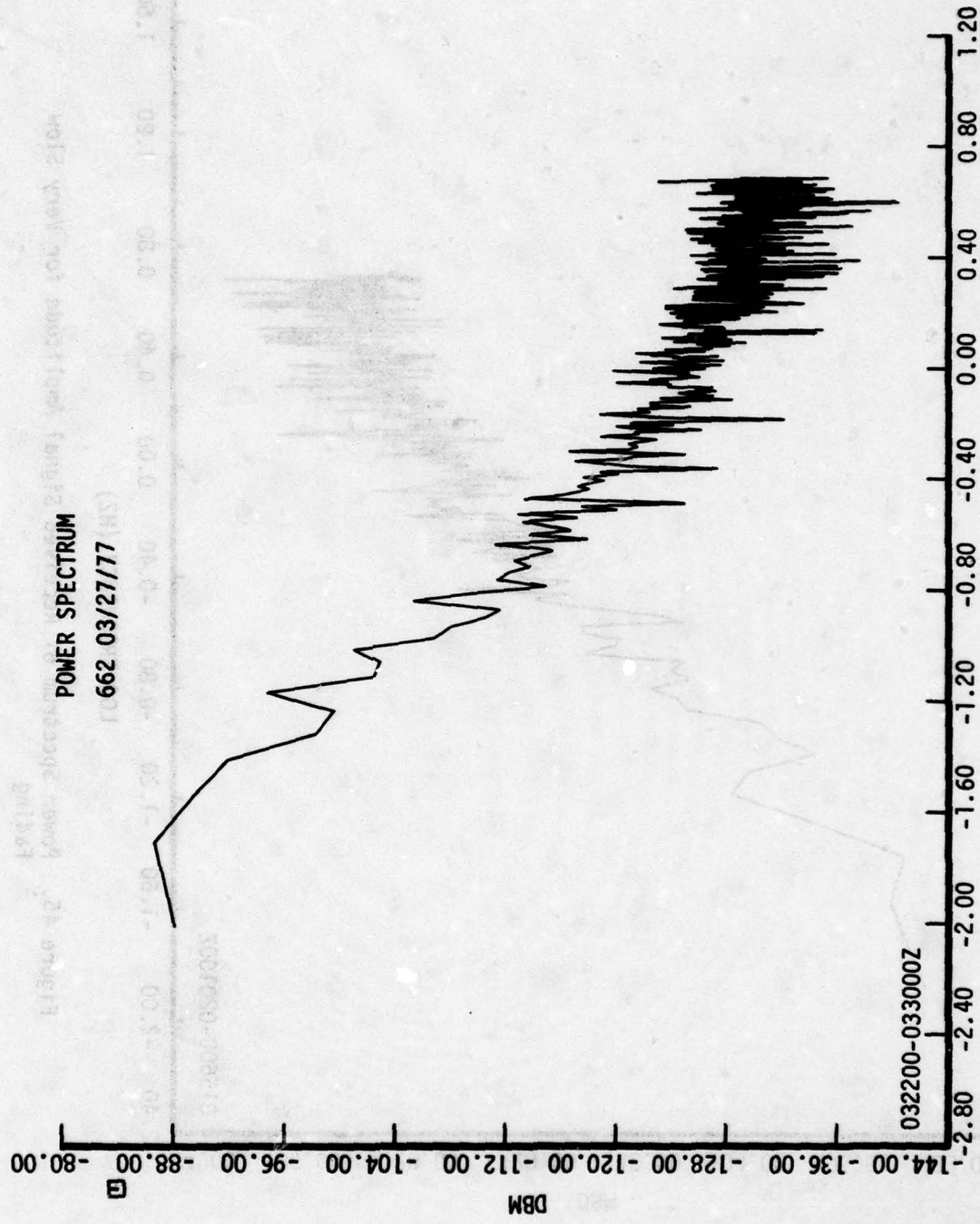

Figure 46. Power Spectrum of Received Signal Amplitude for Extremely Slow Fading

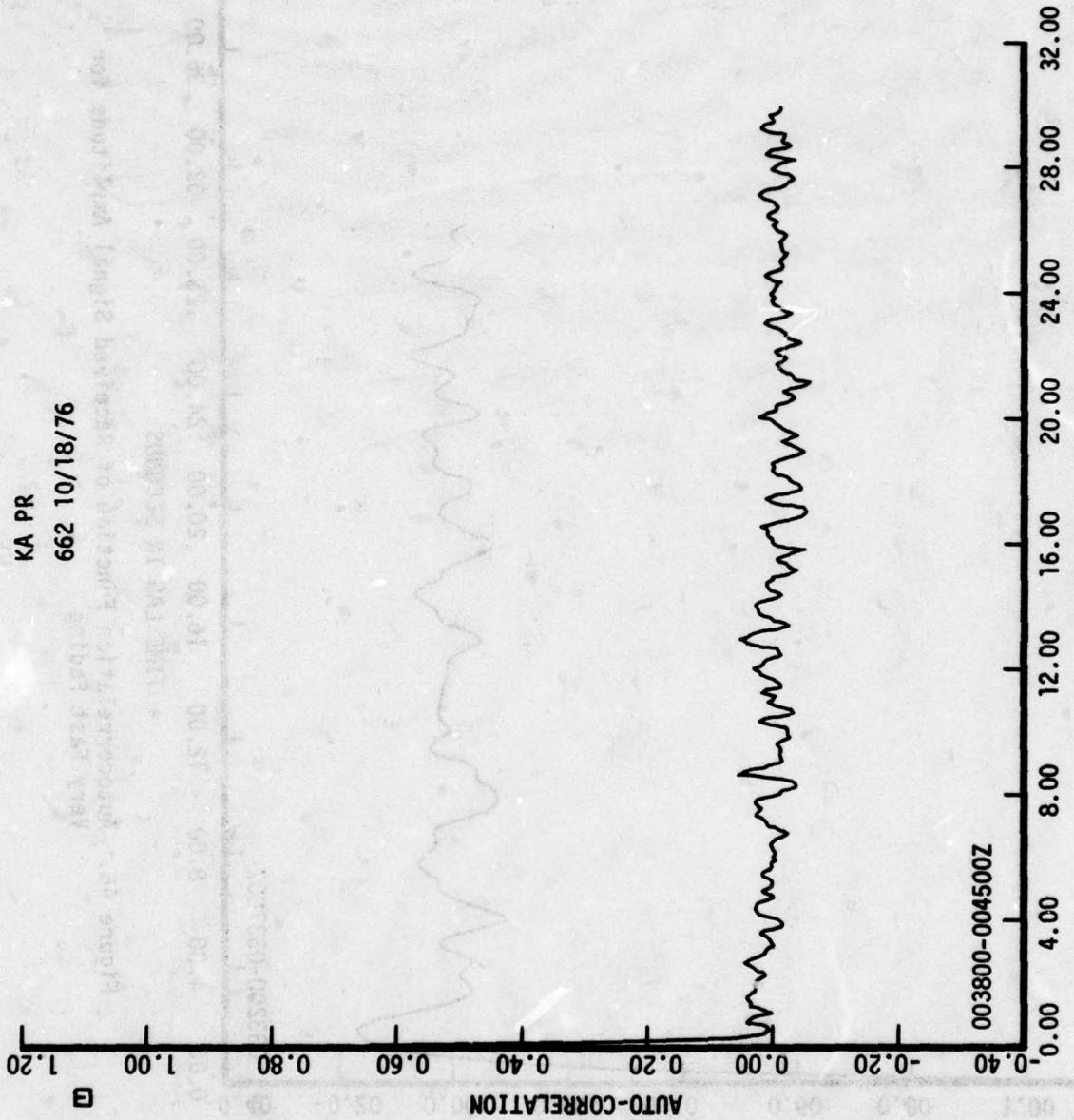

Figure 47. Autocorrelation Function of Received Signal Amplitude for Extremely Fast Fading

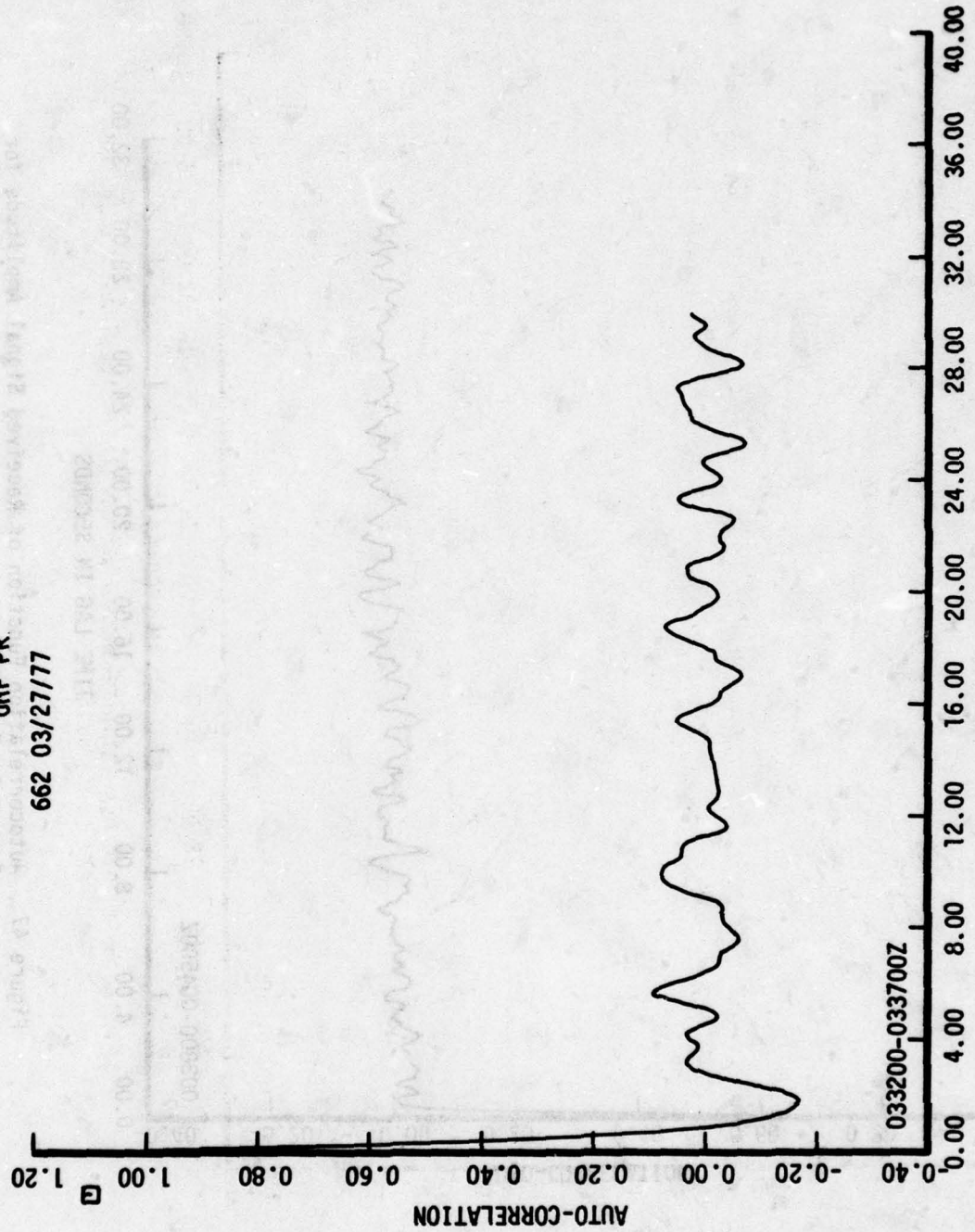

Figure 48. Autocorrelation Function of Received Signal Amplitude for Very Fast Fading

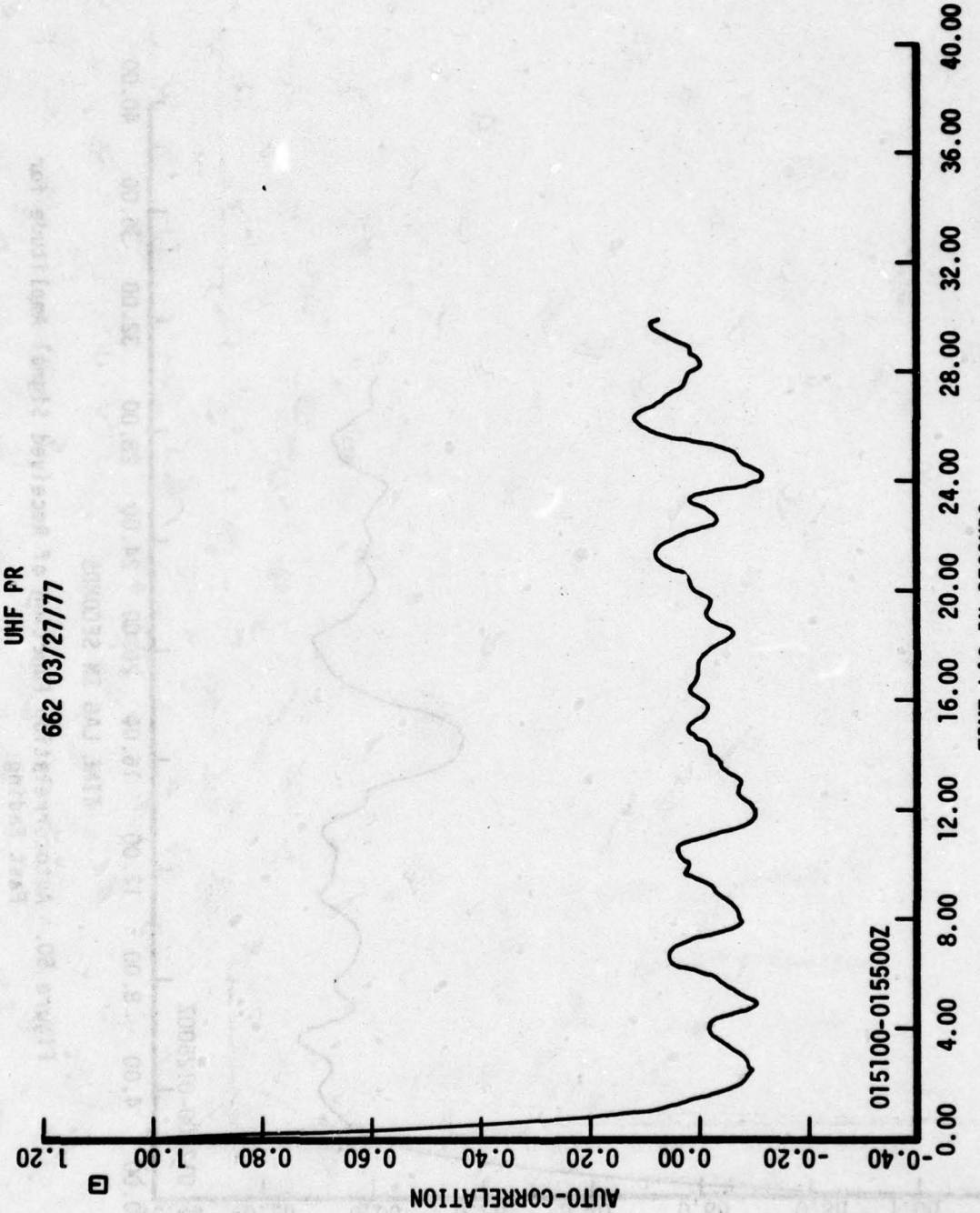

Figure 49. Autocorrelation Function of Received Signal Amplitude for Very Fast Fading

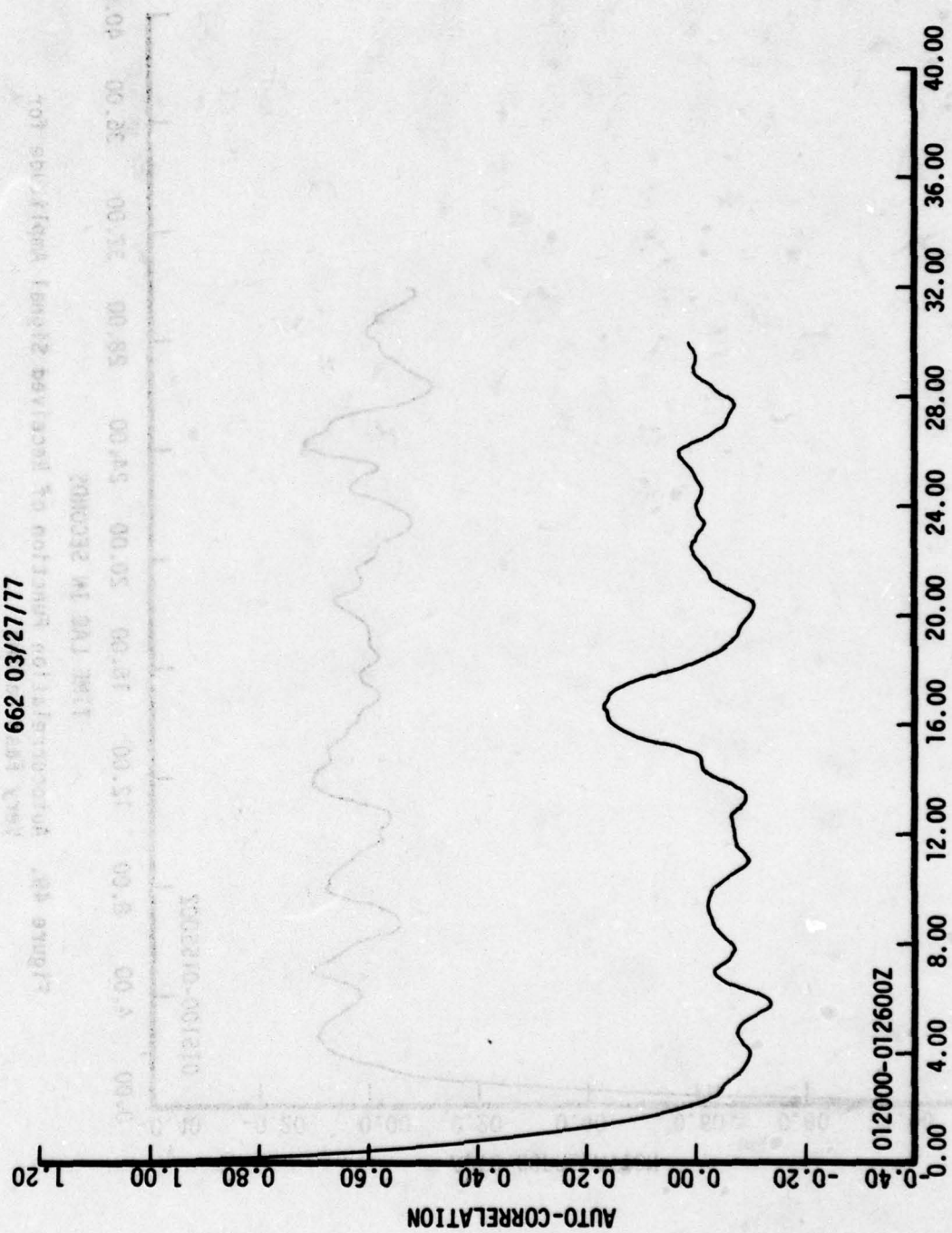

Figure 50. Autocorrelation Function of Received Signal Amplitude for Fast Fading

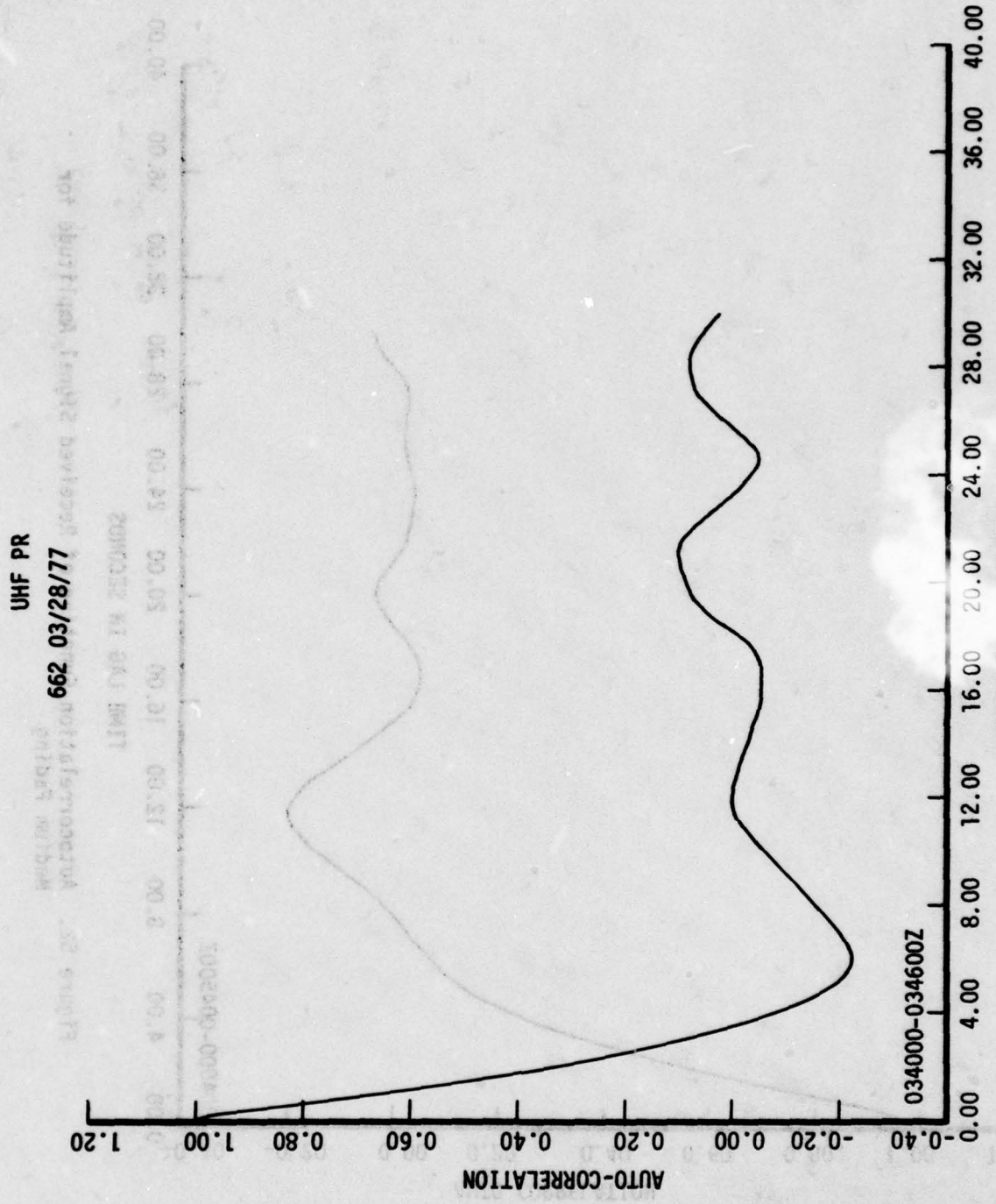

Figure 51. Autocorrelation Function of Received Signal Amplitude for Medium Fading

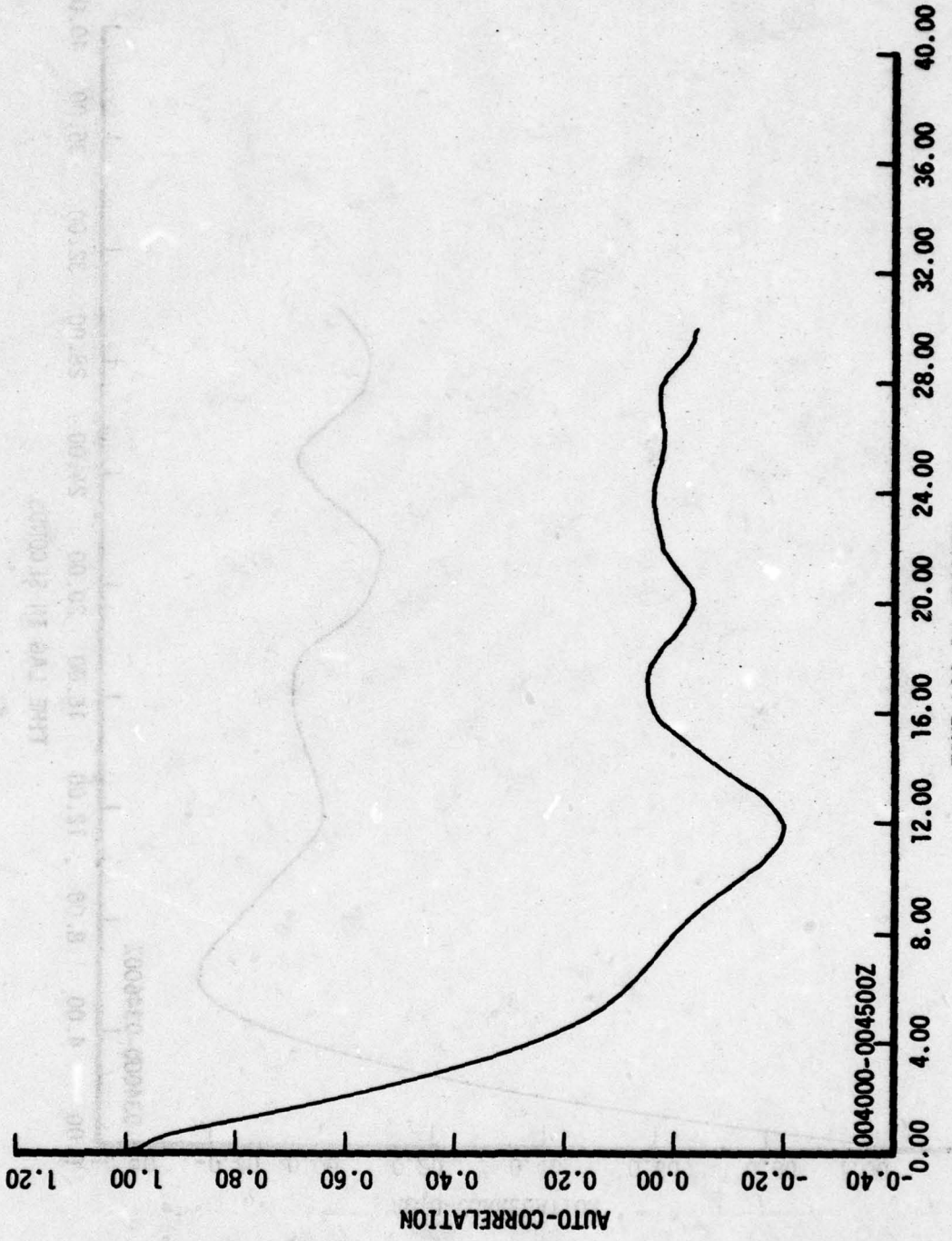

Figure 52. Autocorrelation Function of Received Signal Amplitude for Medium Fading

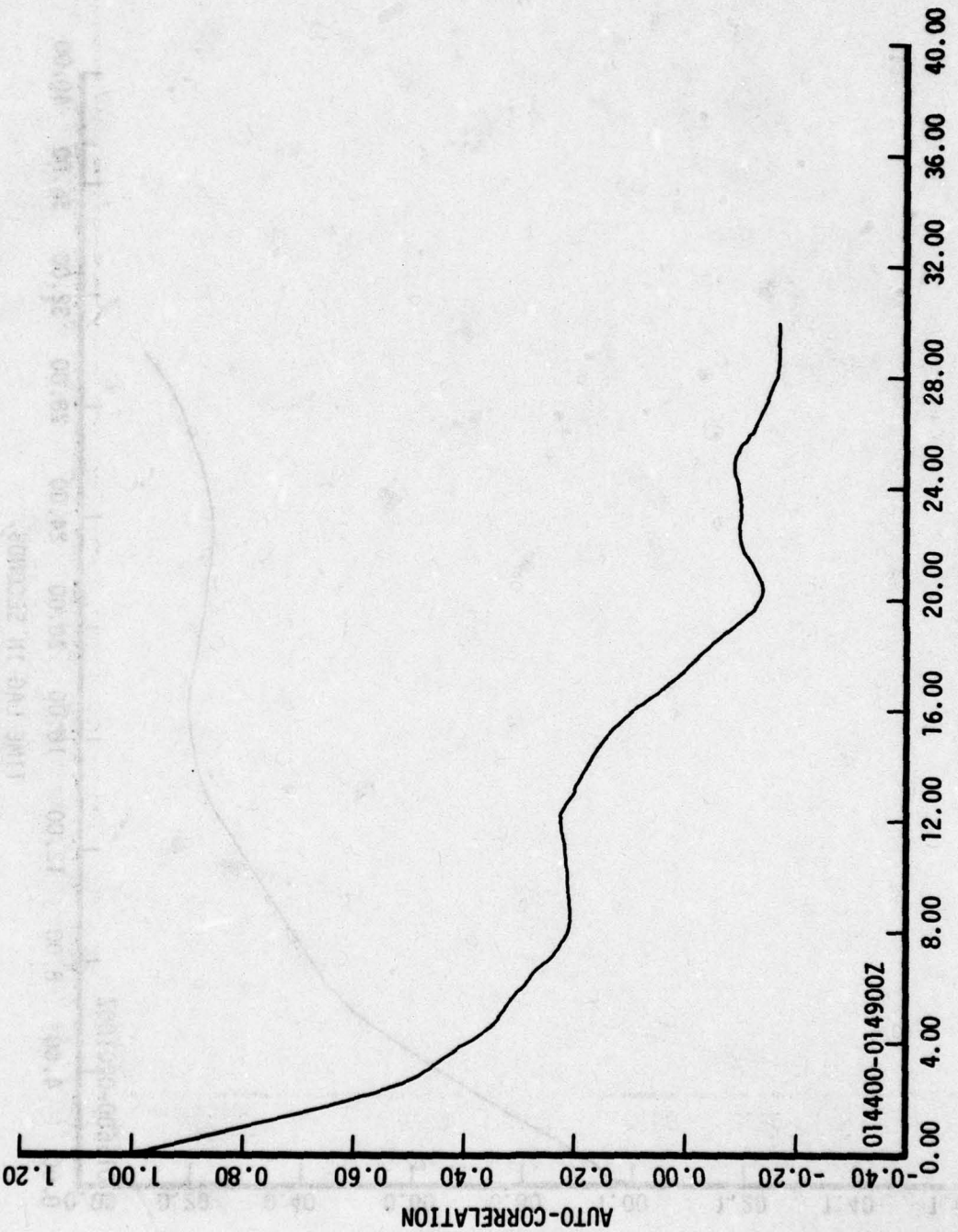

Figure 53. Autocorrelation Function of Received Signal Amplitude for Slow Fading

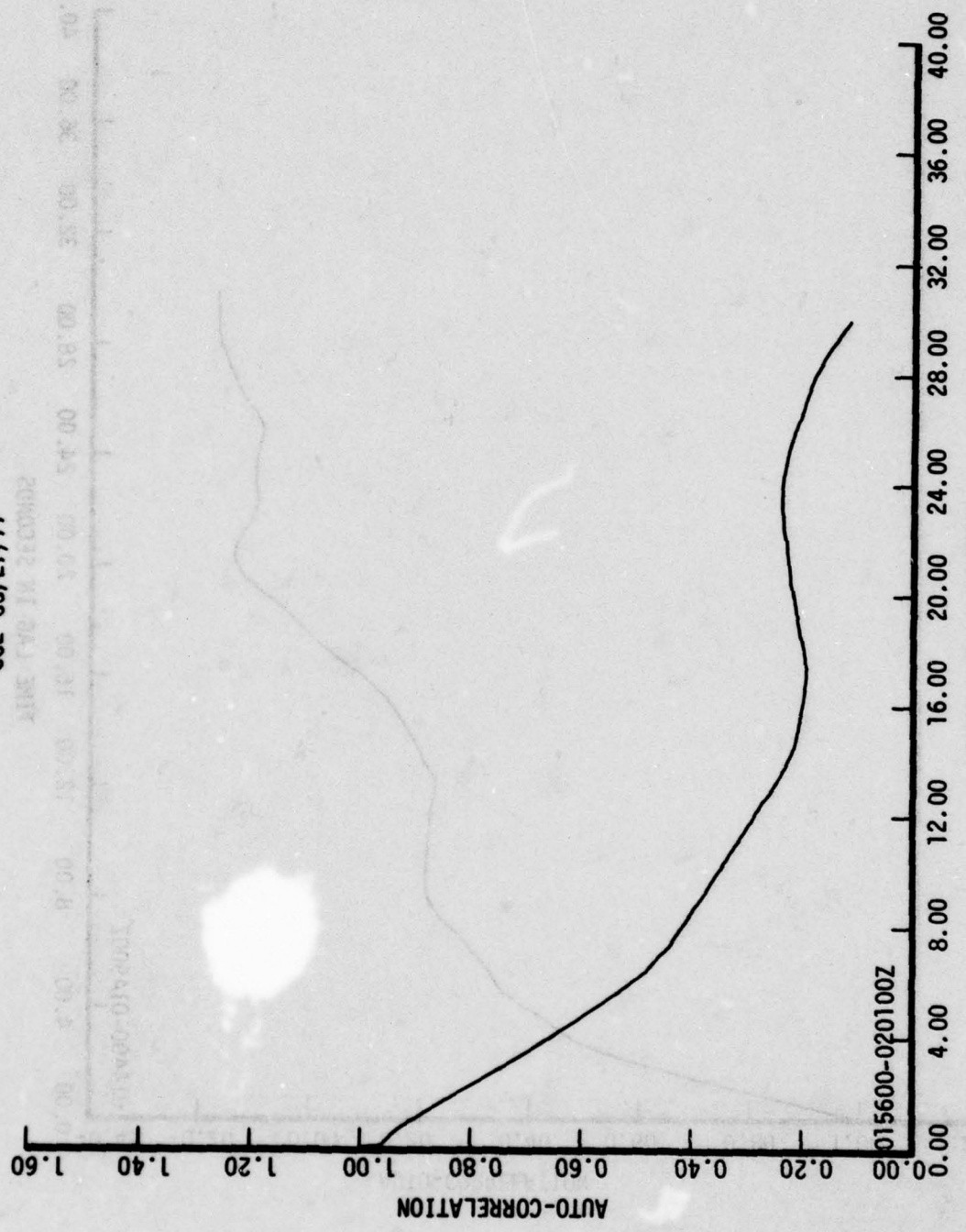

Figure 54. Autocorrelation Function of Received Signal Amplitude for Very Slow Fading

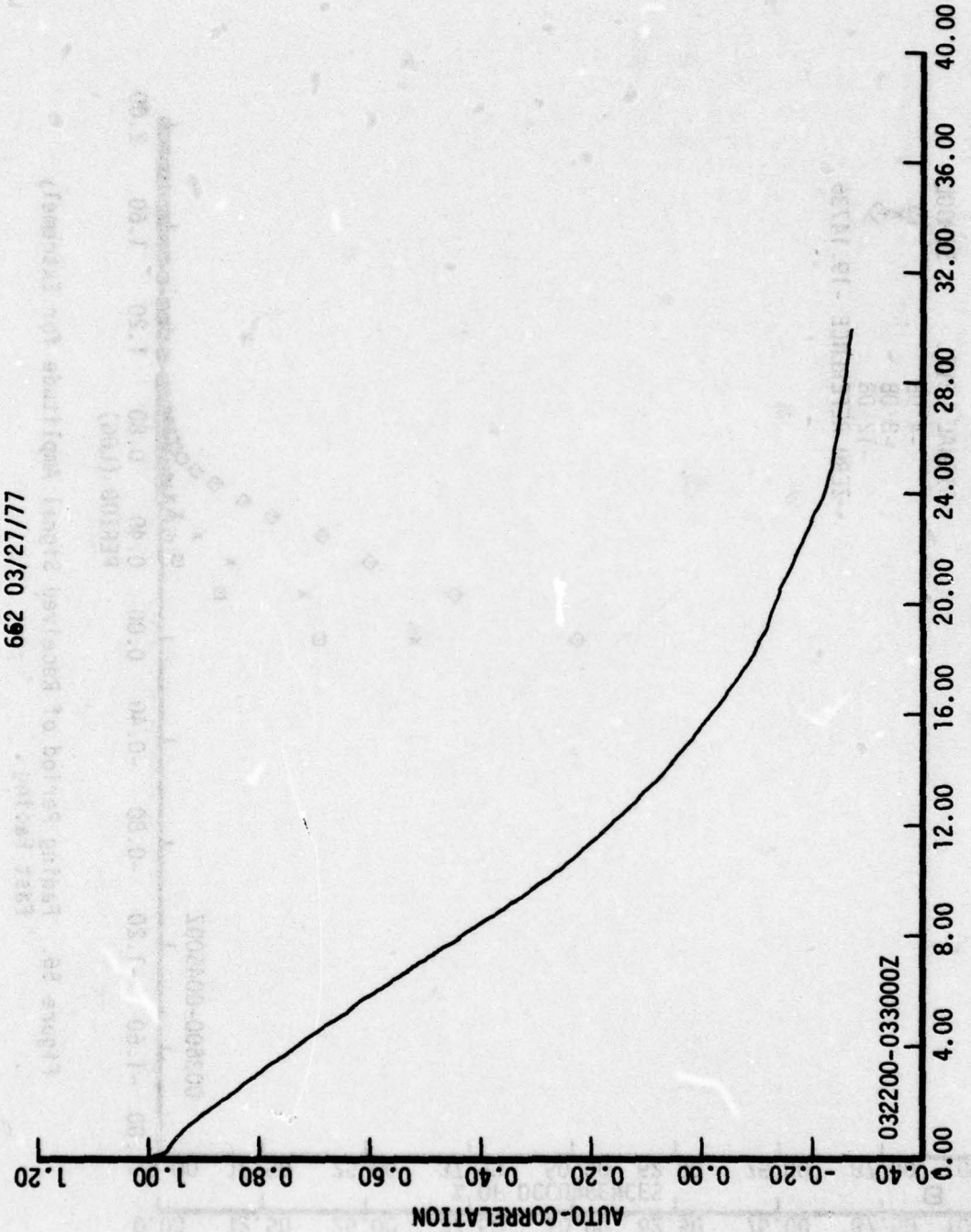

Figure 55. Autocorrelation Function of Received Signal Amplitude for Extremely Slow Fading

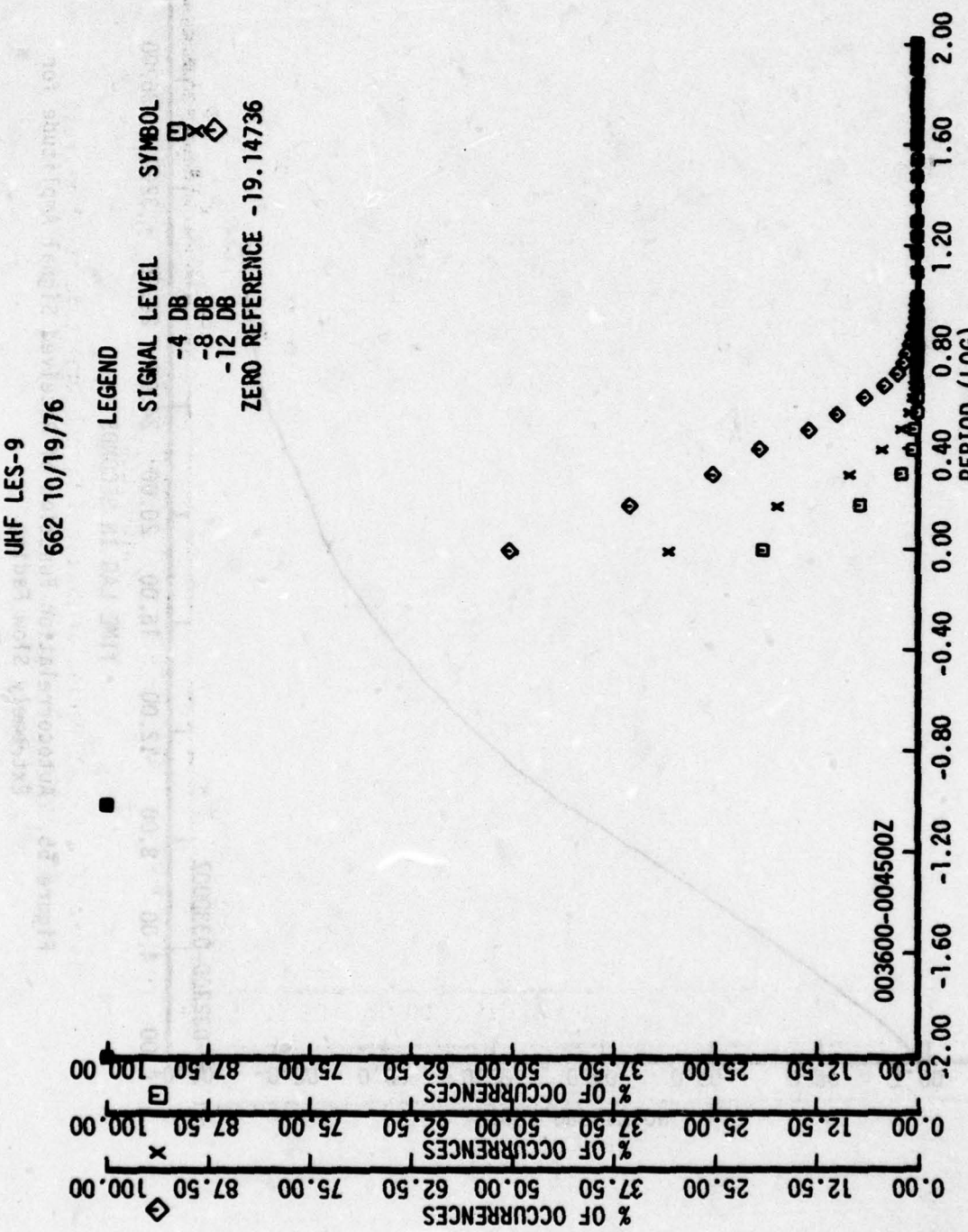

Figure 56. Fading Period of Received Signal Amplitude for Extremely Fast Fading

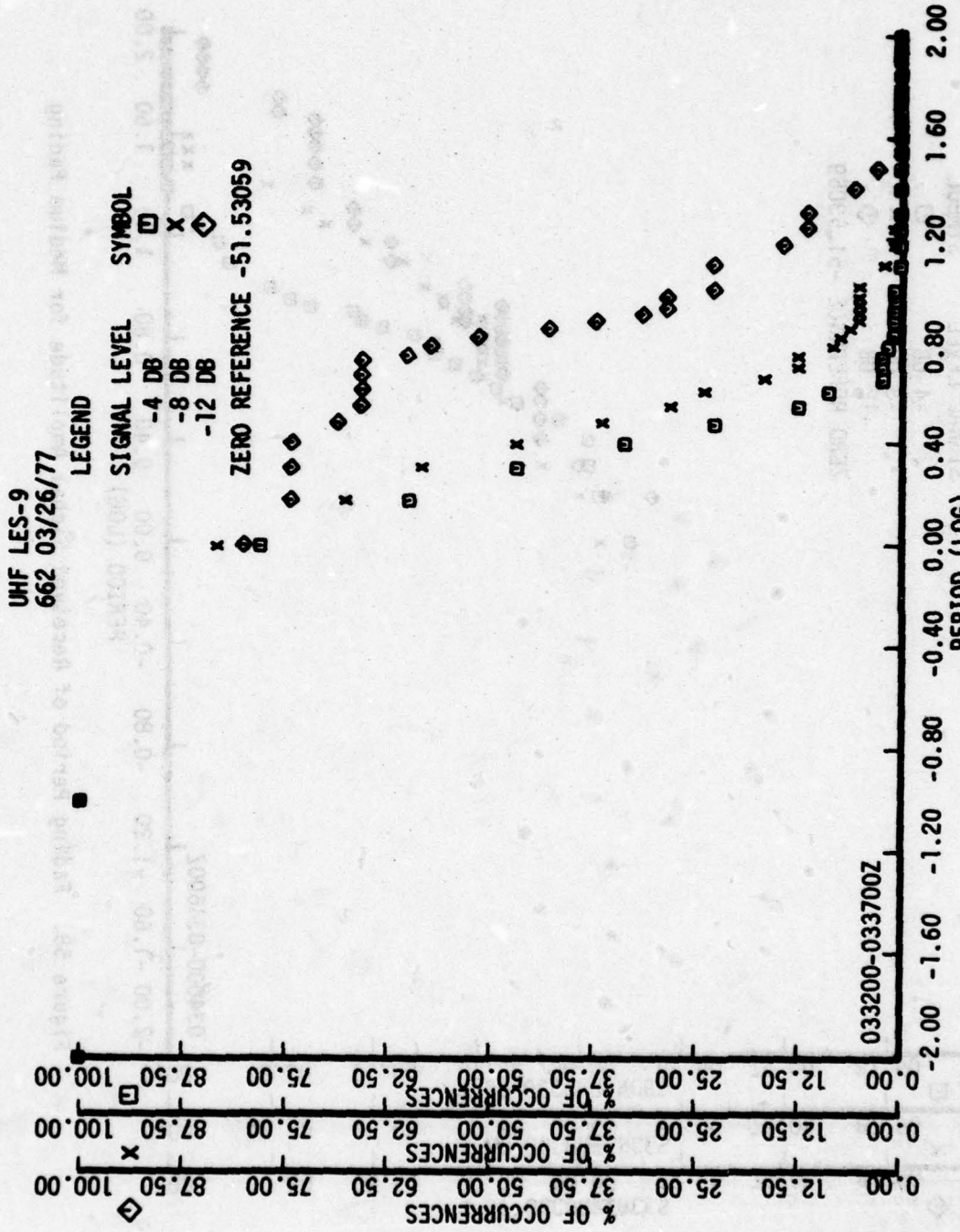

Figure 57. Fading Period of Received Signal Amplitude for Very Fast Fading

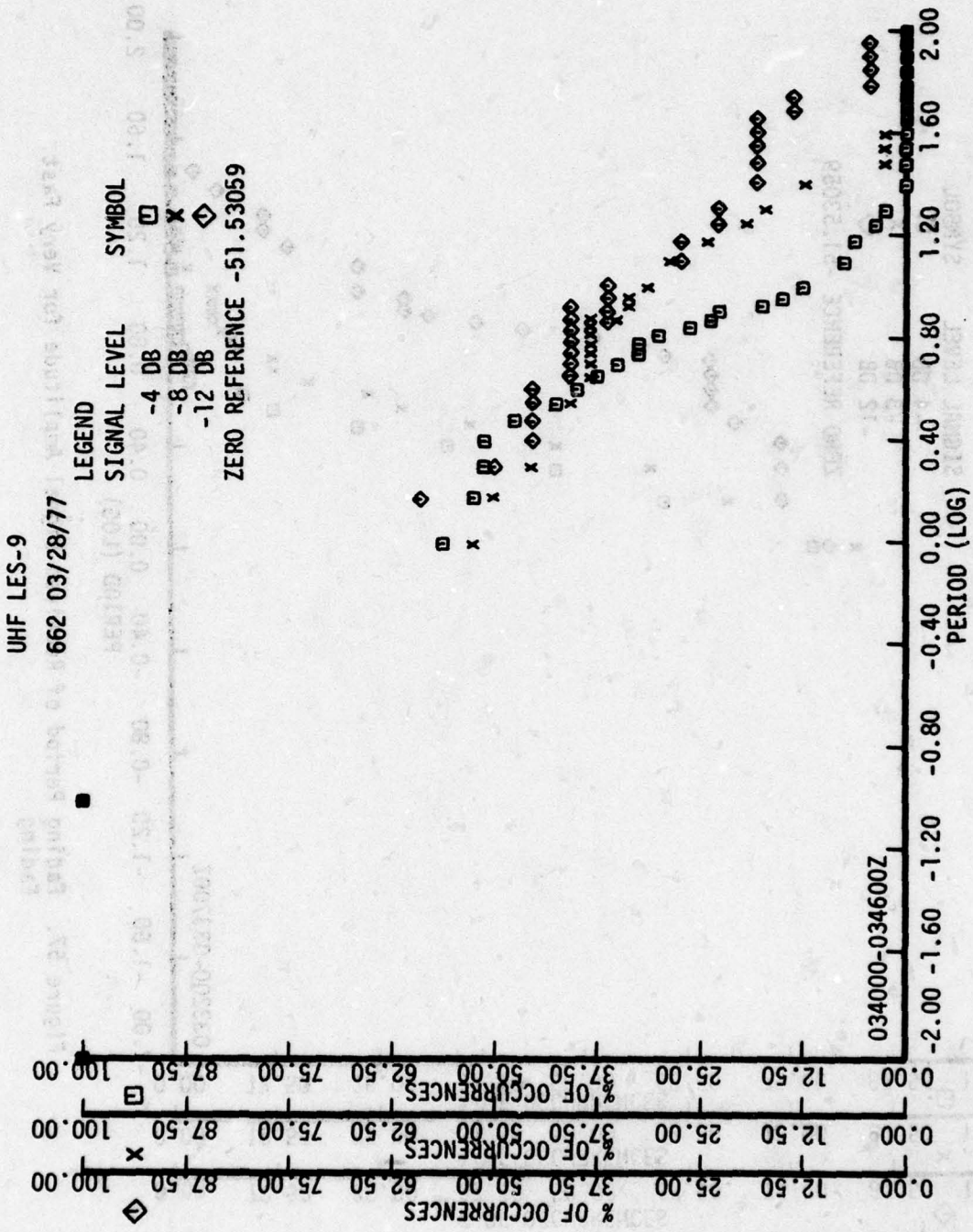

Figure 58. Fading Period of Received Signal Amplitude for Medium Fading

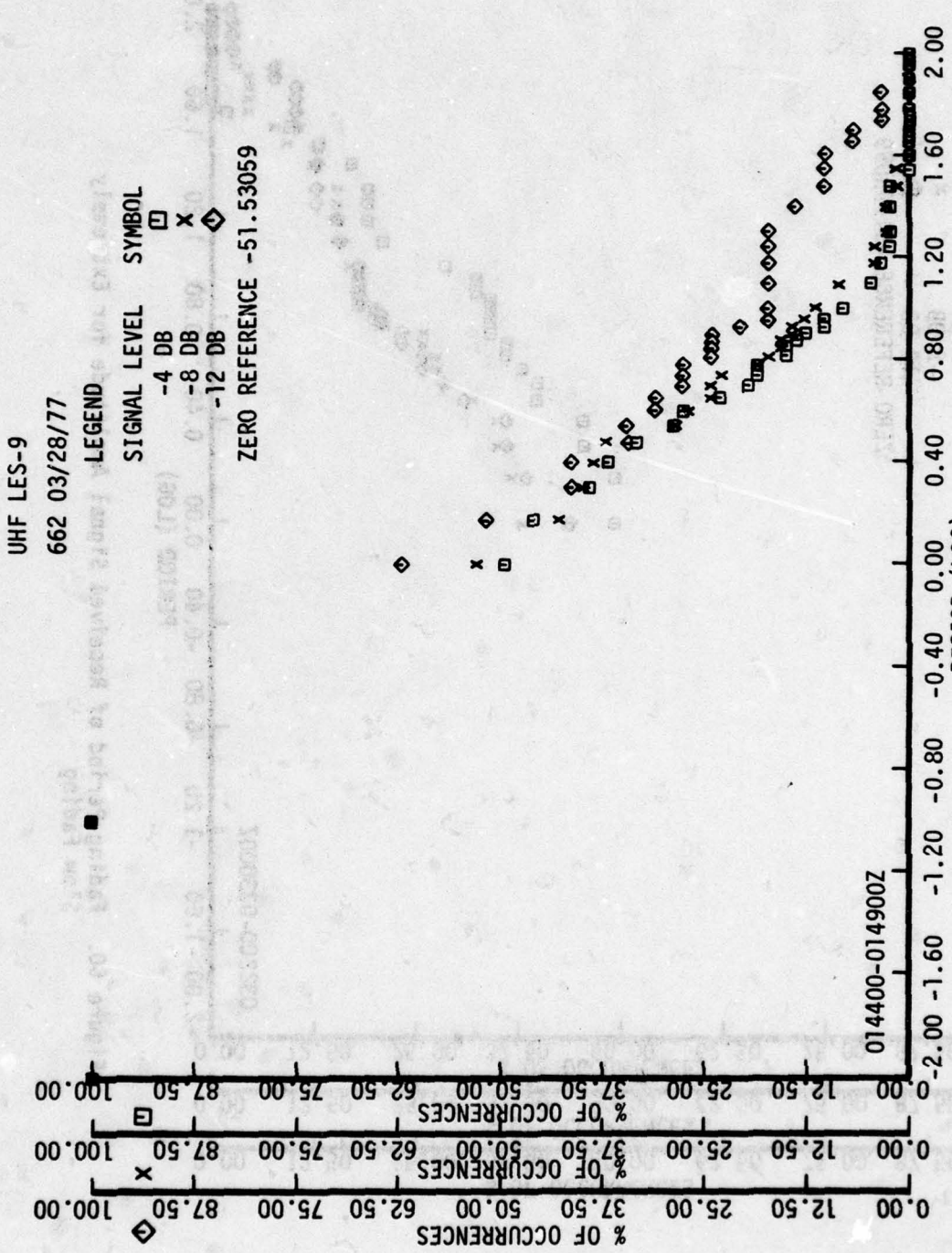

Figure 59. Fading Period of Received Signal Amplitude for Slow Fading

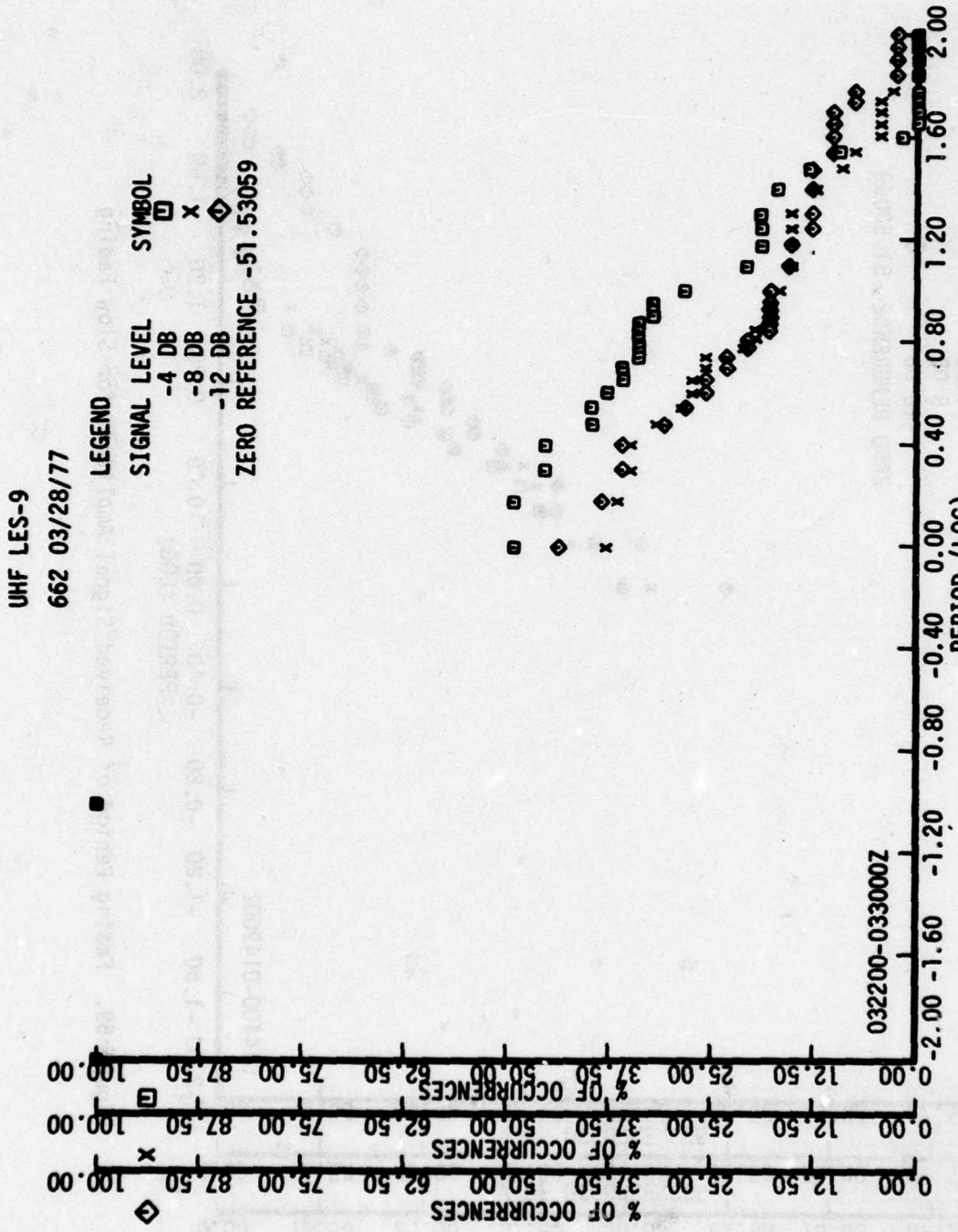

Figure 60. Fading Period of Received Signal Amplitude for Extremely Slow Fading

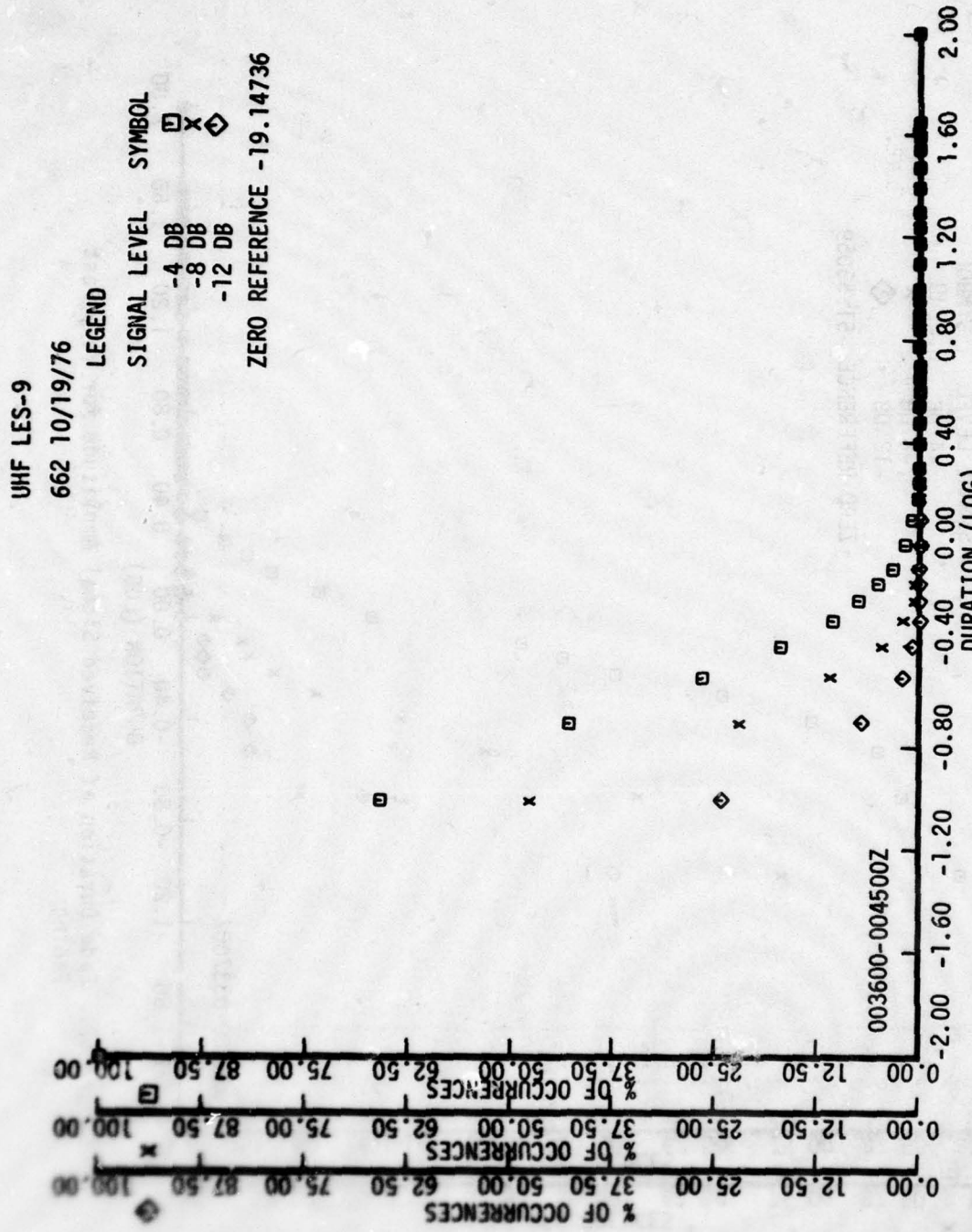

Figure 61. Fade Duration of Received Signal Amplitude for Extremely Fast Fading

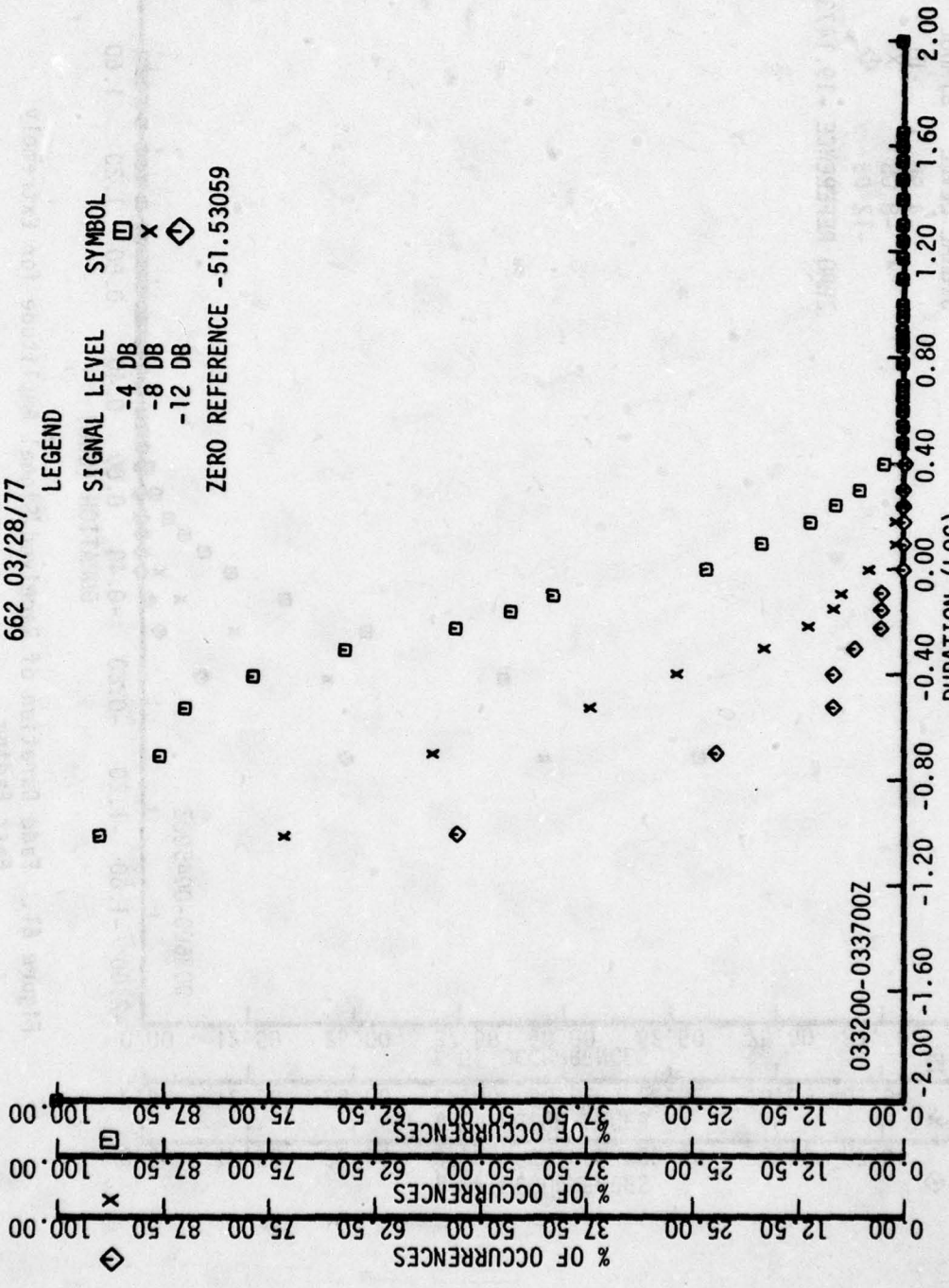

Figure 62. Fade Duration of Received Signal Amplitude for Very Fast Fading

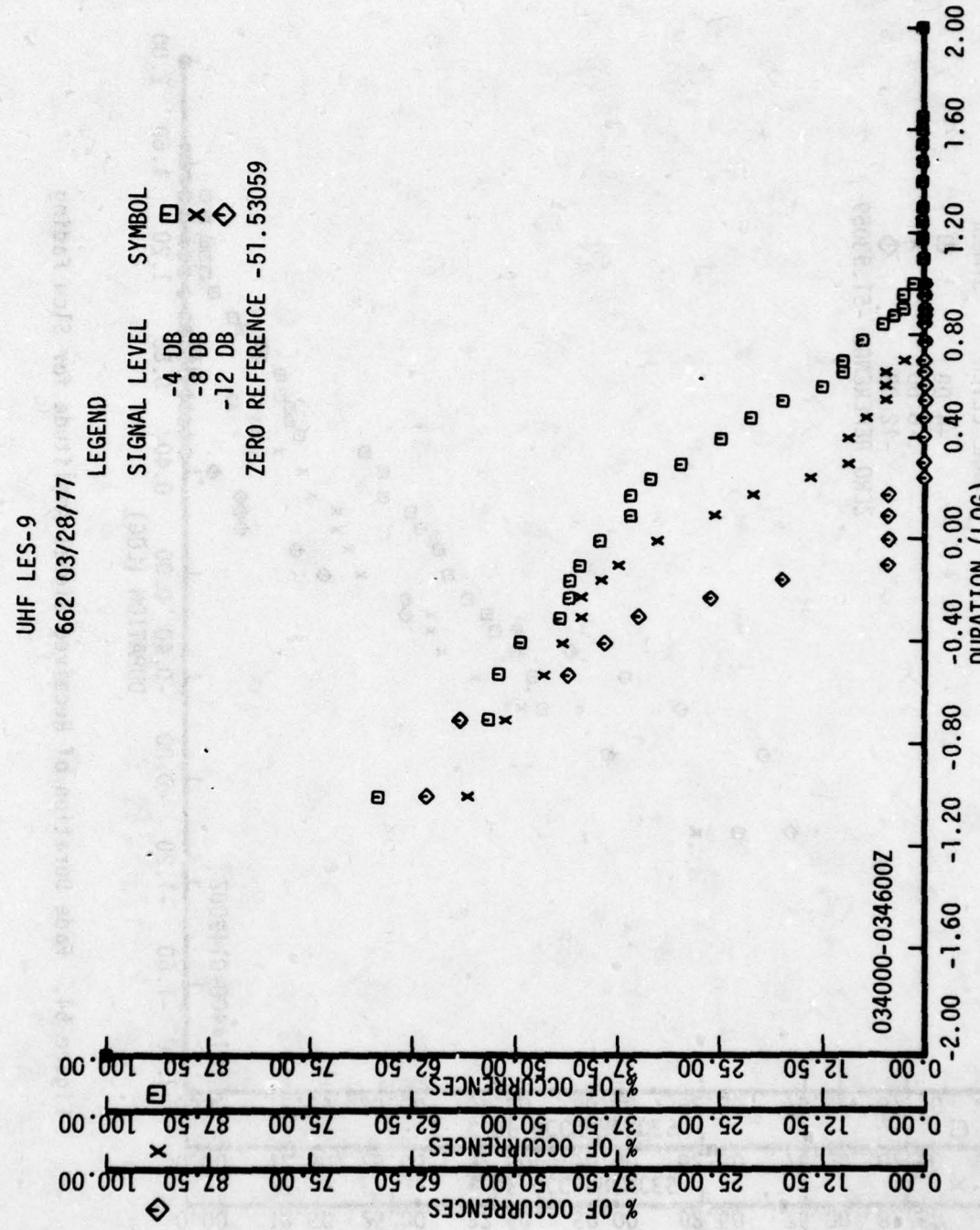

Figure 63. Fade Duration of Received Signal Amplitude for Medium Fading

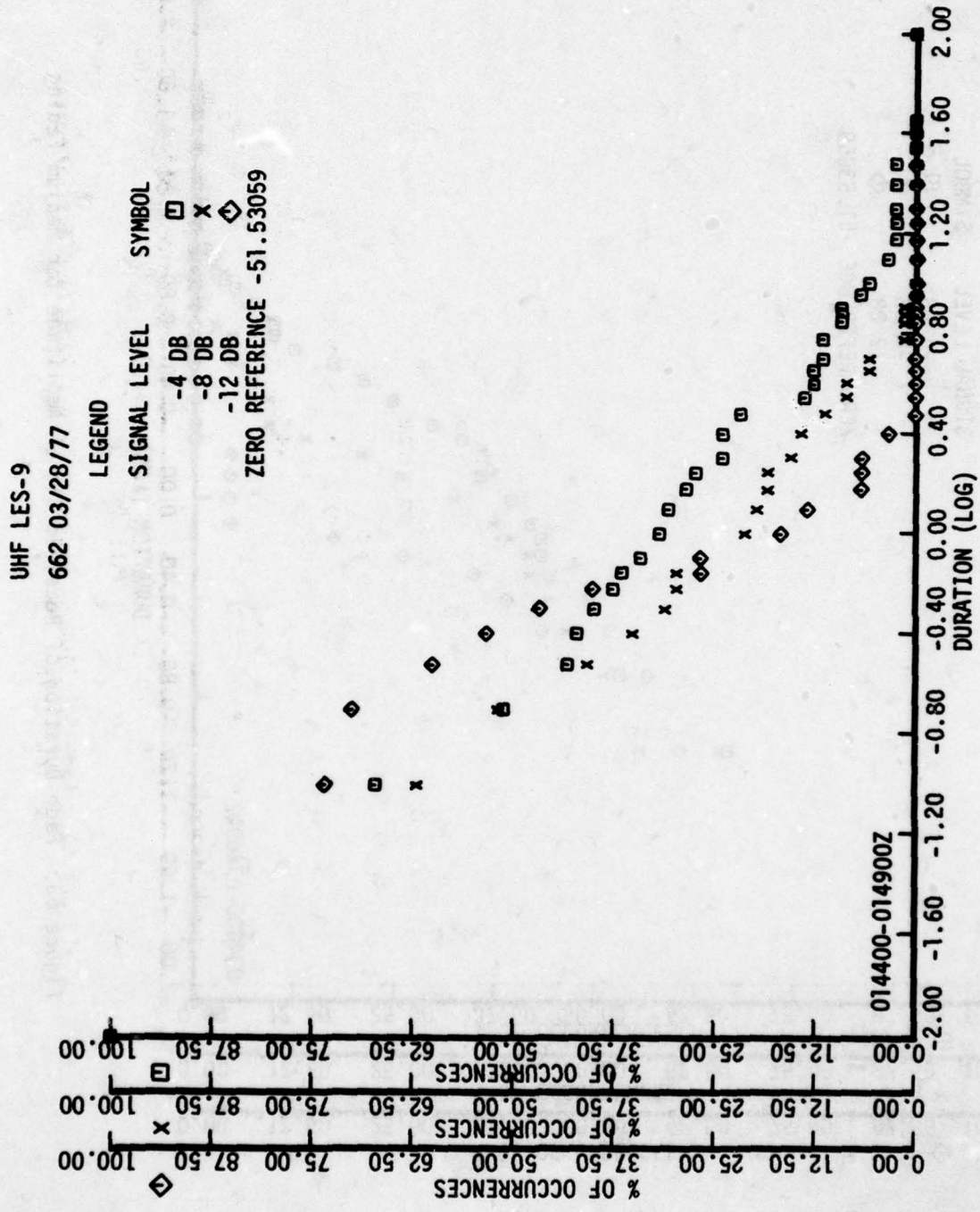

Figure 64. Fade Duration of Received Signal Amplitude for Slow Fading

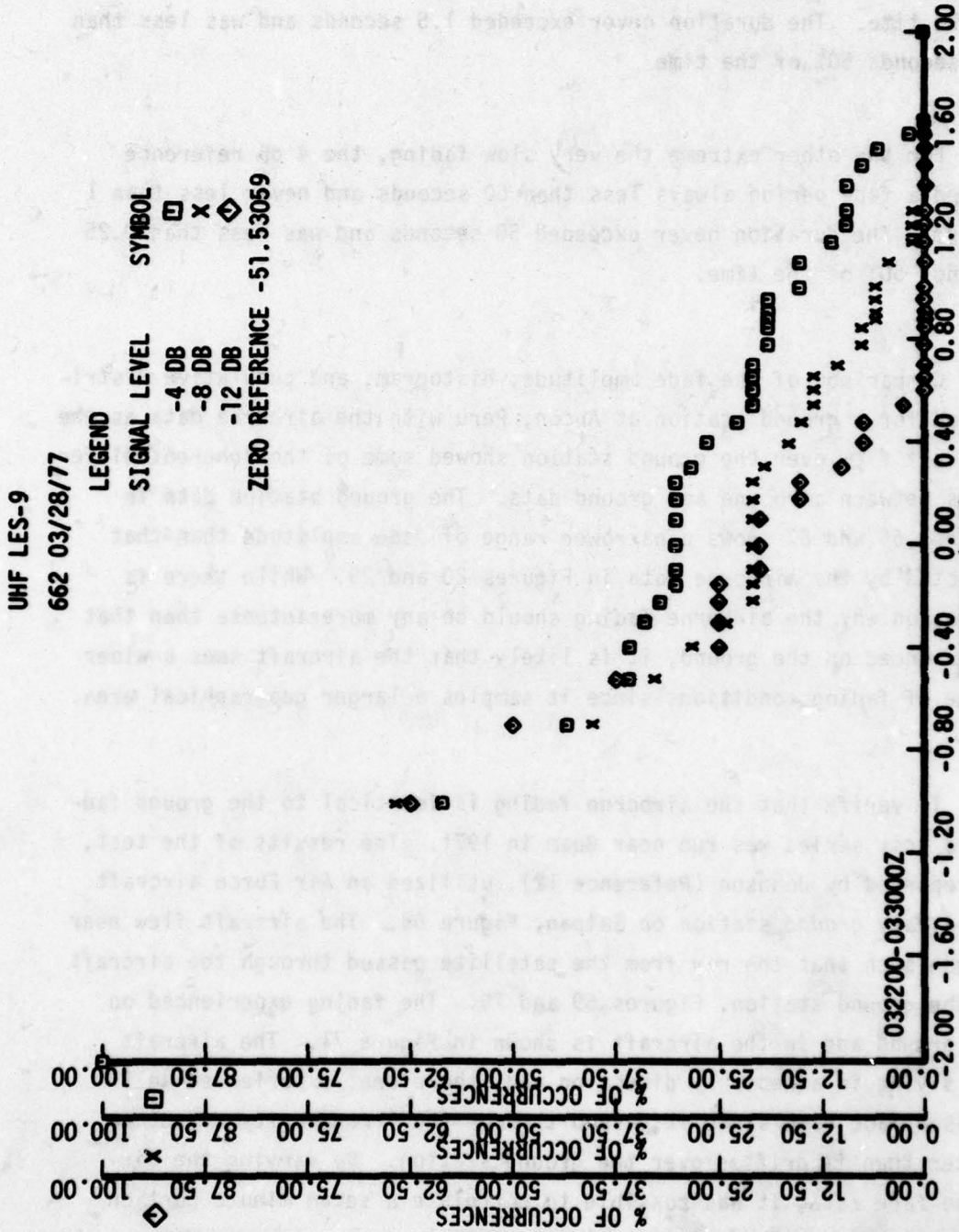

Figure 65. Fade Duration of Received Signal Amplitude for Extremely Slow Fading

For the extremely fast fade the reference of 4 dB below the mean showed a fade period always less than 2.5 seconds and less than 0.3 seconds 50% of the time. The duration never exceeded 1.5 seconds and was less than 0.2 seconds 50% of the time.

For the other extreme the very slow fading, the 4 dB reference showed a fade period always less than 60 seconds and never less than 1 second. The duration never exceeded 50 seconds and was less than 0.25 seconds 50% of the time.

Comparison of the fade amplitude, histogram, and cumulative distribution for a ground station at Ancon, Peru with the airborne data as the aircraft flew over the ground station showed some of the inherent differences between airborne and ground data. The ground station data in Figures 66 and 67 shows a narrower range of fade amplitude than that depicted by the airborne data in Figures 20 and 29. While there is no reason why the airborne fading should be any more intense than that experienced on the ground, it is likely that the aircraft sees a wider range of fading conditions since it samples a larger geographical area.

To verify that the airborne fading is identical to the ground fading a test series was run near Guam in 1971. The results of the test, as reported by Johnson (Reference 12), utilized an Air Force aircraft and a Navy ground station on Saipan, Figure 68. The aircraft flew near Saipan such that the ray from the satellite passed through the aircraft to the ground station, Figures 69 and 70. The fading experienced on the ground and in the aircraft is shown in Figure 71. The aircraft was flying in a westerly direction and, therefore, experienced an increased fade rate since it passed through the irregularity structure faster than it drifted over the ground station. By varying the airborne fade rate, it was possible to correlate a seven minute portion of the ground data with a one minute portion of the airborne data,

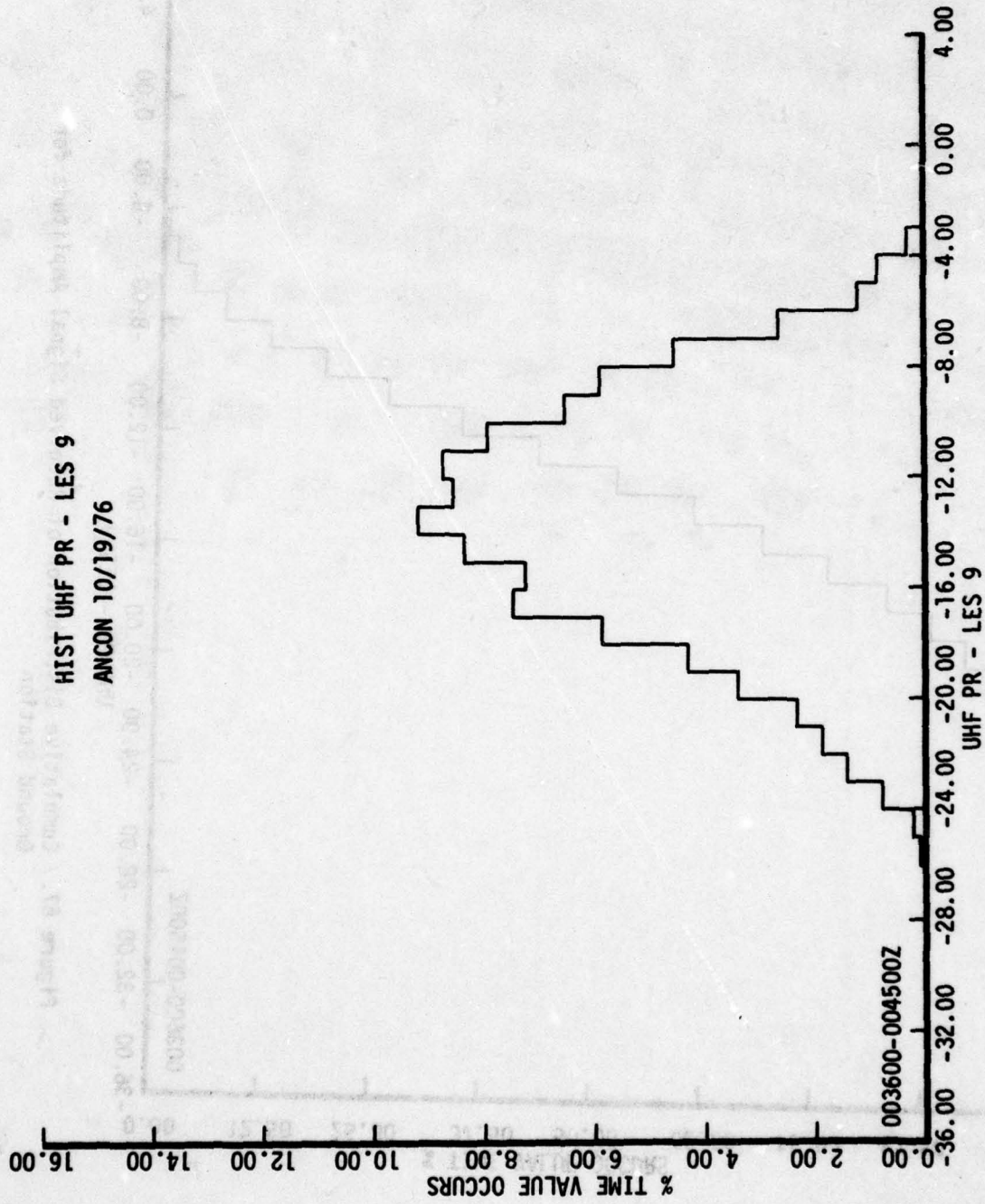

Figure 66. Histogram of Received Signal Amplitude for Ground Station

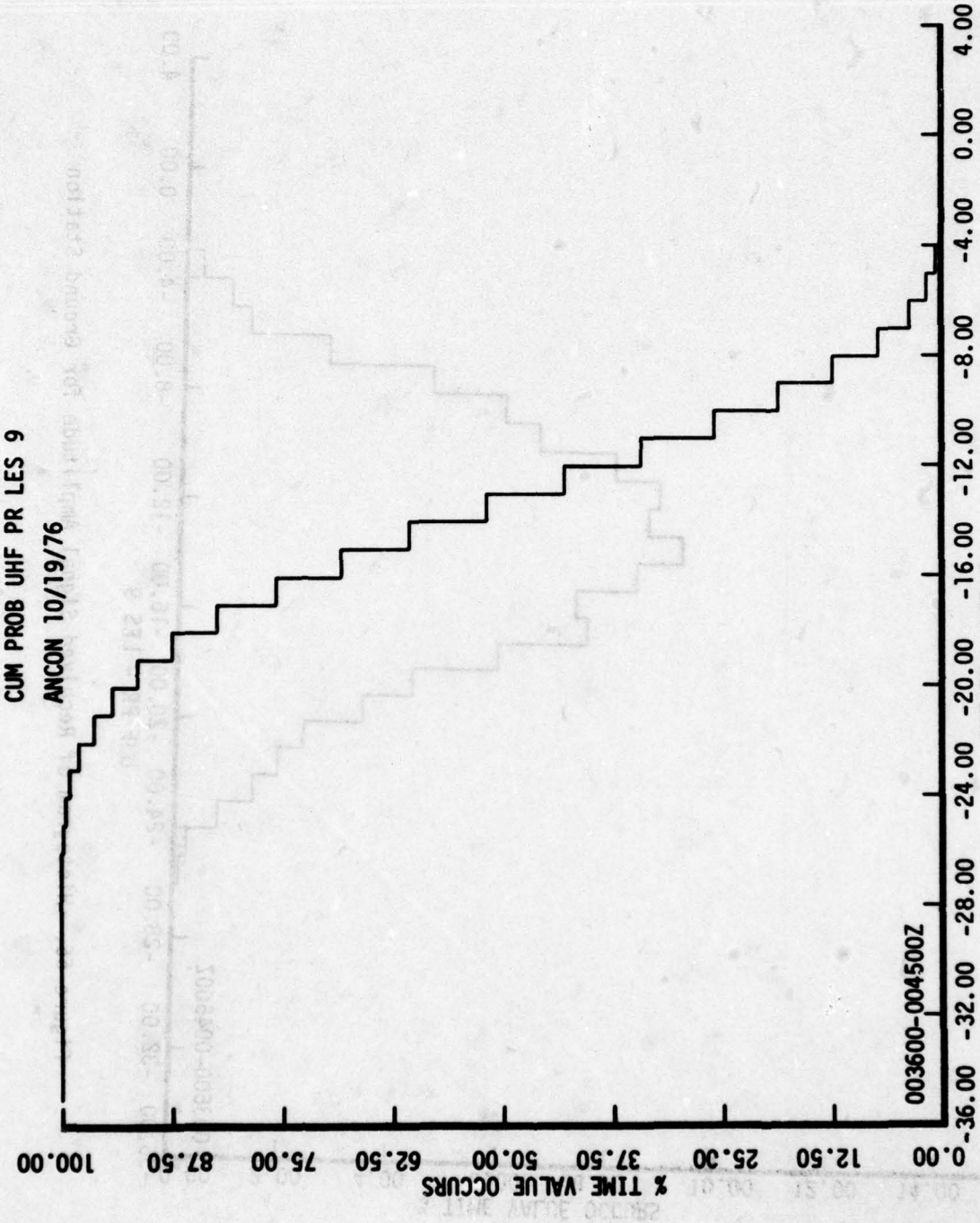

Figure 67. Cumulative Distribution of Received Signal Amplitude for Ground Station

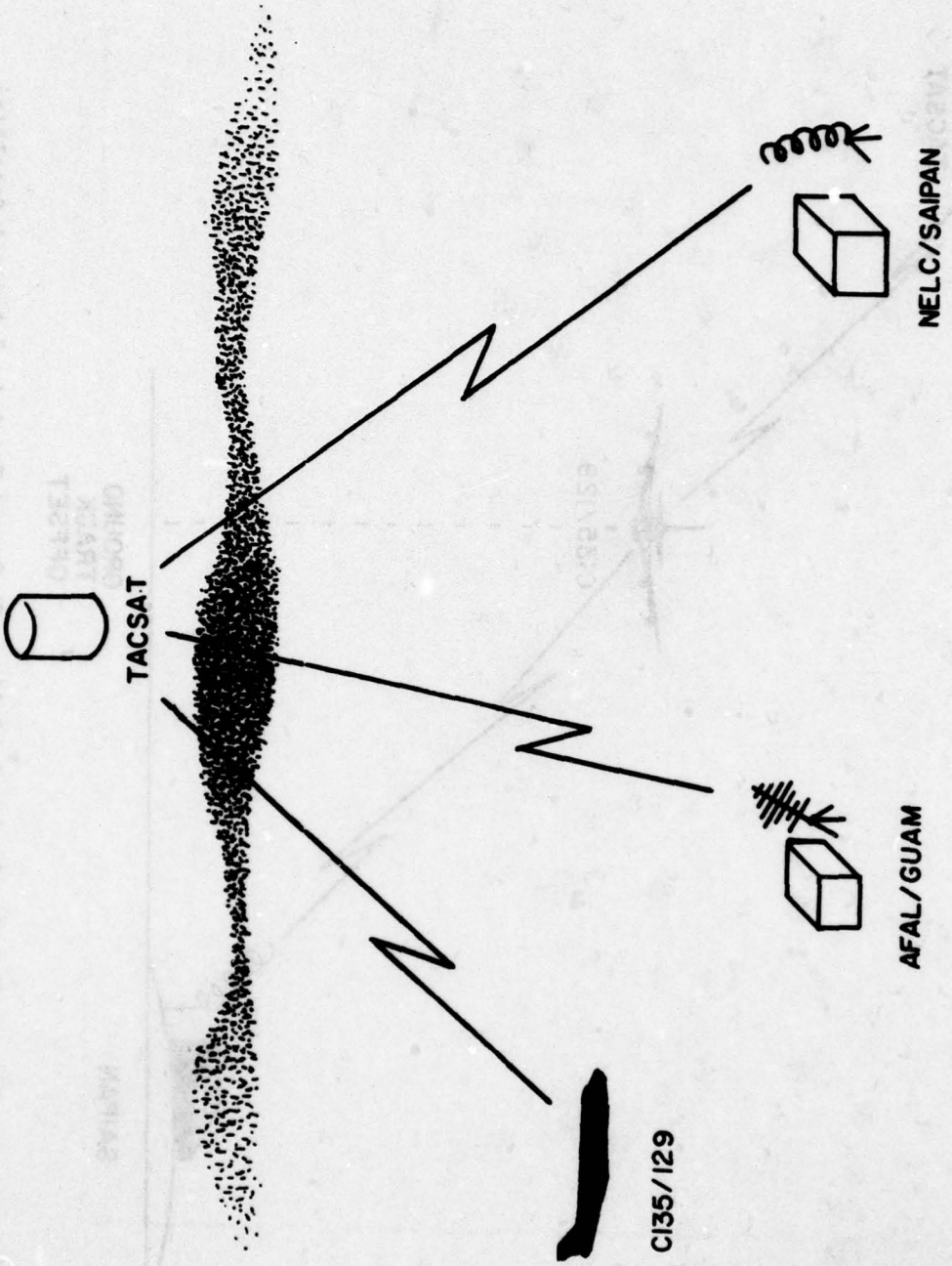

Figure 68. Pacific Test Configuration

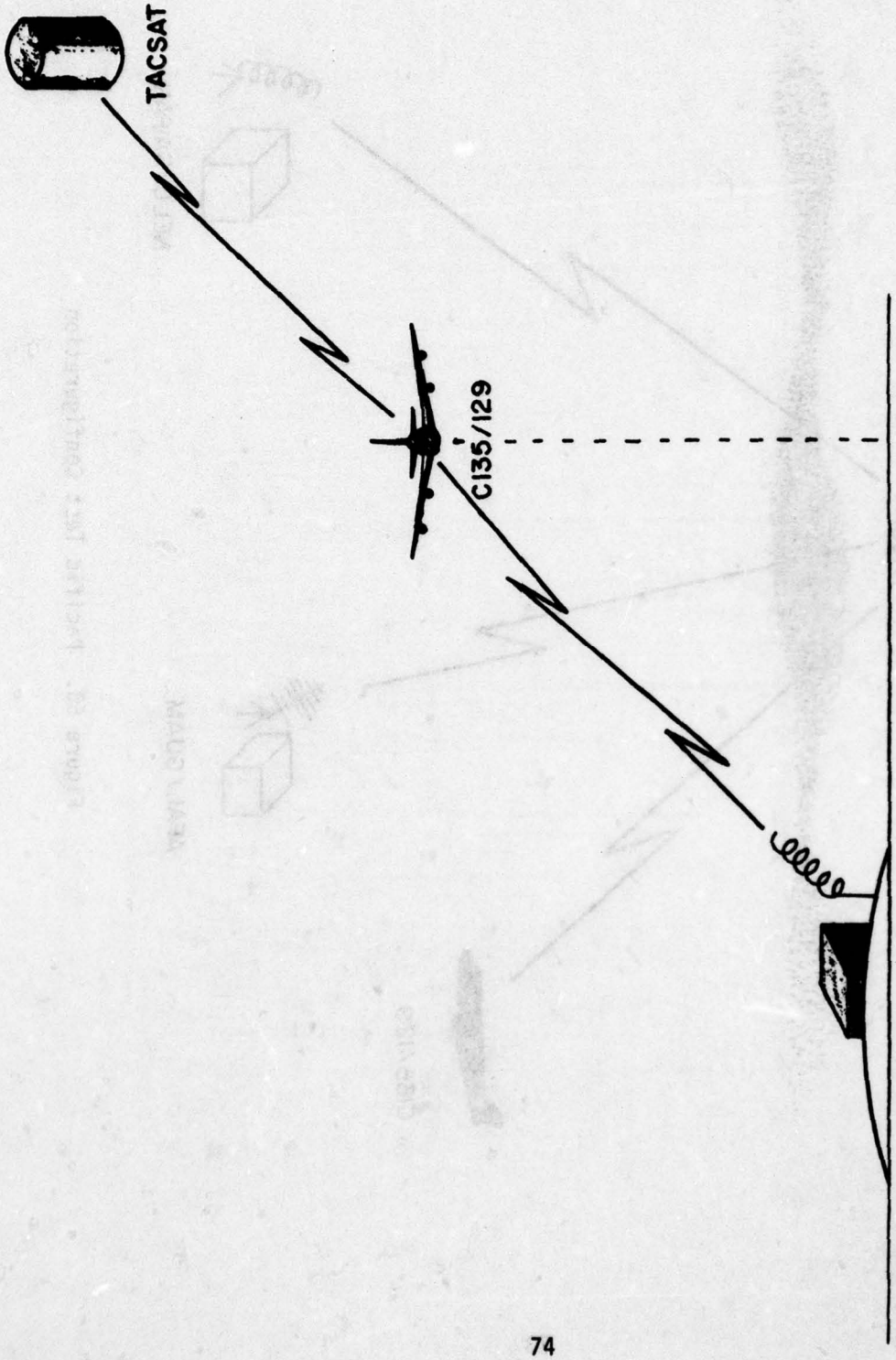

Figure 69. Displacement of Aircraft Ground Track to Intercept Satellite Ray

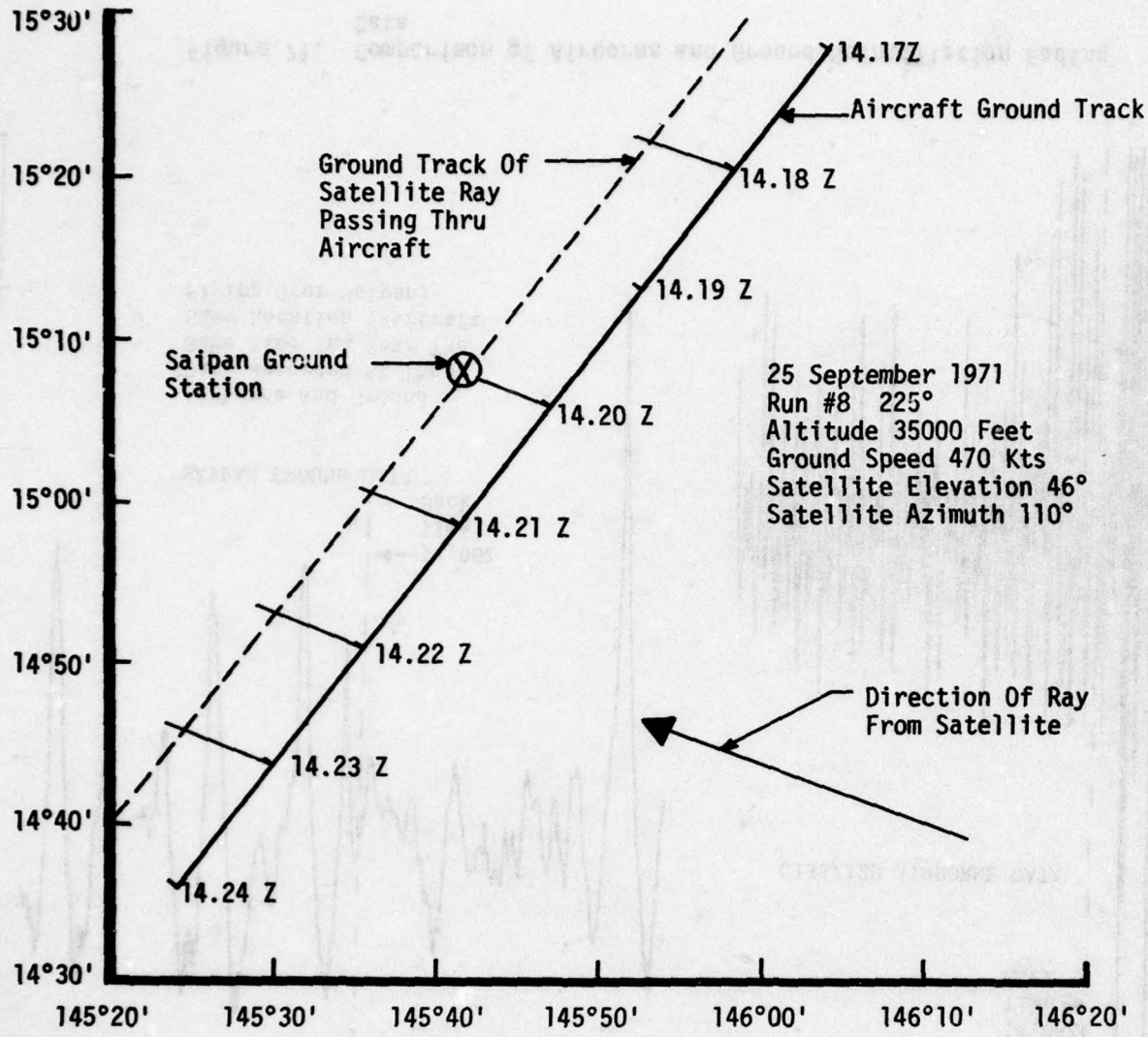

Figure 70. Ground Track of Scintillation Flight Test

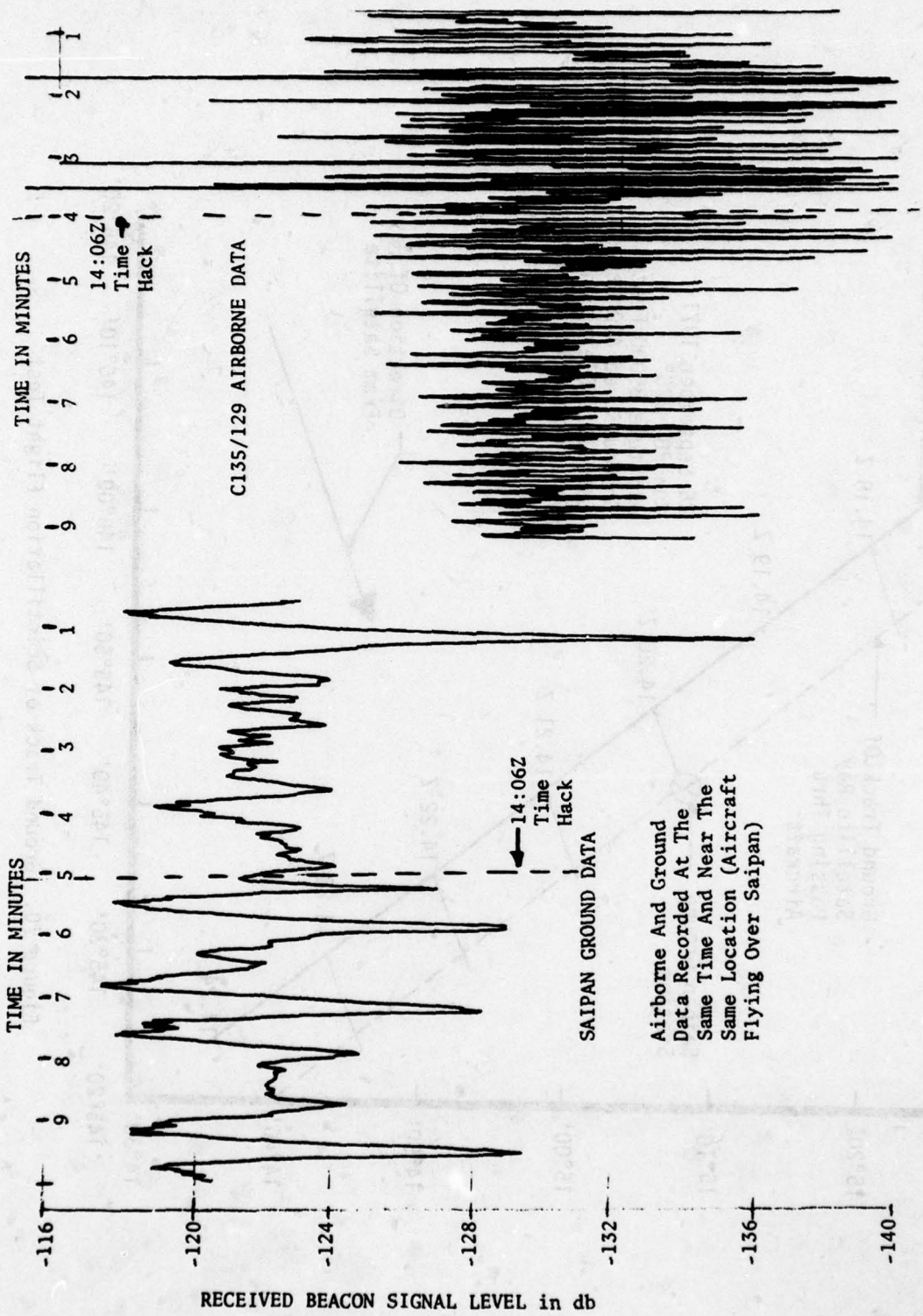

Figure 71. Comparison of Airborne and Ground Scintillation Fading Data

Figure 72. After finding the correct factor to match the airborne and ground data, a cross correlation was run, Figure 73. A peak correlation of over 0.7 was achieved.

In addition to the amplitude scintillation data, phase scintillation measurements can be of importance in the modeling of the ionospheric effects. Figure 74 (Reference 16) shows a two minute plot of equatorial amplitude fading which was recorded in March 1977. Two very deep fades, approximately 30 dB, occurred during the two minute period along with several 5 to 8 dB enhancements. During most of the amplitude fading the phase scintillation was limited to a fraction of a radian per second. However, during the two very deep fades phase scintillation rates of 10 to 15 radians per second were experienced, Figure 75. Another example of equatorial amplitude and phase scintillation is shown in Figures 76 and 77. In this segment numerous 20 to 30 dB fades occurred during the three minute sample. Again, sharp phase scintillation accompanied the deep amplitude scintillations.

The effect of the fading on the incoming signal power level appears to be sensitive to the type of fading experienced. During a ground test in Peru, data was taken which showed considerable variation in the mean over the three-hour test period. The amplitude and rate of the signal fading are displayed in Figure 78 along with the mean. Little or no change was noted in the mean at the onset of scintillation fading at 20:16 Local(L). At 2100(L) the rate of fading decreased and the amplitude dropped. At that time the mean decreased approximately 3 dB. The fading changed again around 2145(L) to a higher rate and amplitude. The mean responded by increasing almost 5 dB.

The S_4 Index shows the onset of fading and the change of fading type around 2100(L) and 2145(L). For the most part the S_4 Index indicated intense or saturated fading, Figure 78.

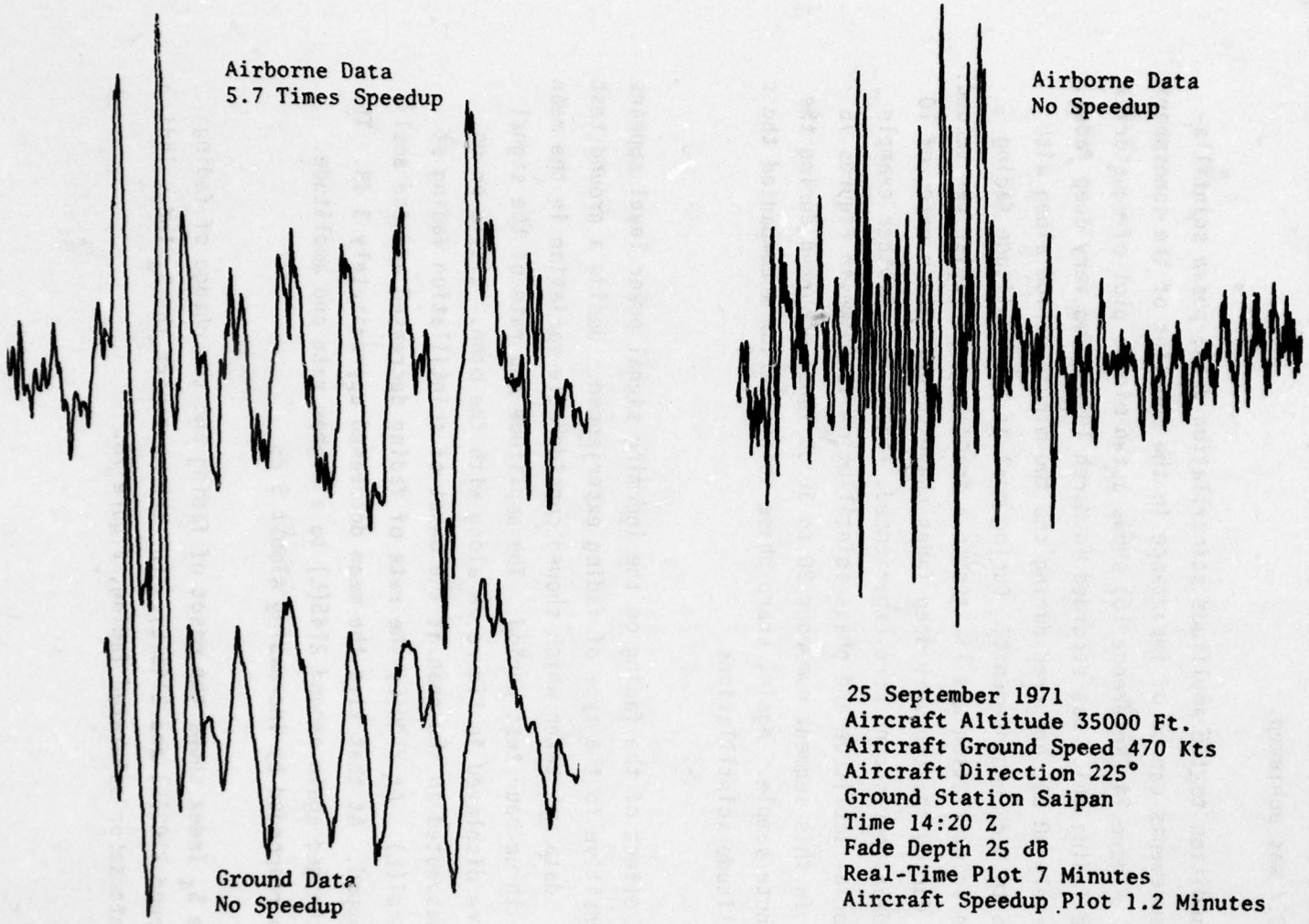

Figure 72. Comparison of Airborne and Ground Scintillation Fading Data

AD-A068 758 AIR FORCE AVIONICS LAB WRIGHT-PATTERSON AFB OH F/G 20/14
THE EFFECT OF IONOSPHERIC SCINTILLATIONS FADING ON AIRCRAFT-TO---ETC(U)
FEB 79 A J JOHNSON

UNCLASSIFIED AFAL-TR-78-171 NL

2 OF 2
AD A068758

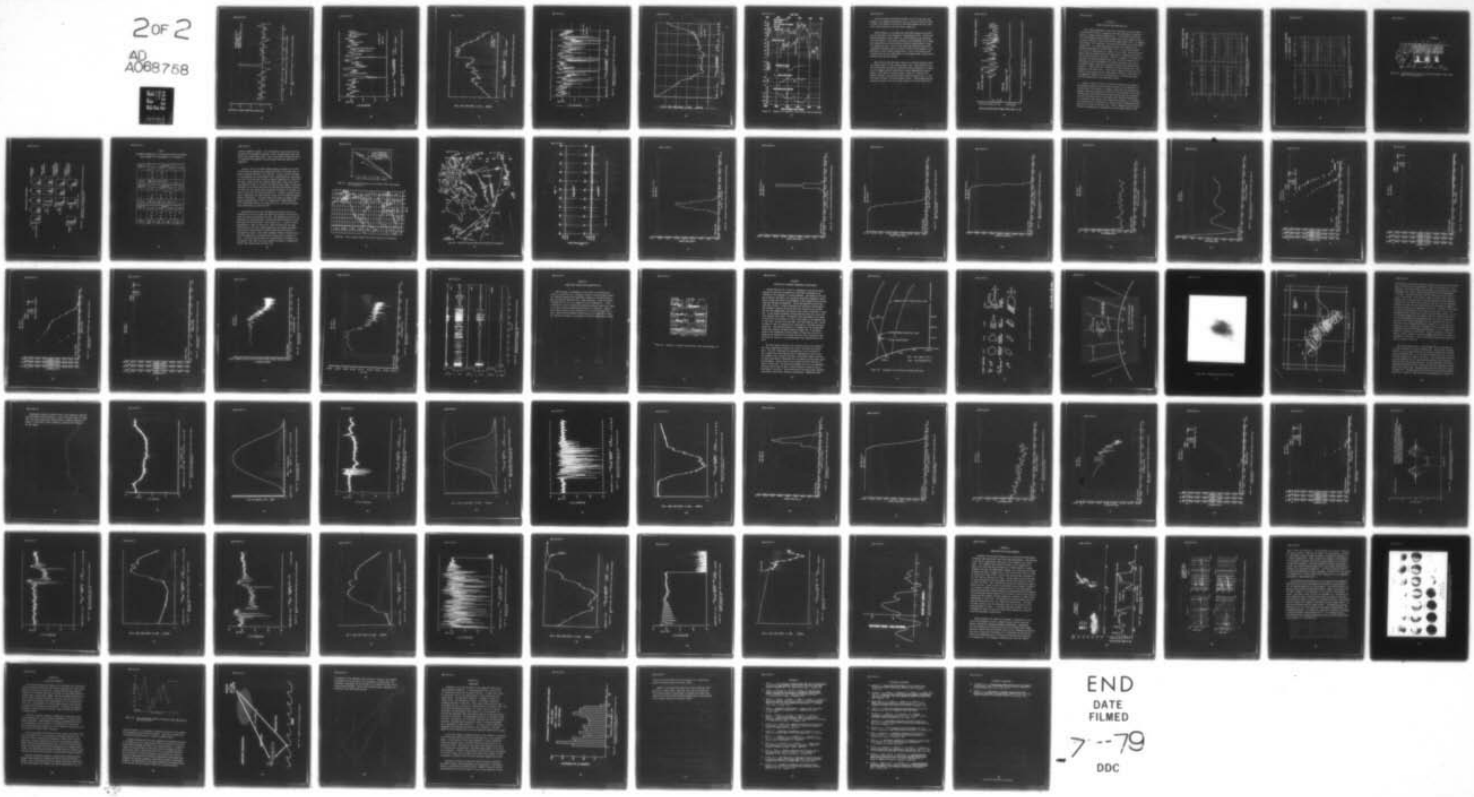

END
DATE FILMED
-7-79
DDC

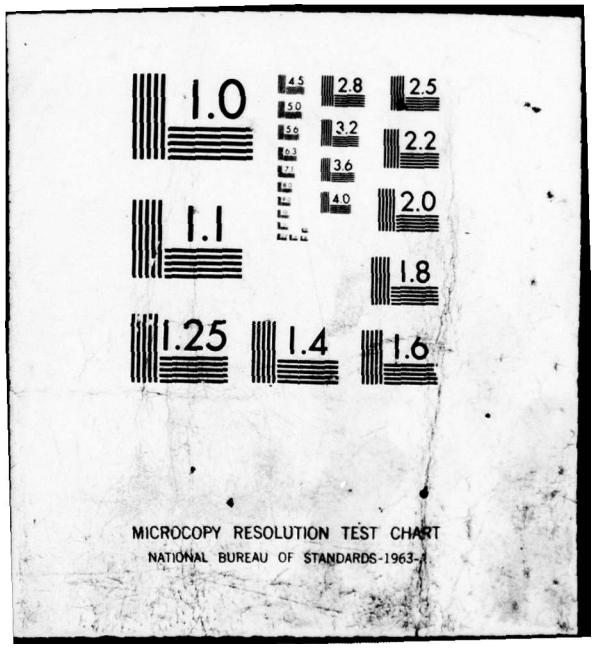
1.0
1.1
1.25
1.4
1.6
1.8
2.0
2.2
2.5
2.8
3.2
3.6
4.0
4.5
5.0
5.6
MICROCOPY RESOLUTION TEST CHART
NATIONAL BUREAU OF STANDARDS-1963-A

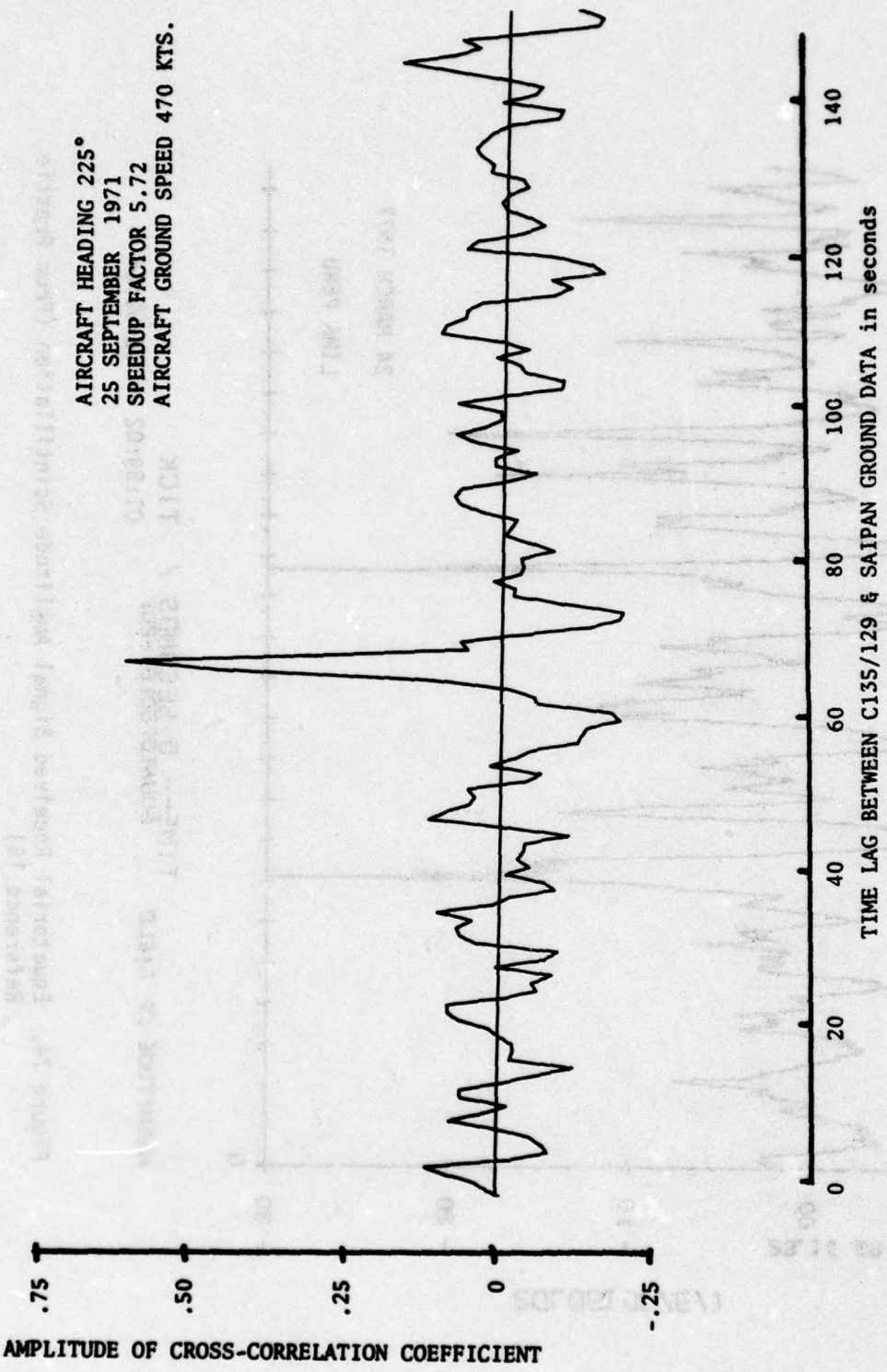

Figure 73. Cross-Correlation Function for Airborne and Ground Fading Data

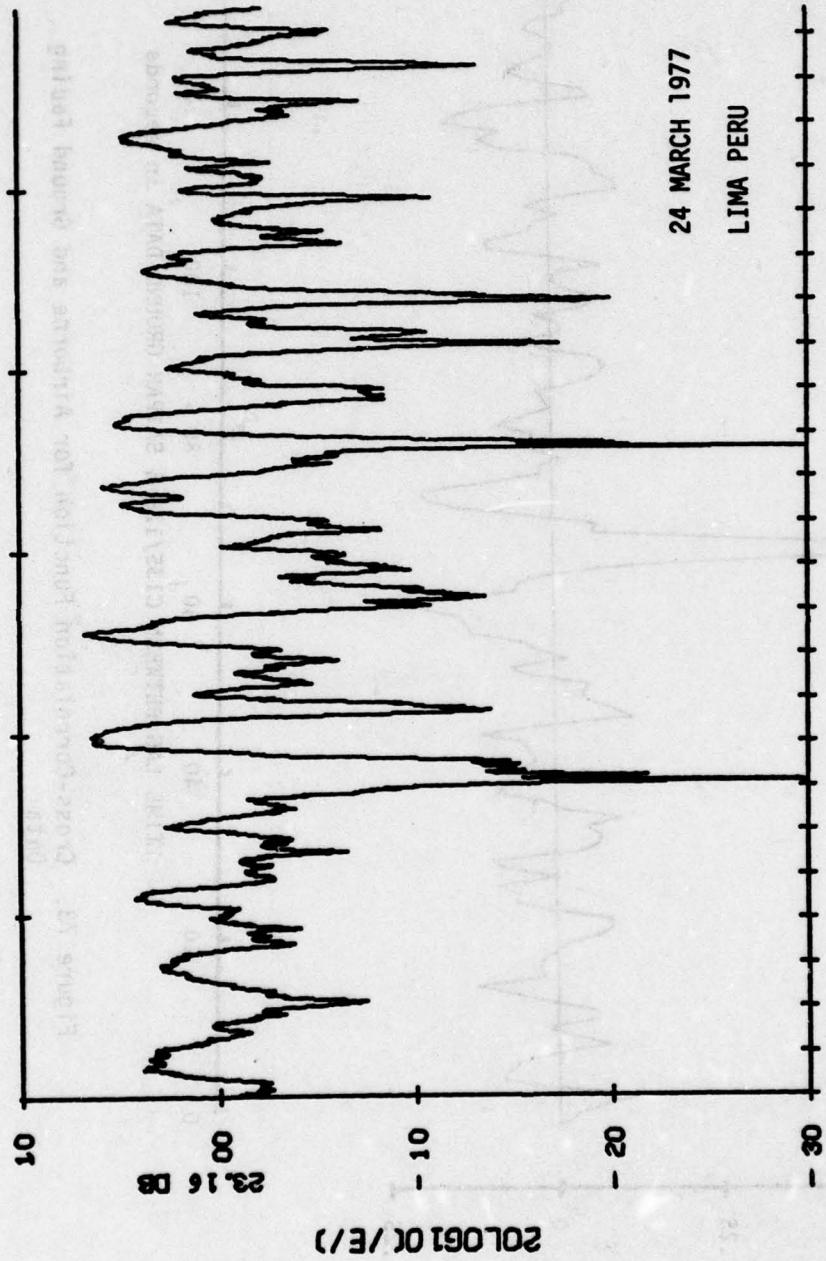

Figure 74. Equatorial Received Signal Amplitude Scintillation (From Prettie Reference 16)

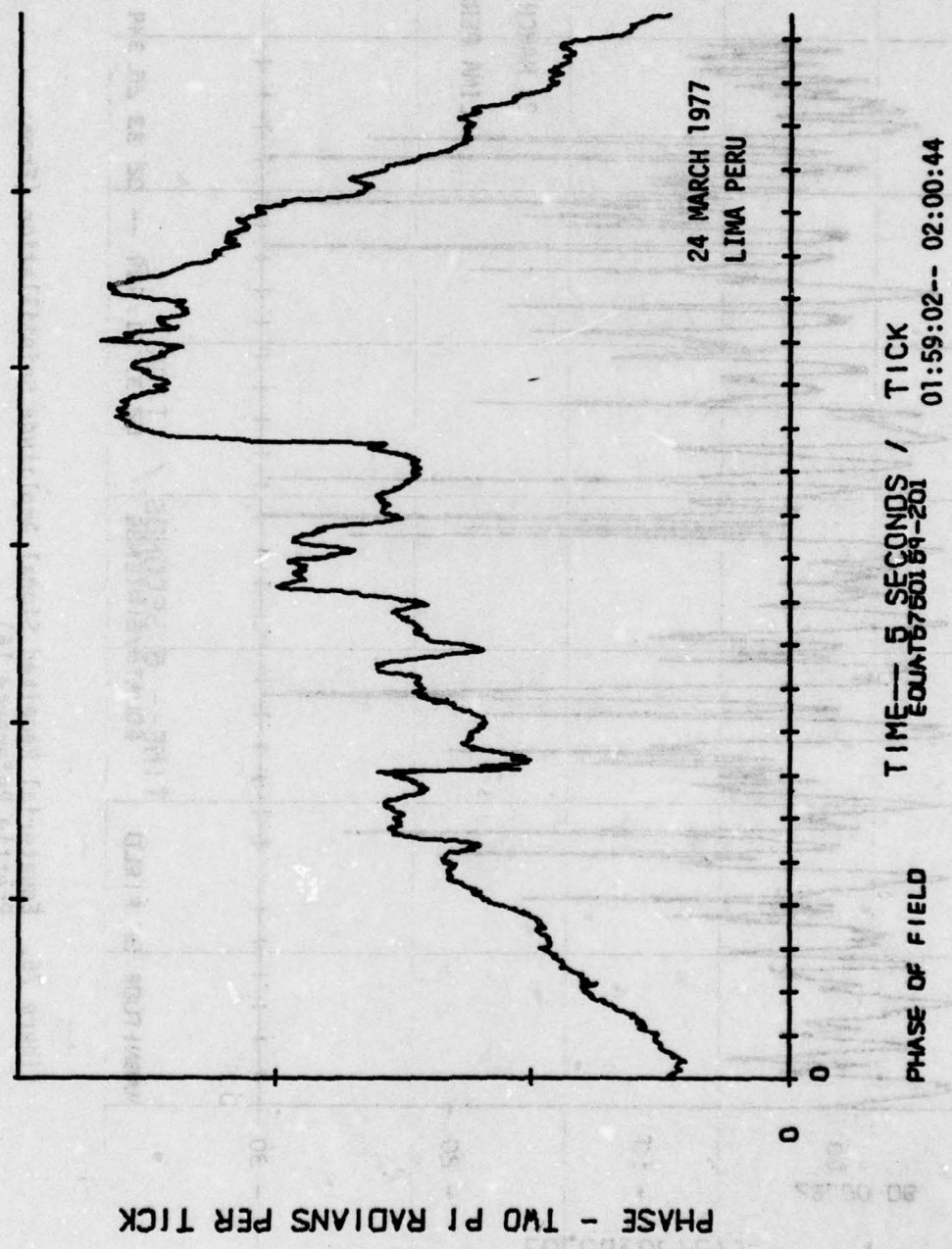

Figure 75. Equatorial Received Signal Phase Scintillation (From Prettie Reference 16)

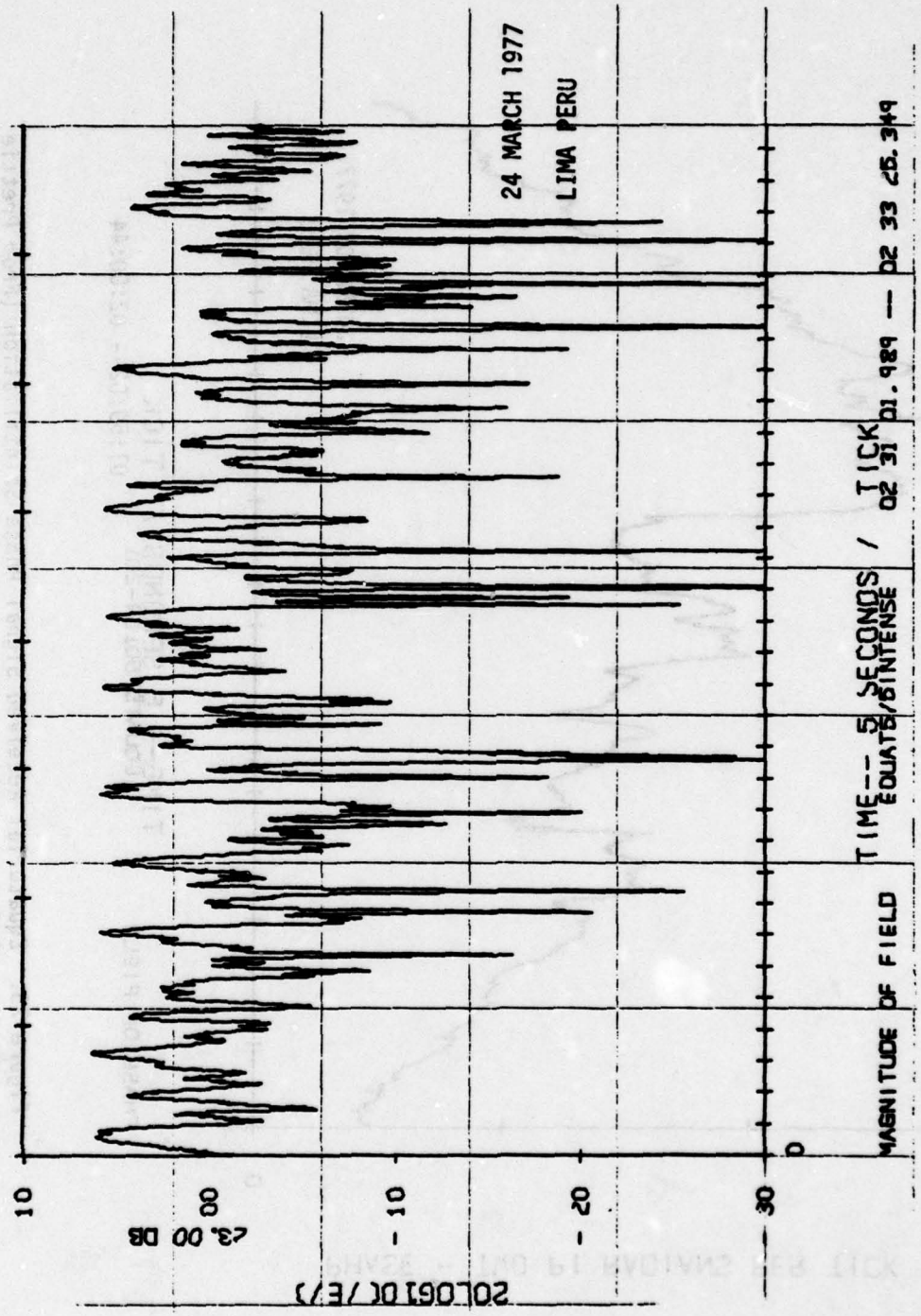

Figure 76. Equatorial Received Signal Amplitude Scintillation (From Prettie Reference 16)

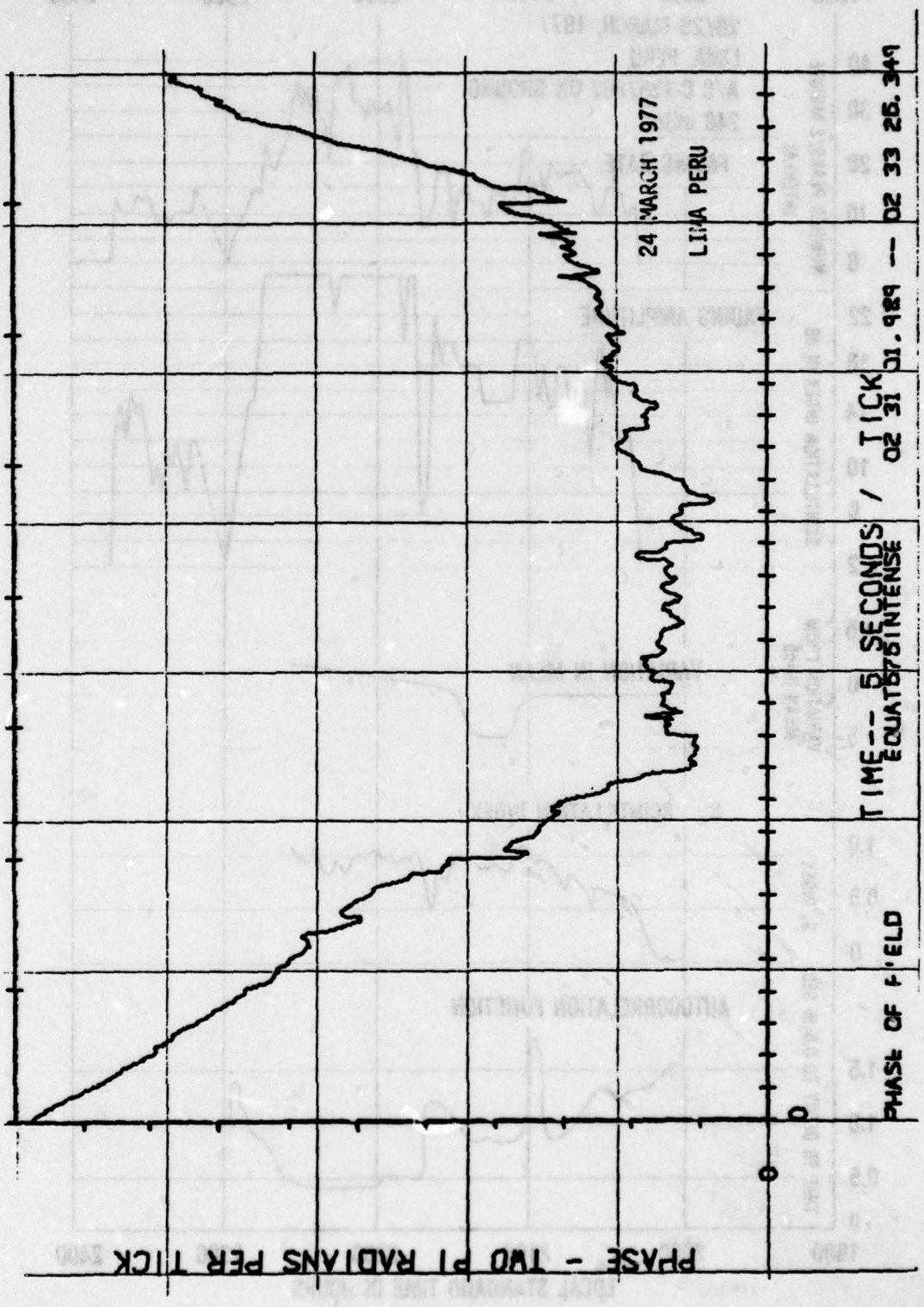

Figure 77. Equatorial Received Signal Phase Scintillation (From Prettie Reference 16)

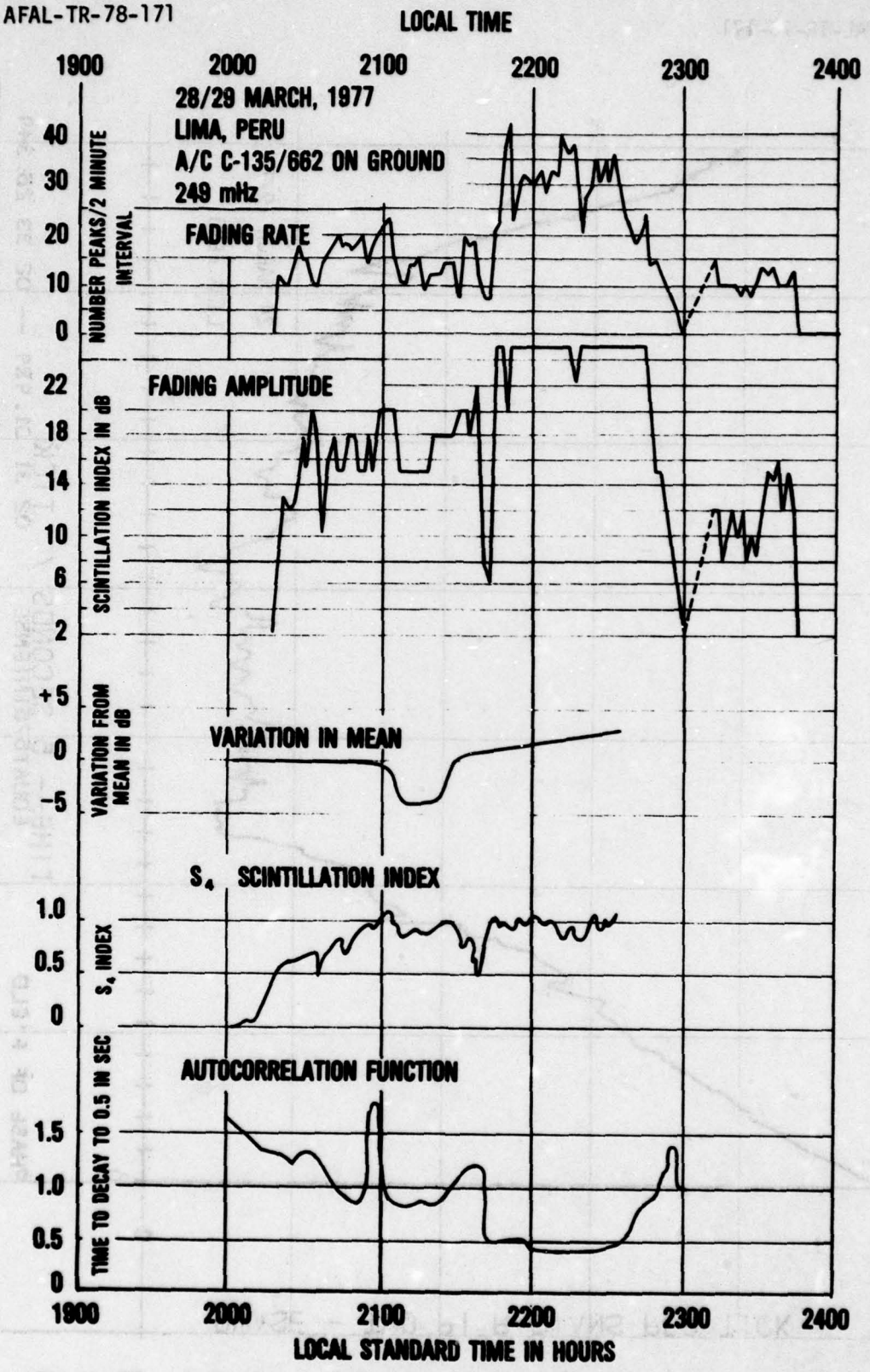

Figure 78. Comparison of Equatorial Scintillation Fading Parameters

The auto correlation function provides a mirror of the fade rate. Changes in the fading characteristics such as the fast fading from 2145 to 2240(L) are evident in the plot of the time at which the auto correlation function drops to half its value, Figure 78.

Spaced antennas on the ground have been used to measure the direction and velocity of the ionospheric irregularity's drift. Paulson and Hopkins (Reference 6) have shown very high correlation over distances up to 1000 meters. Data taken by Whitney, et al (Reference 14) at Ancon, Peru showed that the cross correlation between spaced antennas varied as a function of time. Early in the night poor correlation was often experienced, probably either to vertical motion of the ionospheric irregularities or very intense irregularities. Later in the evening high correlation was usually experienced as the already formed irregularities drifted across the two antennas.

While 25 to 35 dB fades occur regularly in the UHF frequency range, the fading at SHF (7.5 GHz) seldom exceeds 1 dB. Simultaneous UHF and SHF scintillation data taken at Ascension Island by Johnson et al (Reference 17) showed large UHF scintillation fading accompanied by approximately 1 dB of SHF scintillation fading, Figure 79. The SHF curve showed a periodic 2 dB cyclical signal variation occurring at a 1 cycle per second rate due to satellite antenna wobble. Superimposed upon the envelope over this curve was a slowly varying 1 dB scintillation fade.

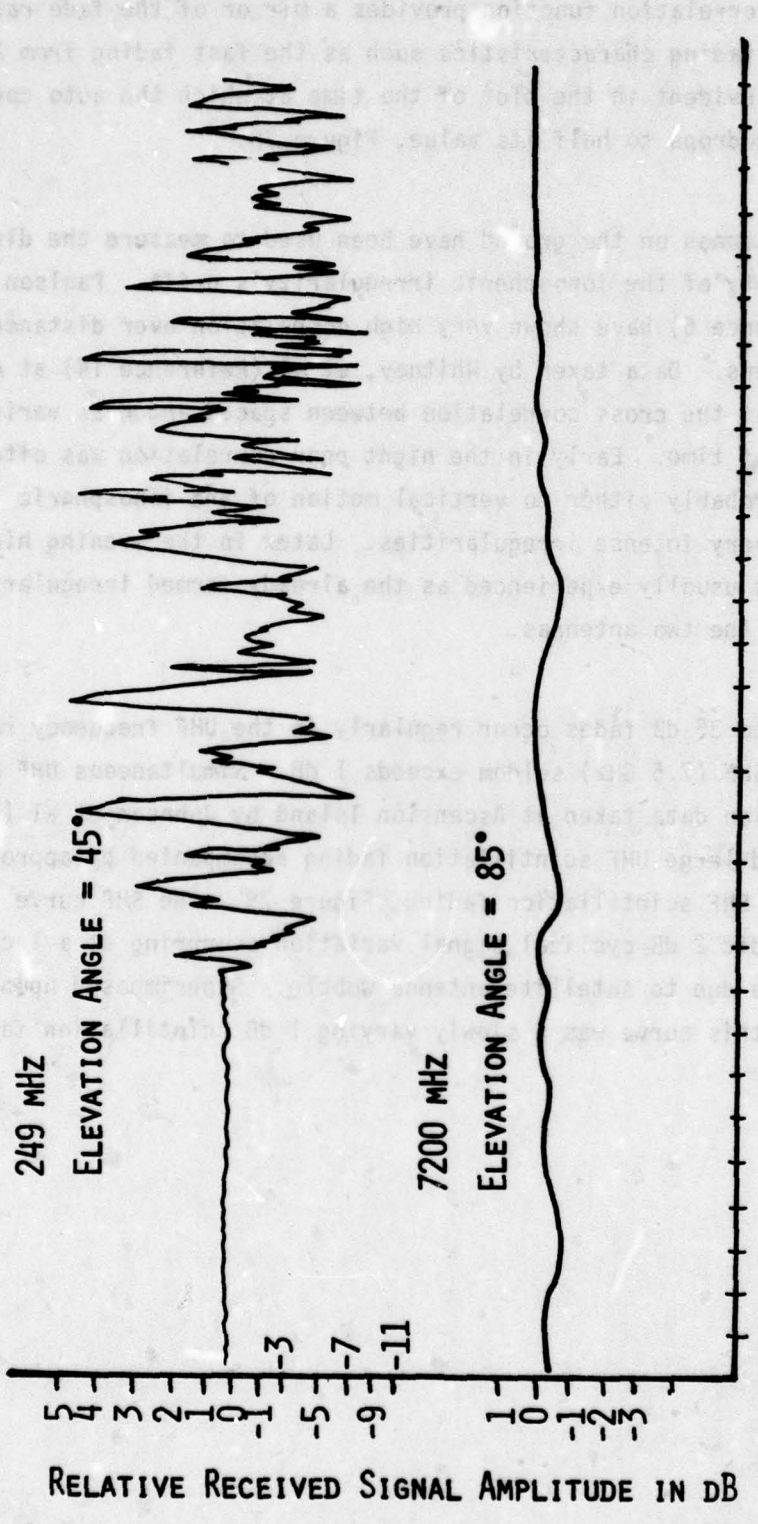

Figure 79. Simultaneous UHF and SHF Scintillation Fading

SECTION III

POLAR SCINTILLATION CHARACTERISTICS

The F region ionosphere in the Polar area tends to be more complicated and more difficult to quantify than the midlatitude or equatorial region, as noted by Aarons (Reference 2). In this region small scale (1 to 10 kilometer) field aligned irregularities cause ionospheric scintillation fading on aircraft-to-satellite communication links. In general, the fading is still confined to the VHF and UHF region with little effect noted at SHF. In a model developed by Aarons, et al (Reference 5) a frequency dependence of the fade depth is $F^{-1.9}$ for the Polar region. As a result of observations at a number of Polar sites, Aarons has developed an empirical model showing the probability of fading versus time of day for each month of the year. The other variables in the model are the solar flux and the magnetic index, Kp. The plots by Aarons et al (Reference 5) show the probability of fading occurrence to be low in the winter months, Figure 80, and peaking up during the summer months, Figure 81. These curves still indicate a diurnal variation due to the movement of the auroral oval. These figures support the conclusion that fading can be expected to occur more often in the Polar region than in the equatorial region, but it is expected to be of smaller amplitude than that experienced in the equatorial region.

During a series of flights in the Polar region, data was taken on percentage occurrence of scintillation by Aarons, et al (Reference 3). In that report five regions, or regimes, (Figure 82) were defined with Regime #1 being the ionosphere totally south of the auroral oval; Regime #2 being that area in which the ray passes through both the ionosphere south of the oval and part of the auroral oval, Regime #3 being where it is totally in the auroral oval, Regime #4 being where it is partially in the auroral oval and partially in the polar cap; and Regime #5 being where it is totally in the polar cap. Table I (Reference 3) and Figure 83 show the probability of occurrence of various depth fading in the

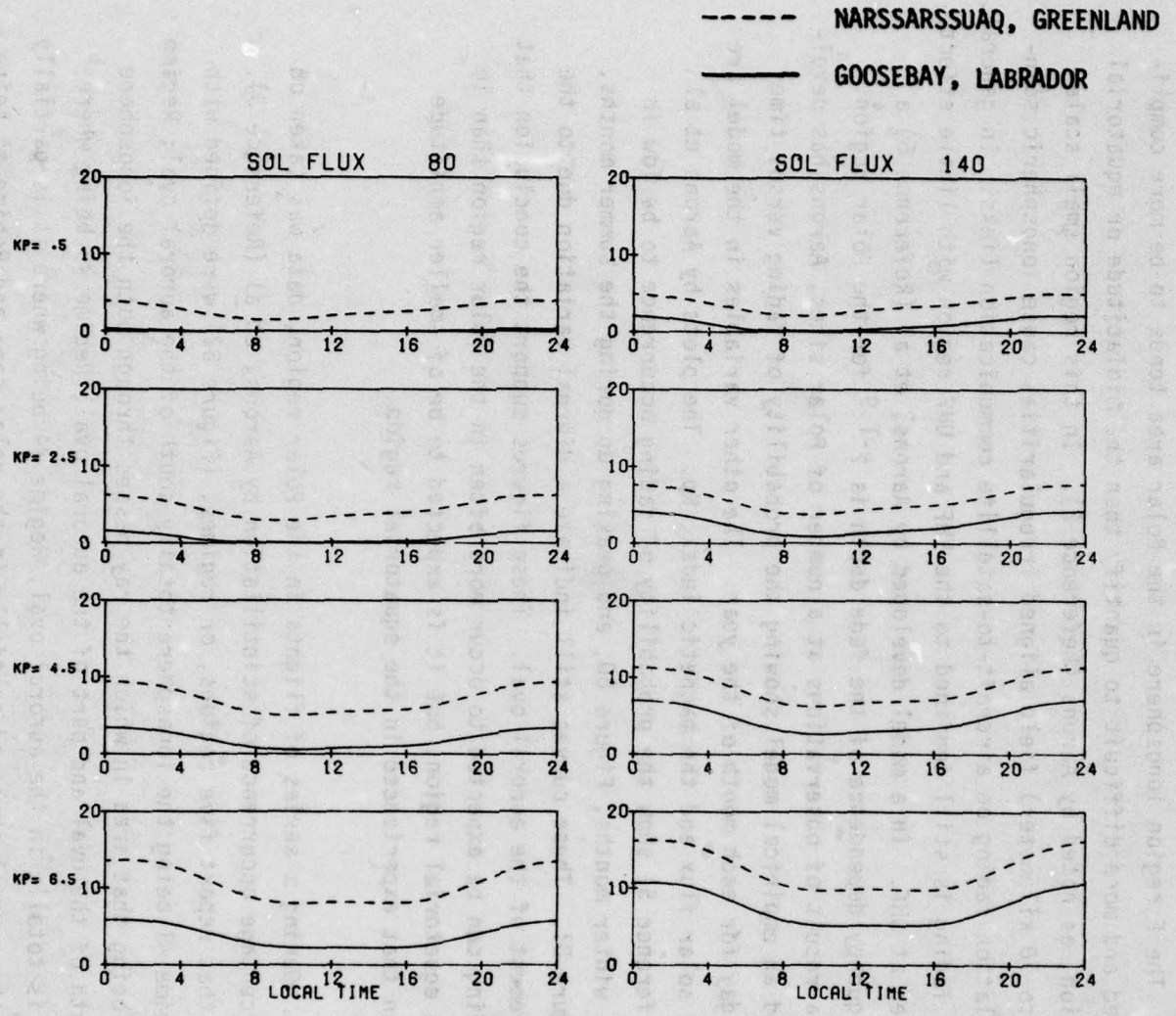

Figure 80. High Latitude Scintillation Fading Occurrence for December (From Aarons et al Reference 5)

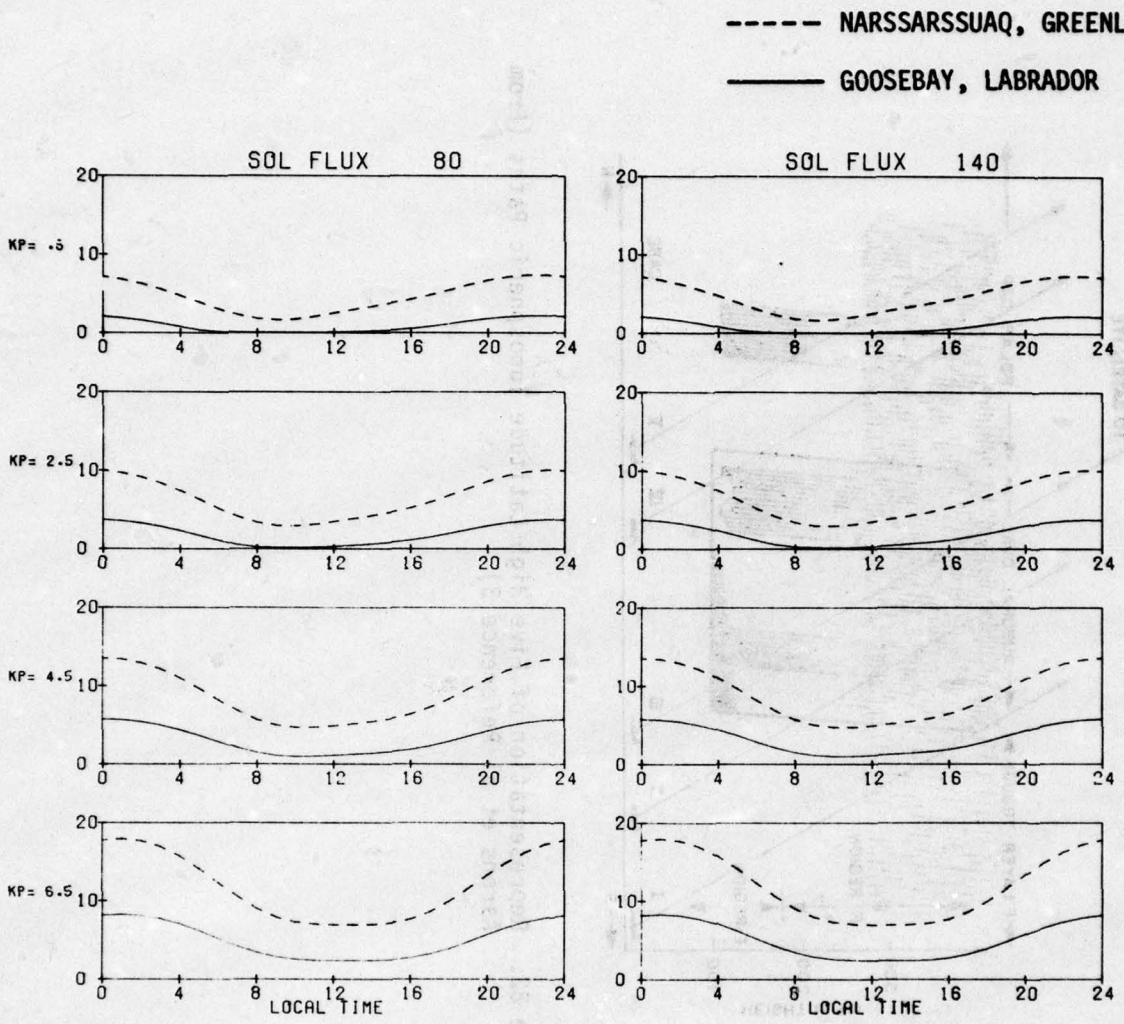

Figure 81. High Latitude Scintillation Fading Occurrence for June (From Aarons et al Reference 5)

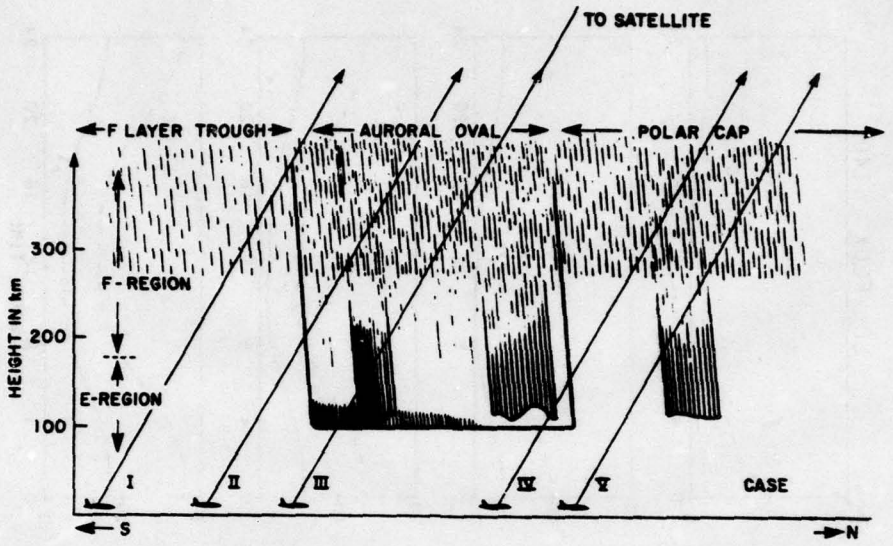

Figure 82. Representation of Five High Latitude Ionospheric Paths (From Aarons et al Reference 3)

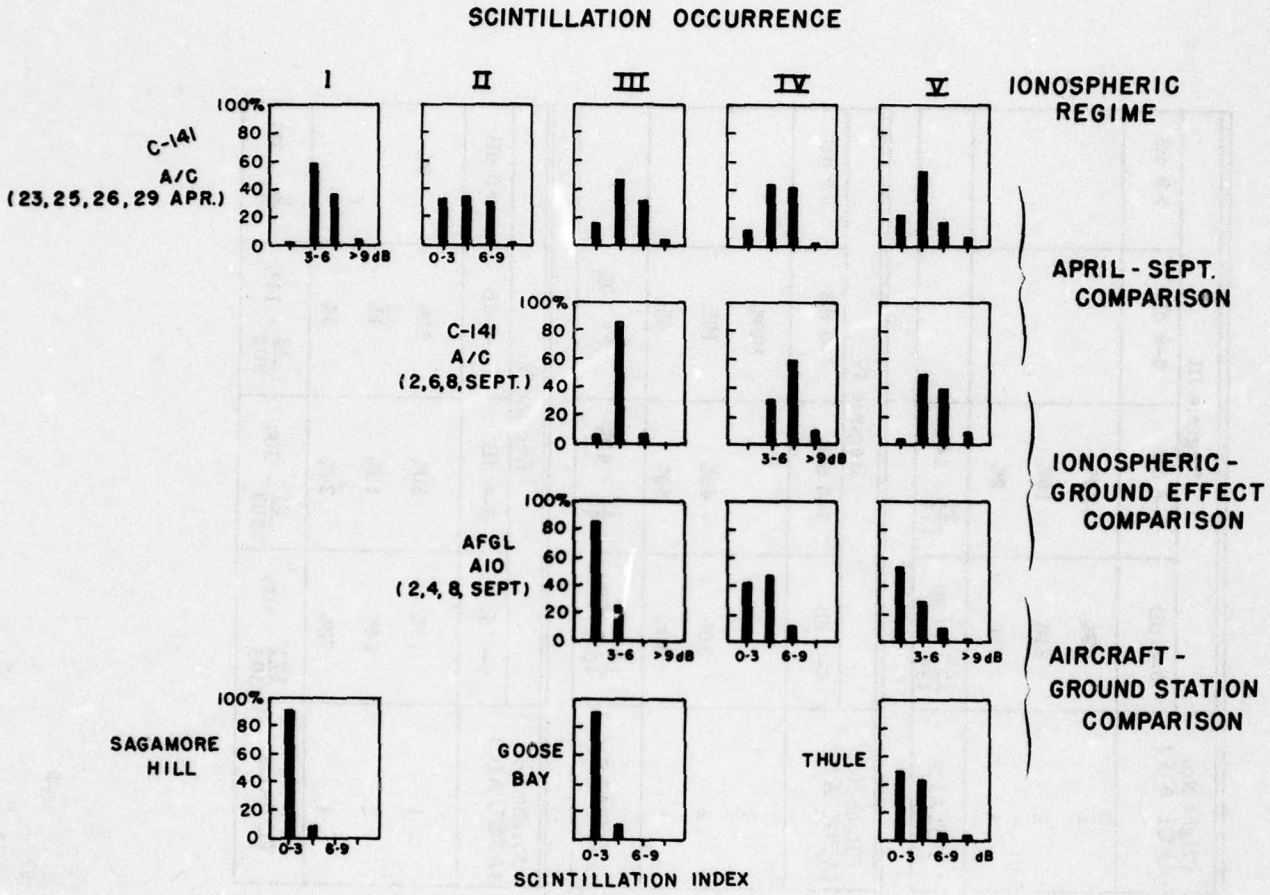

Figure 83. Compilation of Ground and Airborne Scintillation Test Results (From Aarons et al Reference 3)

TABLE 1

OCCURRENCE FREQUENCIES OF SCINTILLATION INDICES BY REGIMES FOR SEPTEMBER TEST (FROM AARONS et al REFERENCE 3)

Flight No. (AFGL A/C)	Regime III			
	0–3 dB	3–6 dB	6–9 dB	>9 dB
1	67%	33%		
2	81%	19%		
4	98%	2%		
TOTALS	$\frac{149}{174}$ = 86%	$\frac{25}{174}$ = 14%		

Flight No. (AFGL A/C)	Regime IV			
	0–3 db	3–6 dB	6–9 dB	>9 dB
1			100%	
2	36%	45%	18%	
4	46%	50%	4%	
TOTALS	$\frac{17}{40}$ = 42%	$\frac{19}{40}$ = 47%	$\frac{4}{40}$ = 10%	

Flight No. (AFGL A/C)	Regime V			
	0–3 db	3–6 dB	6–9 dB	>9 dB
1	13%	50%	29%	8%
2	84%	15%	1%	
4	72%	24%	3%	
TOTALS	$\frac{171}{303}$ = 56%	$\frac{91}{303}$ = 30%	$\frac{33}{303}$ = 11%	$\frac{8}{303}$ = 3%

various ionospheric regimes. It is interesting to note that while the probability of occurrence of fading is high, the fade depths were relatively low, usually below 10 dB. This is also shown in Figure 84 where the cumulative distribution of scintillation fading for Goose Bay is summarized.

During a series of flights between Norway and Alaska in June 1977, scintillation was observed for approximately 40% of the flight path as shown by Johnson (Reference 18), Figure 85. During a series of flights in the Greenland area during January 1977, scintillation was experienced less than 10% of the time as shown by Johnson (Reference 19), Figure 86. The type of fading which was observed ranged from a rather fast, noise like fading (16 June) to a rather slow fade (15 Aug), shown in Figure 87. Histograms of the fading amplitude and cumulative distribution functions for these two fade samples show considerable difference in the fade structure as can be seen by Figures 88 through 91. Likewise, the auto correlation, fade period, and fade duration curves vary for these two samples, Figures 92 through 97. The power spectra for these two samples shows a slope of approximately f^{-3} and f^{-2}, respectively, Figures 98 and 99. The 15 June fading showed an S_4 Index of only 0.2, while the 16 August fading exhibited an S_4 Index of 0.25.

Observations of data from the DNA-002 satellite by Rino, et al (Reference 8) in Alaska showed both amplitude and phase scintillation occurring regularly throughout the year. One unexpected result was the occurrence of significant phase scintillation under conditions of very weak amplitude scintillations in the auroral oval. A sample of Rino's measurements is shown in Figure 100. Rino concluded that the phase scintillation in the Polar region appeared to be stronger than phase scintillation associated with a similar amplitude scintillation in the equatorial region. Rino noted a geometric effect in that the scintillation appeared to be strongest when looking along a constant "L" shell. This would indicate that the irregularities are aligned along the magnetic line field lines and a greater thickness of irregularity results from looking along the field line.

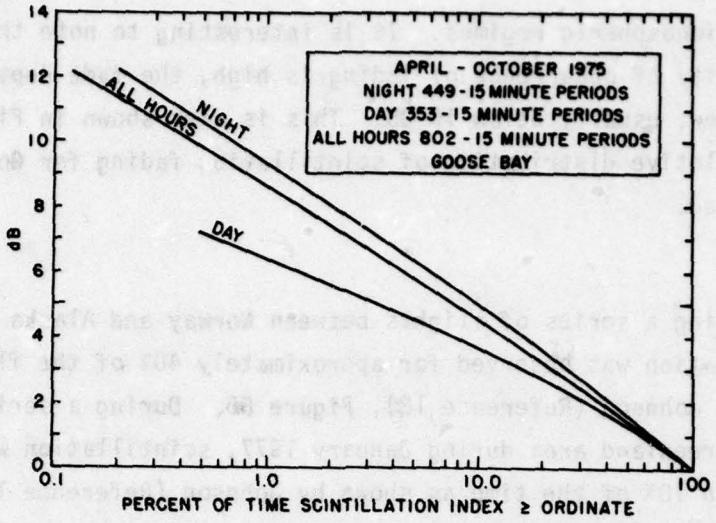

Figure 84. Cumulative Distribution of Scintillation Index (From Aarons et al Reference 3)

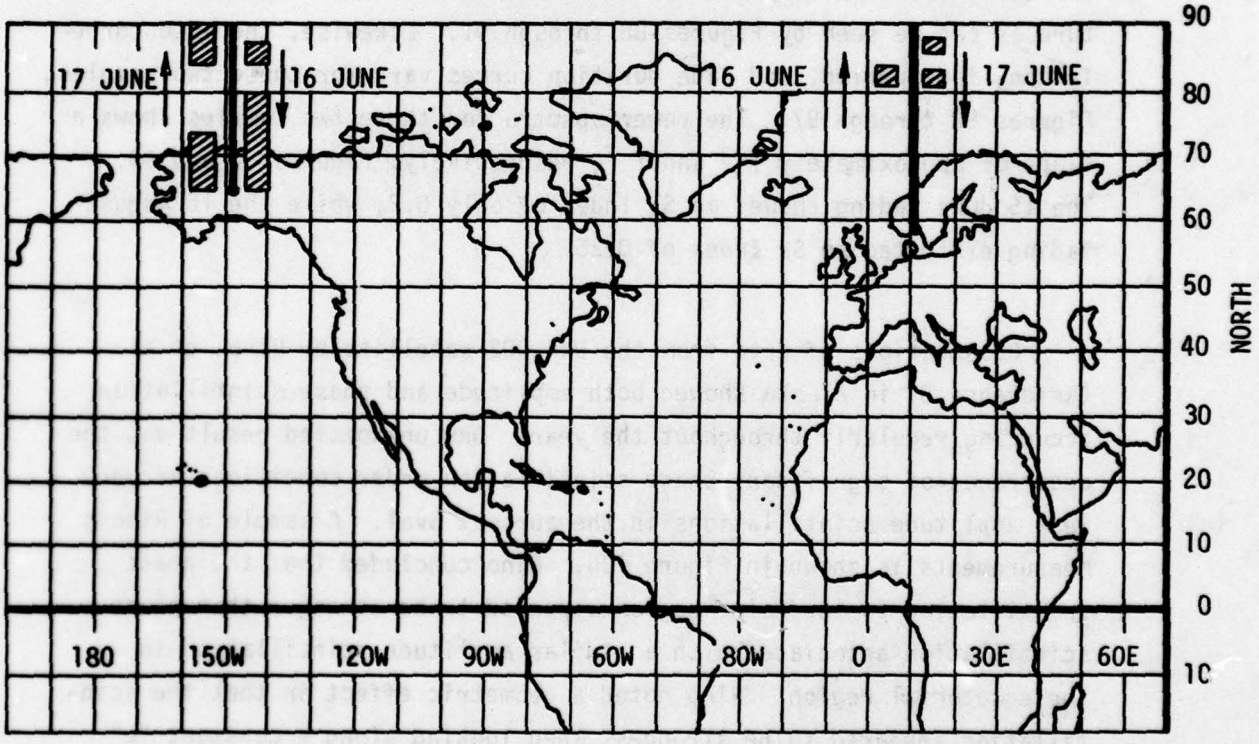

Figure 85. Polar Locations Where Scintillation Fading Was Encountered

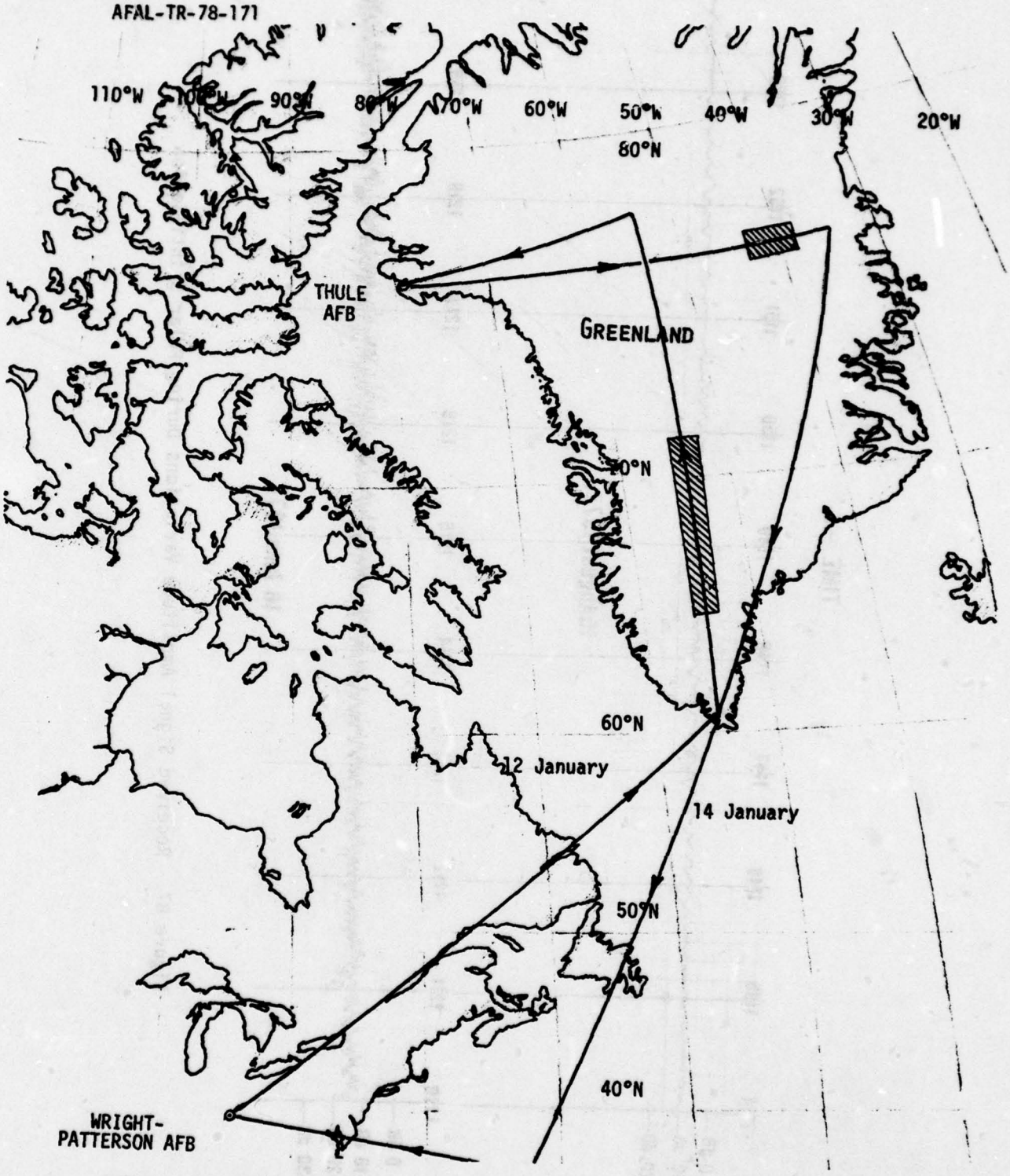

Figure 86. Greenland Locations Where Scintillation Was Encountered

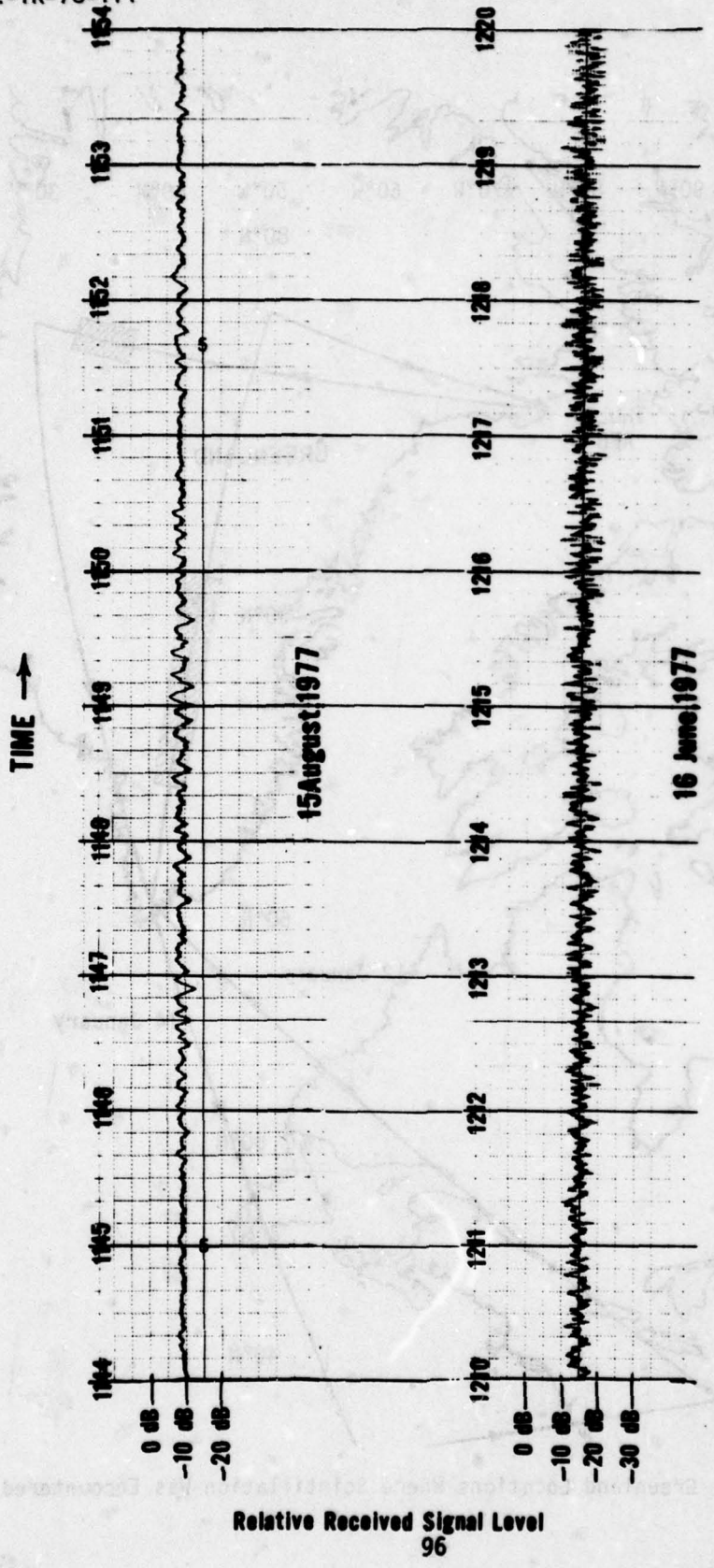

Figure 87. Received Signal Amplitude Variations During Polar Scintillation

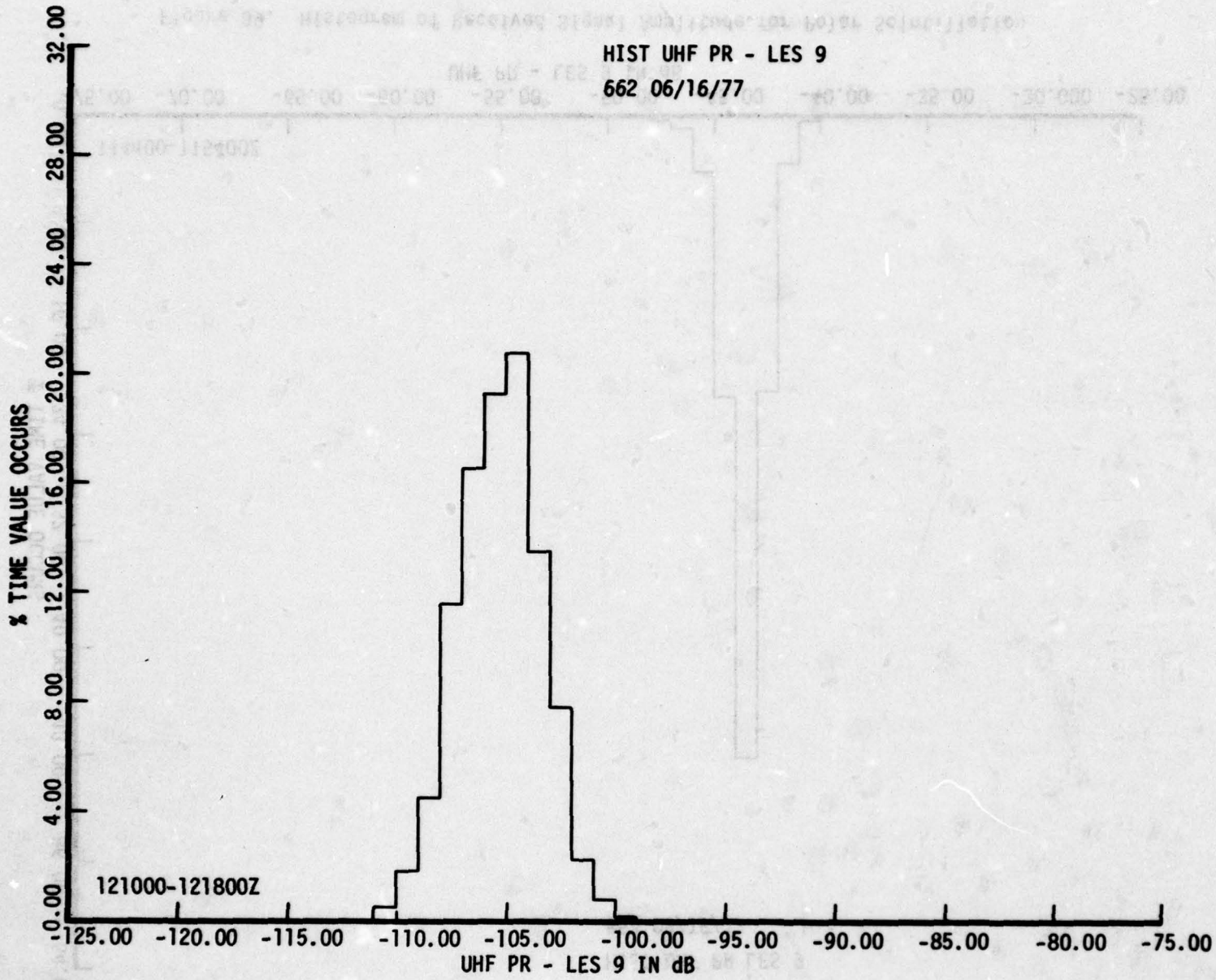

Figure 88. Histogram of Received Signal Amplitude for Polar Scintillation

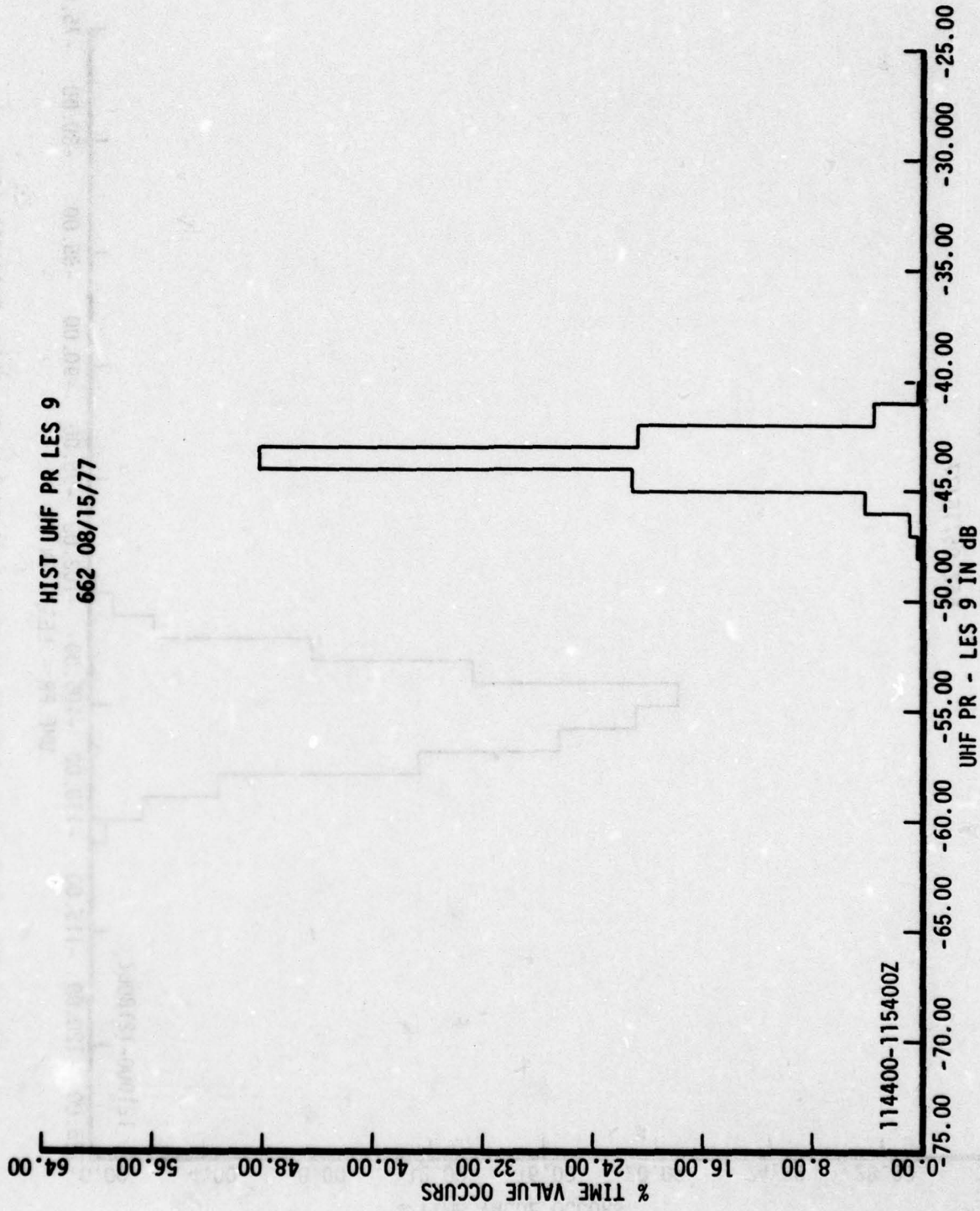

Figure 89. Histogram of Received Signal Amplitude for Polar Scintillation

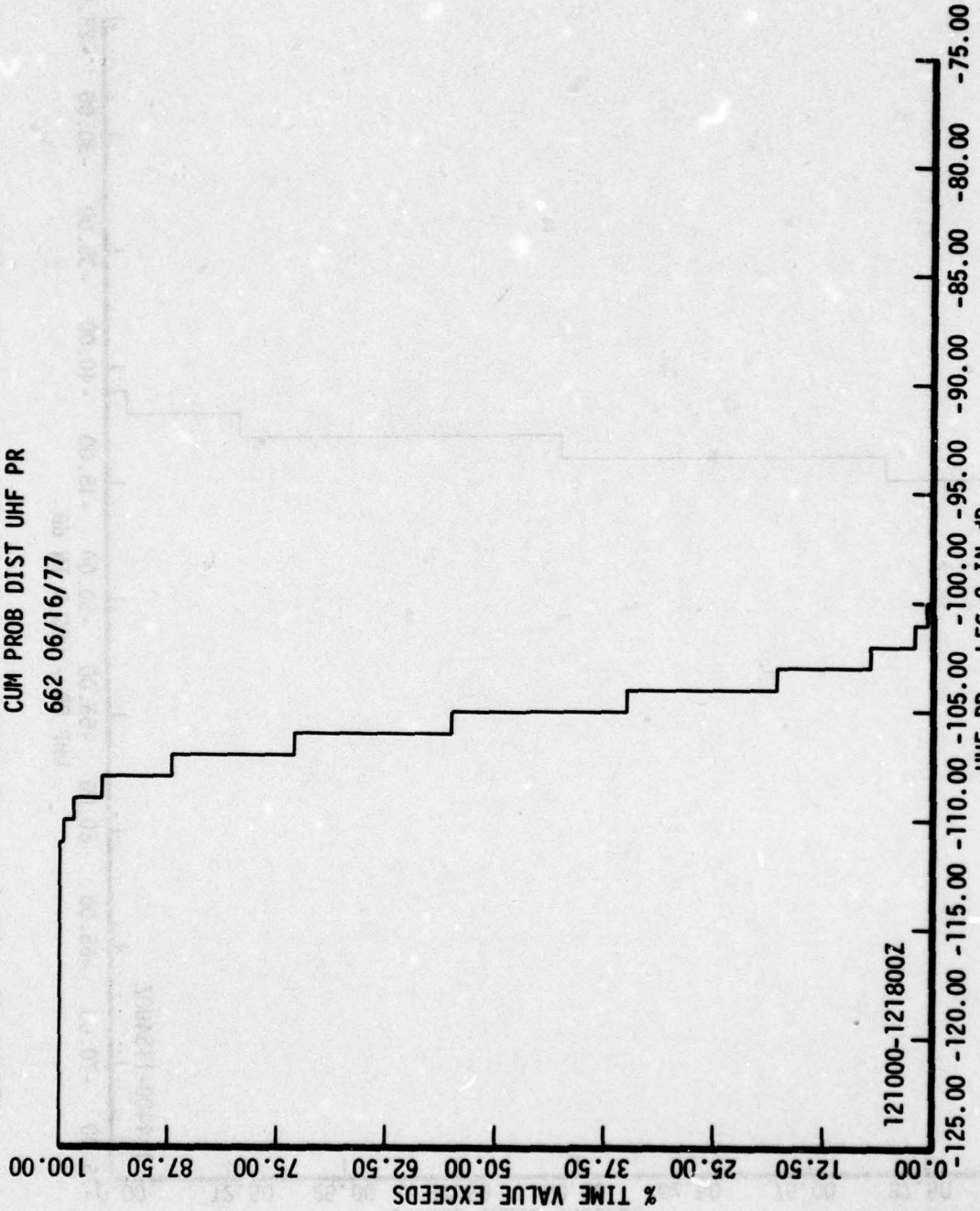

Figure 90. Cumulative Distribution of Received Signal Amplitude for Polar Scintillation

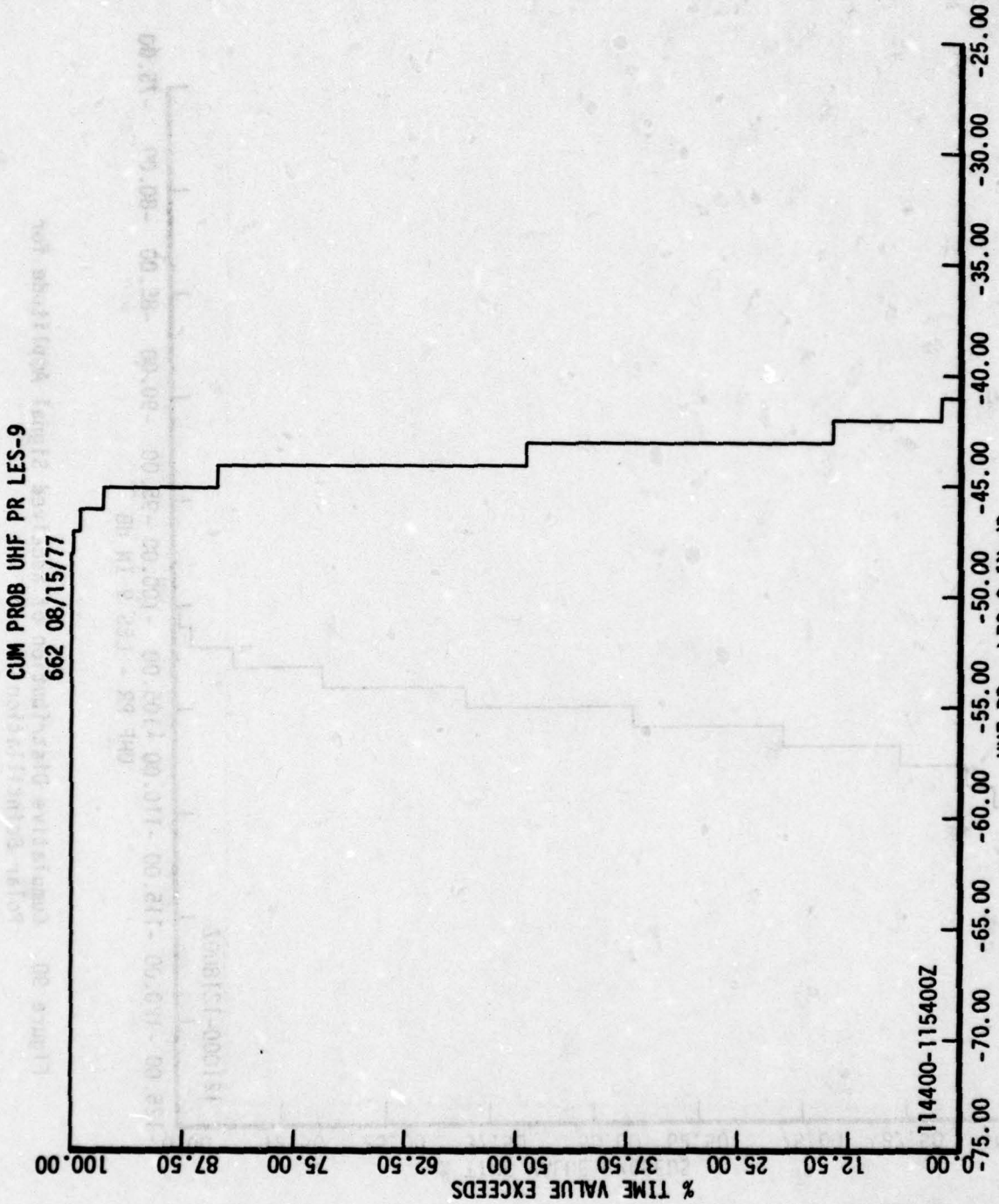

Figure 91. Cumulative Distribution of Received Signal Amplitude for Polar Scintillation

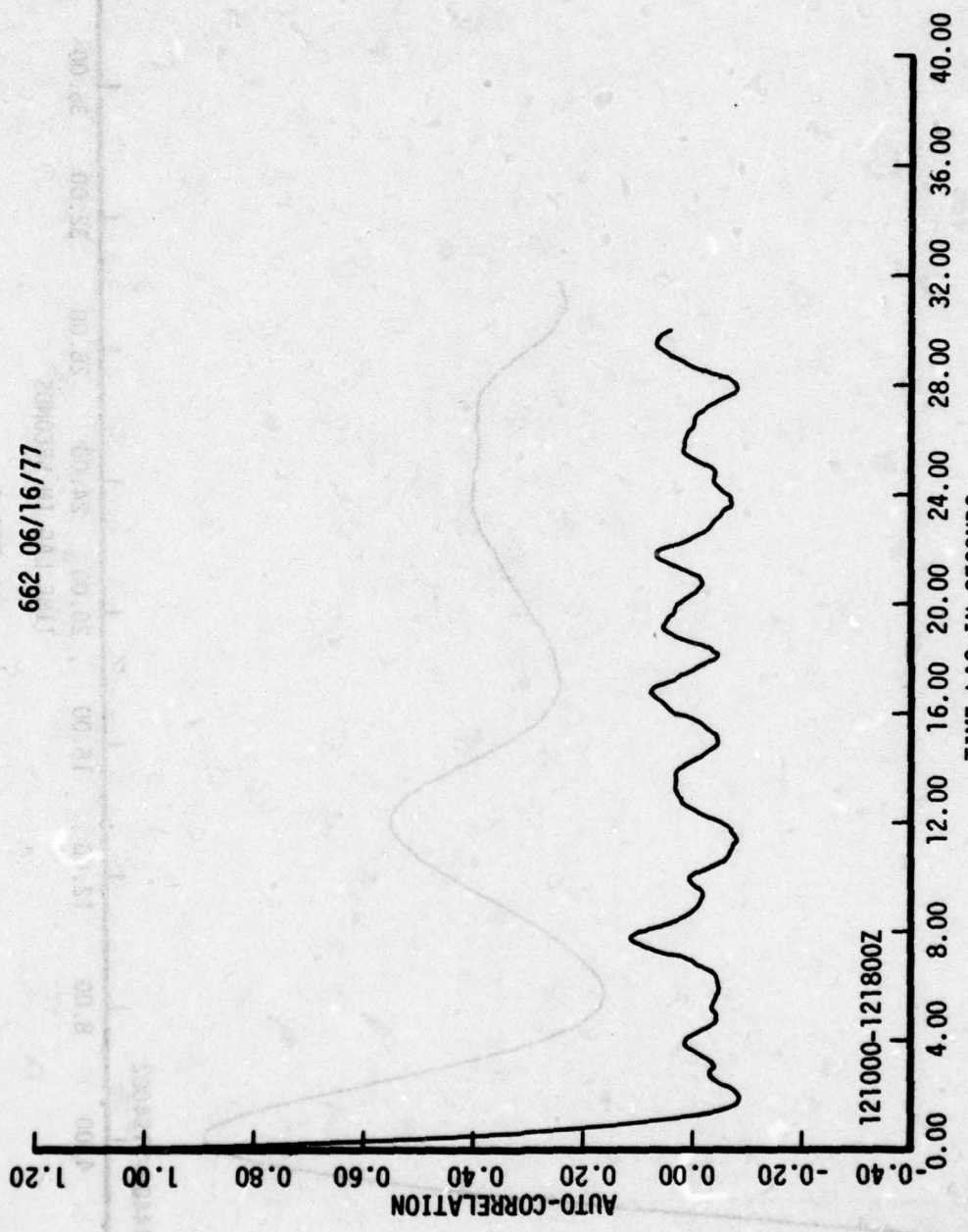

Figure 92. Autocorrelation Function of Received Signal Amplitude for Polar Scintillation

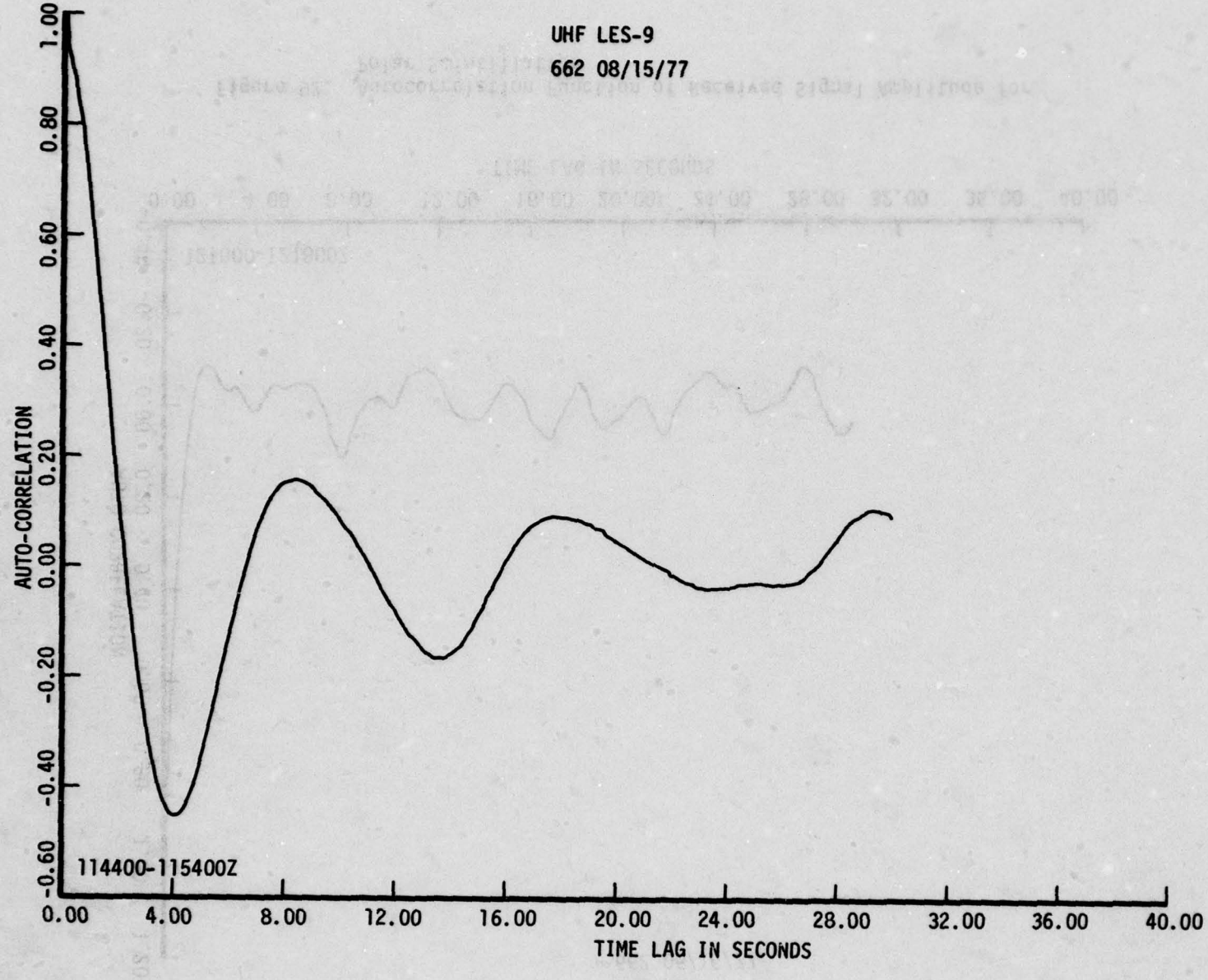

Figure 93. Autocorrelation Function of Received Signal Amplitude for Polar Scintillation

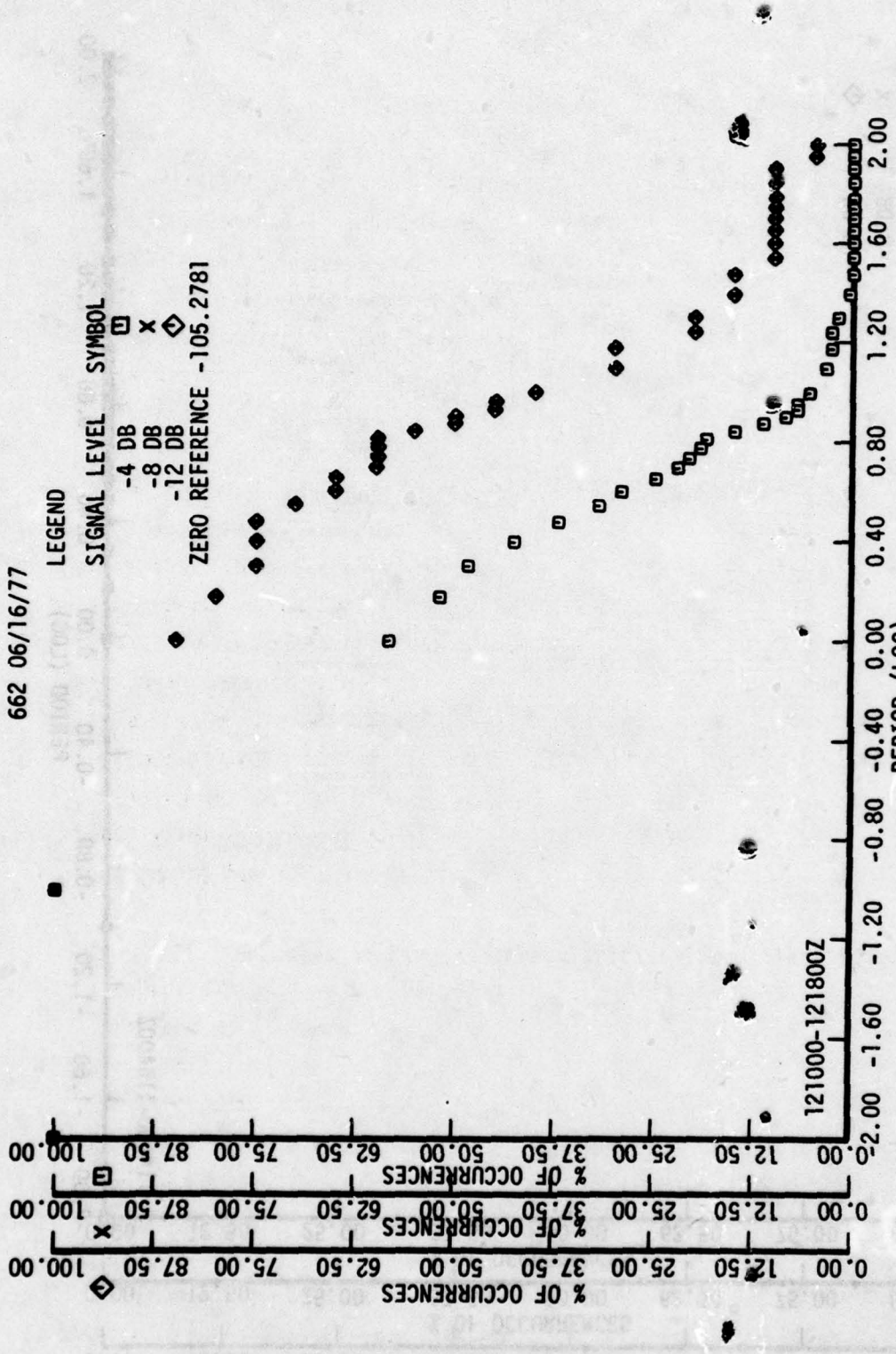

Figure 94. Fading Period of Received Signal Amplitude for Polar Scintillation

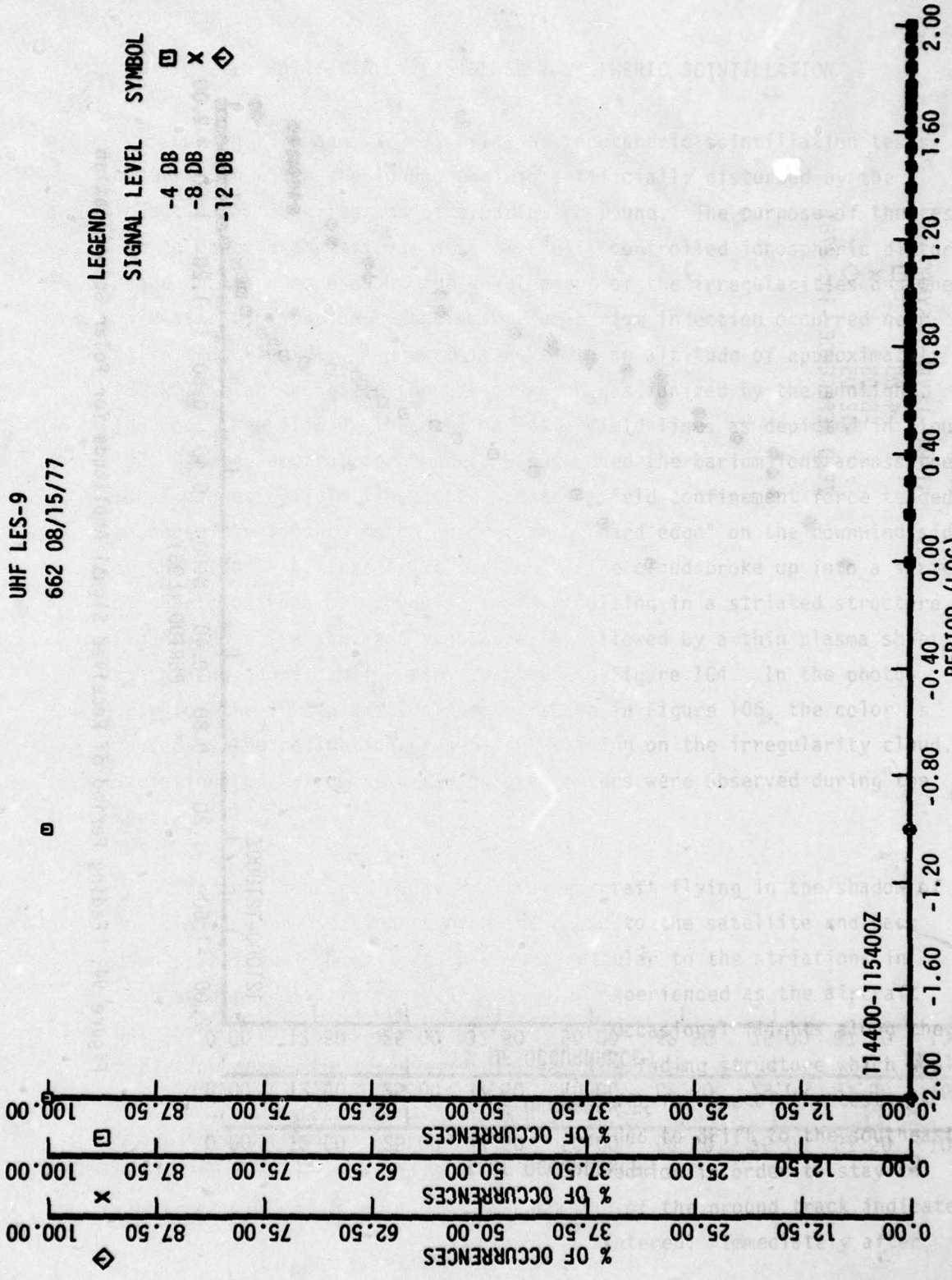

Figure 95. Fading Period of Received Signal Amplitude for Polar Scintillation

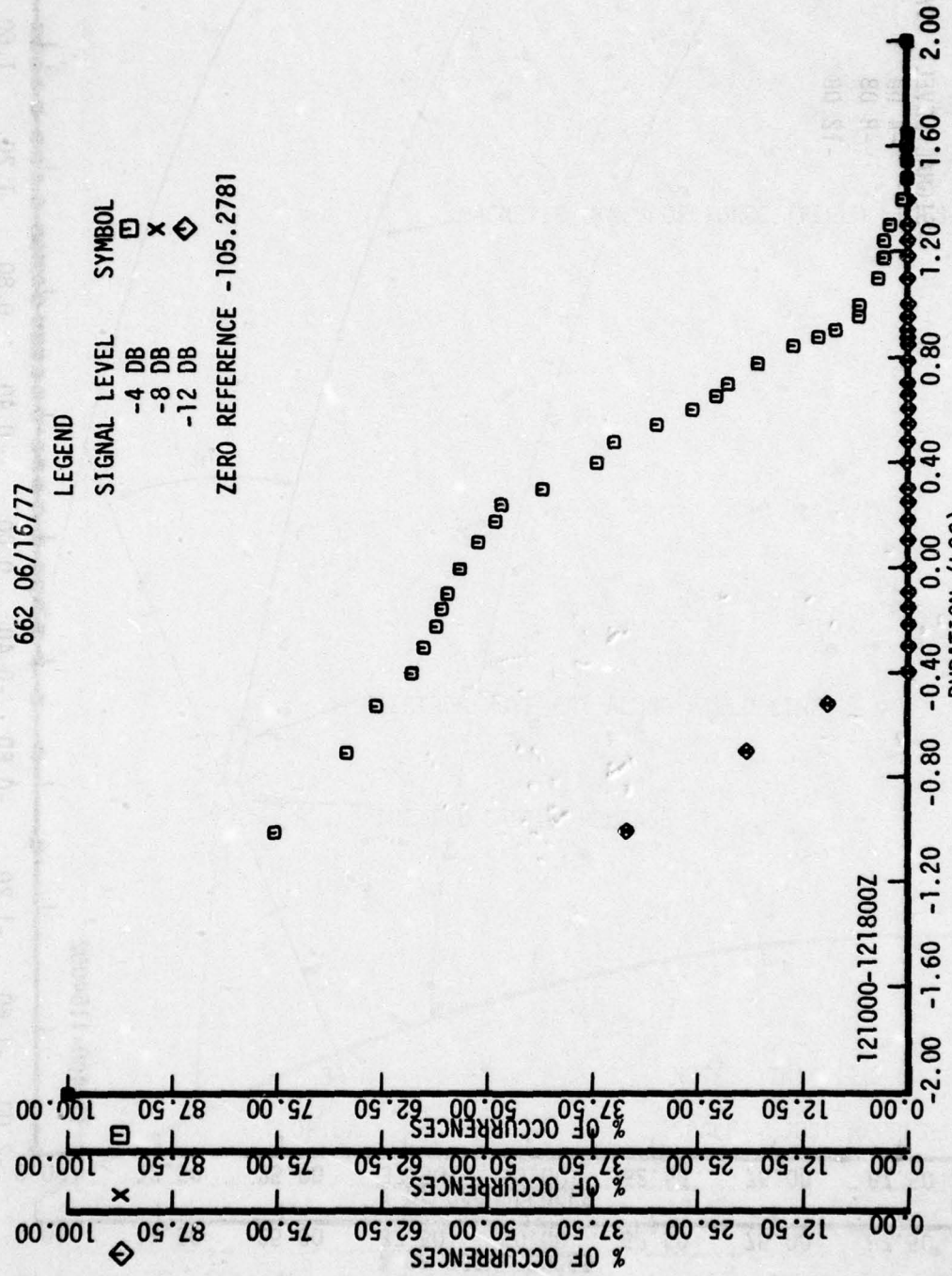

Figure 96. Fading Duration of Received Signal Amplitude for Polar Scintillation

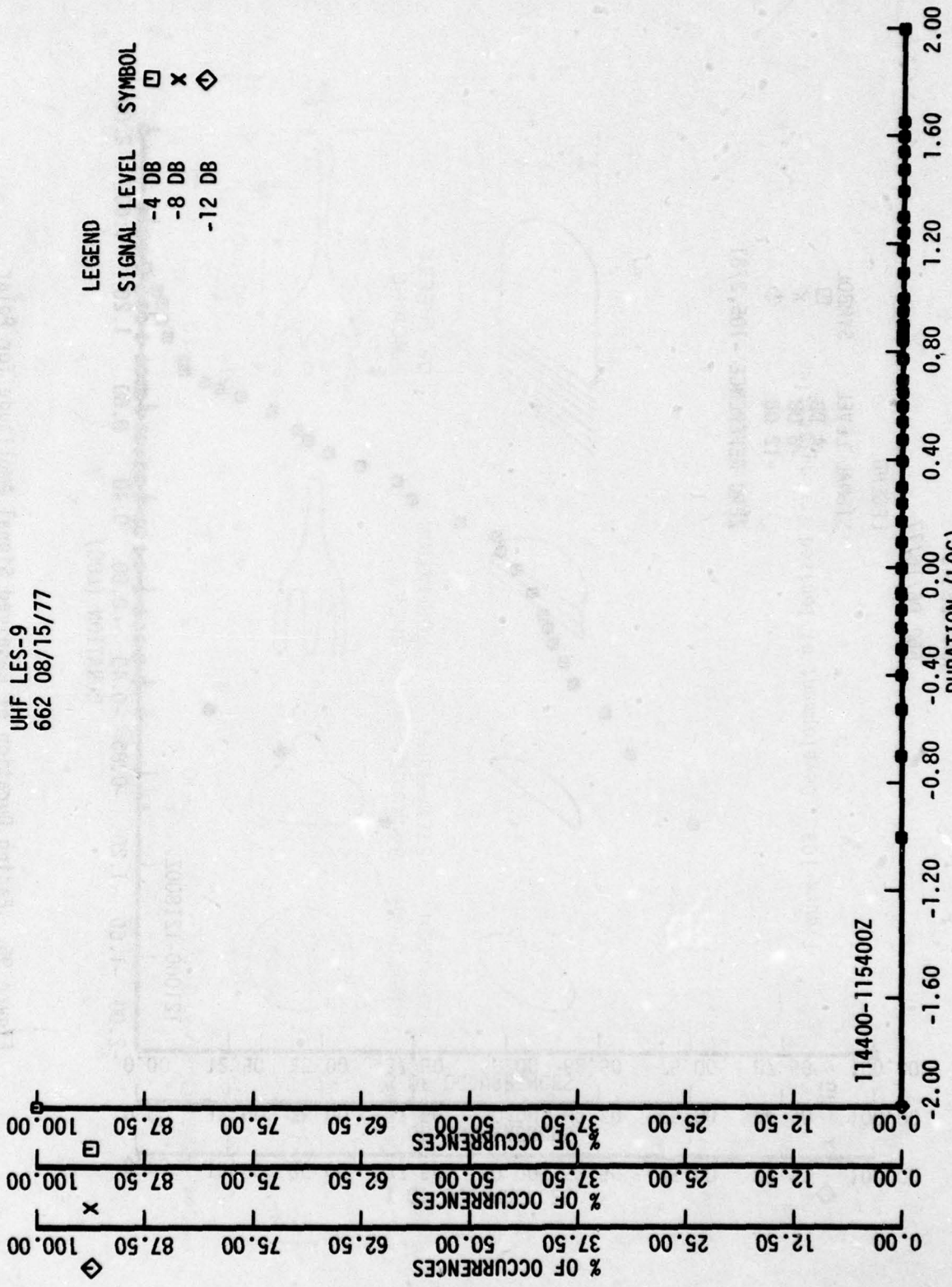

Figure 97. Fading Duration of Received Signal Amplitude for Polar Scintillation

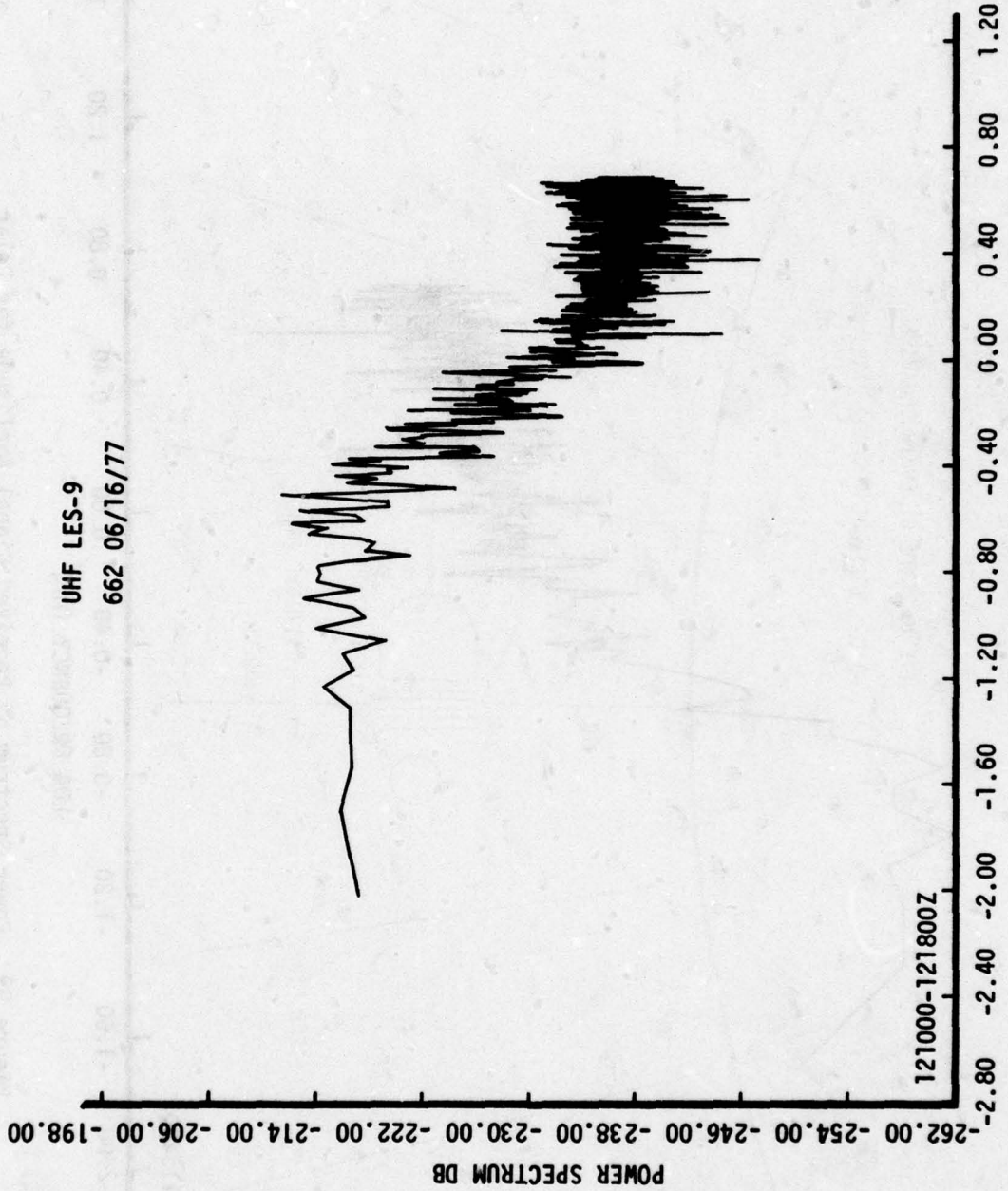

Figure 98. Power Spectrum of Received Signal Amplitude for Polar Scintillation

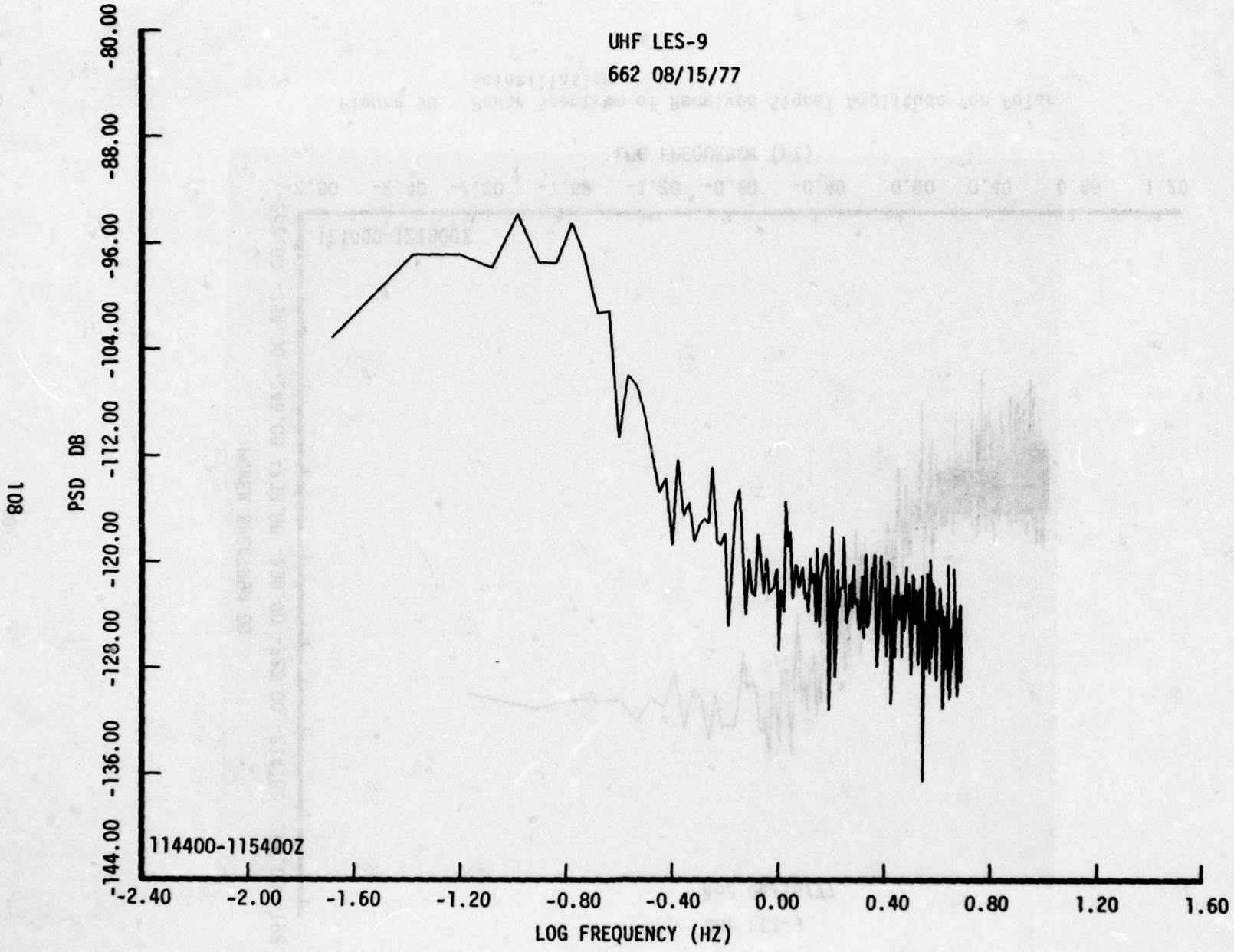

Figure 99. Power Spectrum of Received Signal Amplitude for Polar Scintillation

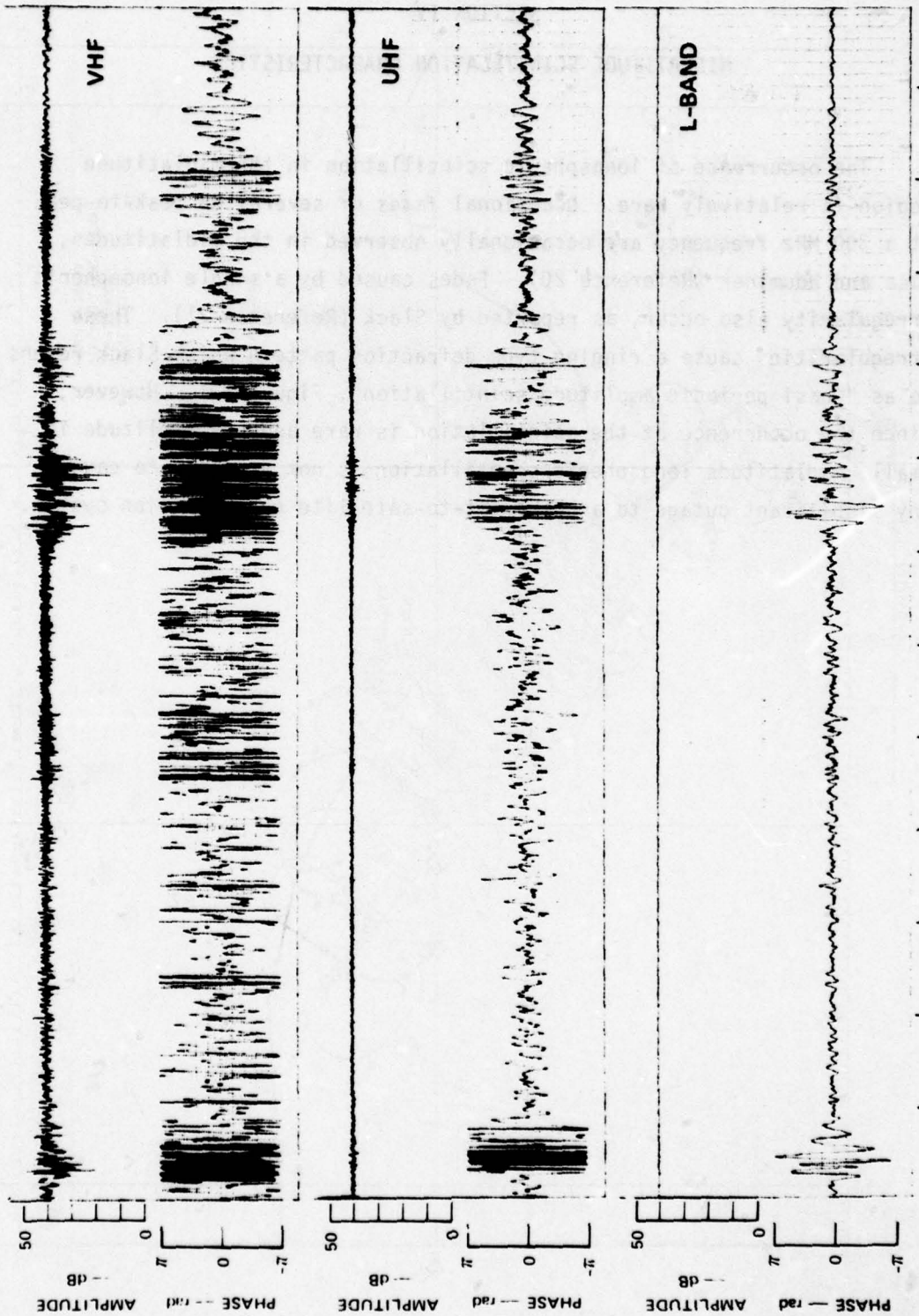

Figure 100. Detrended Received Signal Recordings for Polar Scintillation (From Rino et al Reference 8)

SECTION IV

MIDLATITUDE SCINTILLATION CHARACTERISTICS

The occurrence of ionospheric scintillation in the midlatitude region is relatively rare. Occasional fades of several dB peak-to-peak at a 300 MHz frequency are occasionally observed in the midlatitudes, Mass and Houminer (Reference 20). Fades caused by a single ionospheric irregularity also occur, as reported by Slack (Reference 21). These irregularities cause a ringing type defraction pattern which Slack refers to as "Quasi periodic amplitude scintillation", Figure 101. However, since the occurrence of the scintillation is rare and the amplitude is small, midlatitude ionospheric scintillation is not expected to cause any significant outage to an aircraft-to-satellite communication system.

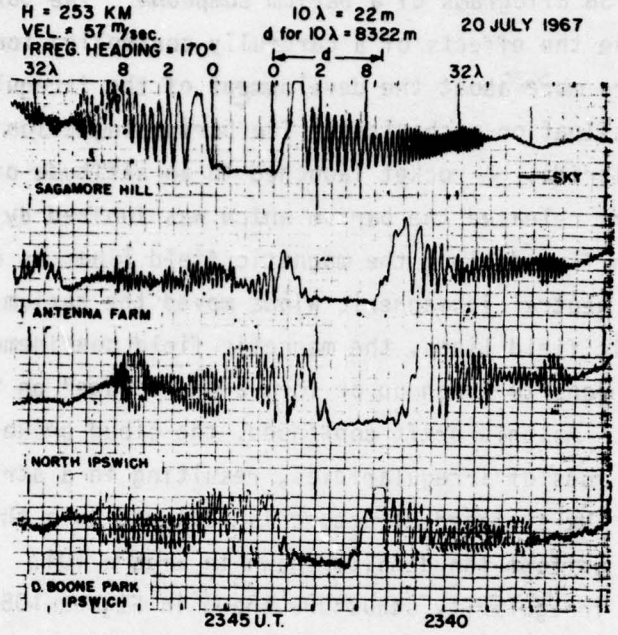

Figure 101. Examples of Ringing Irregularities (From Slack Reference 21)

SECTION V

ARTIFICIALLY DISTURBED IONOSPHERIC SCINTILLATION

During 1976 and 1977 a series of ionospheric scintillation tests occurred in which the ionosphere was artificially disturbed by the injection of 38 kilograms of a barium compound. The purpose of the test was to observe the effects of a carefully controlled ionospheric disturbance to learn more about the development of the irregularities and their late-time dissipation mechanisms. The barium injection occurred near Eglin AFB, Florida. A rocket launched to an altitude of approximately 180 kilometers released the barium which was ionized by the sunlight. The ions then flowed along the magnetic field lines as depicted in Figure 102. As the neutral ionospheric winds moved the barium ions across the local magnetic field lines, the magnetic field confinement force tended to cause the ions to bunch up or form a "hard edge" on the downwind side of the cloud. As this drift continued, the cloud broke up into a series of sheets or rods of irregularities, resulting in a striated structure, Figure 103. The striated structure is followed by a thin plasma sheet containing a uniform ion density shown in Figure 104. In the photograph of the irregularity structure shown in Figure 105, the color is caused by the reflection of sunlight shining on the irregularity cloud. Striations as narrow as a few hundred meters were observed during the test.

The test concept involved a test aircraft flying in the shadow of the cloud, communicating through the cloud to the satellite and back down. The usual flight path was perpendicular to the striations in such a manner that rapid fading would be experienced as the aircraft cut through various striated structures. Occasional flights along the striation were made to investigate the slow fading structure which would be encountered. Ground track of the aircraft for one of the tests is shown in Figure 106. The barium cloud tended to drift to the southeast, requiring the aircraft to move in that direction in order to stay in the shadow of the cloud. The wide portion of the ground track indicates areas where scintillation fading was encountered. Immediately after

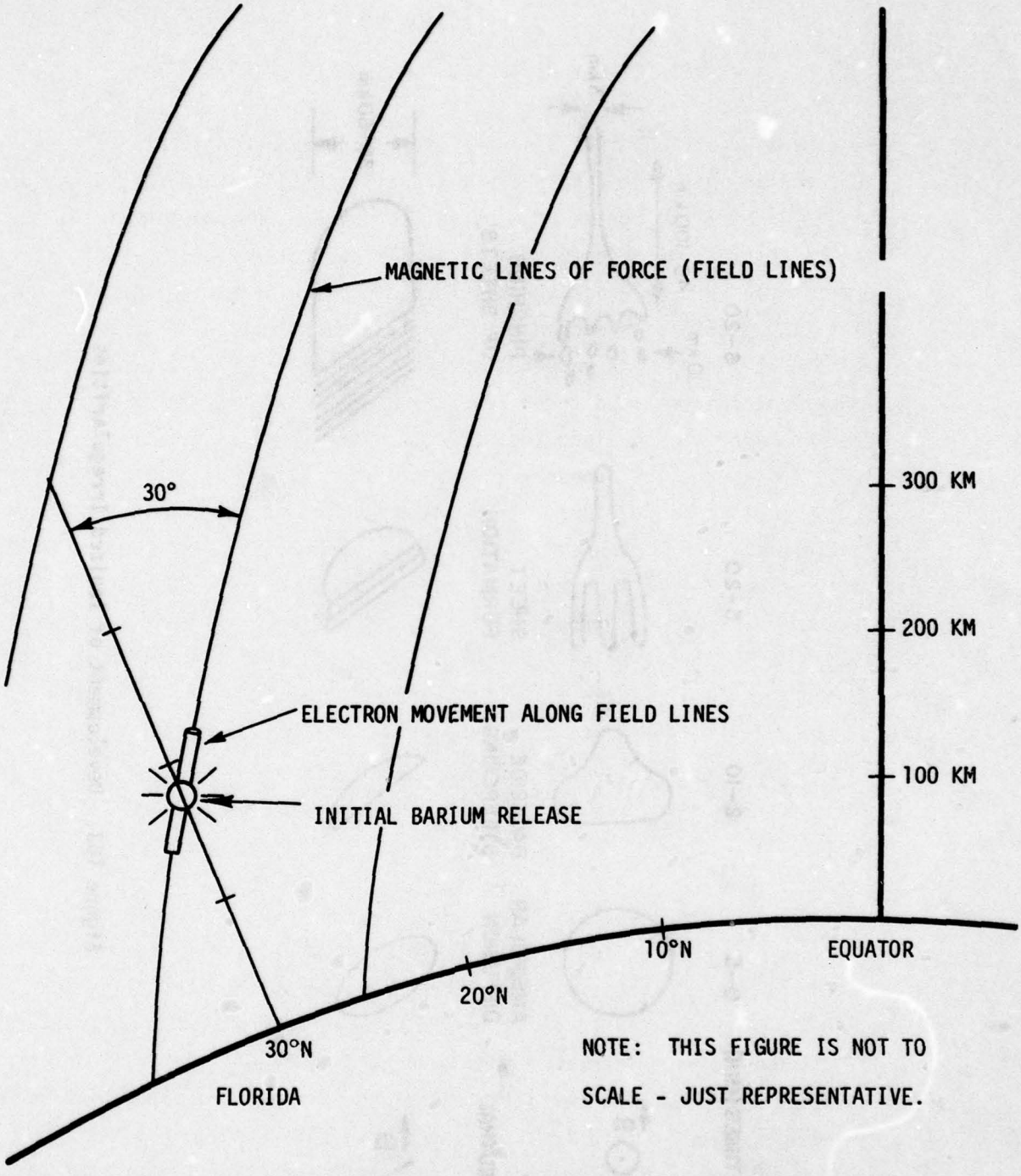

Figure 102. Propagation of Free Electrons Along Field Lines

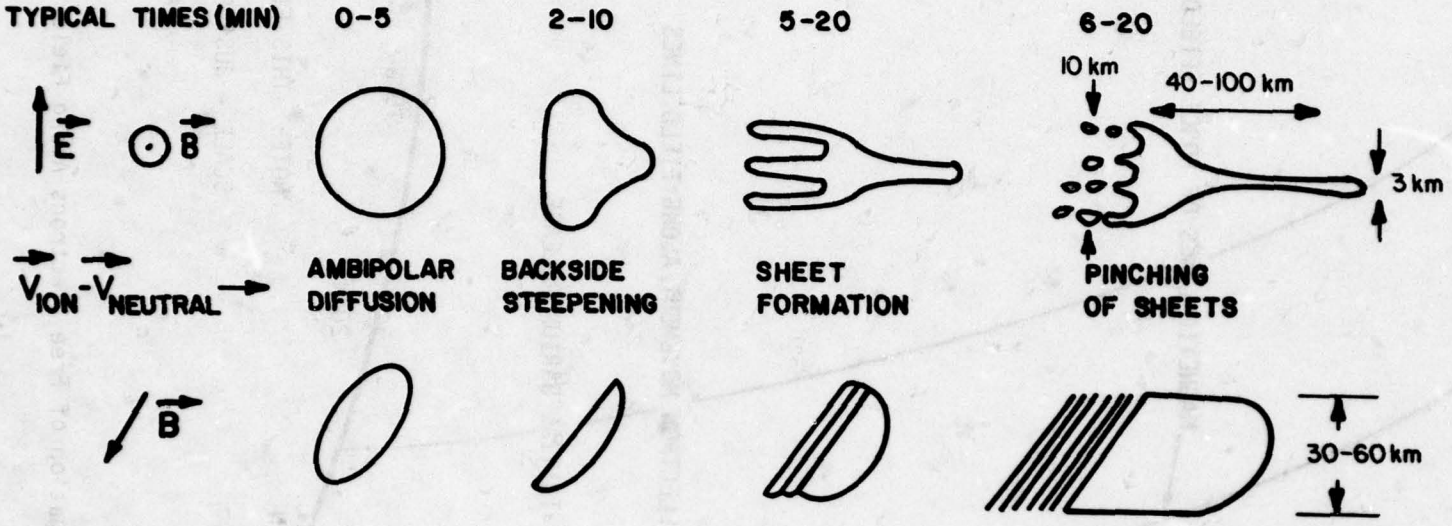

Figure 103. Development of Ionized Irregularities

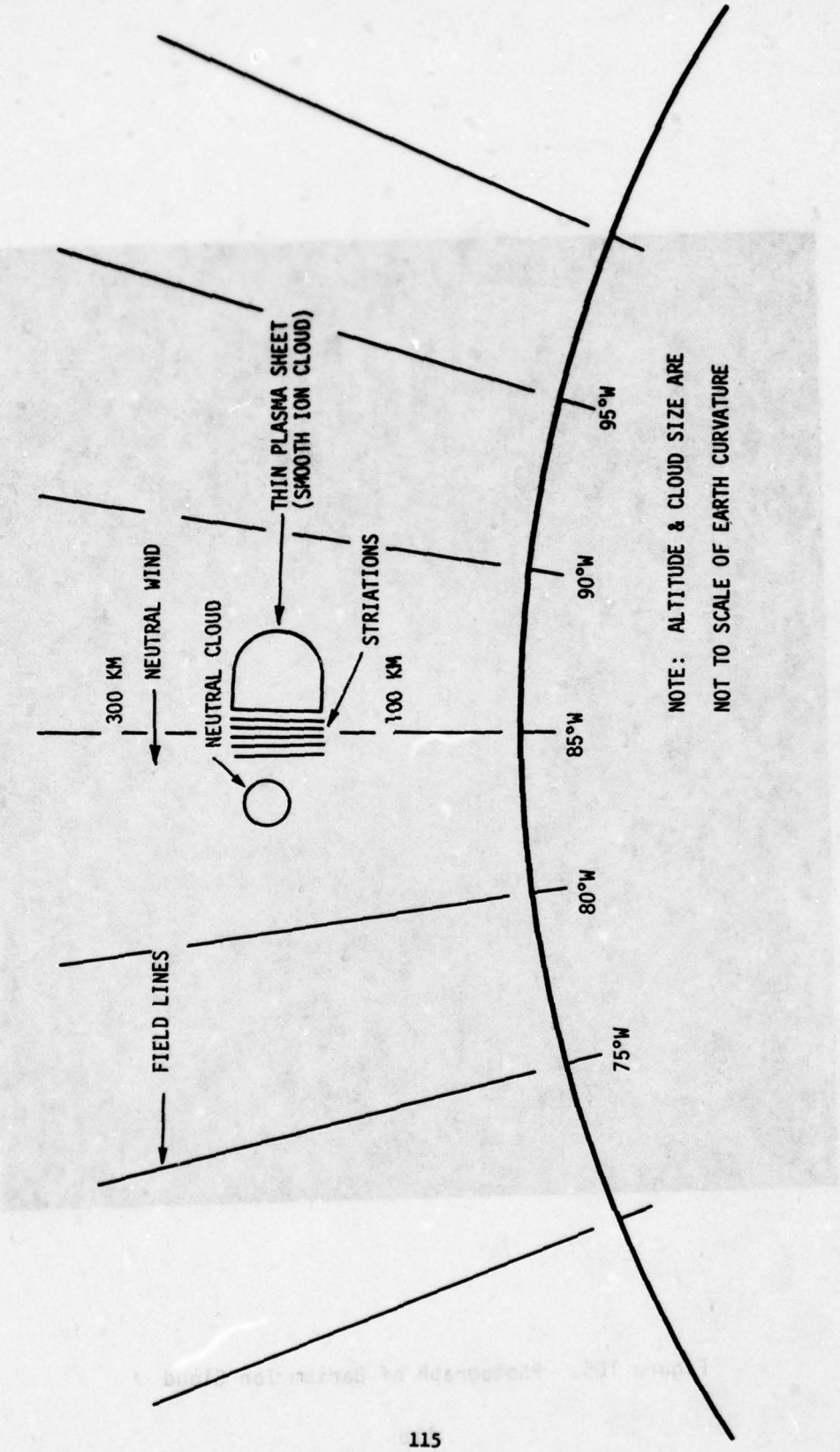

Figure 104. Movement of Barium Ion Cloud

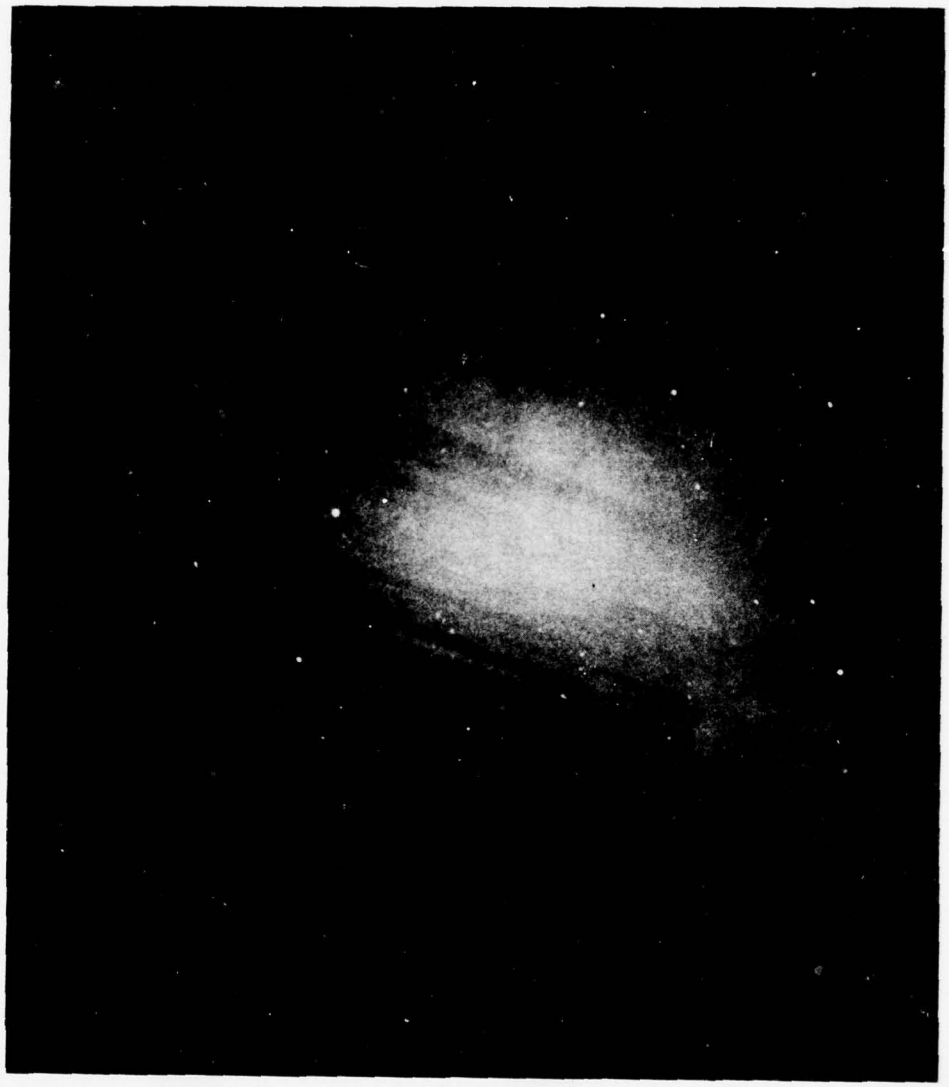

Figure 105. Photograph of Barium Ion Cloud

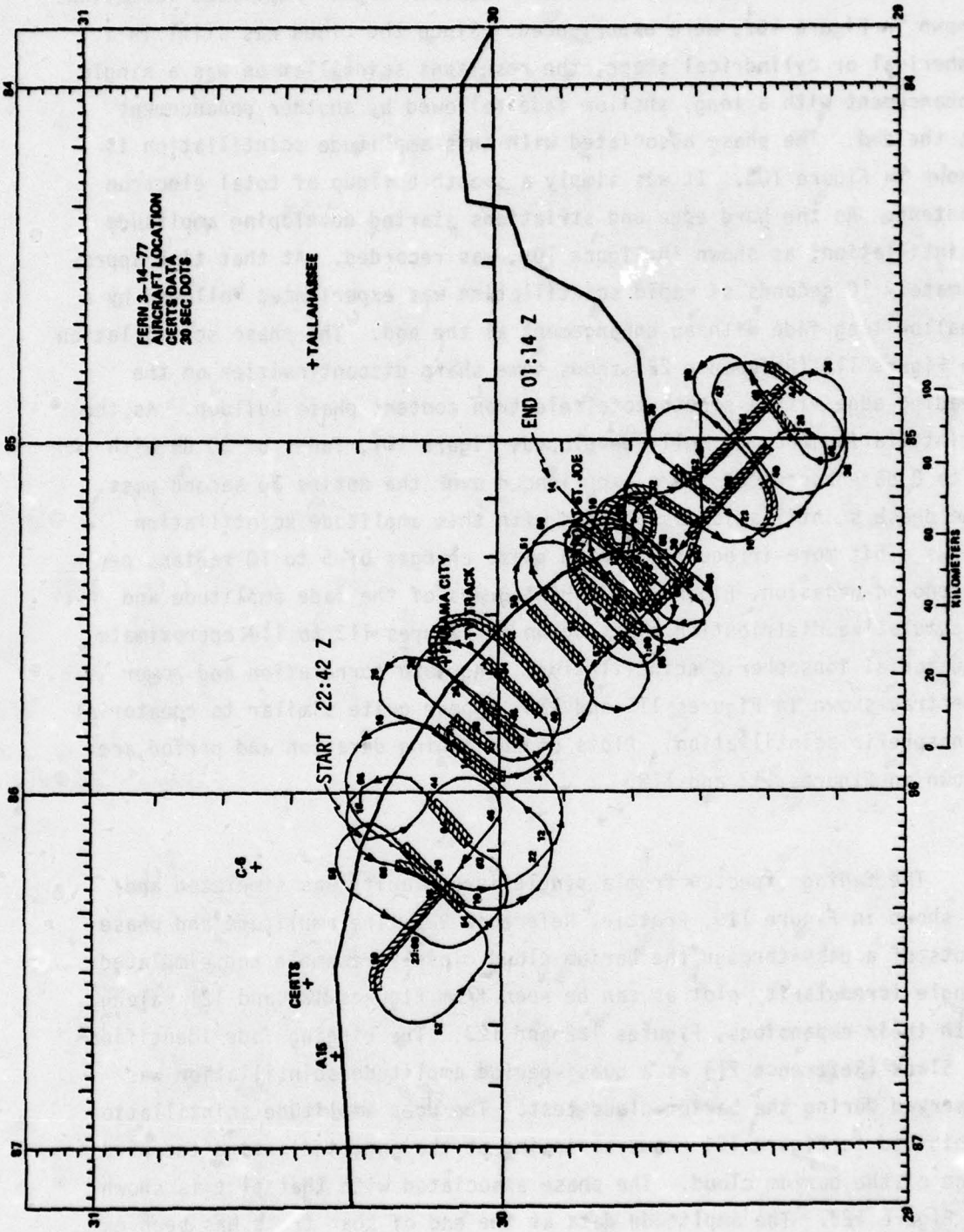

Figure 106. Plot of Aircraft Ground Track During Test Flight

the injection of the barium cloud the received signal amplitude variations shown in Figure 107, were experienced. Since the cloud was still in a spherical or cylindrical shape, the resultant scintillation was a single enhancement with a long, shallow fade followed by another enhancement at the end. The phase associated with this amplitude scintillation is shown in Figure 108. It was simply a smooth buildup of total electron content. As the hard edge and striations started developing amplitude scintillation, as shown in Figure 109, was recorded. At that time approximately 10 seconds of rapid scintillation was experienced followed by a shallow long fade with an enhancement at the end. The phase scintillation in Figure 110 (Reference 22) shows some sharp discontinuities on the leading edge with a smooth total electron content phase buildup. As the scintillation becomes fully developed, Figure 111, fades of 30 dB with 5 to 8 dB enhancements were experienced over the entire 30 second pass. The phase scintillation associated with this amplitude scintillation shows a bit more irregularity with phase changes of 5 to 10 radians per second on occasion, Figure 112. Histograms of the fade amplitude and accumulative distribution plots shown in Figures 113 to 114 approximate equatorial ionsopheric scintillation. The auto correlation and power spectra, shown in Figures 115 and 116, appear quite similar to equatorial ionospheric scintillation. Plots of the fading duration and period are shown in Figures 117 and 118.

The fading expected from a single irregularity was simulated and is shown in Figure 119, Prettie, Reference 22. The amplitude and phase plots of a pass through the barium cloud closely resemble the simulated single irregularity plot as can be seen from Figures 120 and 121, along with their expansions, Figures 122 and 123. The ringing fade identified by Slack (Reference 21) as a quasi-period amplitude scintillation was observed during the barium cloud test. The deep amplitude scintillation exhibited in Figure 124 shows a ringing at the end, indicating the hard edge of the barium cloud. The phase associated with that plot is shown in Figure 125. The amplitude data at the end of that trace has been expanded and is shown in Figure 126 with the expanded phase in Figure 127.

Measurements through the barium cloud of two frequencies separated by approximately 90 MHz resulted in a cross correlation shown in Figure 128. This cross correlation indicates that a frequency separation of 90 MHz is sufficient to almost completely decorrelate the fading of the two signals.

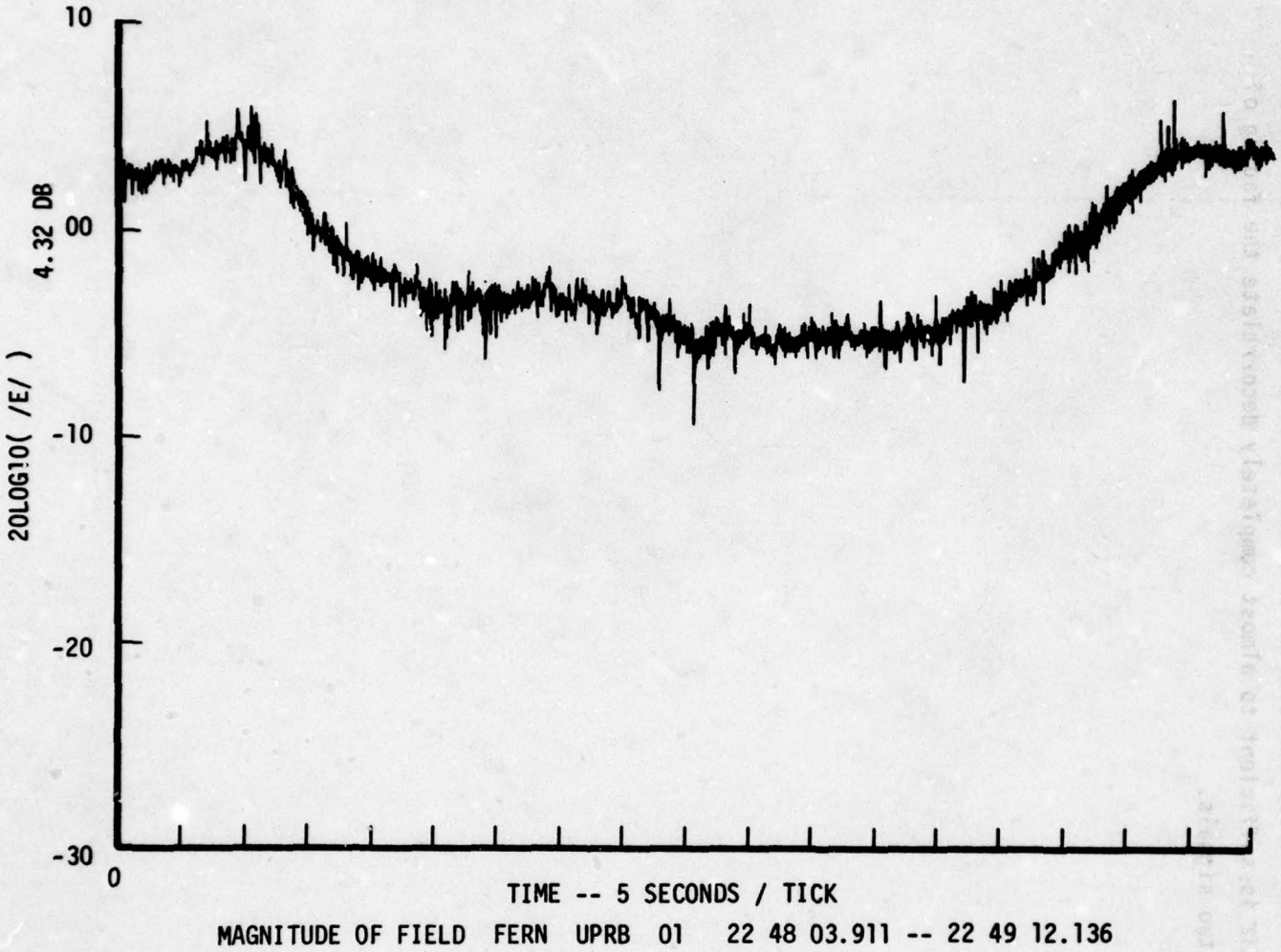

Figure 107. Received Signal Amplitude for Early Time Ion Cloud (From Prettie et al Reference 22)

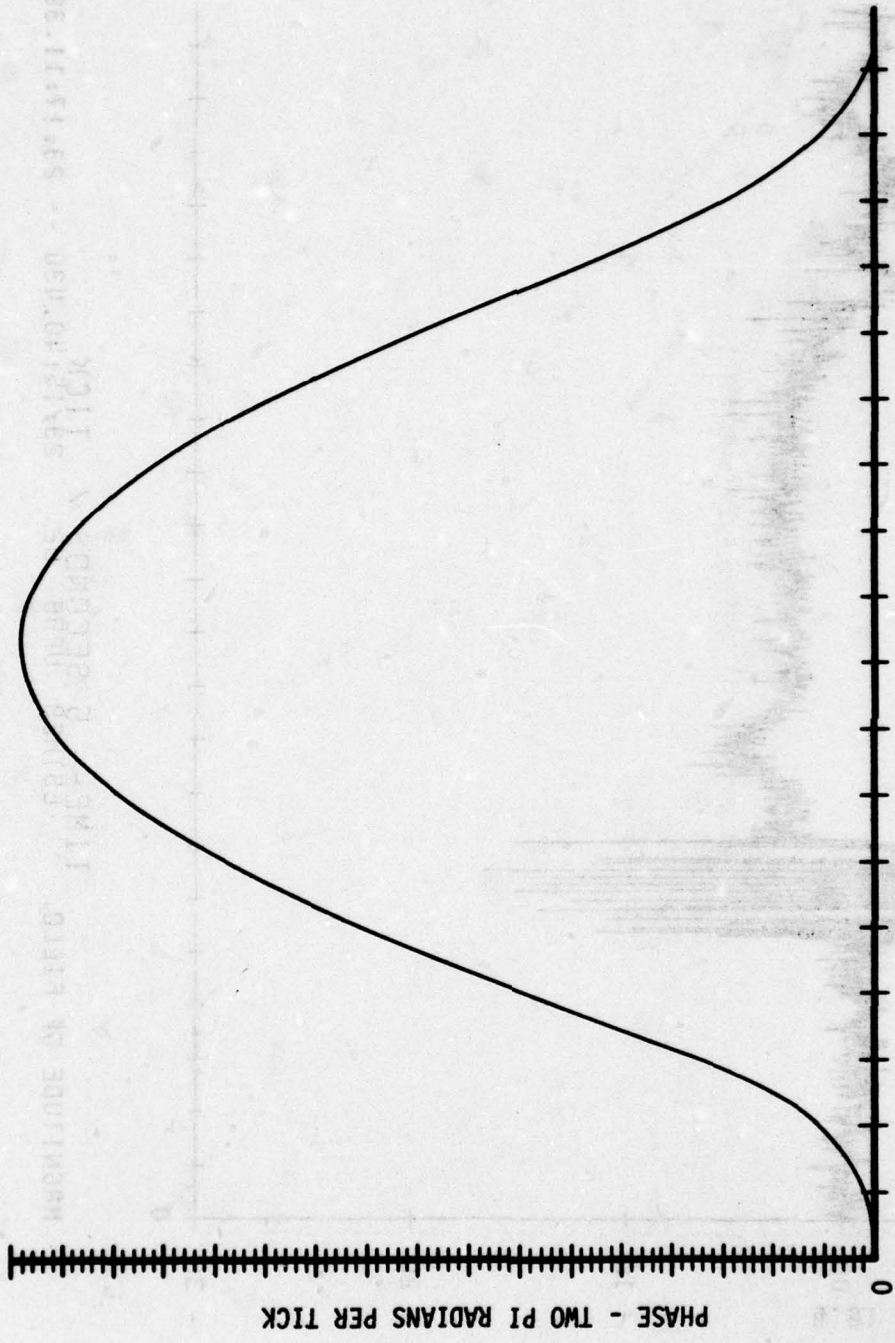

Figure 108. Received Signal Phase for Early Time Ion Cloud (From Prettie et al Reference 22)

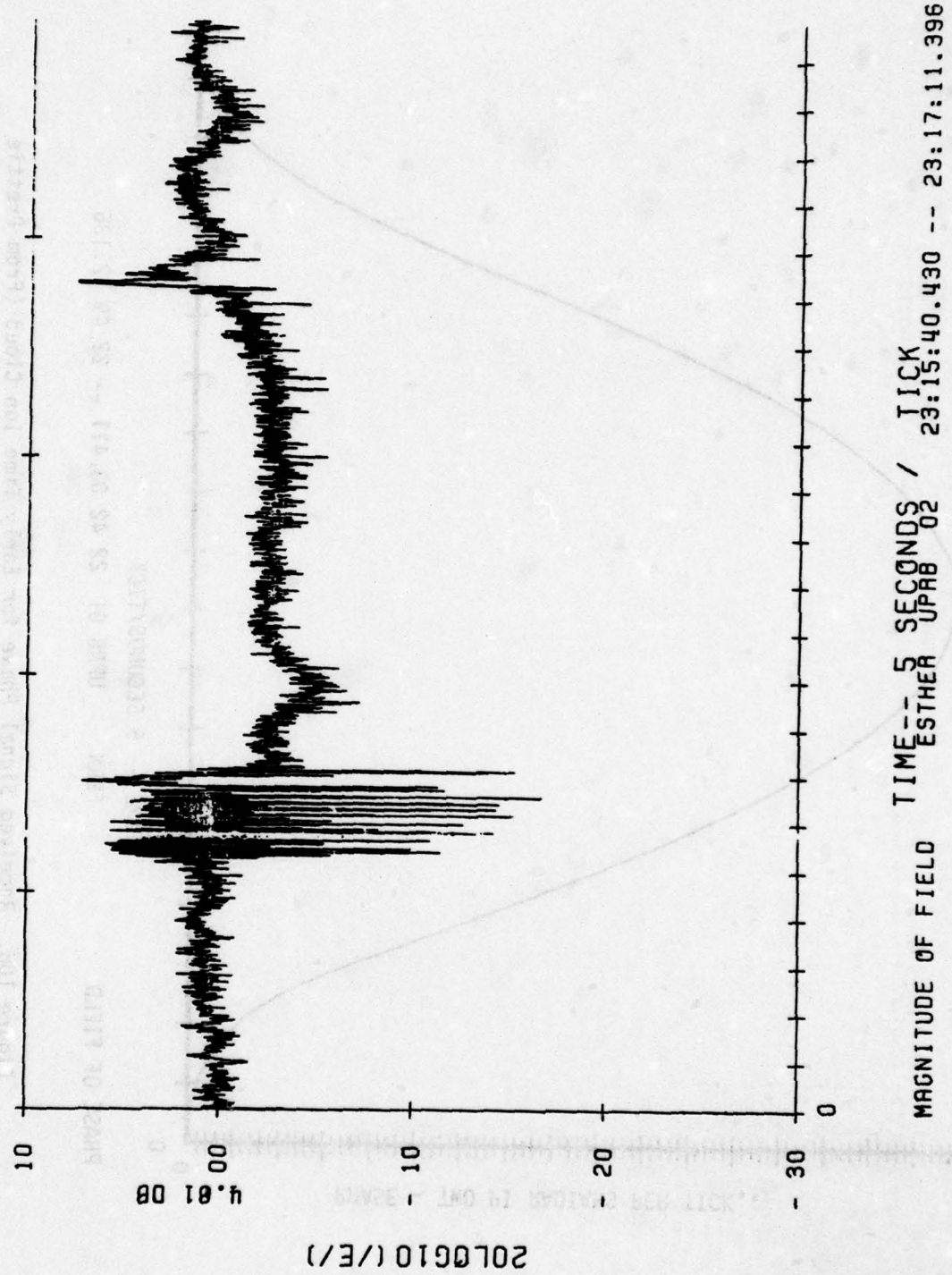

Figure 109. Received Signal Amplitude for Partially Striated Ion Cloud (From Prettie et al Reference 22)

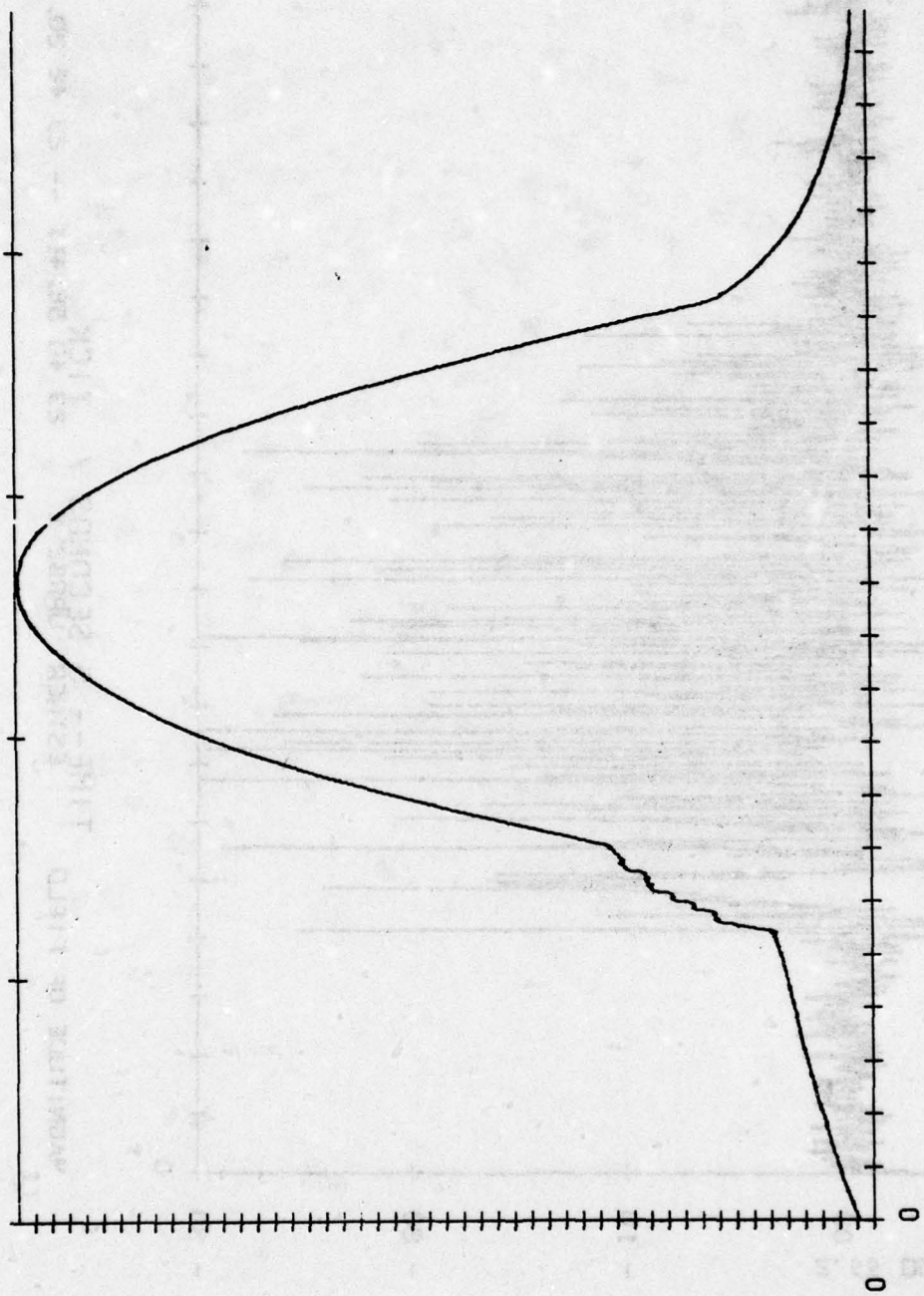

Figure 110. Received Signal Phase for Partially Striated Ion Cloud (From Prettie et al Reference 22)

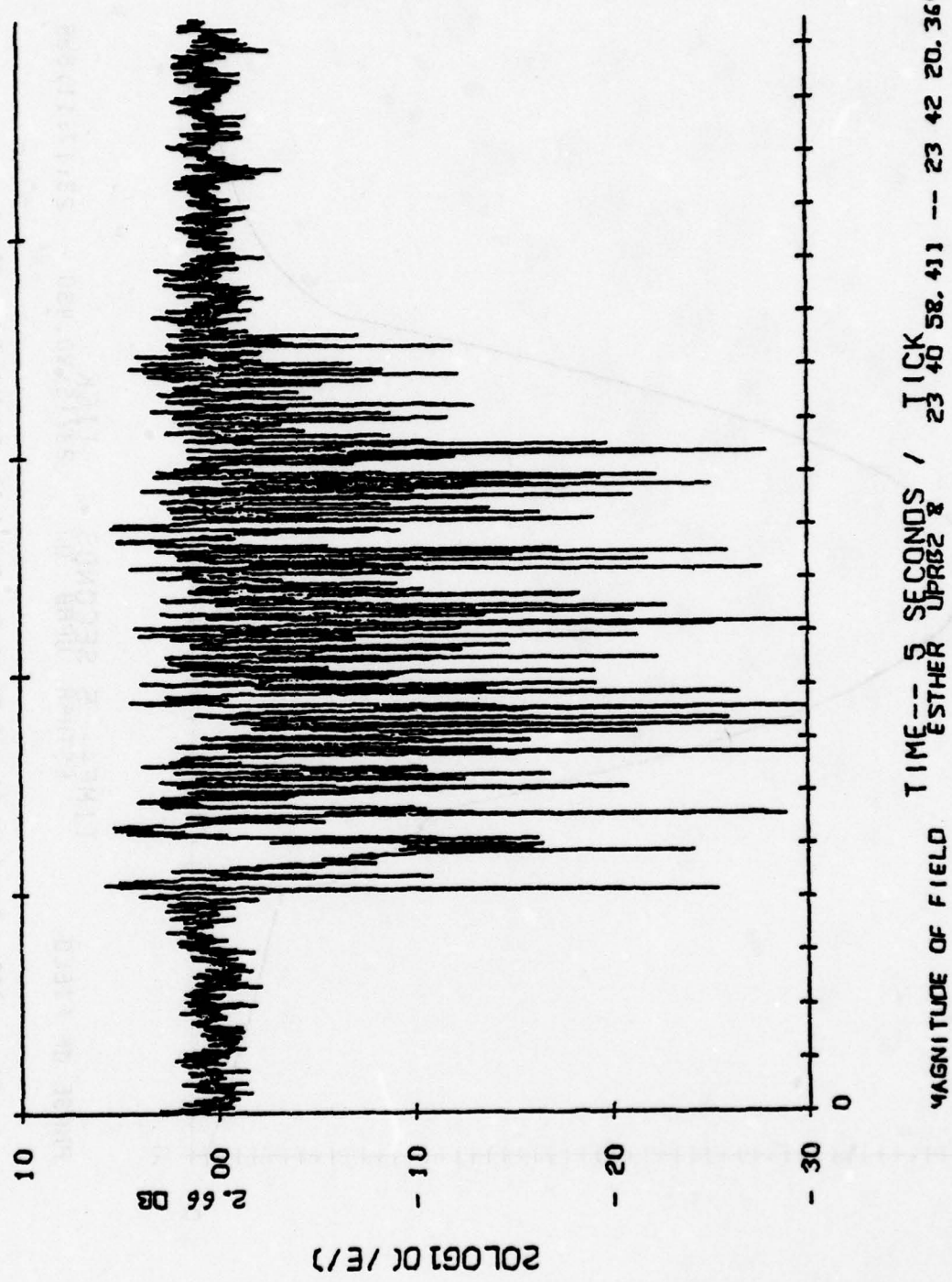

Figure 111. Received Signal Amplitude for Fully Striated Ion Cloud (From Prettie et al Reference 22)

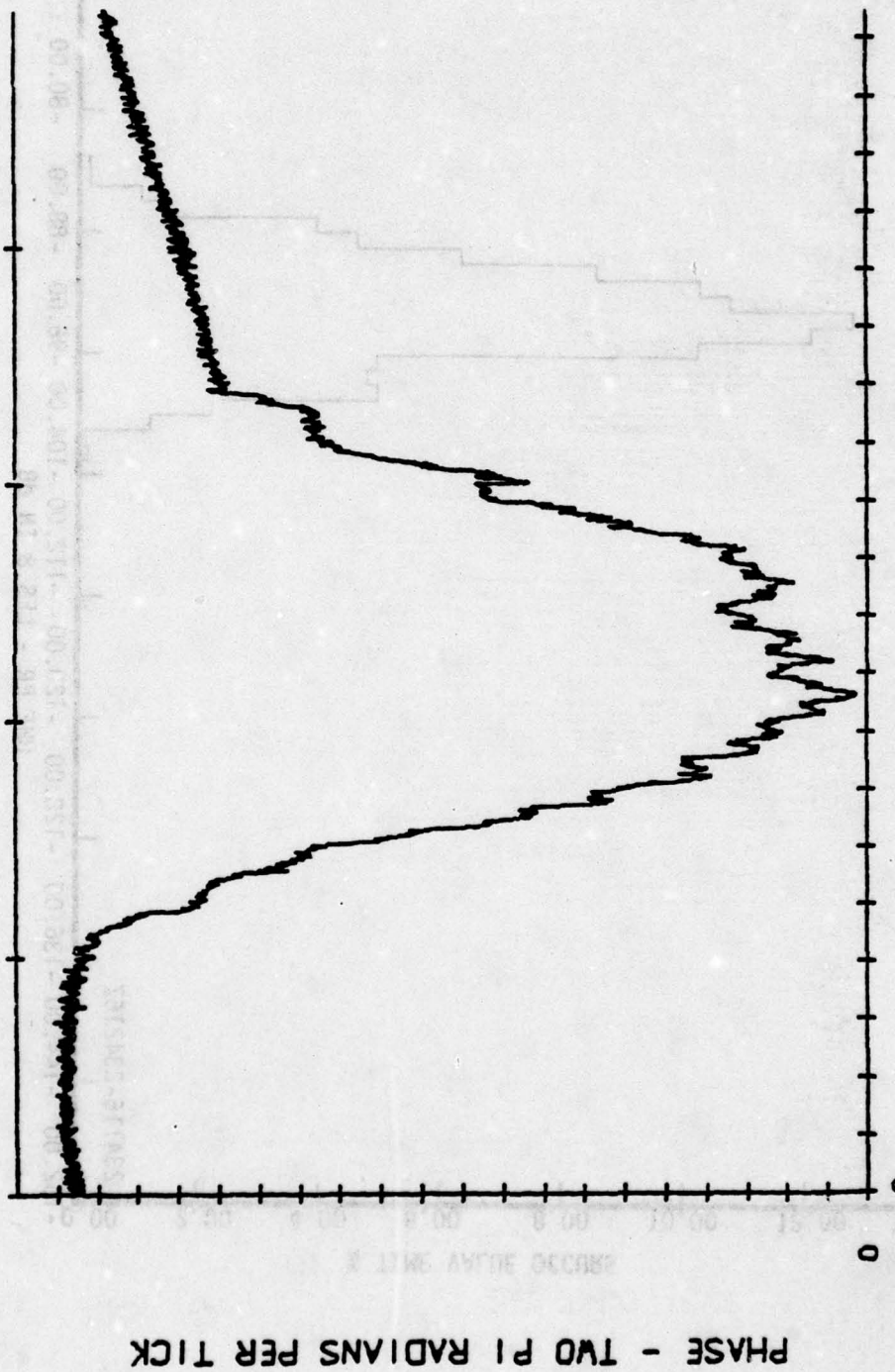

Figure 112. Received Signal Phase for Fully Striated Ion Cloud (From Prettie et al Reference 22)

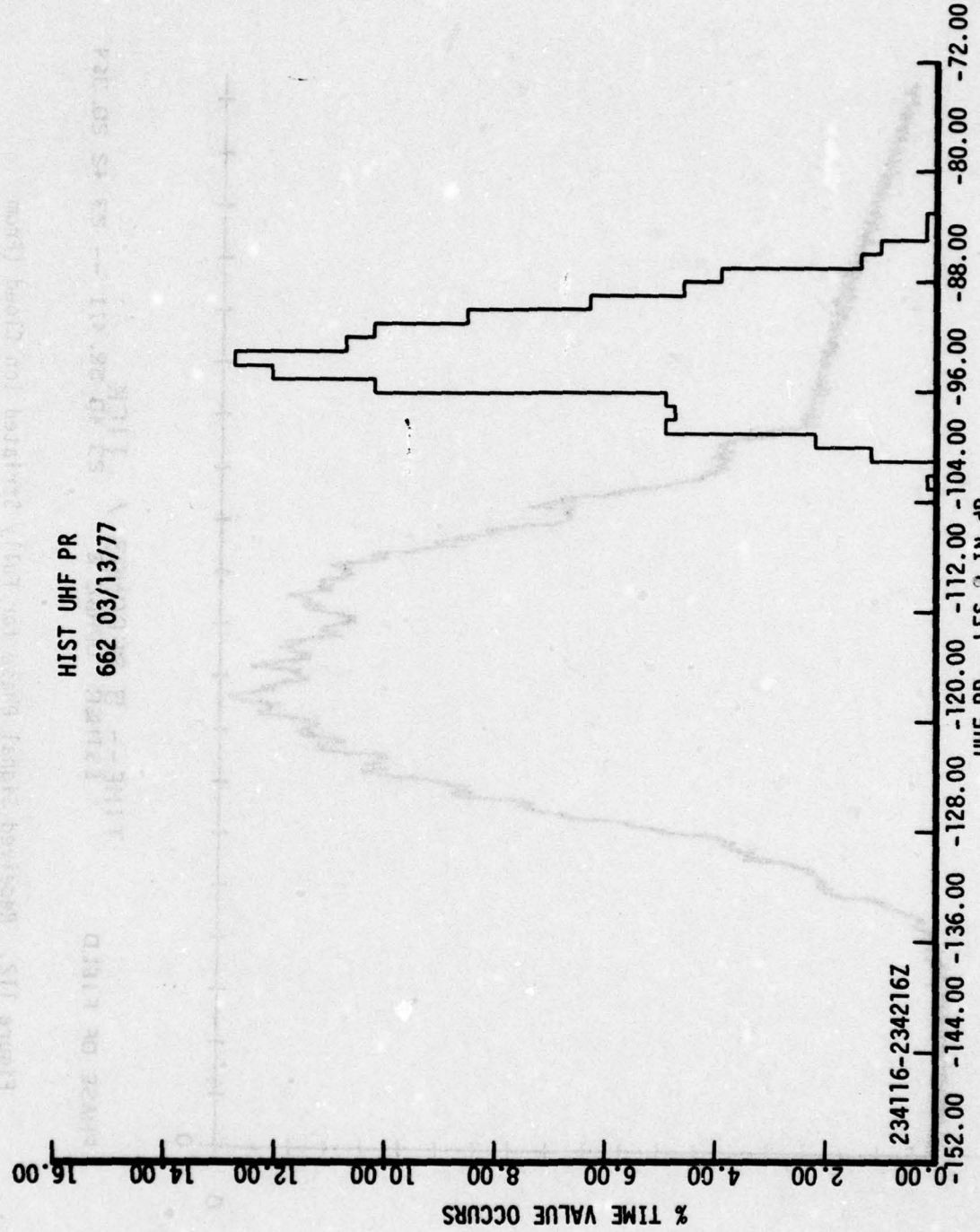

Figure 113. Histogram of Received Signal Amplitude for Artificial Scintillation

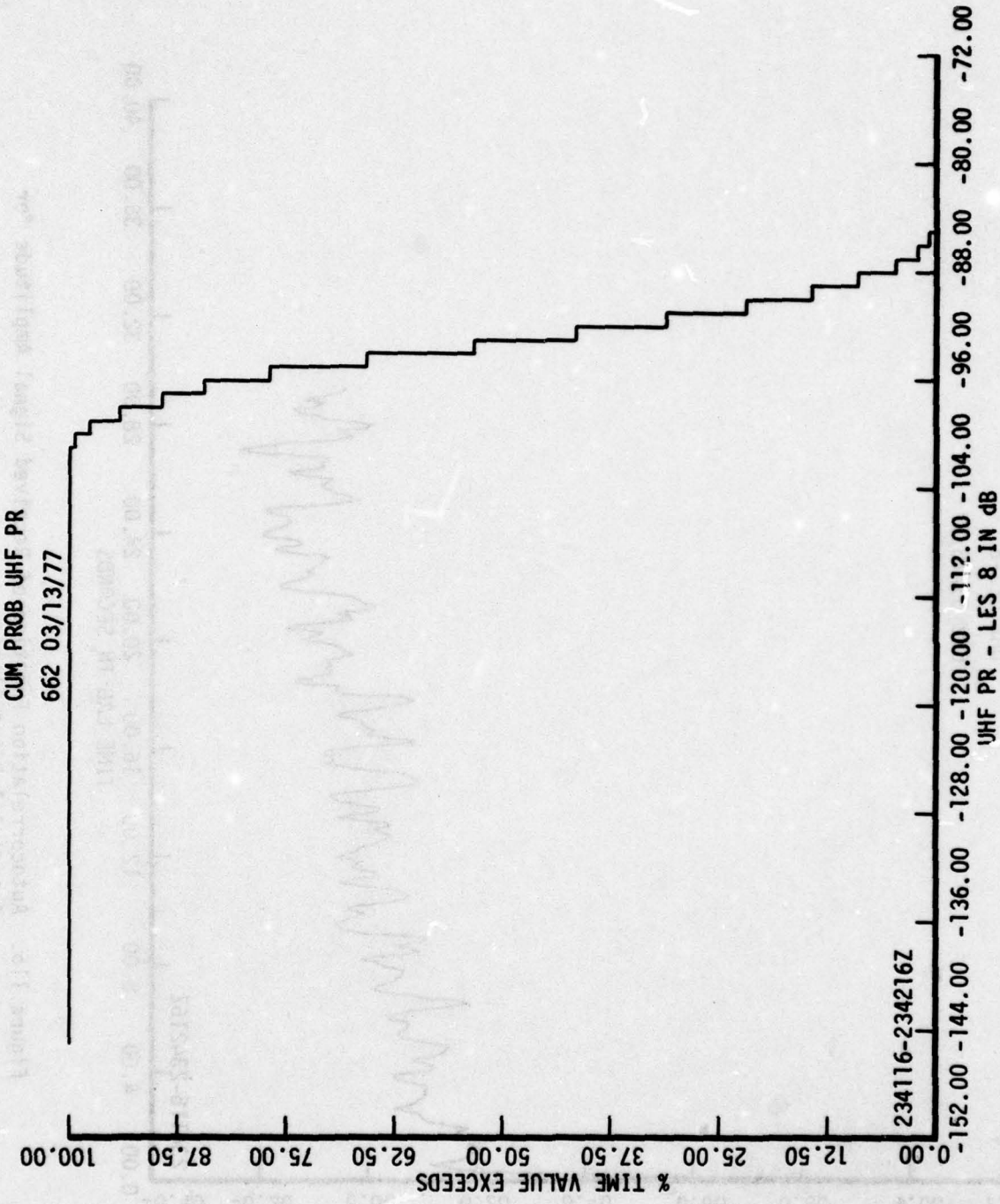

Figure 114. Cumulative Distribution of Received Signal Amplitude for Artificial Scintillation

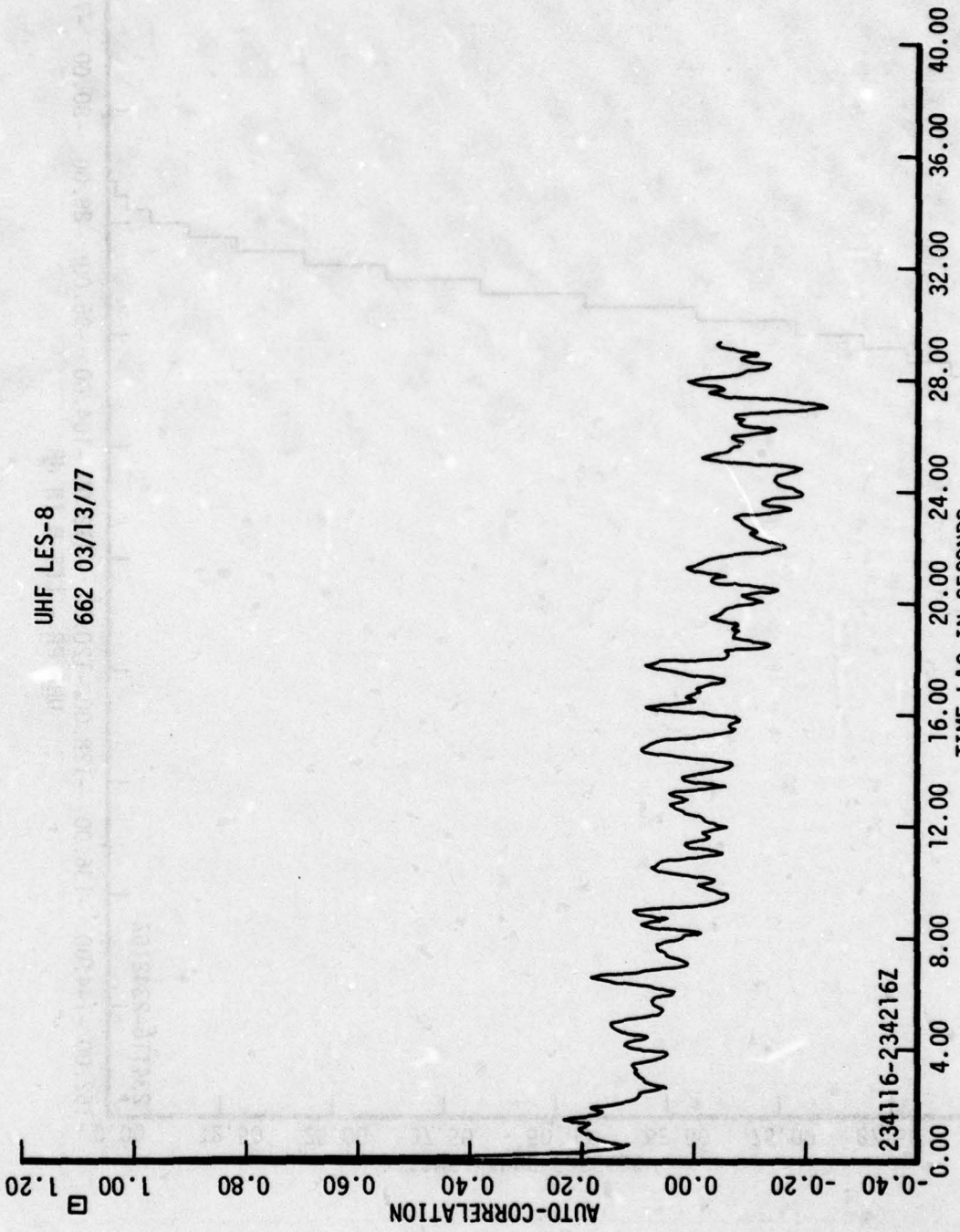

Figure 115. Autocorrelation Function of Received Signal Amplitude for Artificial Scintillation

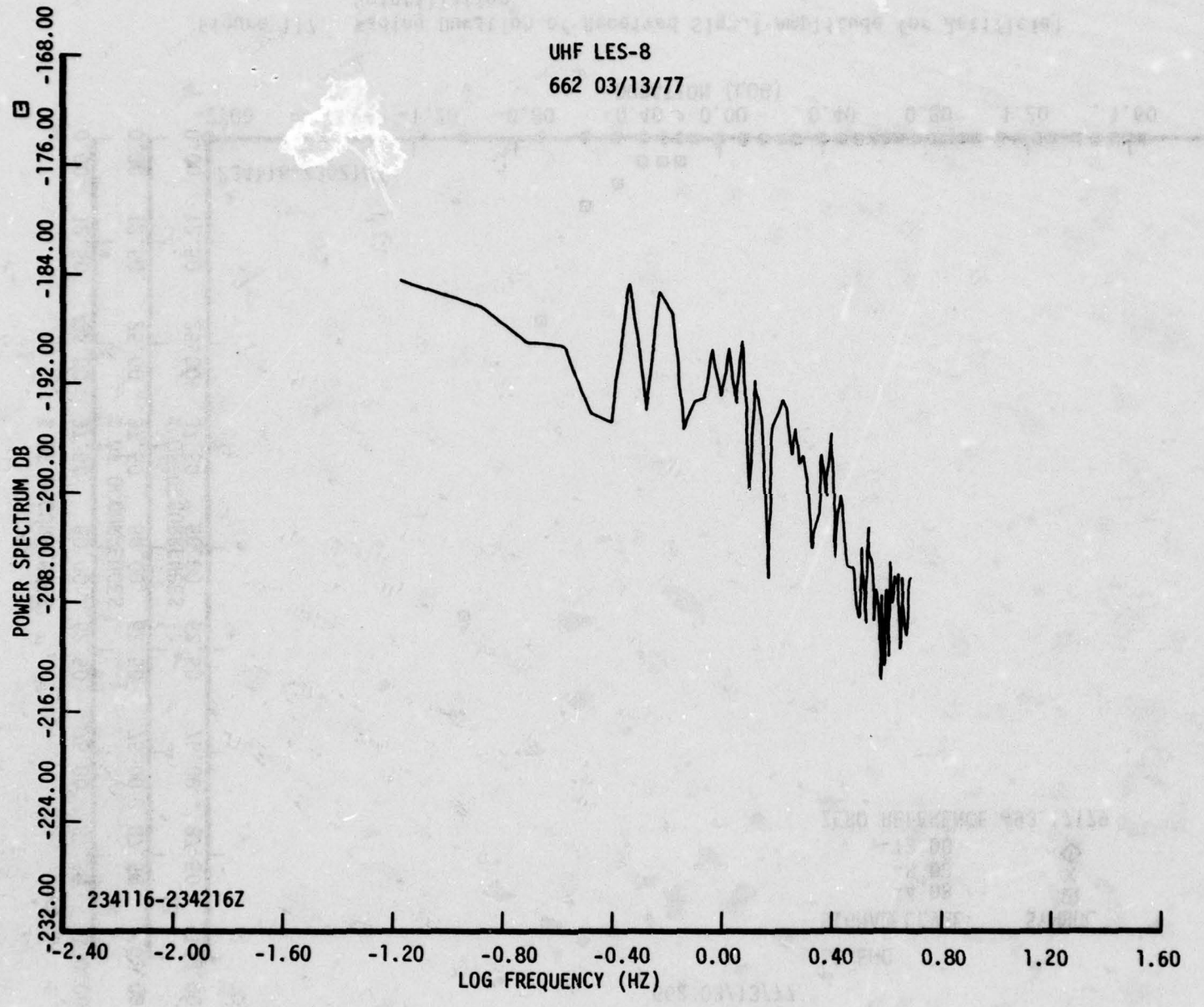

Figure 116. Power Spectrum of Received Signal Amplitude for Artificial Scintillation

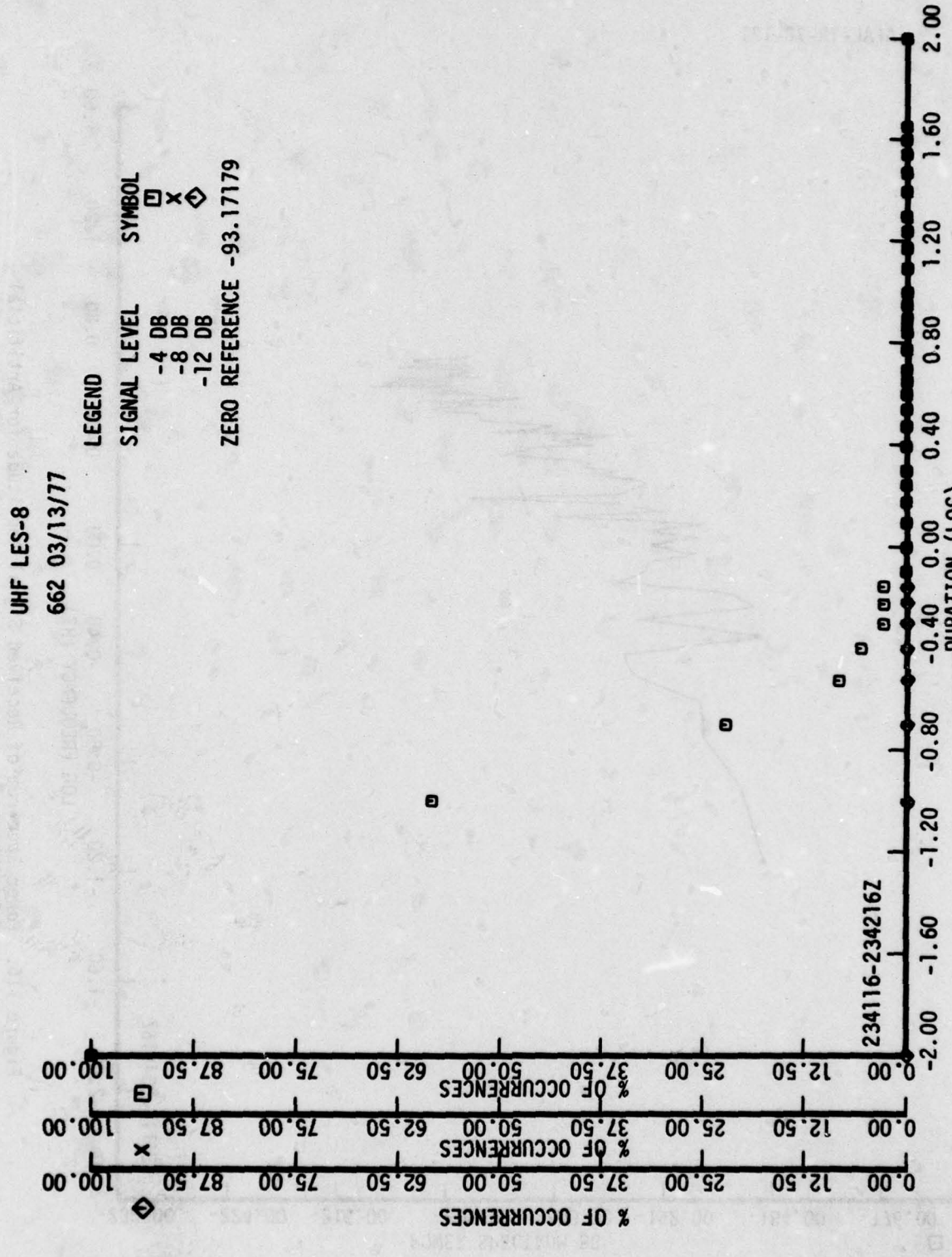

Figure 117. Fading Duration of Received Signal Amplitude for Artificial Scintillation

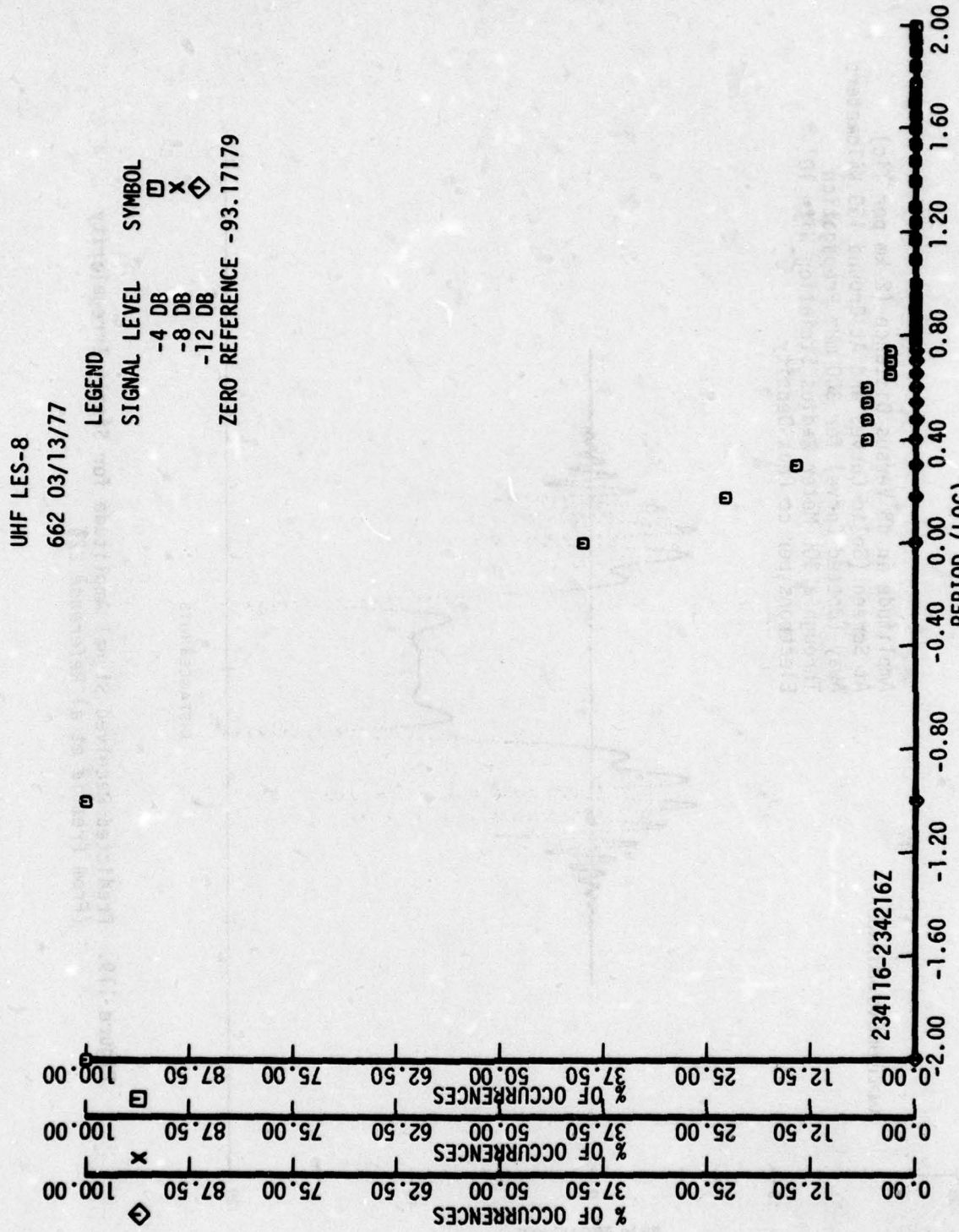

Figure 118. Fading Period of Received Signal Amplitude for Artificial Scintillation

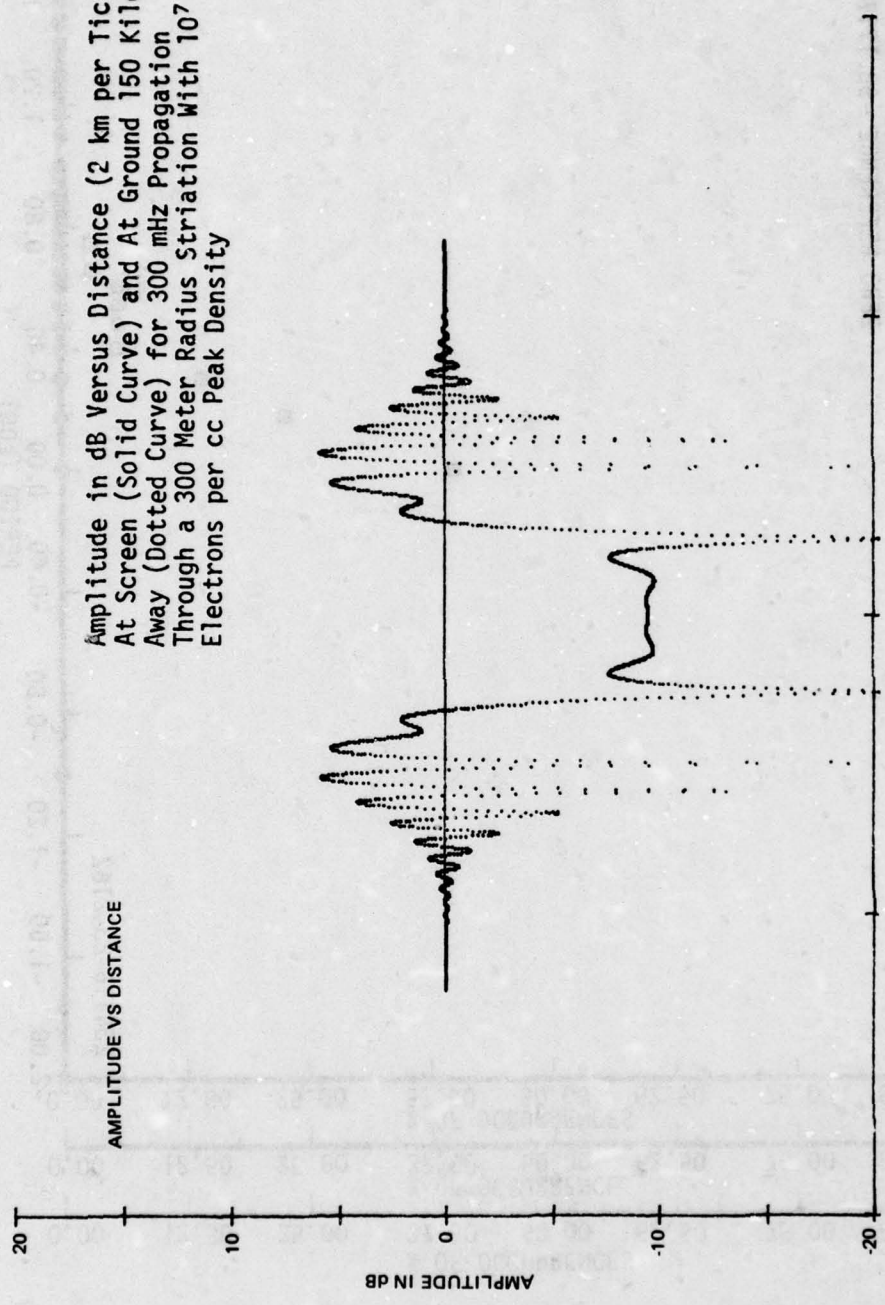

Figure 119. Predicted Received Signal Amplitude for Single Irregularity (From Prettie et al Reference 22)

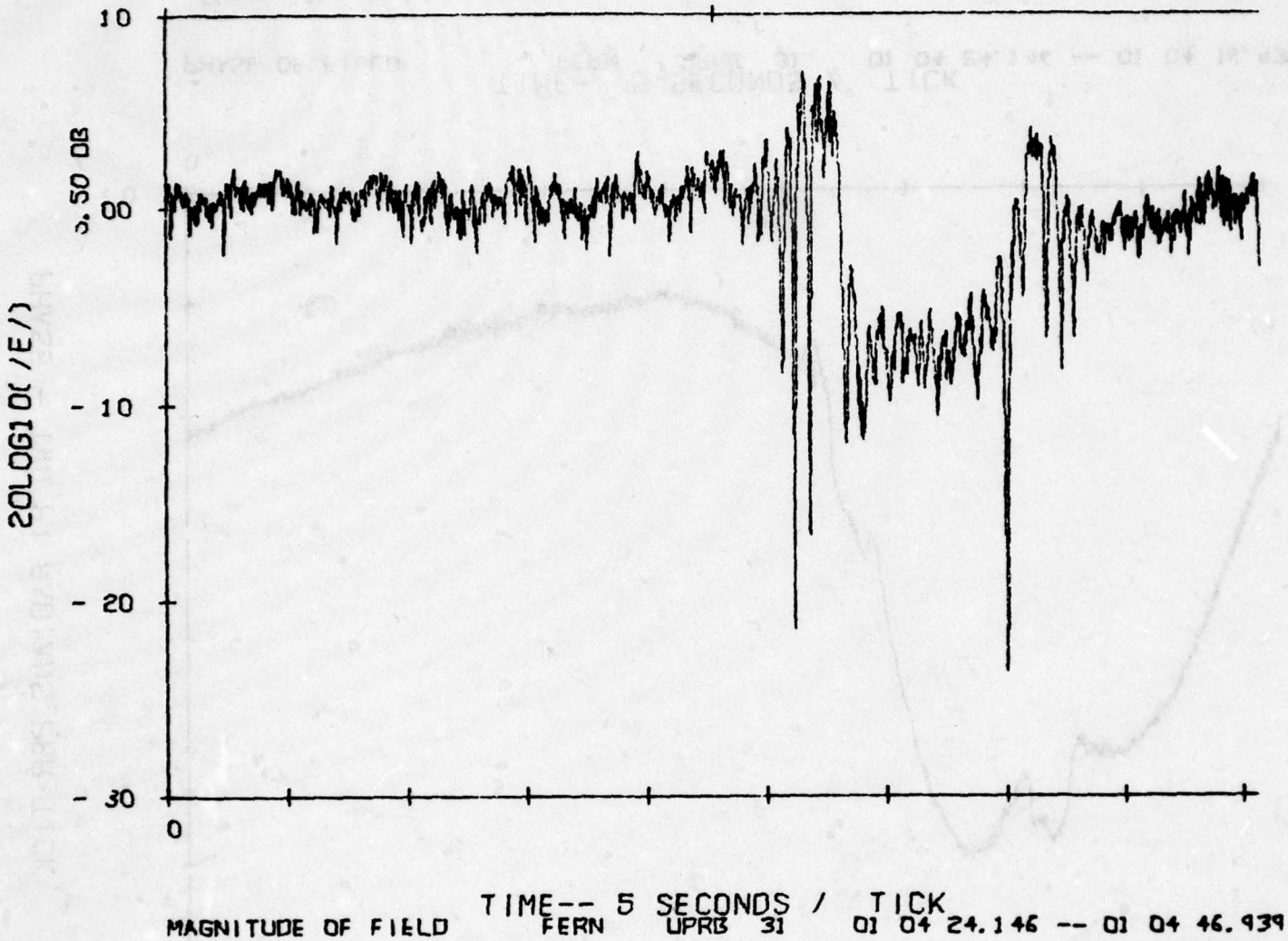

Figure 120. Measured Received Signal Amplitude (Early Time Effect)
(From Prettie Reference 16)

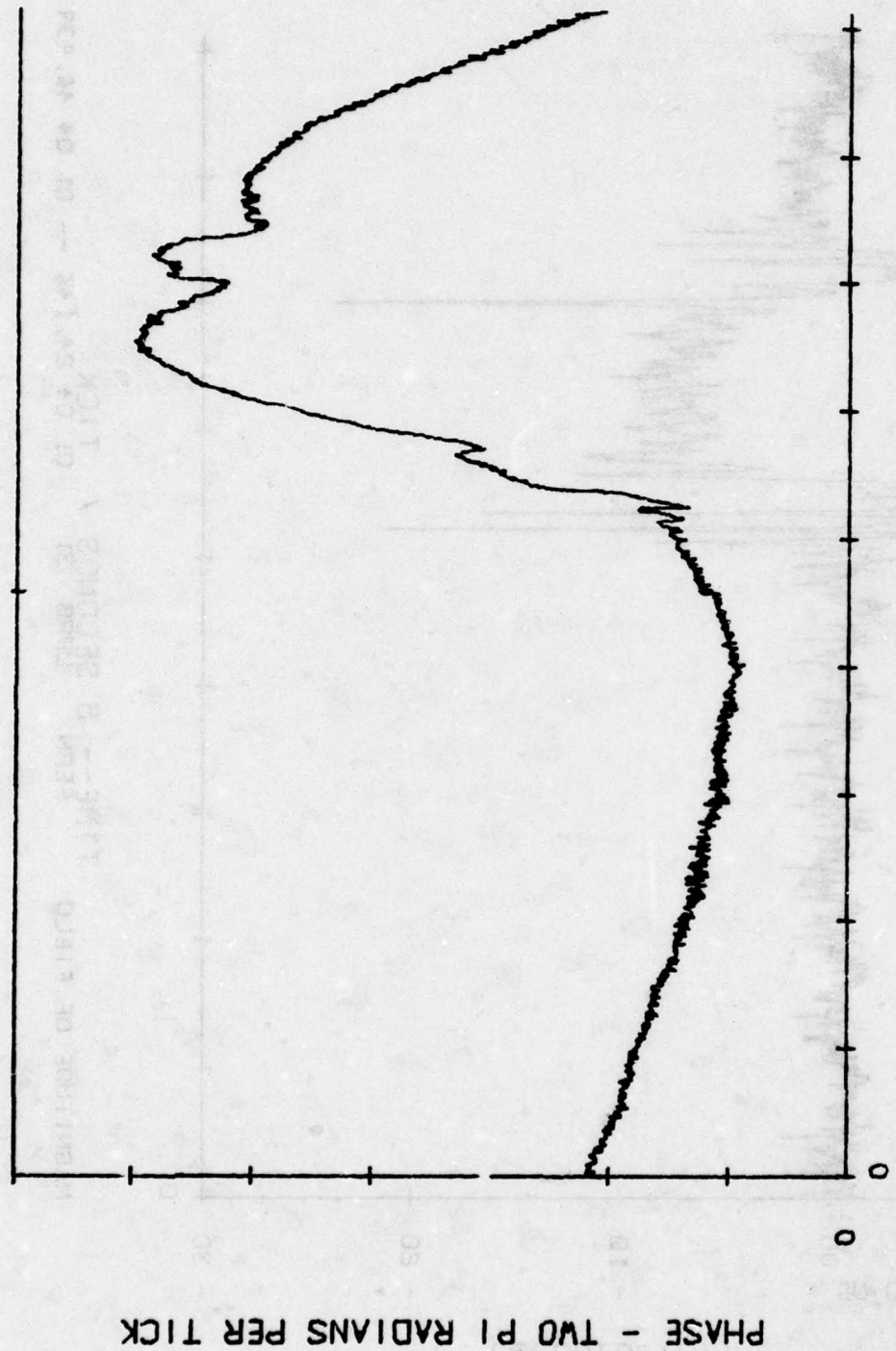

Figure 121. Received Signal Phase (Early Time Effect) - (From Prettie Reference 16)

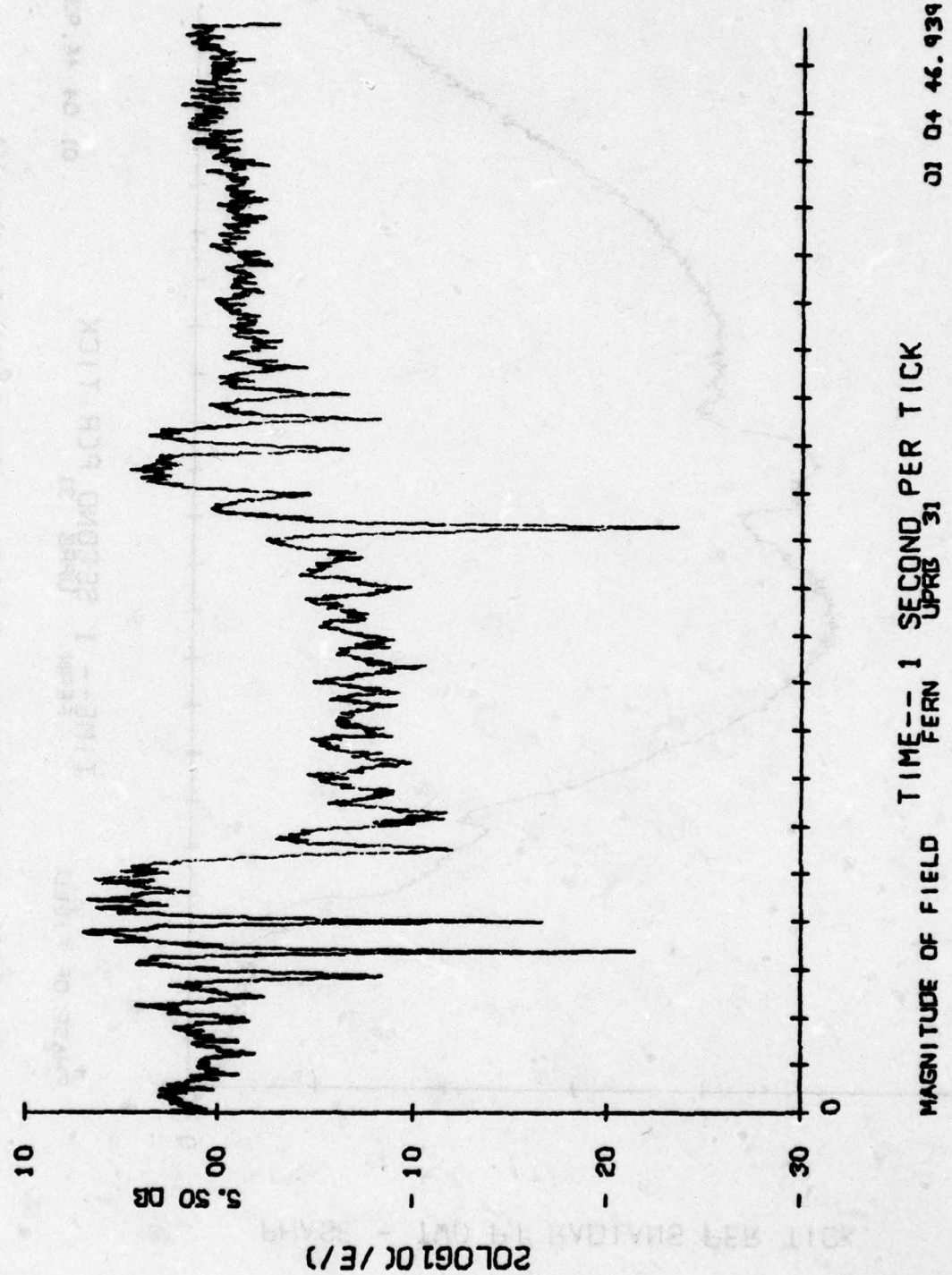

Figure 122. Expanded Received Signal Amplitude (From Prettie Reference 16)

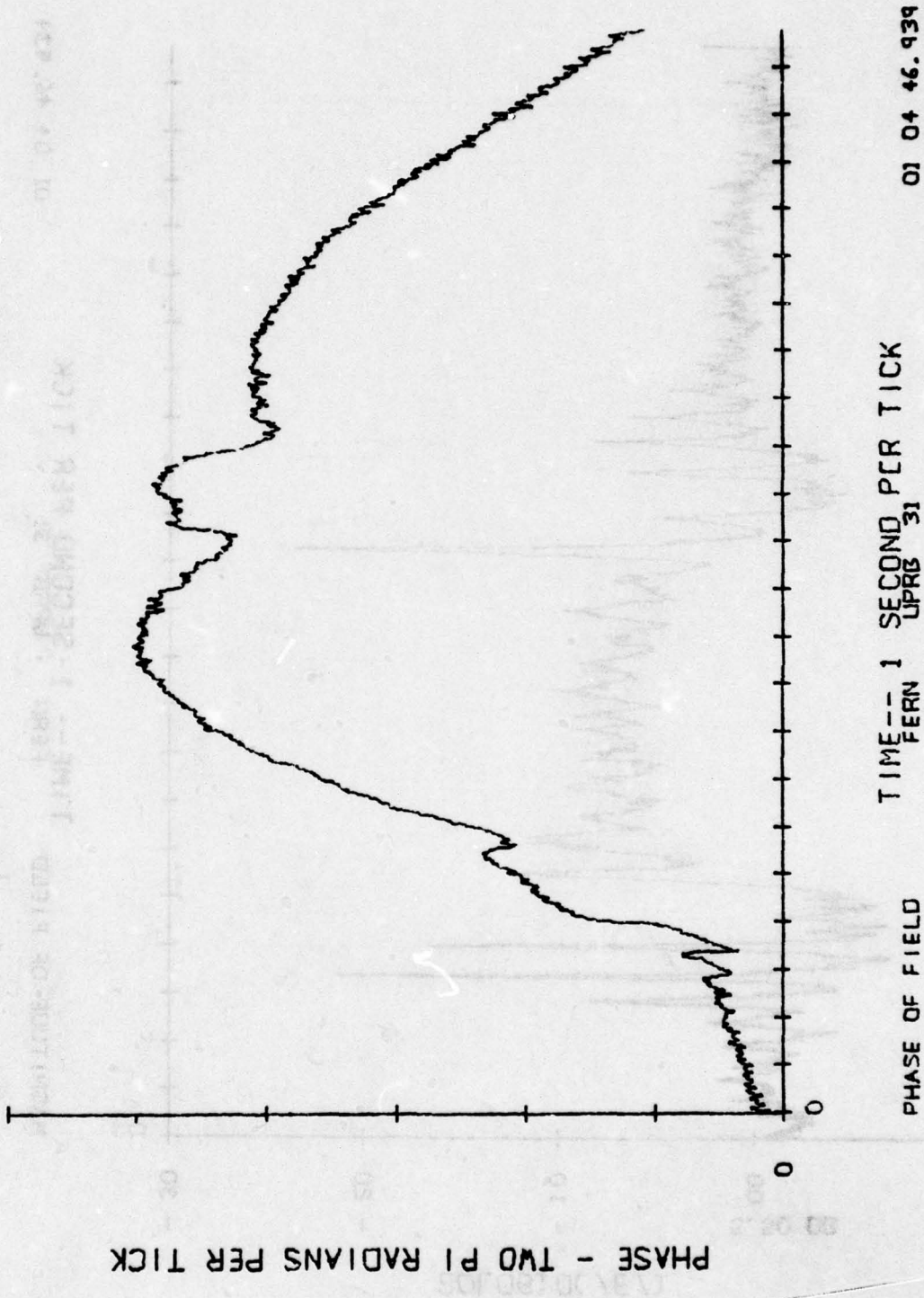

Figure 123. Expanded Received Signal Phase (From Prettie Reference 16)

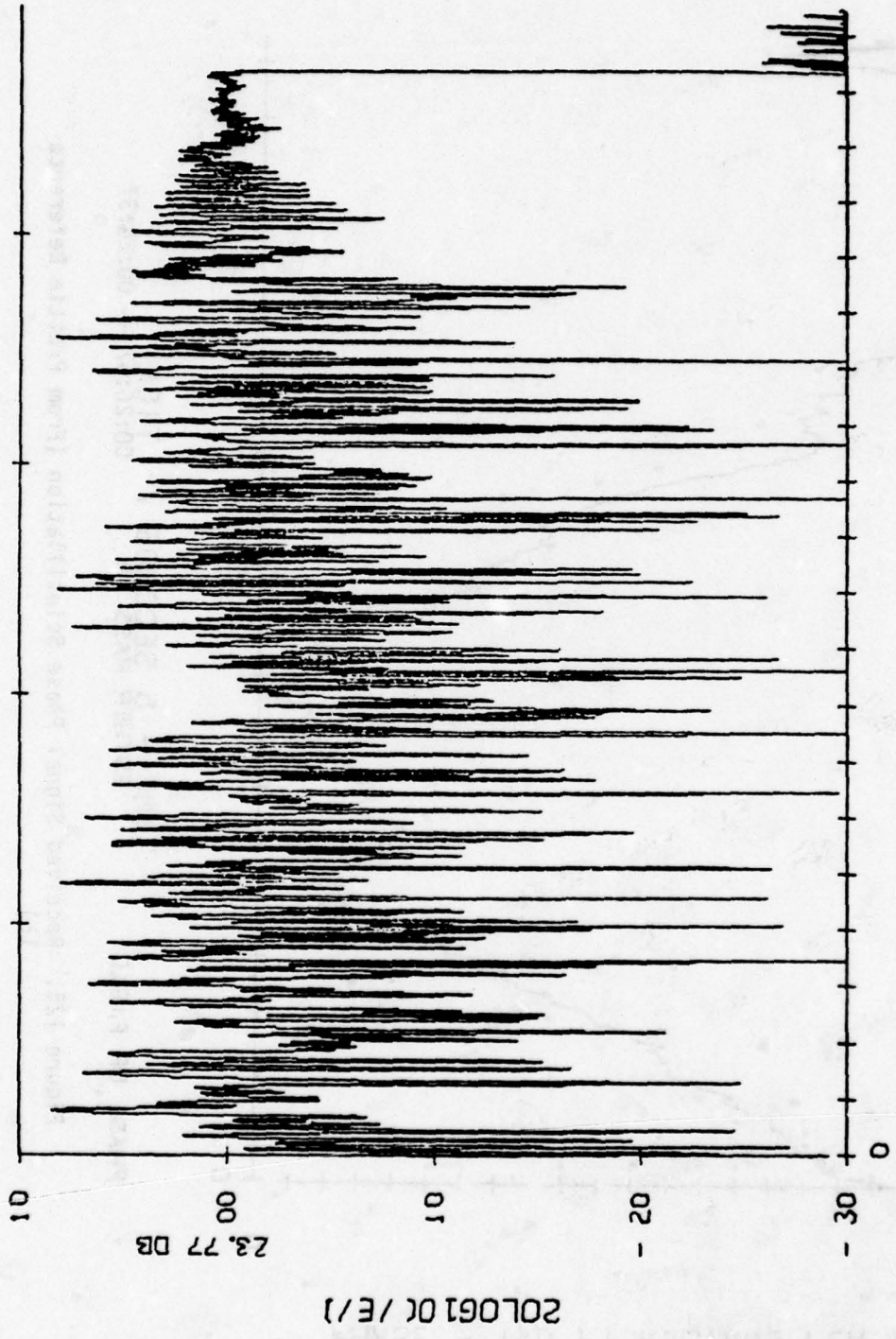

Figure 124. Received Signal Amplitude Scintillation (From Prettie Reference 16)

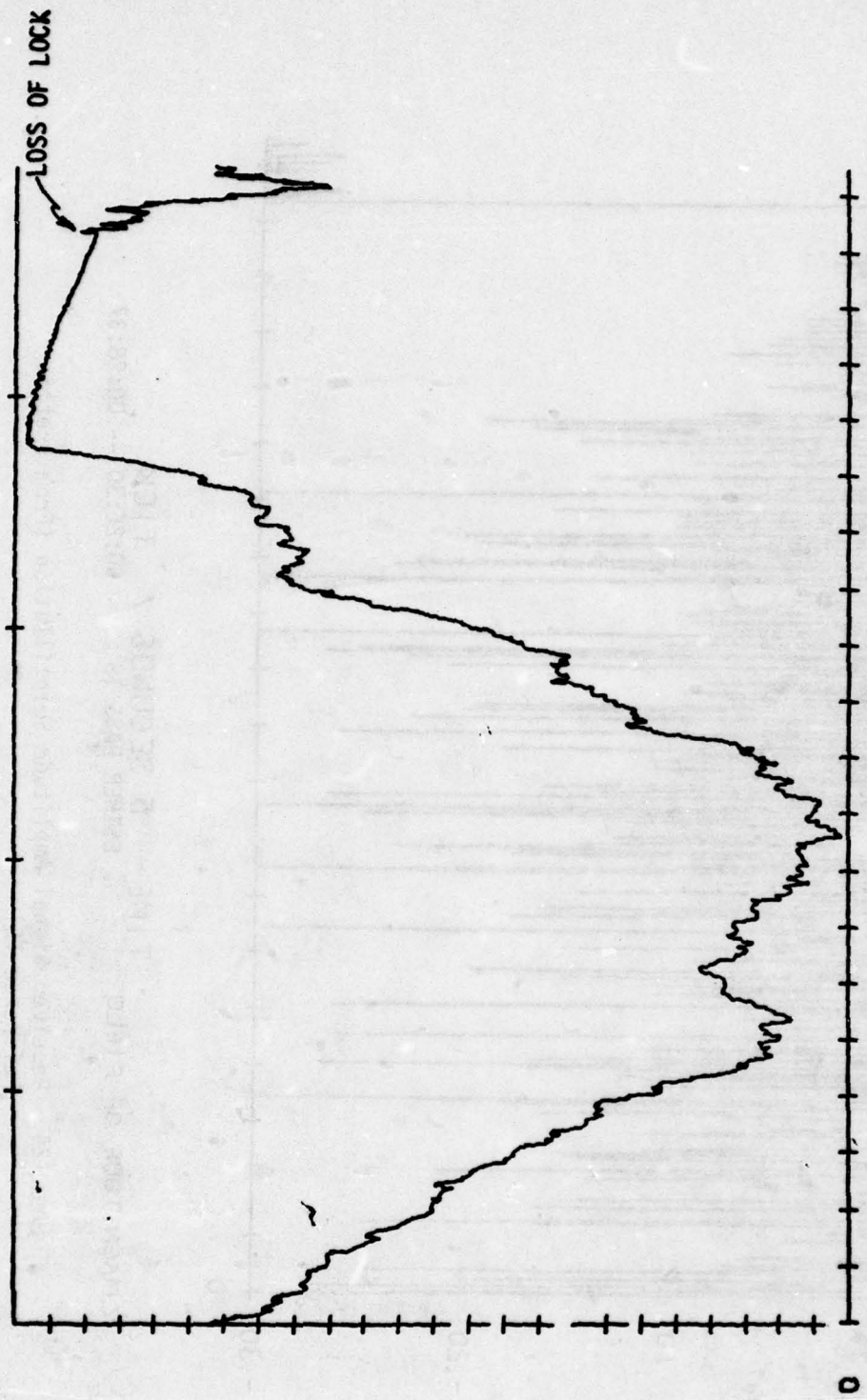

Figure 125. Received Signal Phase Scintillation (From Prettie Reference 16)

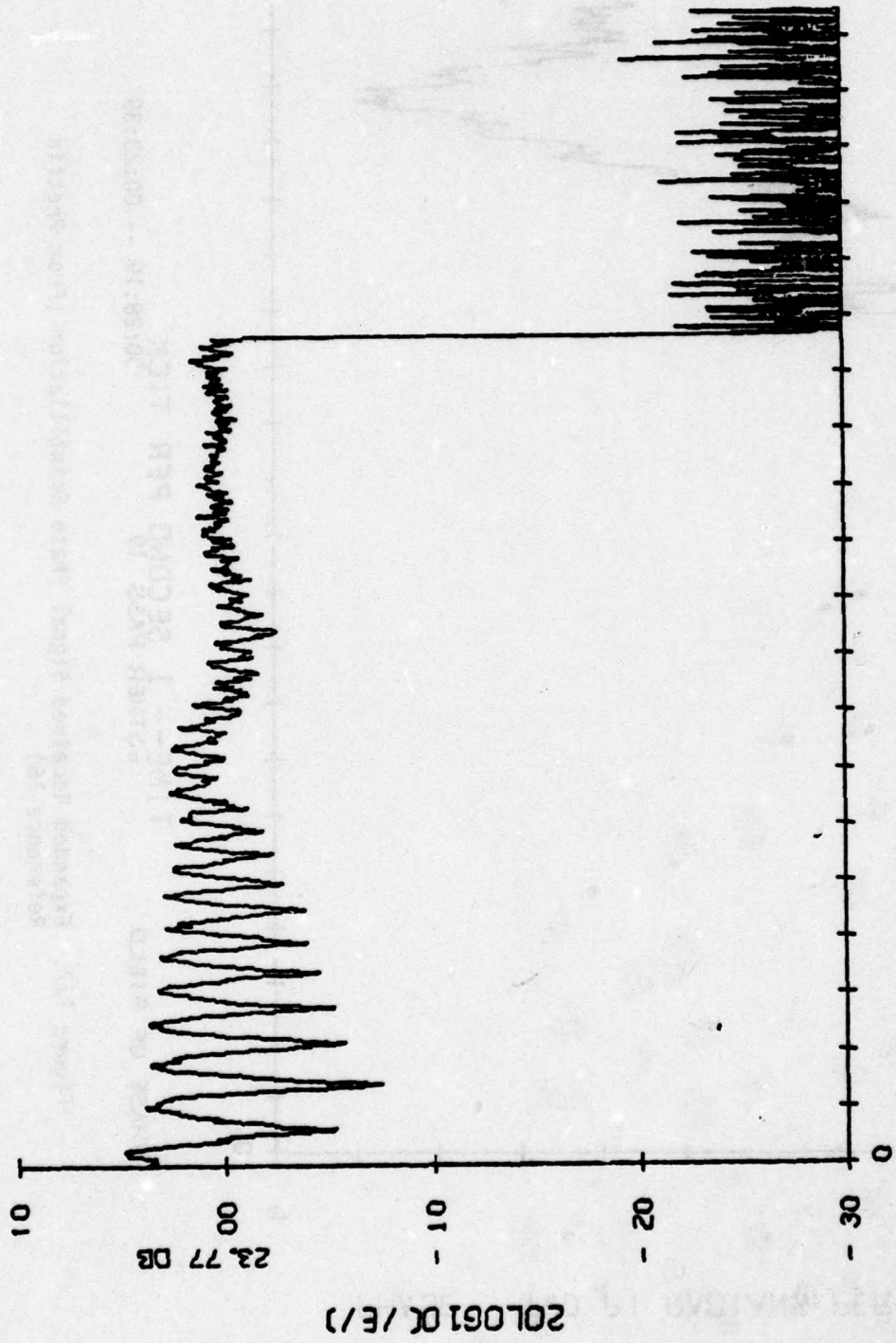

Figure 126. Expanded Received Signal Amplitude Scintillation (From Prettie Reference 16)

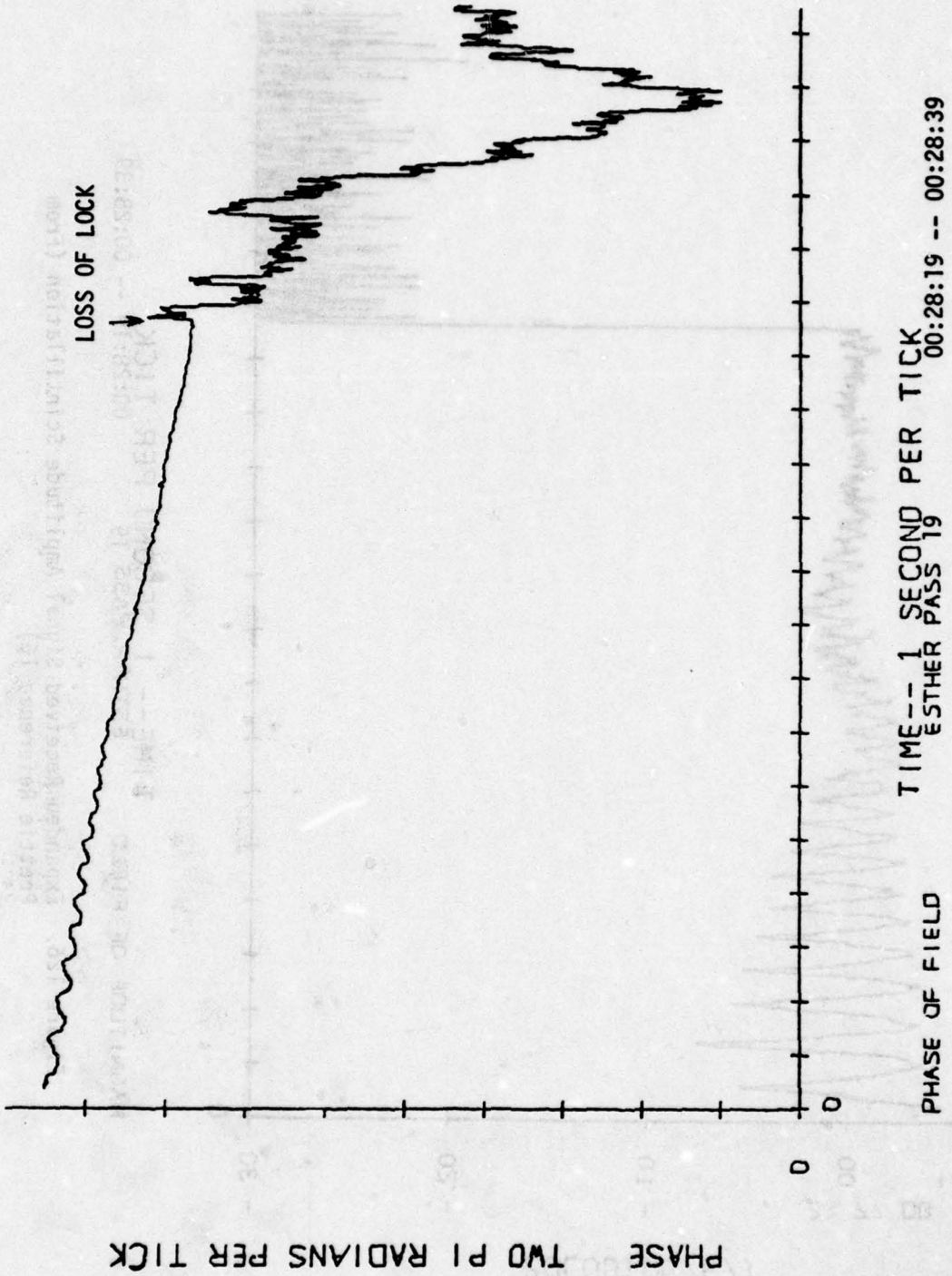

Figure 127. Expanded Received Signal Phase Scintillation (From Prettie Reference 16)

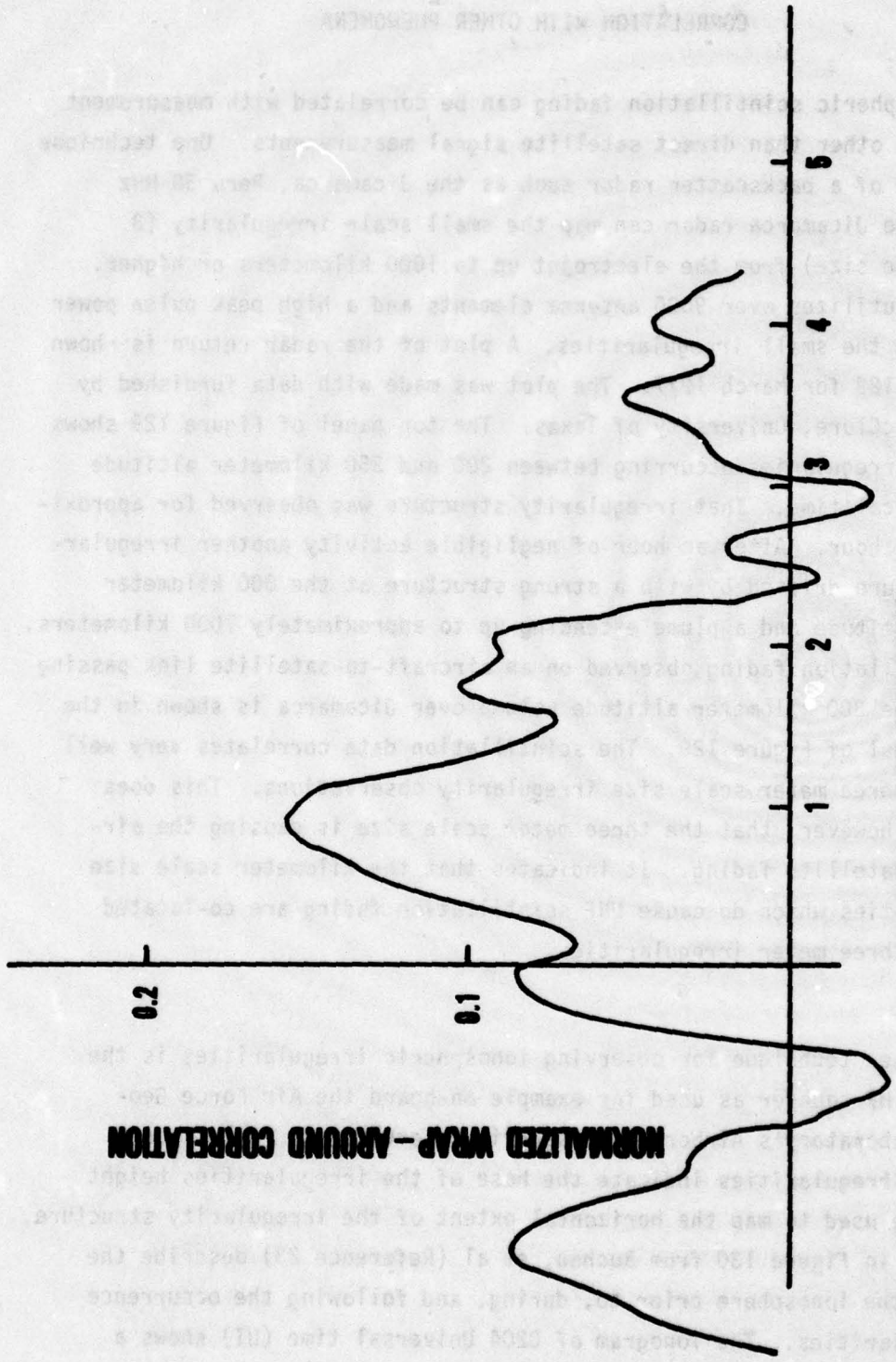

Figure 128. Cross Correlation of Uplink and Downlink Received Signal Amplitude (From Prettie et al Reference 22)

SECTION VI

CORRELATION WITH OTHER PHENOMENA

Ionospheric scintillation fading can be correlated with measurement techniques other than direct satellite signal measurements. One technique is the use of a backscatter radar such as the Jicamarca, Peru 50 MHz radar. The Jicamarca radar can map the small scale irregularity (3 meter scale size) from the electrojet up to 1000 kilometers or higher. Jicamarca utilizes over 9000 antenna elements and a high peak pulse power to measure the small irregularities. A plot of the radar return is shown in Figure 129 for March 1977. The plot was made with data furnished by Dr. Phil McClure, University of Texas. The top panel of Figure 129 shows a strong irregularies occurring between 200 and 350 kilometer altitude at 1940 local time. That irregularity structure was observed for approximately one hour. After an hour of negligible activity another irregularity structure drifted by with a strong structure at the 300 kilometer minimum altitude and a plume extending up to approximately 1000 kilometers. The scintillation fading observed on an aircraft-to-satellite link passing through the 300 kilometer altitude volume over Jicamarca is shown in the bottom panel of Figure 129. The scintillation data correlates very well with the three meter scale size irregularity observations. This does not mean, however, that the three meter scale size is causing the aircraft-to-satellite fading. It indicates that the kilometer scale size irregularities which do cause UHF scintillation fading are co-located with the three meter irregularities.

Another technique for observing ionospheric irregularities is the use of an HF sounder as used for example on-board the Air Force Geophysics Laboratory's Airborne Ionospheric Observatory. Reflections from the irregularities indicate the base of the irregularities height and can be used to map the horizontal extent of the irregularity structure. The plots in Figure 130 from Buchau, et al (Reference 23) describe the state of the ionosphere prior to, during, and following the occurrence of irregularities. The ionogram of 0204 Universal time (UT) shows a

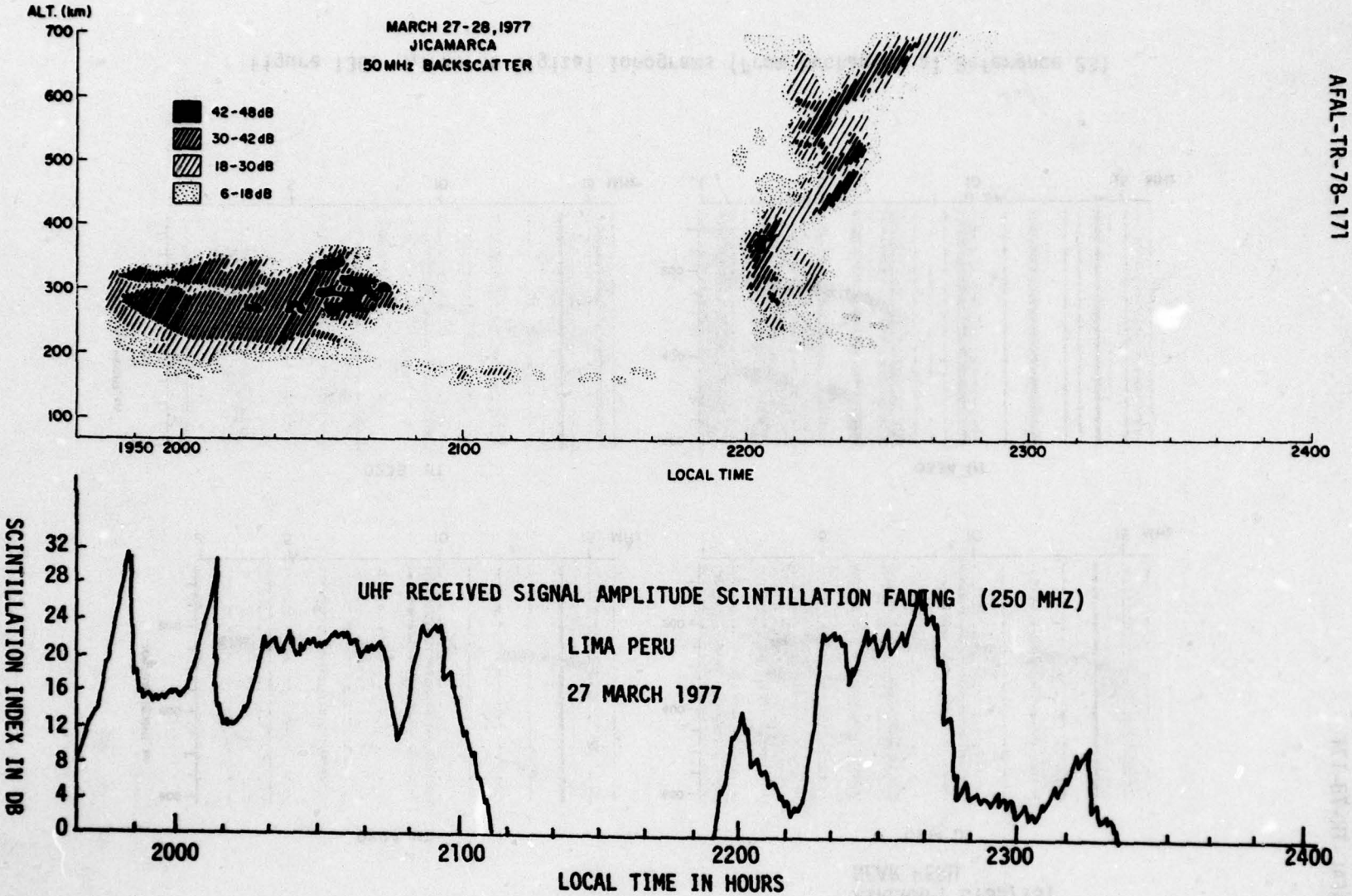

Figure 129. Comparison of 50 MHz Jicamarca Radar Return and 250 MHz Scintillation Fading

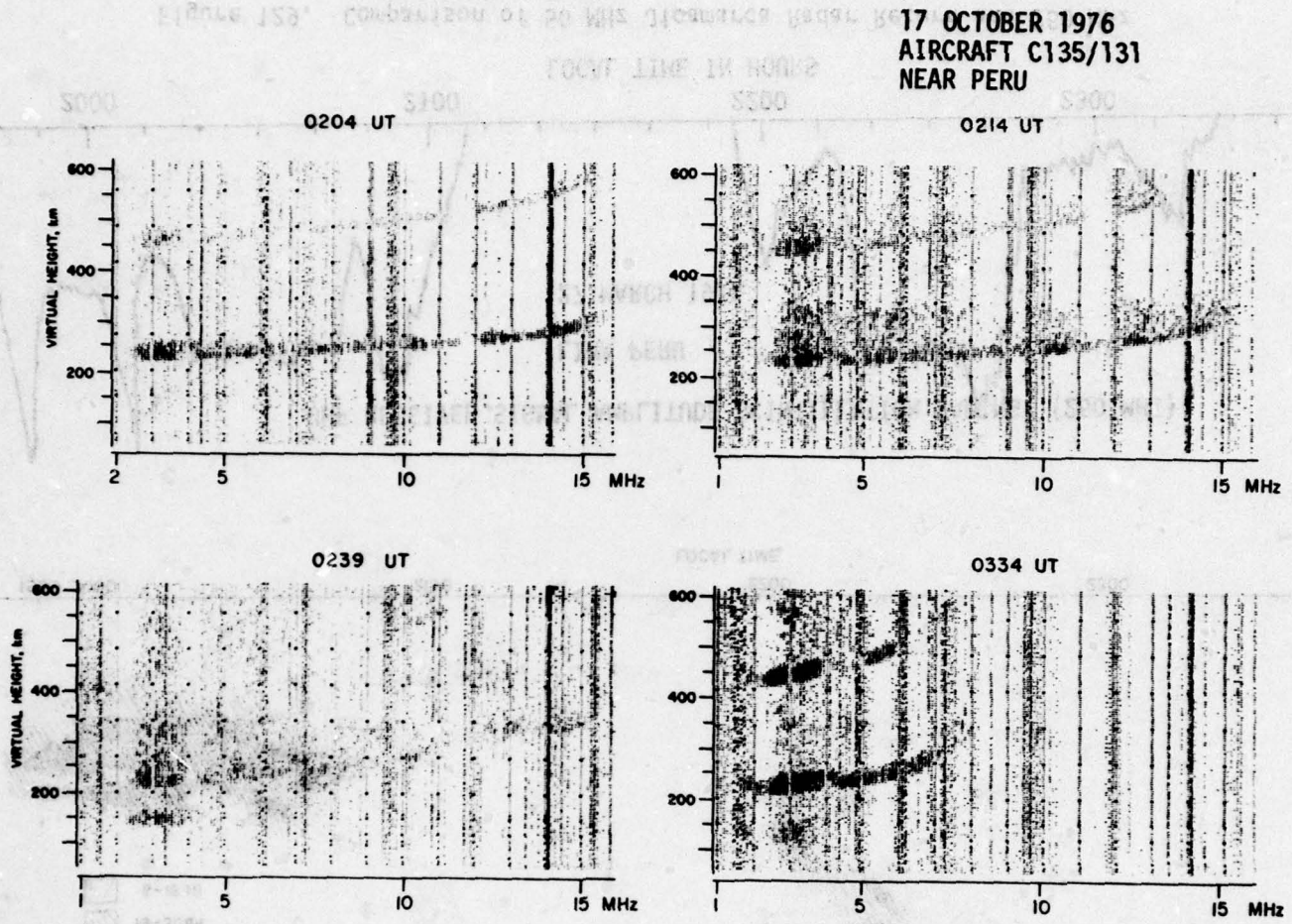

Figure 130. Airborne Digital Ionograms (From Buchau et al Reference 23)

typical night time ionosphere. The narrowness of the traces indicates a well-defined smooth F layer and the absence of irregularities. The 0214 UT frame shows a typical spread F ionogram, indicating the presence of F region irregularities. These irregularities appeared simultaneously with the onset of deep UHF scintillation fading observed on a ray path through this ionosphere. The echoes observed at 0239 UT show strong spread F and a well-defined oblique trace in the spread, indicating the presence of a large scale irregularity. The final ionogram at 0234 UT indicates the restoration of quiet ionospheric conditions with the absence of irregularities. The UHF scintillation fading quit as the ionosphere approached its undisturbed state.

A new observation technique being used by the Air Force Geophysics Laboratory is the large scale mapping of the 6300 Å air glow emission with an airborne imagining all sky photometer. The 6300 Å emission is a measure of the electron content of the lower F region. Any structure in the lower F region is thus observable as a structure in the airglow images. The results shown in Figure 131 from Weber et al (Reference 15) show a depletion region extending from horizon to horizon in the north-south direction, moving in a westerly to easterly direction. The airglow depletion region first appears on the western horizon around 0200 UT. It moves to an overhead position around 0330 UT. The depletion region had dimensions of at least 1200 kilometers north-south by approximately 165 kilometers east-west. The region was traveling at a velocity of 92 m/sec, reaching the eastern horizon around 0430 UT. This depletion region correlated with the Jicamarca backscatter and observed UHF scintillation fading Buchau et al (Reference 24).

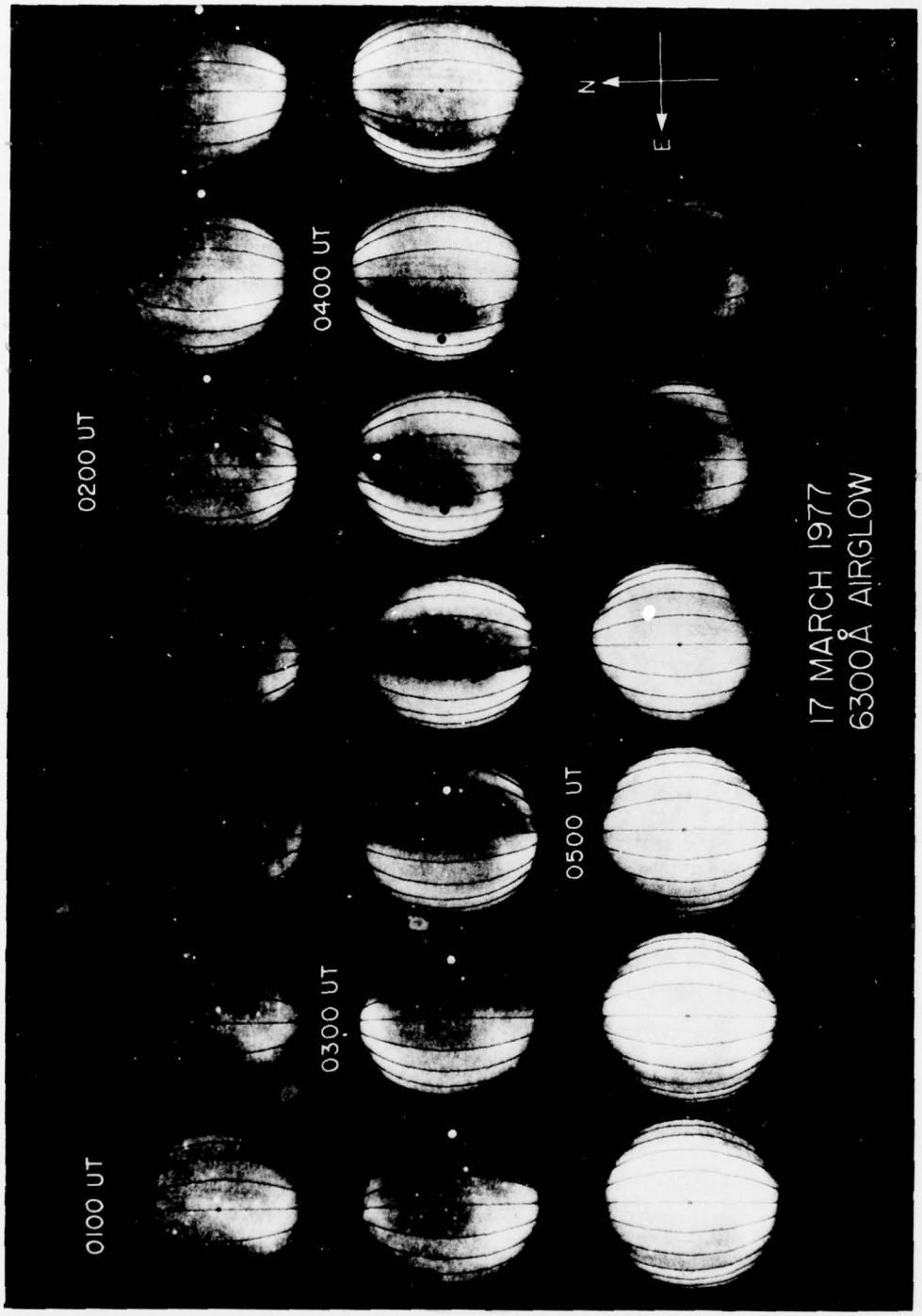

Figure 131. 6300 Å Airglow Showing Electron Depletion in Equatorial Ionosphere (From Weber et al Reference 15)

SECTION VII

MITIGATION TECHNIQUES

The obvious mitigation techniques such as avoiding the scintillation region or providing sufficient link margin to overcome the scintillation often do not prove to be practical. Antenna diversity with antennas spaced up to a kilometer apart has been shown to be extremely effective by Naval Ocean Systems Center (NOSC), Paulson and Hopkins (Reference 6). By utilizing a predetection combiner, the error rate during a scintillation period was reduced from an unacceptable 10^{-2} to an undetectable error rate. Unfortunately for airborne applications antenna spacings of greater than 30 meters are not practical. Therefore, the antenna diversity, or antenna spacing technique, remains applicable primarily to ground systems.

Sufficient frequency separation accompanied by some type of combining technique will provide adequate performance in a scintillation fading environment. Measurements by Fremouw of the DNA 002 satellite et al (Reference 8) and by Prettie et al (Reference 22) during the barium cloud experiment showed that at UHF frequencies decorrelation can occur with 50 to 100 MHz signal separation.

The use of message interleaving and error correction coding or time diversity appears to be a very practical mitigation technique. The results of the Air Force Avionics Laboratory's (AFAL) fade resistant modem test, Fischbach (Reference 25) and Air Force Weapons Laboratory (AFWL) simulations, Wittwer (Reference 26), show that interleaving and coding can significantly improve the performance of the communications system. The interleaving and coding technique should be tailored to the fade rate and fade duration expected to optimize the message throughput.

The use of satellite diversity, two satellites relaying the same message, can successfully overcome the effect of the scintillation fading. Cross correlation plots of the two UHF satellites taken during the Peru Test (Figure 132) showed a correlation coefficient of 0.1 or

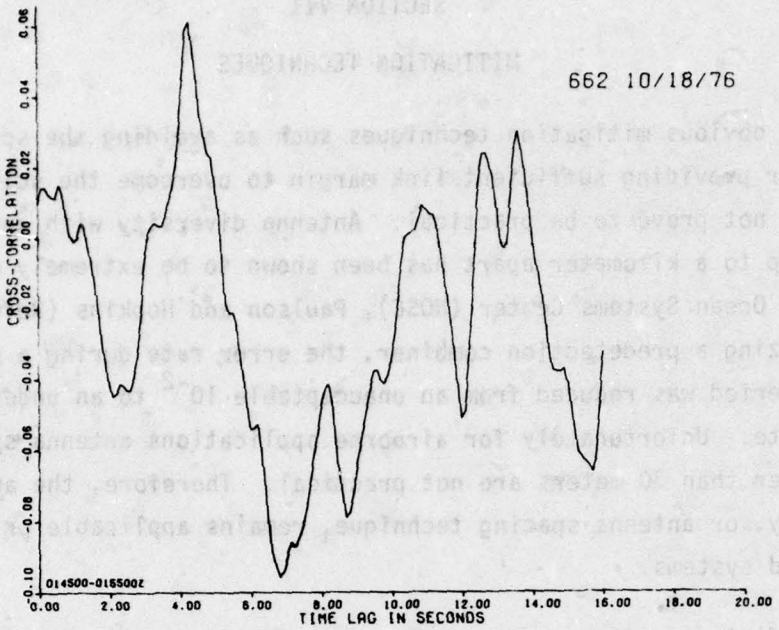

Figure 132. Cross Correlation Function of Received Signal Amplitude on Two UHF Satellites

less was achieved. The ionospheric intersection points for this example were separated by more than 300 kilometers. Some type of combining or switching would be required to utilize the unfaded signal.

Another technique which has been suggested for mitigating the effect of the fading is to use a path diversity to the satellite by utilizing the multipath situation available to an airborne receiver. As shown in Figure 133, one path would be the direct path to an antenna on top of the aircraft, while a second path would be via a multipath reflection off of the earth's surface to antenna on the bottom of the aircraft. These two signal paths are sufficiently separated as they traverse the ionosphere to make any ionospheric fading they encounter uncorrelated. Therefore, the combination of the signal received on the top and bottom of the aircraft can significantly improve the system performance.

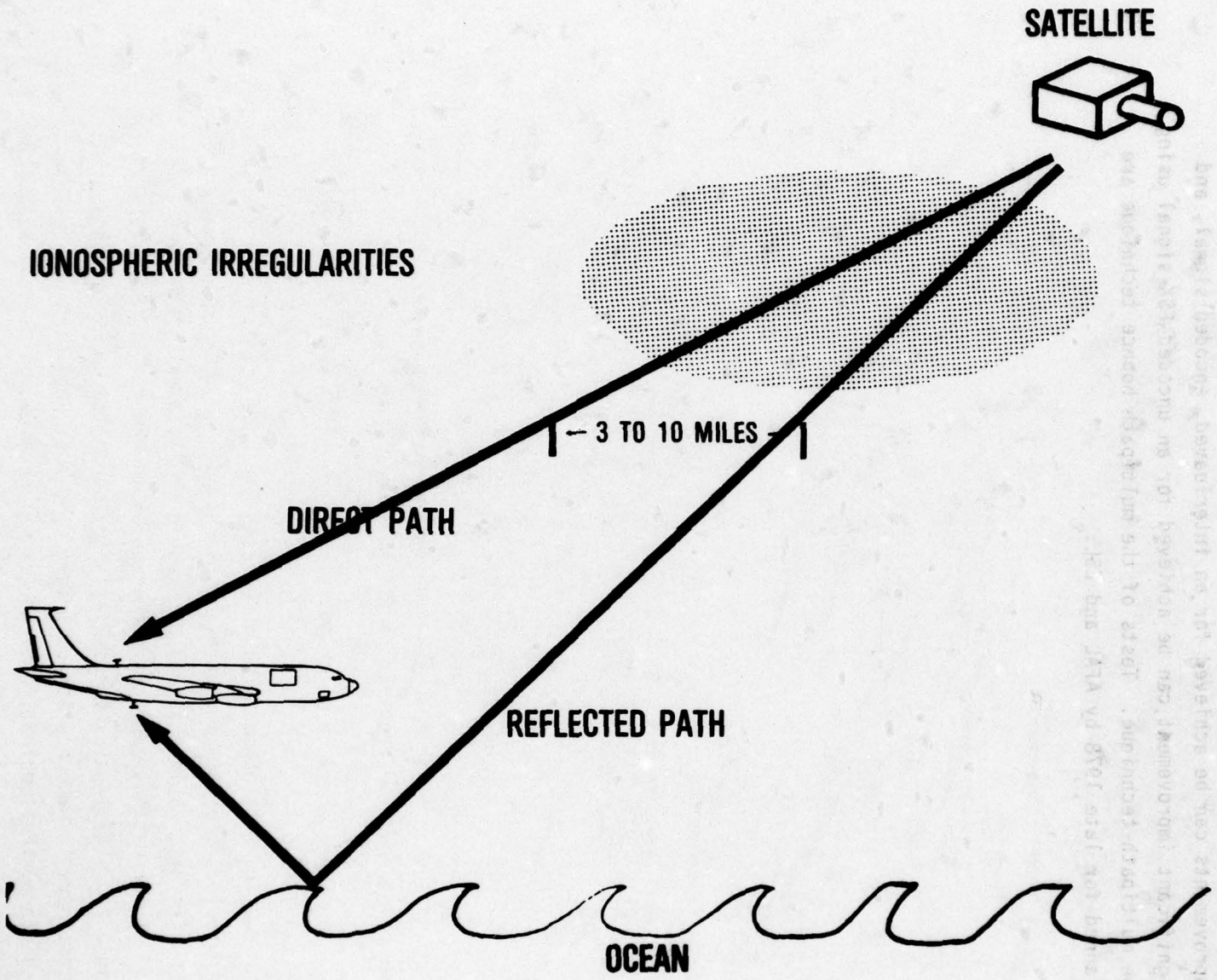

Figure 133. Geometry of Fade Mitigation Technique

A simulation of the technique, done by Prettie, indicates that moderate improvements can be achieved for an interleaved, encoded signal, and significant improvement can be achieved for an uncoded FSK signal using the multipath technique. Tests of the multipath bounce technique are planned for late 1978 by AFAL and ESL.

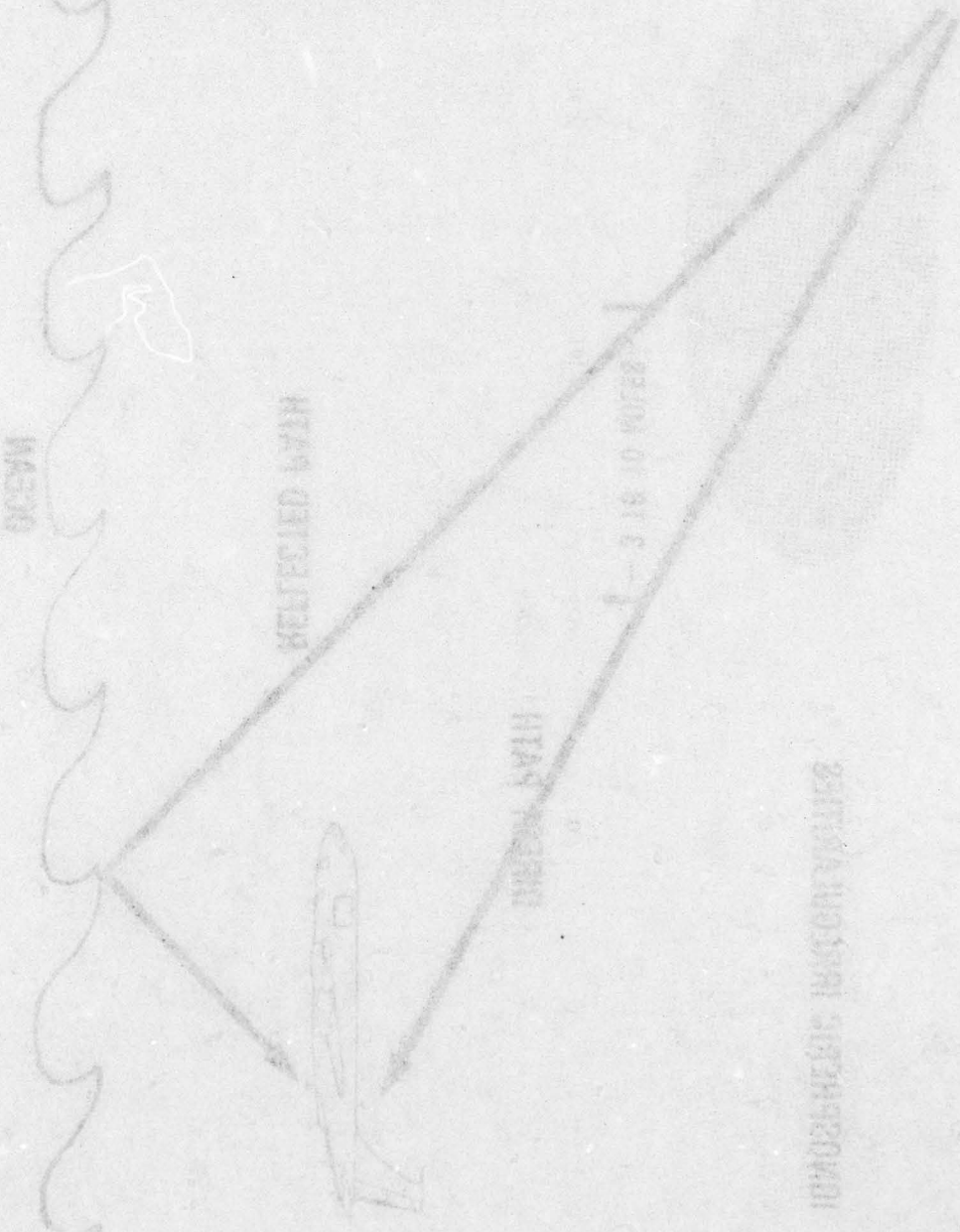

SECTION VIII

CONCLUSIONS

Ionospheric scintillation fading in the equatorial regions has a strong seasonal dependence. In some equatorial areas, such as Peru, the fading peaks during the two equinox periods. In other areas, such as the western Pacific, the fading appears to peak during the local summer period. The equatorial fading is, in general, limited to a region of $\pm 20°$ from the magnetic equator. The fading is generally extremely deep when it does occur. Data taken by AFGL indicates that 25 dB fades are just as likely to be encountered as 5 dB fades, Figure 134. The onset of fading usually occurs 1 to 2 hours after local sunset. Fading may occur sporadically over the next 4 to 5 hour period. An aircraft may experience fade rates from one fade per second to as low as one fade in 90 seconds. The corresponding duration of the fade is from a tenth of a second to 10 or 15 seconds, depending upon aircraft flight direction. The amplitude of equatorial fading is frequency dependent with a dependence of approximately f^{-2}. The phase scintillation which accompanies the amplitude scintillation does not appear to be rapid enough to affect moderate data rate phase modulated communication systems.

In the Polar region an airborne terminal can be expected to encounter scintillation more often but with less amplitude than in the equatorial region. Scintillation at Ultra High Frequencies is often encountered during the daylight hours in the Polar region but almost never in the equatorial region. Fade rates of one cycle in five seconds to one cycle in 30 seconds may be experienced. Amplitude fading depths of 5 to 10 dB can be expected. Slightly stronger phase scintillation may be experienced in the Polar region, but this phase scintillation still appears to offer no problem to a moderate data rate phase modulated communication signal.

Interleaving, coding on a multipath bounce mitigation techniques can greatly improve system performance during ionospheric scintillation fading in the Equatorial or Polar regions. However, due to the smaller fading amplitude in the Polar region, it may be more economical to just

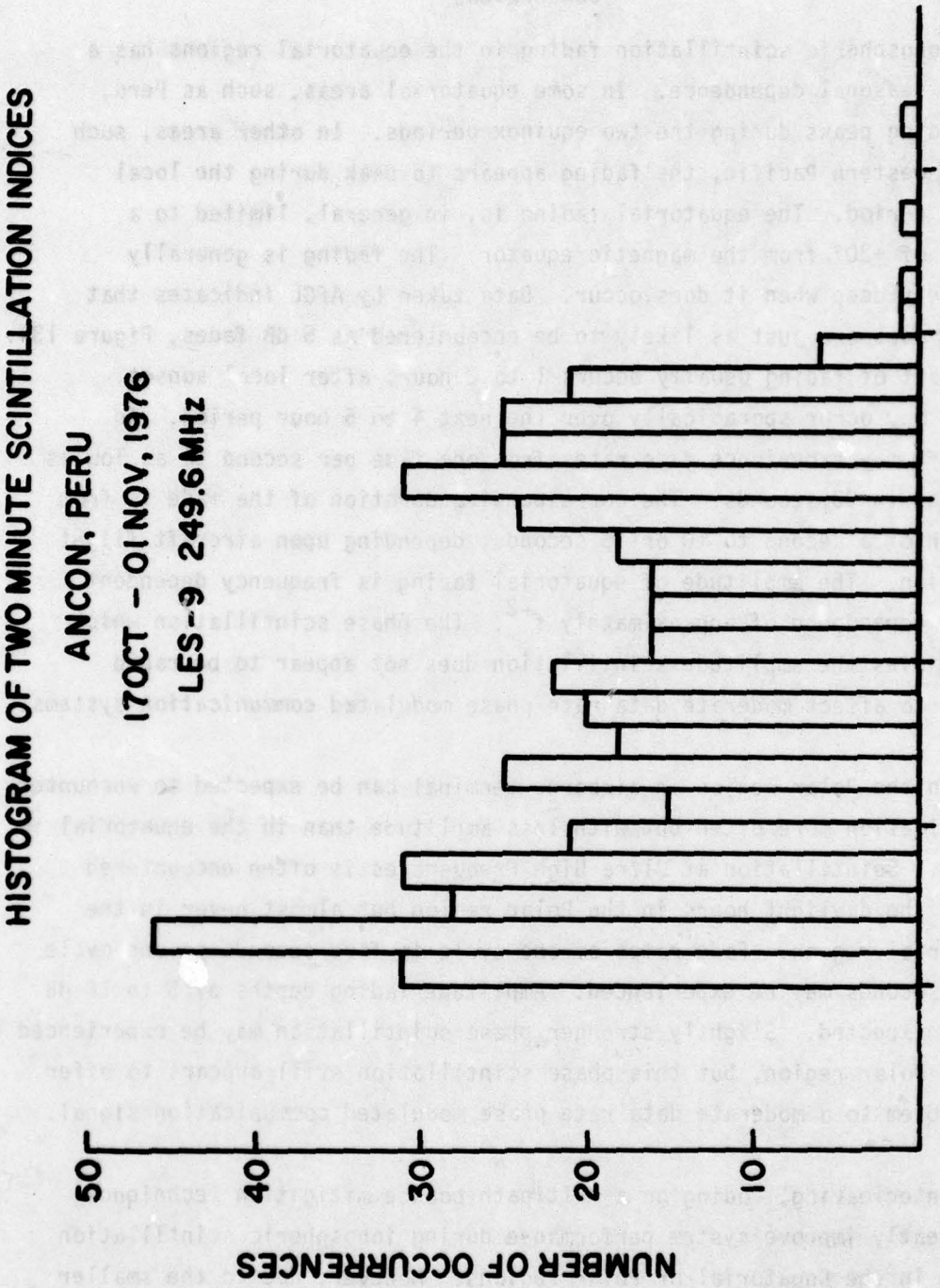

Figure 134. Histogram of Scintillation Index Levels for Ancon Peru (From Whitney et al Reference 14)

increase the system fade margin to 10 dB which will significantly reduce the fading problem in the Polar region.

Fading in the midlatitude region occurs very seldom and, when observed, is usually weak. Therefore, the effect of ionsopheric scintillation fading in midlatitudes is expected to be small when compared with other airborne satellite communication system problems such as antenna blockage and multipath fading.

REFERENCES

1. Aarons, J. (Ed.) A Survey of Scintillation Data and Its Relationship to Satellite Communications; AFCRL-70-0053, Air Force Cambridge Research Laboratories, L. G. Hanscom Field, Mass., January 1970.

2. Aarons, J., Whitney, H., Allen, R., Seemann, D., High Latitude Models; Observations and Analysis of Ionospheric Scintillation; AFCRL-TR-73-0048, Air Force Cambridge Research Laboratory, L. G. Hanscom Field, Mass., 12 January 1973.

3. Aarons, J., Buchau, J., Mullen, J., Weber, E., Whalen, J., Whitney, H.: Ground and Airborne Scintillation Studies of AFSATCOM DT&E/IOT&E; AFGL-TR-76-0164, Air Force Geophysics Laboratory, L. G. Hanscom Field, Mass., 2 August 1976.

4. Aarons, J. Equatorial Scintillation: A Review; AFGL-TR-76-0078, Air Force Geophysics Laboratory, L. G. Hanscom Field, Mass., 13 April 1976.

5. Aarons, J., Mullen, J., Whitney, H., Martin, E., Bhavhina, K., Whalen L., A High-Latitude Empirical Model of Scintillation Excursion: Phase I; AFGL-TR-76-0210, Air Force Geophysics Laboratory, L. G. Hanscom Field, Mass., 17 September 1976.

6. Paulson, M. R., Hopkins RUF, Spatial Distribution Characteristics of Equatorial Scintillation, NOSC-TR-113, Naval Ocean Systems Center, San Diego, Calif., 2 May 1977.

7. Crane, R. K., Morphology of Ionospheric Scintillation; Lincoln Laboratory Technical Note 1974-29, Lexington, Mass., 21 May 1974.

8. Rino, C. L., Fremouw, E. J., Livingston, R. C., Cousins, M. D., Fair, B. C.; Wideband Satellite Observations; DNA-4399F, Defense Nuclear Agency, Washington, D.C., June 1977.

9. McClure, J. P., Hanscom, W. B., Hoffmann, J. H., Plasma Bubbles and Irregularities in the Equatorial Ionosphere; Journal of Geophysics Research 82:2650 - 2656 -- May 1977.

10. Basu, S., Khan, B., Model of Equatorial Scintillation From In Situ Measurements; AFGL-TR-76-0080, Air Force Geophysics Laboratory, L. G. Hanscom Field, Mass., 13 April 1976.

11. Nichols, B. E., UHF Fading From A Synchronous Satellite Observed at Kwajalein October 1970 Through June 1972; Lincoln Laboratory Technical Note 1974-19, Lexington, Mass., 22 March 1974.

12. Johnson, A. L., Equatorial Ionospheric Scintillation Flight Testing, AFAL-TR-72-363, Air Force Avionics Laboratory, Wright-Patterson AFB, Ohio, December 1972.

REFERENCES (CONTINUED)

13. Barkham, N., Scintillation Fading Data, Private Communication Advanced Development Laboratory, Salisbury, South Australia, 5 Feb 1977.

14. Whitney, H. E., Buchau, J., Johnson, A. L., Mullen J. P., Weber, Capt and E. J., Report on Peru Scintillation Test-October 1976 and March 1977 AFGL-TR-77-0282. Air Force Geophysics Laboratory Hanscom AFB, MA, 8 December 1977.

15. Weber, Capt, E. J., Buchau, J., Eather, R. H., Mende, S. B., North-South Aligned Equatorial Airflow Depletions, Journal of Geophysical Research Vo. 83 No. A2 pp 712-716, 1 February 1978.

16. Prettie, C., Scintillation Amplitude And Phase Results; Private Communications, ESL Inc. Sunnyvale, Calif. May 1978.

17. Johnson, A. L., Beach, R. C., Grizinski, T. A.; UHF/SHF Ionospheric Scintillation Test, AAI-TM-73-6, Air Force Avionics Laboratory, Wright-Patterson AFB, OH, 8 April 1973.

18. Johnson, A. L., Test Results From June 1977 Polar Flight Test; AFAL-TM-77-57-AAD; Air Force Avionics Laboratory, Wright-Patterson AFB, Ohio, 8 October 1977.

19. Johnson, A. L., (1977) Greenland Flight Test Report; Air Force Avionics Laboratory, Memo Wright-Patterson AFB, Ohio, 29 January 1977.

20. Mass, J., Houminer Z., Ionospheric Research Using Satellites; AFCRL-TR-69-0317, Air Force Cambridge Research Laboratory, L. G. Hanscom Field, Mass., 28 February 1969.

21. Slack, F. F., The Ringing Irregularity In Ionospheric Scintillation; AFCRL-68-0263, Air Force Cambridge Research Laboratories, L. G. Hanscom Field, Mass., May 1968.

22. Prettie, C., Johnson, A., Marshall, J., Grizinski, T., Swanson, R., Project STRESS Satellite Communication Test Results; AFAL-TR-77-158, Air Force Avionics Laboratory, Wright-Patterson AFB, Ohio, July 1977.

23. Buchau, J., Weber, Capt E. J., Whitney, H. E., New Insight into Ionospheric Irregularities and Associated VHF/UHF Scintillations AGARD Conference Preprint No. 239, Digital Communications in Avionics, AGARD pp-23, Munich, Germany, 5 June 1978.

24. Buchau, J., Weber, Capt. E. J., McClure, J. P., Radio and Optical Diagnostics Applied to an Isolated Equatorial Scintillation Event; AFGL-TR-78-0080 Air Force Geophysics Laboratory, Hanscom AFB, Mass., 5 April 1978.

REFERENCES (CONCLUDED)

25. Fischbach, W. O., Fade Resistant Modem Operation With Ionospheric Scintillation; AFAL-TM-77-40-AAD, Air Force Avionics Laboratory, Wright-Patterson AFB, Ohio, 1 July 1977.

26. Wittwer, L. A., Performance of Advanced Frequency-Shift-Key Modulation Techniques in Scintillation; AFWL-TR-77-182, Air Force Weapons Laboratory, Kirtland AFB, New Mexico, February 1978.

*U.S.Government Printing Office: 1979 — 657-002/525